

1-1-2006

## Study of gas density profile about a plastic test piece under vacuum

Hari Krishnan  
*University of Nevada, Las Vegas*

Follow this and additional works at: <https://digitalscholarship.unlv.edu/rtds>

---

### Repository Citation

Krishnan, Hari, "Study of gas density profile about a plastic test piece under vacuum" (2006). *UNLV Retrospective Theses & Dissertations*. 1953.  
<http://dx.doi.org/10.25669/tp43-fghx>

This Thesis is protected by copyright and/or related rights. It has been brought to you by Digital Scholarship@UNLV with permission from the rights-holder(s). You are free to use this Thesis in any way that is permitted by the copyright and related rights legislation that applies to your use. For other uses you need to obtain permission from the rights-holder(s) directly, unless additional rights are indicated by a Creative Commons license in the record and/or on the work itself.

This Thesis has been accepted for inclusion in UNLV Retrospective Theses & Dissertations by an authorized administrator of Digital Scholarship@UNLV. For more information, please contact [digitalscholarship@unlv.edu](mailto:digitalscholarship@unlv.edu).

# NOTE TO USERS

Page(s) not included in the original manuscript and are unavailable from the author or university. The manuscript was scanned as received.

93, 161

This reproduction is the best copy available.

**UMI**<sup>®</sup>



STUDY OF GAS DENSITY PROFILE ABOUT A PLASTIC TEST PIECE UNDER  
VACUUM

by

Hari Krishnan

Bachelor of Engineering  
University of Madras, India  
2002

A thesis submitted in partial fulfillment  
of the requirement for the

**Master of Science Degree in Electrical Engineering  
Department of Electrical and Computer Engineering  
Howard R. Hughes College of Engineering**

**Graduate College  
University of Nevada, Las Vegas  
May 2006**

UMI Number: 1436766

### INFORMATION TO USERS

The quality of this reproduction is dependent upon the quality of the copy submitted. Broken or indistinct print, colored or poor quality illustrations and photographs, print bleed-through, substandard margins, and improper alignment can adversely affect reproduction.

In the unlikely event that the author did not send a complete manuscript and there are missing pages, these will be noted. Also, if unauthorized copyright material had to be removed, a note will indicate the deletion.

**UMI**<sup>®</sup>

---

UMI Microform 1436766

Copyright 2006 by ProQuest Information and Learning Company.

All rights reserved. This microform edition is protected against unauthorized copying under Title 17, United States Code.

ProQuest Information and Learning Company  
300 North Zeeb Road  
P.O. Box 1346  
Ann Arbor, MI 48106-1346



**Thesis Approval**  
The Graduate College  
University of Nevada, Las Vegas

March 27, 20 06

The Thesis prepared by

Hari Krishnan

Entitled

"Study of Gas Density Profile About a Plastice Test

Piece Under Vaccum"

is approved in partial fulfillment of the requirements for the degree of

Master of Science in Electrical Engineering

Robert A. Schutt Jr  
Examination Committee Chair

Debra L. ...  
Dean of the Graduate College

John P. ...  
Examination Committee Member

R. ...  
Examination Committee Member

William Cullineth  
Graduate College Faculty Representative

## ABSTRACT

### **Study of Gas Density Profile About a Plastic Test Piece Under Vacuum**

by

Hari Krishnan

Dr. Robert A. Schill, Jr., Examination Committee Chair  
Associate Professor  
Department of Electrical Engineering  
University of Nevada, Las Vegas

Nevada Shocker is a 540KV,  $7\Omega$ , 50ns, pulsed power device based on Marx Bank and Blumlein technologies. When this machine fires, the energy is funneled to a plastic insulator supported by two circular electrodes. The purpose is to study the surface breakdown properties of the plastic. It is hypothesized that a thin layer of gas exists between hard vacuum and the solid. The goal is to determine change in the gas profile and suggest how it may contribute to surface flashover.

Stimulated desorption techniques such as photon stimulated desorption and thermal stimulated desorption are employed in characterizing the gas profile. The plastic under test is Rexolite. A vacuum system with Rexolite plastic is brought down to pressure levels of  $10^{-8}$  to  $10^{-9}$  Torr to study the presence of the thin layer of select gas molecules. A Nd: YAG pulsed laser is used to stimulate the surface of the plastic under vacuum.

## TABLE OF CONTENTS

ABSTRACT .....	iii
LIST OF FIGURES .....	vi
LIST OF TABLES .....	x
ACKNOWLEDGEMENTS.....	xii
CHAPTER 1 INTRODUCTION .....	1
1.1 Thesis Objective.....	1
1.2 Surface Flashover .....	2
1.2.1 Preflashover .....	10
1.3 Outgassing .....	11
1.3.1 Outgassing rates of various materials .....	12
1.3.2 Outgassing by desorption .....	13
1.4 Properties of the plastic .....	15
1.5 Outgassing rates – Measurement methods .....	15
1.5.1 Technique used to measure the outgassing rate of the plastic .....	17
1.6 Organization of Thesis .....	18
CHAPTER 2 INTRODUCTION .....	20
2.1 Measurement of absorption coefficient ( $\alpha$ ) .....	21
2.2 Calculation of phase coefficient ( $\beta$ ) .....	24
2.3 Determination of number of bound electrons per unit volume .....	25
2.4 Calculation of resonant frequency .....	26
2.4.1 Electronic Polarization .....	27
2.4.2 Determination of resonant frequency ( $\omega_1$ ) & the damping term ( $\nu$ ).....	30
2.5 Determination of energy dissipated .....	33
2.6 Determination of Temperature .....	39
2.7 Determination of Initial velocity .....	40
CHAPTER 3 LOCALIZED THERMAL AND PHOTON STIMULATED DESORPTION TEST STAND AND LOGISTICS.....	42
3.1 Introduction .....	42
3.2 Vacuum Priming of the Desorption Test Stand .....	44
3.2.1 System start-up procedure .....	45
3.2.2 Venting and Vacuum Priming .....	47
3.3 Polishing procedure .....	50
3.4 Spectrometer experiment .....	60
3.5 Pretest on rexolite plastic and view port .....	62
3.6 Experiment procedure .....	63



CHAPTER 4	EXPERIMENTAL STUDY AND DATA ANALYSIS .....	101
4.1	Experimental Preparation .....	101
4.2	Data Interpretation .....	106
4.3	Analysis .....	121
4.4	Discussion of all calculations .....	130
CHAPTER 5	FUTURE STUDIES .....	206
5.1	Future studies .....	206
APPENDIX		
A	MATLAB PROGRAM .....	208
B	BOUNDARY CONDITION DERIVATION .....	209
REFERENCES	.....	214
VITA	.....	219

## LIST OF FIGURES

Figure 3.1	Experimental Setup.....	68
Figure 3.2	Vacuum system block diagram (TOP VIEW) .....	69
Figure 3.3	Vacuum system block diagram (SIDE VIEW). .....	70
Figure 3.4(a)	Top view of the experimental set up .....	71
Figure 3.4(b)	Top view of the experimental set up. ....	72
Figure 3.5	Cooling system for polishing on a lathe machine .....	73
Figure 3.6	Lapping machine used to grind and polish the ends of samples seven through nine .....	74
Figure 3.7	Test samples.....	74
Figure 3.8(a)	One inch diameter, polished, Rexolite samples (Sample 1) viewed through a 20x times optic microscope and digitally enhanced. ....	75
Figure 3.8(b)	One inch diameter, polished, Rexolite samples (Sample 2) viewed through a 20x times optic microscope and digitally enhanced. ....	76
Figure 3.8(c)	One inch diameter, polished, Rexolite samples (Sample 3) viewed through a 20x times optic microscope and digitally enhanced. ....	77
Figure 3.8(d)	One inch diameter, polished, Rexolite samples (Sample 4) viewed through a 20x times optic microscope and digitally enhanced. ....	78
Figure 3.8(e)	One inch diameter, polished, Rexolite samples (Sample 5) viewed through a 20x times optic microscope and digitally enhanced. ....	79
Figure 3.8(f)	One inch diameter, polished, Rexolite samples (Sample 6) viewed through a 20x times optic microscope and digitally enhanced. ....	80
Figure 3.9(a)	One and one quarter inch diameter, polished, Rexolite samples (Sample 7) viewed through a 20x times optic microscope and digitally enhanced... ..	81
Figure 3.9(b)	One and one quarter inch diameter, polished, Rexolite samples (Sample 8) viewed through a 20x times optic microscope and digitally enhanced... ..	82
Figure 3.9(c)	One and one quarter inch diameter, polished, Rexolite samples (Sample 9) viewed through a 20x times optic microscope and digitally enhanced... ..	83
Figure 3.10(a)	Scattering tests on 1" Rexolite plastic sample (Sample 1) using He-Ne Laser.....	84
Figure 3.10(b)	Scattering tests on 1" Rexolite plastic sample (Sample 2) using He-Ne Laser.....	85
Figure 3.10(c)	Scattering tests on 1" Rexolite plastic sample (Sample 3) using He-Ne Laser.....	85

Figure 3.10(d)	Scattering tests on 1" Rexolite plastic sample (Sample 4) using He-Ne Laser.....	85
Figure 3.10(e)	Scattering tests on 1" Rexolite plastic sample (Sample 5) using He-Ne Laser.....	86
Figure 3.10(f)	Scattering tests on 1" Rexolite plastic sample (Sample 6) using He-Ne Laser.....	86
Figure 3.11(a)	Scattering tests on 1.25" Rexolite plastic sample (Sample 7) using He-Ne Laser.....	87
Figure 3.11(b)	Scattering tests on 1.25" Rexolite plastic sample (Sample 8) using He-Ne Laser.....	87
Figure 3.11(c)	Scattering tests on 1.25" Rexolite plastic sample (Sample 9) using He-Ne Laser.....	88
Figure 3.12(a)	Quantitative analysis of scattering through plastic sample one corresponding to Fig. 3.10a subplots (i), (ii), (iii) and(iv) respectively.....	90
Figure 3.12(b)	Quantitative analysis of scattering through plastic sample one corresponding to Fig. 3.10b subplots (i) and (ii) respectively.....	90
Figure 3.12(c)	Quantitative analysis of scattering through plastic sample one corresponding to Fig. 3.10c subplots (i) and (ii) respectively.....	91
Figure 3.12(d)	Quantitative analysis of scattering through plastic sample one corresponding to Fig. 3.10d subplots (i) and (ii) respectively.....	91
Figure 3.12(e)	Quantitative analysis of scattering through plastic sample one corresponding to Fig. 3.10e subplots (i) and (ii) respectively.....	92
Figure 3.12(f)	Quantitative analysis of scattering through plastic sample one corresponding to Fig. 3.10f subplots (i) and (ii) respectively.....	92
Figure 3.12(g)	Quantitative analysis of scattering through plastic sample one corresponding to Fig. 3.10g subplots (i) and (ii) respectively.....	93
Figure 3.12(h)	Quantitative analysis of scattering through plastic sample one corresponding to Fig. 3.10h subplots (i) and (ii) respectively.....	93
Figure 3.12(i)	Quantitative analysis of scattering through plastic sample one corresponding to Fig. 3.10i subplots (i) and (ii) respectively.....	94
Figure 3.13(a)	Top view of the Spectrometer Experiment Setup.....	95
Figure 3.13(b)	Side view of the Spectrometer Experiment Setup.....	95
Figure 3.14(a)	Spectrometer graph – transmitted light without plastic, transmitted and reflected light with plastic at normal incidence...	96

Figure 3.14(b)	Difference between data points of transmitted light without plastic, transmitted and reflected light with plastic at normal incidence .....	96
Figure 3.15	Pretests on rexolite sample.....	97
Figure 3.16	Optical Setup for deflecting the beam.....	98
Figure 3.17	RGA scan for mass numbers between 1 and 100.....	99
Figure 3.18	Ideal shot locations on the Rexolite samples.....	100
Figure 3.19	Laser beam profile.....	100
Figure 4.1(a)	RGA Data Plots (Sample 1).....	132
Figure 4.1(b)	RGA Data Plots (Sample 1, Shot 1).....	133
Figure 4.1(c)	RGA Data Plots (Sample 1, Shot 2).....	134
Figure 4.1(d)	RGA Data Plots (Sample 1, Shot 3).....	135
Figure 4.1(e)	RGA Data Plots (Sample 1, Shot 4).....	136
Figure 4.1(f)	RGA Data Plots (Sample 1, Shot 5).....	137
Figure 4.2(a)	RGA Data Plots (Sample 2).....	138
Figure 4.2(b)	RGA Data Plots (Sample 2, Energy: 77 mJ).....	139
Figure 4.2(c)	RGA Data Plots (Sample 2, Energy: 85 mJ).....	140
Figure 4.2(d)	RGA Data Plots (Sample 2, Viewport).....	141
Figure 4.2(e)	RGA Data Plots (Sample 2, Chamber Walls).....	142
Figure 4.2(f)	RGA Data Plots (Sample 2, After viewport and chamber walls).....	143
Figure 4.3(a)	RGA Data Plots (Sample 3).....	144
Figure 4.3(b)	RGA Data Plots (Sample 3, Center).....	145
Figure 4.4(a)	RGA Data Plots (Sample 4).....	146
Figure 4.4(b)	RGA Data Plots (Sample 4, Viewport).....	147
Figure 4.4(c)	RGA Data Plots (Sample 4, after viewport).....	148
Figure 4.4(d)	RGA Data Plots (Sample 4, chamber walls).....	149
Figure 4.4(e)	RGA Data Plots (Sample 4, after chamber walls).....	150
Figure 4.5	RGA Data Plots (Sample 5).....	151
Figure 4.6	RGA Data Plots (Sample 6).....	152
Figure 4.7(a)	RGA Data Plots (Sample 7, optically polished).....	153
Figure 4.7(b)	RGA Data Plots (Sample 7, optically polished).....	154
Figure 4.8(a)	RGA Data Plots (Sample 8, optically polished, Infrared).....	155
Figure 4.8(b)	RGA Data Plots (Sample 8, optically polished, Infrared).....	156
Figure 4.8(c)	RGA Data Plots (Sample 8, optically polished, Green Light).....	157
Figure 4.8(d)	RGA Data Plots (Sample 8 optically polished, Green Light).....	158
Figure 4.9(a)	RGA Data Plots (Sample 9, optically polished, Green Light).....	159
Figure 4.9(b)	RGA Data Plots (Sample 9, optically polished, Green Light).....	160
Figure 4.9(c)	RGA Data Plots (Sample 9, optically polished, Infrared).....	161
Figure 4.9(d)	RGA Data Plots (Sample 9, optically polished, Infrared).....	162
Figure 4.10(a)	RGA Data Plots (Chamber Walls 532 nm).....	163
Figure 4.10(b)	RGA Data Plots (Chamber Walls 1064 nm).....	164

Figure 4.10(c)	RGA Data Plots (Chamber Walls, Faraday Cup Mode).....	165
Figure 4.11	RGA Data Plots (Viewport 532 nm).....	166
Figure 4.12	Detector Capture Area.....	167
Figure B.1	Wave components in four region system .....	209

## LIST OF TABLES

Table 1.1	Typical outgassing rates for select materials [21] .....	19
Table 3.1	Temperature studies on rexolite surface during polishing with cooling .....	53
Table 3.2	Sample geometry and polishing technique .....	58
Table 3.3(a)	Opacity studies on the Rexolite samples under test without viewport .....	59
Table 3.3(b)	Opacity studies on the Rexolite samples under test with viewport .....	59
Table 4.1	Shot Data (Sample 1) .....	168
Table 4.2(a)	Shot Data (Sample 2) .....	169
Table 4.2(b)	Shot Data (Sample 2, Energy: 77 mJ) .....	169
Table 4.2(c)	Shot Data (Sample 2, Energy: 85 mJ) .....	170
Table 4.2(d)	Shot Data (Sample 2, Viewport) .....	170
Table 4.2(e)	Shot Data (Sample 2, Chamber walls) .....	171
Table 4.2(f)	Shot Data (Sample 2, after viewport and chamber walls) .....	172
Table 4.3(a)	Shot Data (Sample 3) .....	172
Table 4.3(b)	Shot Data (Sample 3, Center) .....	173
Table 4.4(a)	Shot Data (Sample 4) .....	174
Table 4.4(b)	Shot Data (Sample 4, Viewport) .....	175
Table 4.4(c)	Shot Data (Sample 4, after viewport) .....	176
Table 4.4(d)	Shot Data (Sample 4, Chamber walls) .....	176
Table 4.4(e)	Shot Data (Sample 4, after chamber walls) .....	177
Table 4.5	Shot Data (Sample 5) .....	178
Table 4.6	Shot Data (Sample 6) .....	179
Table 4.7(a)	Shot Data (Sample 7) .....	181
Table 4.7(b)	Shot Data (Sample 7) .....	183
Table 4.8(a)	Shot Data (Sample 8, Infrared) .....	184
Table 4.8(b)	Shot Data (Sample 8, Infrared) .....	184
Table 4.8(c)	Shot Data (Sample 8, Green light) .....	187
Table 4.8(d)	Shot Data (Sample 8, Green light) .....	188
Table 4.9(a)	Shot Data (Sample 9, Green light) .....	190
Table 4.9(b)	Shot Data (Sample 9, Green light) .....	190
Table 4.9(c)	Shot Data (Sample 9, Infrared) .....	193
Table 4.9(c)	Shot Data (Sample 9, Infrared) .....	193
Table 4.10(a)	Shot Data (Chamber Walls, 532 nm) .....	195
Table 4.10(b)	Shot Data (Chamber Walls, 532 nm) .....	196
Table 4.10(c)	Shot Data (Chamber Walls, Faraday Cup Mode) .....	197
Table 4.11	Shot Data (Viewport, 532 nm) .....	198
Table 4.12	Partial Pressure Gain of RGA .....	199

Table 4.13(a)	Number of emitted molecules (Sample 6, shot 1)	.....200
Table 4.13(b)	Number of emitted molecules (Sample 6, shot 2)	.....200
Table 4.13(c)	Number of emitted molecules (Sample 6, shot 3)	.....201
Table 4.13(d)	Number of emitted molecules (Sample 8, shot 3)	.....201
Table 4.13(e)	Number of emitted molecules (Sample 8, shot 7)	.....202
Table 4.13(f)	Number of emitted molecules (Sample 8, shot 13)	.....202
Table 4.13(g)	Number of emitted molecules (Viewport, Infrared, shot 1)	.....203
Table 4.13(h)	Number of emitted molecules (Viewport, Green light, shot 2)	...204
Table 4.13(i)	Number of emitted molecules (Chamber walls, Infrared, shot 2)	204

## ACKNOWLEDGEMENTS

I take this opportunity to express my sincere and deepest gratitude to my advisor Dr. Robert A. Schill, Jr. for giving me the opportunity to work on this research project. I thank him for his invaluable patience, guidance and support throughout my academic program at UNLV. His assistance during my research work was instrumental in completing the thesis.

I would like to thank Mr. Stan Goldfarb, for sharing his immense knowledge on vacuum science and technology and for his constant support throughout the duration of the project. His guidance and help has proved to be crucial while building the vacuum system for the experiment.

I also thank my committee members Dr. Rama Venkat, Dr. Yahia Baghzouz and Dr. William Culbreth for their support at various stages of this thesis and for being in my committee.

I would like to thank Dr. Richard Kant, for sharing his diverse knowledge at different junctures of this thesis.

Grateful I am to my parents for their patience, guidance and encouragement during my research work and throughout my life.

I would like to thank Dr. Ved Nayyar, Mr. Mark Popek, Mr. Craig Nielson and my colleagues Satyasundeeep Radhakrishna Gurujala, Anoop George, Brandon Blackstone, Vijay Anand Subramanian, Shaoru Garner, Timothy Atobatele for their help during various stages of the research.



## CHAPTER 1

### INTRODUCTION

#### 1.1 Thesis Objective

The Nevada Shocker is powered by a nine capacitor (31.1nF in series configuration) 540 kV (max), 4.5 kJ (max) Marx Bank driving a water filled 50 ns pulse forming Blumlein (17.8pF charging capacitance; two 1.37 $\mu$ F/m, 61.3nH/m distributed discharging capacitance and inductance) triggered by a self-breaking water switch discharging to a  $10^{-6}$  Torr ( $1.33 \times 10^{-4}$  Pa) vacuum region by way of a  $7\Omega$  water filled discharging coaxial transmission line. A trigatron switch energized with an isolated mini capacitor bank is used to erect the Marx bank. The trigatron switch and erecting electrodes are contained in a gas manifold pressurized to  $20 \pm 1$  psi with dry air. Upon Blumlein discharge, the energy in part is funneled to a plastic sample under test supported by two circular electrodes. The purpose is to study the surface breakdown properties of the plastic sample. It is hypothesized that a thin layer of gas exists between hard vacuum and the solid medium. The goal is to determine if a gas density profile near the plastic surface exists and how it may contribute to surface flashover. To study the presence of gas molecules, a plastic sample will be isolated in a  $10^{-9}$  to  $10^{-10}$  Torr ( $1.33 \times 10^{-7}$  to  $1.33 \times 10^{-8}$  Pa) vacuum system and stimulated with a 1 mm diameter, 3-5 ns pulse of 1064 nm or 532 nm photons. Charged particulates if

emitted from the plastic surface may initiate flashover. The presence of the charges is beyond the scope of this effort. Different mechanisms of surface flashover and its characteristics are discussed in this chapter. Further, outgassing rates and properties of different materials are examined.

## 1.2 Surface Flashover

Surface flashover is basically defined as the voltage breakdown along the surface of an insulator. Select literature suggests that surface flashover of insulators [1] in vacuum, generally, is initiated by emission of electrons from the cathode triple junction. The cathode triple junction is the point where the electrode, insulator and vacuum meet.

As the electrons impact the insulator surface, electron multiplication takes place [1]. This process of multiplication can be accomplished by two methods: 1) as a surface secondary electron emission avalanche and/or 2) as an electron cascade in a thin surface layer. In accord with the latter method, the gases diffuse to and desorb from the insulator surface as a result of pressure differentials and thermal or dynamic effects. The desorbed gas is then ionized leading to the surface flashover of insulators. Generally, surface flashover of an insulator is divided into three stages: 1) the initiation stage, 2) the development stage and 3) the final stage [1].

A model in which a Secondary Electron Emission Avalanche (SEEA) leads to a complete breakdown is discussed by Anderson and Brainard [2]. The model assumes that an initial layer of adsorbed gas covers a ceramic surface in

vacuum. This layer is generally a few monolayers thick. Electron stimulated desorption of the adsorbed gas results when the electrons initiated at the triple point or present in the gas layer bombard the surface of the insulator. This forms a partially ionized gas cloud. The electric field at the triple junction is enhanced by the presence of charged particles near the electrode surface, further increasing the electron emission. This increase in electron emission leads to an increase in the current along the insulator surface limited by space charge effects. A regenerative process at this stage causes a quick surface flashover of the insulator. This model was also used to predict the behavior of the time delay between the application of the voltage pulse and the flashover of the surface. They found that for voltage pulses in the nanosecond range, the time delay is proportional to the inverse square of the applied electric field.

Using a similar model described above, R.A. Anderson and W.K. Tucker [3] studied the surface flashover from bipolar stress. Insulators placed in vacuum in this model are stressed with bipolar voltage waveforms. Under unipolar stress, the flashover field varied as the inverse square root of the prebreakdown time delay over the first few nanoseconds. Ions were swept away rapidly as the flashover field became less dependent on delay.

Another mechanism for flashover was proposed by Cross [4]. According to Cross, the surface flashover is triggered by emission of a large burst of electrons from the triple point junction. This charges the successive areas on the insulator negatively, forcing the electrons from the burst to strike the anode. A

channel of excited gas present from the anode to the cathode causes the discharge closure along the channel.

The occurrence of breakdown within the adsorbed gas layer was considered by Bugaev [5, 6]. Electrons emitted from the triple junction induce a gas discharge avalanche in this adsorbed gas layer, producing a plasma and breakdown. This is similar to that of a streamer in a gas discharge.

The propagation of electrons in a conduction band of the insulator leads to desorption of surface gas. This mechanism was predicted for the intermediate phase of surface flashover [7, 8]. The intermediate phase can be initiated in two ways: 1) by the injection of electrons into the insulator through tunneling at the cathode and 2) by the excitation of electrons at a point on the surface of the insulator resulting from high local fields, photoemission, and ion or electron impact. In the second case, the excited electrons will be emitted into the vacuum and the insulator. In both cases, the electric field accelerates the injected electrons within the insulator. These electrons gain energy while suffering inelastic collisions. As soon as the energy exceeds the band gap of the insulator, the inelastic collisions create an electron cascade along the surface. A fraction of these cascade electrons will be emitted into the vacuum. The external electric field drives these electrons towards the anode. A steady increase in the flow of electrons along the insulator was observed. This is similar to a Secondary Electron Emission Avalanche, but its cause is quite different. This electron cascade model also predicts the formation of a surface charge on the insulator.

The ionization cascade also produces stimulated desorption of gases present near or on the surface of the insulator. In this model the electrons near the surface of the insulator makes inelastic collisions with the adsorbed gas molecules. Enough energy is transferred through these collisions to liberate the adsorbed gas molecules. Final flashover occurs in the desorbed surface gas [7, 8].

Jaitly and Sudarshan [9] put forward a similar mechanism based on collisional-ionization at the insulator surface. They found that the surface microstructure and the chemical state of the insulator surface strongly influence the pre-breakdown and breakdown phenomena. A general design strategy for improving the breakdown strength were considered based on the following: a) providing stress relief at the cathode triple junction, b) reducing x-ray production in the gap between the insulator surface and electrode, and c) reducing the interaction with the insulator surface of electrons emitted at the cathode triple junction. The electrons in the surface sub-layer at the dielectric-vacuum interface allow positive charge generation by internal ionization processes. More electron emission takes place due to increased local stress. The positive charges which drift towards the cathode, aid in this increased emission of electrons. Electrons are produced either by field emptying of traps or by injection at the cathode triple junction. The collision-ionization process builds up faster near the cathode end due to a large stress, with an increase in the applied voltage. With further increase in the applied voltage, the collision-ionization process becomes more effective and the positive charge density in the surface layer increases. The rate

of collision-ionization decreases towards the anode end of the insulator and increases near the cathode end. Upon further increase in the applied voltage, the process becomes regenerative until a threshold level is reached, which develops highly conducting plasma along the solid-vacuum surface interface, causing breakdown.

An anode initiated surface flashover mechanism was first considered by Anderson [10]. In his model, flashover initiation requires plasma generation in a small area near the insulator surface. The generated plasma is maintained at or near anode potential through electron emission. If the plasma potential falls below that of the anode potential, then sufficient electrons could be emitted from the plasma to the anode in order to raise the plasma potential to near anode potential. A strong electric field component results from the edge of the plasma, along the insulator surface. Filamentary branches develop because the electric field exceeds the dielectric strength of the material. Localized breakdown at the branch tips, the cause of the surface damage, generates the new plasma necessary to carry the field enhancement forward. With the decrease in the electric field, the growth of filaments into the bulk of the insulator is reduced.

According to V. Belyaev [11], surface flashover occurs when the ionization multiplication coefficient, which is the electrons emitted from the cathode junction, exceeds a critical value. A powerful electron emission source at the cathode-insulator junction must be present for flashover to occur. The desorption of neutral particles and ions accompanies the interaction of the flow of electrons with the dielectric surface. The flow of electrons along the surface can

be increased with an increase in the field strength provided enough electrons are present at the cathode junction and act as a powerful emission source. Surface flashover begins with an avalanche type increase in near surface current. The gas thermal desorption and evaporation of substances of the insulator and electrodes cause further development of ionization. This leads to a steady increase of current in the interelectrode gap and a final formation of surface flashover.

An electron multiplication process for cylindrical envelopes was proposed by I.D.Smith [12]. In cylindrical insulators one can come across fringing fields or surface irregularity, which produces an undesired field component. This causes the electron leaving the insulator or nearby cathode to re-encounter the wall after gaining energy in the field. The rise in current depends on the value of the secondary electron coefficient. If this value exceeds unity then the surface current may rise in this region on the surface. A significant distortion and enhancement of the electric field take place in a few nanoseconds. This process eventually bridges the gap between the anode and the cathode by propagating into regions where it usually does not occur.

Electrical breakdown is the condition at which the voltage across the insulator collapses. This condition is assumed to result from the ionization growth in the desorbed gases.

When subjected to a DC high voltage, the surfaces of insulators in vacuum become positively charged. This happens by electron multiplication through a secondary emission process [13]. The electrons drift towards the

anode by repeated collisions with the insulator. The electron bombardment of the insulator surface causes a release of neutral and ionized atoms and molecules by electron stimulated desorption. Some of the desorbed neutral atoms become ionized due to the electron collisions. Accumulation of positive ions enhances the electric field at the cathode end of the insulator. As a result there is an increase in the field emitted electrons, rate of gas desorption, and ionization in the gas. The probability for secondary electron release is a function of the impinging energy of the incident electrons and the insulator material. The roughness and the contamination of the surface also play an important role in the secondary electron release. The dependence of flashover electric field on the insulating material is reduced.

According to Gray [14], the surface flashover is a local, high pressure phenomenon for dc and microsecond pulse voltages. In the process of flashover initiation, the desorbed gases from the insulator surfaces are more important than the dielectric surface properties. The large quantities of desorbed species can be considered as local high pressure regions. By applying a high potential across an insulator, flashover can be achieved. The flashover process also takes place due to the surface leakage current across insulator causing desorption of physisorbed gases from the insulator surface (ohmic heating). Emission of electrons from the triple point junction causes ionization in gas leading to Townsend avalanche and breakdown. This also results in the flashover. Further desorption due to stimulated electron bombardment of the insulator surface also occurs, resulting in flashover. Flashover can also be expected to occur during



the thermal and ionic bombardment of the insulator surface which leads to the additional desorption and vaporization of insulator molecules increasing the neutral number density in the flashover region. Increased ionization in the gas phase leads to a fully developed flashover discharge.

Surface deterioration of the insulator plays an important role in the variation of the flashover field strength. Surface conditioning appears to increase the hold-off field. To a degree the hold-off field decreases as the number of discharges increase. This has been attributed to carbonaceous products formed resulting from previous discharges. From a breakdown point of view, the presence of minute conducting particles and films on the surface helps the insulator surface to stabilize. Conditioning of electrodes help the smooth surfaces become rougher and rough surfaces become smoother [15]. These effects of particles on the insulator surface tend to reduce the total secondary emission yield and also increase the insulation conductivity between the electrodes. This increase in conductivity in turn increases the leakage current and leads to an increase in desorption of gases. This effect may increase or decrease the breakdown strength. The desorption of gases from the surface of the insulator depends on the applied voltage [16]. Also the flashover voltage doubled for a decrease of around 2% of desorbed gas [17].

W.A.Stygar *et al* [18] studies the effects of flashover of insulators, rexolite in particular. W.A.Stygar *et al* performed a number of experiments on rexolite and Polymethyl-methacrylate (PMMA) and explains that rexolite would be of superior use as a dielectric in high voltage vacuum insulator interface of an accelerator. A

number of different configurations were used in the tests. All the configurations included a standard 45° vacuum-insulator interface. A 45° angle was chosen to optimize the flashover strength of rexolite. The pressure in the vacuum region during a shot was  $6.2 \times 10^{-7} - 1.3 \times 10^{-5}$  Torr ( $8.265 \times 10^{-5} - 1.733 \times 10^{-3}$  Pa). A total of 9 different insulator-electrode configurations were tested. Eight of the configurations used rexolite as the insulator. It was observed that for particular configurations with an anode plug, a rexolite insulator can increase the peak electromagnetic power that can be transmitted across a vacuum interface by a factor of 2.9.

### 1.2.1 Preflashover

T.S. Sudarshan and C.R. Li [19] explain that the occurrence of preflashover events from a photomultiplier tube (PMT) is usually associated with a pulse current of several milliamperes and light signals. The preflashover activity depends on the applied voltage and usually occurs near the peak voltage. For every shot taken at a particular voltage, the preflashover current decreases and the luminosity decreases. But when a higher voltage is applied the preflashover event occurs again.

Preflashover can occur due to various reasons [19]. They can be due to the adsorbed gases on the surface of the insulator. The origin of preflashover can be associated with two processes: (1) local avalanches in the gas phase at localized micro void regions (the gas phase results from gas desorption due to partial discharges in micro voids) and (2) trapping/detrapping and impact-ionization processes involving defects in the solid surface layer.

The light signal from a photomultiplier tube is accompanied with preflashover current [19]. In this case the light emission is attributed to the localized plasmas produced by impact ionization. It was also observed that the light signals are seen without current and local plasmas. This is due to the de-excitation or recombination of electrons and holes. The recombination takes place in the band gap where the defects are concentrated.

### 1.3 Outgassing

The study of outgassing and the outgassing rates of different materials have been an important part in the construction of vacuum equipment [20]. Outgassing is the evolution of gas from a solid or liquid in a vacuum. Outgassing flux or outgassing rate of a solid or liquid is defined as the quantity of gas leaving the surface per unit time per unit of exposed geometric surface, or per unit mass of the sample, at a specified time after the start of evacuation. Degassing is the deliberate removal of gas from a solid or liquid in vacuum as a result of the impact of molecules, electrons, ions, or photons or by heating.

The outgassing rate depends on the previous environmental and thermal conditions to which the materials were exposed. The measured (or net) outgassing rate is the difference between the intrinsic outgassing rate and the rate of readsorption on the surfaces in the test chamber.

#### 1.3.1 Outgassing rates of various materials

E.D. Erikson, T.G. Beat, D.D. Berger and B.A. Frazier [21] discuss the outgassing rates of various materials. The outgassing rate of a material depends

on the material properties and the vacuum system parameters. The materials studied include chlorinated polyvinylchloride, polyethylene, aluminum sheet, carbon foam, monel knitted wire mesh and stainless steel substrates. The gases liberated from materials are of importance. Typically the test chamber was brought down in pressure to  $10^{-7}$  Torr ( $1.33 \times 10^{-5}$  Pa) before any tests were performed. A vacuum bake-out at  $150^{\circ}\text{C}$  was performed to bring the pressure down. A minimum of 10 hours was allowed for the chamber to cool down to room temperature prior to loading the test samples. Of the materials studied, the main gas constituents liberated were  $\text{H}_2\text{O}$ ,  $\text{H}_2$  and  $\text{CO}/\text{N}_2$ . Outgassing rates of the materials mentioned were recorded over a period of 100 hours. The data obtained at the end of 1 hour and 100 hours are given in Table 1.1. Relative humidities were also changed for each test in the range of 25% to 50% with no noticeable effects observed.

### 1.3.2 Outgassing by desorption

Desorption is the release of adsorbed atoms and/or molecules, either neutral or ionized, from the surface of a solid or liquid as a result of the impact of molecules, electrons, ions, and photons or by thermal energy at the temperature of the material [22]. Photon stimulated desorption is said to occur when a beam of photons is directed at a surface causing desorption of adsorbed molecules. The photons set up excited vibrational states in the adsorbed molecules which lead to their desorption. Photon stimulated desorption is frequently used in association with synchrotron radiation due to the intense and tunable light source. Typically, electron stimulated desorption is conducted with low energy

beams in the range of a few 100 eV. The rate of desorption depends on the binding energies of the various gases to the surface, the surface temperature and surface coverage. Typically the energy of an electron must exceed 300 keV before atoms in a solid can be displaced by an elastic or kinematic mechanism [23].

Adsorption can be either physical adsorption or chemical adsorption. In physical adsorption the gas molecules are attracted weakly by van der Waals forces with binding energies of less than 40 kJ/mol (0.4 eV). In chemical adsorption the actual chemical bonding occurs between the gas molecules and atoms on the surface of the vacuum material. The binding energies are in the range from 80 kJ/mol to 800 kJ/mol (0.8 – 8 eV) [24]. As the pressure of the gas increases, so does the quantity of gas adsorbed at constant temperature.

Outgassing caused by electron stimulated desorption plays an important role in the temporal flashover development [25]. The induced gas desorption resulting from impacting electrons causes a local rise in the gas density above the surface of the sample.

The outgassing rate of water and ammonia in/on quartz [26] was studied by using the thermal desorption mass spectroscopy technique. Thermal desorption studies determined the contamination on the quartz surface and the activation energies. The experimental setup included a 30 W CO<sub>2</sub> (10.6 μm) laser to heat the samples in a vacuum chamber typically at 10<sup>-9</sup> Torr (1.33 x 10<sup>-7</sup> Pa). The laser was focused on the sample so that the sample was the hottest object in the vacuum chamber. The use of resistance heaters were avoided since it

contributed to more outgassing when compared to the sample under test. Results showed that, ammonia adsorbed onto the quartz sample while in the vacuum system had multiple sources. One possible source could be water and nitrogen combining on hot filaments. Ammonia found in the system had partial pressures in the mid  $10^{-11}$  Torr ( $1.33 \times 10^{-9}$  Pa) range.

Karl Jousten [24] suggests two outgassing scenarios. Molecules diffuse through the bulk material of a vacuum chamber, enter the surface, and desorb from it. Secondly, molecules that have been adsorbed previously (during venting), desorb when the chamber is pumped to vacuum. Both the effects limit the lowest achievable pressure in the vacuum chamber and increases the pump down time for high and ultra high vacuum to be achieved. The outgassing molecules can be a source of impurities. Another source of outgassing could be the vaporization of atoms or molecules from a material with a vapor pressure higher or comparable to the chamber pressure that is applied to the chamber.

Vacuum systems are typically baked to remove the adsorbed gas molecules. Usually bake-out is performed for systems that have gas molecules with binding energies in the range of 71.17-104.67 kJ/mol (0.71-1.04 eV) or higher [24]. Different parameters such as the pressure desired after bake-out, binding energies of adsorbed molecules, and the material determine the time duration for which the temperature has to be raised.

## 1.4 Properties of the plastic

Outgassing studies are focused on rexolite plastic. Rexolite is a cross-link of di-vinyl benzene ( $C_{10}H_{10}$ ) and polystyrene ( $C_8H_8$ ). The dielectric constant (relative permittivity) is 2.53 and the refractive index at a wavelength of 589 nm is 1.59. The properties of the plastic are expected to change when the piece is heated to 237°F (114°C).

## 1.5 Outgassing rates – Measurement methods

There are five conventional methods to measure the outgassing rates [22]. They are: 1) Throughput method, 2) Conductance modulation method, 3) Two-path method, 4) Gas accumulation method and 5) Mass-loss measurement.

These methods are not used. Some reasons are cited below:

In the throughput method, the outgassing rate measured depends on the size of the orifice or the conductance of the tube which connects to the vacuum chamber. The outgassing rate is derived from a pressure drop across a known conductance. Also the throughput method takes into consideration the effects of readsorption of desorbed gases.

In the conductance modulation method, which is a variant of the throughput method, the conductance of the pumping orifice should be known for the measurement of outgassing rates. The outgassing rate from the test chamber is found by measuring the pressures in the test chamber at two different positions of the valve separating the ultra high vacuum and the high vacuum. The experimental chamber has no valves or orifices for measuring the outgassing

rate. A net pressure difference is not measured. Partial pressure studies over a large mass per charge bandwidth are desired. Desorbed atoms and molecules are to be identified.

The two path method is used in systems where the outgassing rates are very low. This method requires the adjoining parts of the test area to be very low in pressure. Further, this requires thorough degassing of the entire system. Similar to the throughput method, this method also depends on the size of the orifice. Outgassing rates are anticipated to be low since stimulated desorption is to occur in a small localized region over a short time duration. Minimizing wall adsorption with detector in plain sight of the desorbed molecules offers a higher chance of detection and hence resolution of measurement. In the experimental setup, not all adjoining parts of the system are at very low pressures.

The mass loss measurement method of obtaining the outgassing rates requires the material to lose some of its mass over a period of time. Therefore, it requires continuous measurement of the sample mass while placed under vacuum. The mass loss technique is an average technique providing little information on the individual atoms and molecules released. Further, special material preparation may be required, altering the nature of the sample under test.

#### 1.5.1 Technique used to measure the outgassing rate of the plastic

Chamber preparation and sample stimulation play a significant role in the desorption studies. The vacuum chamber is first brought down in pressure to about  $10^{-9}$  Torr ( $1.33 \times 10^{-7}$  Pa) without the plastic piece. Under this condition, the



major constituents present in the chamber are studied and recorded. A residual gas analyzer is used as a tool to study the major gas constituents present in the chamber. Upon insertion of the plastic sample under test, it is anticipated that the vacuum pressure will increase by one or two orders of magnitude. Therefore, sample outgassing rates will be more significant than that of the chamber. While placing the plastic inside the vacuum system, an atmosphere of dry nitrogen is maintained by a venting process. This is to minimize the amount of water vapor from adsorbing on the vacuum chamber walls. The temperature of the chamber walls and the time duration in which the chamber is open to atmosphere are monitored. An outgassing base study is performed on an unpolished and a polished plastic test piece without sample stimulation. The data obtained from this plastic is used as a reference for subsequent stimulated studies with polished plastic pieces. The gases adsorbed on the surface of the plastic are removed by normal pumping. Gas molecules embedded below the first few monolayers are stimulated by localized heating. A 3-5ns pulsed Nd: YAG laser of varying energy at the 1064 nm and 532 nm wavelengths provides a controlled, focused means to stimulate the plastic. Outgassing rates and the type of molecules liberated are monitored during each pulsed stimulation. Because the RGA has a slow scan rate to monitor a large range of m/e values, specific m/e values will be examined within the duration of a single stimulus and each pulse of light will be directed at a virgin location on the sample. That is, a localized volume of the sample will not be illuminated more than once when studying more than one range of m/e values.

## 1.6 Organization of Thesis

This thesis is divided into five chapters. Chapter 2 presents with all the theoretical calculations regarding energy dissipated in the sample, change in sample temperature, time of flight studies and attenuation studies of rexolite. Chapter 3 gives an insight of the experimental setup and the various procedures used during the experiment. A brief overview of the various components used in the setup is provided. The results of the experiment are analyzed and discussed in Chapter 4. Chapter 5 closes the report with, in part, suggestions for future research.

Table 1.1 Typical outgassing rates for select materials [21]

Material	Outgassing rate after 1 hour (torr-litres/sec-cm <sup>2</sup> )	Outgassing rate after 100 hours (torr-litres/sec-cm <sup>2</sup> )	% of gases evolved after 1 hour			% of gases evolved after 100 hours		
			H <sub>2</sub>	H <sub>2</sub> O	CO/ N <sub>2</sub>	H <sub>2</sub>	H <sub>2</sub> O	CO/ N <sub>2</sub>
Chlorinated poly-vinyl-chloride	2e-6	2e-7	91	3	4	6	90	3
Polyethylene	5e-7	2e-9	5	77	18	42	34	24
Aluminum sheet	2e-8	5e-10	--	--	--	18	10	60
Carbon foam	1e-5	6e-8	--	--	--	18	77	5
Monel Knitted Wire Mesh	4e-7	5e-9	11	87	2	23	56	21
Stainless Steel (parylene coated)	2e-7	3e-10	8	54	34	2	8	82

## CHAPTER 2

### INTRODUCTION

Simple models are developed in support of the outgassing experiments stimulated by external laser induced methods. Both localized photon and thermal desorption models are examined using the fundamental mode of a pulsed Nd: YAG laser (1064 nm) as the source. The objective of this chapter is to develop semi-theoretical, semi-experimental studies of the parameters of the plastic and estimates of the dynamic properties of the desorbed gases. Therefore, the resonance and absorption properties of Rexolite, temperature change resulting from localized laser heating, photon desorption and emitted gas molecule energies are to be examined.

The sample under test, Rexolite, is a crosslink of polystyrene and di-vinyl benzene. According to the Rexolite properties chart provided by C-Lec plastics, the following parameters are important in the calculations discussed in the chapter. The glass transition temperature or the phase change temperature of the Rexolite is at 114°C (237°F). Phase change implies that the state of the material changes from a solid to a liquid, or liquid to gas, etc. For Rexolite, the phase change is defined as the medium or portion of the medium changing from a solid to gel. When heated to the phase change temperature, the rod may easily change to different shapes. Another phenomenon called crazing also occurs in

the Rexolite plastic. This occurs when the surface of the material exceeds the glass transition temperature and a phase change results while the bulk of the medium is cool. If the contact surface temperature resulting from the polishing and cutting processes are kept below the glass transition temperature, then the properties of the Rexolite material does not change. Methyl ethyl ketone solvent may be used to test for crazing. The dielectric constant (relative permittivity) of the Rexolite is recorded as 2.53. At 589 nm, the tabulated index of refraction  $n = \sqrt{\epsilon\mu} / \sqrt{\epsilon_0\mu_0}$  is 1.59 implying that the above recorded relative permittivity is valid at this frequency.

### 2.1 Measurement of absorption coefficient( $\alpha$ ):

The absorption coefficient of Rexolite may be obtained from the time averaged Poynting vector  $\vec{\phi}$ . The Poynting vector can be expressed as

$$\vec{\phi} = \frac{1}{2} \text{Re}(\vec{E} \times \vec{H}^*) \quad (2.1)$$

where  $\vec{E} = \vec{E}^+ + \vec{E}^-$  and  $\vec{H} = \vec{H}^+ + \vec{H}^-$ . The superscripts imply that the wave is propagating in the  $+\hat{z}$  and  $-\hat{z}$  directions. The positive and negative propagating electric and the magnetic fields are related by

$$H^+ = \frac{E^+}{\eta} \quad (2.2a)$$

$$H^- = -\frac{E^-}{\eta} \quad (2.2b)$$

where  $\eta = \sqrt{\frac{\mu}{\epsilon}}$  is the intrinsic impedance and for air is given by

$\eta = \sqrt{\frac{\mu_0}{\epsilon_0}} \approx 377 \Omega$ . The quantities  $\epsilon$  and  $\mu$  are the permittivity and permeability

of the medium. The positive z-propagating, x-polarized, plane wave electric field and magnetic field in their complex time harmonic form are respectively

$$\vec{E}^+ = E_0 e^{(j\omega t - \gamma z)} \hat{x} \quad (2.3a)$$

$$\vec{H}^+ = H_0^+ e^{(j\omega t - \gamma z)} \hat{y} = \frac{E_0^+}{\eta} e^{(j\omega t - \gamma z)} \hat{y} \quad (2.3b)$$

The time averaged Poynting vector  $\vec{\rho}$  is normal to both the electric and magnetic fields and points along the direction of wave propagation in isotropic mediums with normal dispersion. Using Eqs. (2.2a), (2.2b), (2.3a) and (2.3b), the time averaged Poynting vector can be rewritten in the following form

$$\vec{\rho} = \frac{1}{2} \text{Re}(\vec{E} \times \vec{H}^*) = \frac{E_0^2 e^{-2\alpha z}}{2|\eta|^2} \text{Re}(\eta) \hat{z} \quad (2.4)$$

Here all reflected wave contributions have been omitted. Using equation (2.4) the absorption coefficient,  $\alpha$ , is solved in terms of the total transmitted power and the incident power yielding

$$\alpha = -\frac{\ln \frac{\rho_T}{\rho_i}}{2d} \quad (Np/m) \quad (2.5)$$

where  $\phi_T$  is the total time averaged transmitted power density,  $\phi_i = \frac{E_o^2}{\eta}$  is the time averaged power density just inside the medium and  $d$  is the distance the wave must propagate inside the medium. Equation 2.5 is based on the assumption that the reflected fields (at the second surface) may be neglected. For a large attenuation coefficient, this is usually a reasonable approximation. An optical power meter from Advantest (TQ 8210) is used as a tool to measure the incident, reflected and transmitted powers. A He-Ne laser is shined on the curved surface of the Rexolite plastic and the time averaged incident, reflected, and transmitted powers are measured. The incident power, which is the output power of the laser, is measured yielding 5 mW. The total transmitted power of the laser through the Rexolite plastic is measured to be 4.3 mW and the reflected power is measured as 177  $\mu$ W. The total power just inside the medium is calculated as the difference of the incident power and the reflected power yielding 4.823 mW. The 1 mm radius He-Ne laser radiates in a  $3.14 \times 10^{-6} \text{ m}^2$  circular cross section. Therefore the total transmitted power density is calculated to be  $\phi_T = 1368.73 \text{ W/m}^2$  and the power density just inside the medium is calculated to be  $\phi_i = 1535.208 \text{ W/m}^2$ . The value for  $d$  is taken as the diameter of the Rexolite plastic and is  $2.54 \times 10^{-2} \text{ m}$ . With the aid of Eq. (2.5) and neglecting multiple reflections inside the plastic and curvature effects, the absorption coefficient ( $\alpha$ ) is calculated yielding 2.26 Np/m.

## 2.2 Calculation of phase coefficient ( $\beta$ )

The losses of the Rexolite medium are modeled in the dielectric constant of the material. In the phase domain, the effective dielectric constant is complex. Expressions for both the propagation coefficient and the imaginary part of the dielectric constant are determined.

The propagation coefficient for a general isotropic, linear, homogeneous medium is

$$\gamma = \alpha + j\beta = j\omega\sqrt{\epsilon\mu} \quad (2.6)$$

where  $\omega$  is the angular frequency in rad/sec,  $\epsilon$  is the complex permittivity (effective permittivity) in F/m and  $\mu$  is the permeability in H/m. Since Rexolite is a non-magnetic material,  $\mu_r = 1$  and  $\mu = \mu_0 = 4\pi \times 10^{-7} \text{ H/m}$ . The 633 nm He-Ne laser operates at an angular frequency of  $2.97 \times 10^{15}$  rad/sec. The complex permittivity  $\epsilon$  can be written in terms of its real and imaginary parts yielding

$$\epsilon = \epsilon' - j\epsilon'' \quad (2.7)$$

where  $\epsilon' = \epsilon_0 \epsilon_r$  is the real part of the permittivity,  $\epsilon_0 = 8.85 \times 10^{-12} \text{ F/m}$  is the permittivity of free space and  $\epsilon''$  is the imaginary part of the permittivity representing the losses. Substituting Eq. (2.7) in Eq. (2.6),

$$\alpha + j\beta = j\omega\sqrt{\epsilon\mu} = j\omega\sqrt{(\epsilon' - j\epsilon'')\mu} \quad (2.8)$$

Squaring Eq. (2.8) and separating the real and imaginary parts yields, upon rearrangement, the following expressions for the phase coefficient,  $\beta$ , and the imaginary part of the permittivity

$$\beta = \sqrt{\alpha^2 + \omega^2 \mu \epsilon'} \quad (2.9)$$



$$\varepsilon'' = \frac{2\alpha\beta}{\omega^2\mu} \quad (2.10)$$

These expressions will be employed to determine the properties of the medium in a forthcoming section.

### 2.3 Determination of the number of bound electrons per unit volume ( $N$ )

To determine the resonant frequency due to electronic polarization, an estimate on the number density of bound electrons is determined. The composition of the Rexolite plastic is polystyrene cross linked with di-vinyl benzene. Polystyrene has chemical composition  $C_8H_8$  and di-vinyl benzene has chemical composition of  $C_{10}H_{10}$ . The number of electrons in a hydrogen atom and in a carbon atom is found to be 1 and 6 respectively. Using these values, the number of electrons in 1 molecule of Rexolite ( $C_8H_8$ -  $C_{10}H_{10}$ ) ( $n_e$ ) is 126. The mass of one molecule ( $M_1$ ) of Rexolite plastic ( $C_8H_8$ -  $C_{10}H_{10}$ ) is determined by knowing the mass of a single hydrogen atom ( $1.673 \times 10^{-24}$  g) and a single carbon atom ( $1.994 \times 10^{-23}$  g). The mass of a single  $C_8H_8$ -  $C_{10}H_{10}$  molecule ( $M_1$ ) is  $3.88 \times 10^{-22}$  g and the total mass of the plastic rod (1" diameter and 3/8" height), measured with a Mettler Toledo AG 285 analytical balance, is measured to be 5.075 g. The total number of molecules in the Rexolite plastic ( $n$ ) is determined by taking the ratio of the total mass of the plastic ( $M_2$ ) and the mass of one molecule ( $M_1$ ). Therefore, the total number of molecules in a Rexolite plastic over the entire volume of the piece is calculated to be  $1.31 \times 10^{22}$

molecules. The volume of the 3/8" long, 1" diameter Rexolite plastic under test ( $V$ ) is determined as  $4.83 \times 10^{-6} \text{ m}^3$ . Dividing the total number of molecules in the Rexolite plastic ( $n$ ) by volume ( $V$ ) gives the number of molecules per unit volume ( $N_m$ ) as  $2.7 \times 10^{27} \text{ molecules/m}^3$ . The product of number of molecules per unit volume ( $N_m$ ) and the number of electrons in a single molecule ( $n_e$ ) gives the total number of electrons per unit volume ( $N$ ). Therefore, the number of electrons per unit volume is  $N=3.41 \times 10^{29} \text{ electrons/m}^3$ .

A second technique is used to argue the numbers obtained above based on the size of the molecules. The diameters of hydrogen and carbon atoms are  $1.05 \text{ \AA}$  and  $2.2 \text{ \AA}$  respectively. The distance between two carbon atoms is found to be  $1.42 \text{ \AA}$ . Considering one molecule of  $\text{C}_8\text{H}_8$ - $\text{C}_{10}\text{H}_{10}$  in a straight chain as a rectangle, the total volume is  $3.194 \times 10^{-28} \text{ m}^3$ . Taking the inverse of the volume gives the number of molecules per unit volume as  $3.13 \times 10^{27} \text{ molecules/m}^3$ . Since this value is within an order of magnitude of the number calculated previously, the  $2.7 \times 10^{27} \text{ molecules/m}^3$  value is chosen as reasonable.

#### 2.4 Calculation of the Resonant Frequency

The Rexolite plastic contains only long chain hydrocarbons. Typically, hydrocarbon chains do not exhibit dipolar properties. Neither do they have ionic groups present in their chemical structure. It is non-polar in nature [Dr.Pradip.K. Bhowmik, Associate Professor, Dept. of Chemistry, UNLV]. This assumes the plastic is chemically pure. The impurity content of Rexolite is not known. If the presence of impurities is significant and can be resonated, then a mechanism

exists to transfer electromagnetic energy to thermal energy inside the medium. An experimental study employing spectroscopy techniques presented in Chapter 3 is used to characterize the absorption properties of the plastic under test over the optical spectrum.

#### 2.4.1 Electronic Polarization

The dielectric constant of a material is generally dependent on the frequency. The variation of dielectric constant with frequency is termed as dispersion. For linear, isotropic, homogeneous mediums, the electric polarization vector can be related to the total macroscopic field through the dielectric properties of the medium [30]. This relation is

$$\vec{P} = (\epsilon - \epsilon_o)\vec{E} = \chi_e \epsilon_o \vec{E} \quad (2.11)$$

where  $\chi_e$  is the electric susceptibility,  $\epsilon_o$  is the dielectric constant and  $\vec{E}$  is the total macroscopic vector electric field. The polarization vector  $\vec{P}$  can also be expressed in terms of the dipole moments per unit volume of the medium. Thus,

$$\vec{P} = N \vec{p} = N \alpha \vec{E}'_{local} \quad (2.12)$$

where N is the number of dipoles per unit volume contributing to  $\vec{P}$  and  $\vec{p}$  is the moment of each elementary dipole. The dipole moment p is created by the local electric field  $\vec{E}'_{local}$  acting on the dipole. The term  $\alpha$  is the polarizability. The local electric field  $\vec{E}'_{local}$  is different from the total macroscopic field  $\vec{E}$  due to the contribution of all of the dipoles existing as a result of the electron cloud and the nucleus. The electronic polarization is caused by slight displacement of electrons

surrounding positively charged atomic nuclei under the influence of the local electric field  $\vec{E}'_{local}$ . To obtain a relation between the total macroscopic electric field  $\vec{E}$  and the local field  $\vec{E}'_{local}$ , an average resultant field due to the dipoles in a macroscopic volume is determined. This is accomplished by averaging the dipole fields in a fictitious sphere surrounding the molecule. The total macroscopic electric field is the sum of the local field plus this average field also denoted as the polarization field. This polarization field  $\vec{E}_p$  is related to the polarization by [30]

$$\vec{E}_p = -\frac{\vec{P}}{3\epsilon_0} \quad (2.13)$$

Therefore, the local field  $\vec{E}'_{local}$  is related to the external field as

$$\vec{E}'_{local} = \vec{E} - \vec{E}_p = \vec{E} + \frac{\vec{P}}{3\epsilon_0} \quad (2.14)$$

Now consider a simple model of molecules with electrons elastically bound to the nuclei. The governing electron equation of motion is

$$m \frac{d^2 \vec{r}}{dt^2} = -m\omega_0^2 \vec{r} - m\nu \frac{d\vec{r}}{dt} + \vec{F} \quad (2.15)$$

where  $m$  is the mass of the electron,  $\vec{r}$  is the displacement of the electron,  $-m\omega_0^2 \vec{r}$  is the elastic restoring force,  $\nu$  is the damping coefficient, and  $\vec{F}$  is the Lorentz force acting on the electron [31]. The ions are assumed

stationary. The restoring force is assumed to be proportional to the displacement of the electron and the constant  $\omega_0$  is the frequency of the free oscillations of the electron under the influence of the restoring force alone. The Lorentz force is given by

$$\vec{F} = e(\vec{E}'_{local} + \vec{v} \times \vec{B}'_{local}) \quad (2.16)$$

Where  $e$  is the charge of an electron,  $\vec{v}$  is the velocity of an electron [31]. The second term in the Lorentz force is negligible compared to the first term if we assume  $|\vec{v}| \ll c$ . Consider a time harmonic field of the form  $\exp(j\omega t)$ . The polarization vector is given by  $\vec{P} = Ne\vec{r}$ , where  $N$  is the bound electrons per unit volume. Equation (2.15) for a time harmonic field can be written as

$$-m\omega^2\vec{r} = -m\omega_0^2\vec{r} - j\omega m\nu\vec{r} + e\left(\vec{E} + \frac{Ne\vec{r}}{3\epsilon_0}\right) \quad (2.17a)$$

Rearranging Eq. (2.17a), the total macroscopic electric field is

$$\vec{E} = \frac{1}{e} \left\{ m\omega_0^2\vec{r} - \frac{Ne^2\vec{r}}{3\epsilon_0} - m\omega^2\vec{r} + j\omega m\nu\vec{r} \right\} \quad (2.17b)$$

Noting that  $\vec{D} = \epsilon_0 \epsilon_r \vec{E}$ ,  $\vec{E} = \epsilon_0 \vec{E} + \vec{P}$  and using  $\vec{P} = Ne\vec{r}$ , the relative permittivity  $\epsilon_r$  is

$$\epsilon_r(\omega) = 1 + \frac{\omega_{pe}^2}{(\omega_0^2 - \omega^2 + j\omega\nu)} = \epsilon'_r(\omega) - j\epsilon''_r(\omega) \quad (2.18a)$$

where

$$\omega_1^2 = \omega_o^2 - \frac{\omega_{pe}^2}{3} \quad (2.18b)$$

and

$$\omega_{pe} = \sqrt{\frac{N e^2}{\epsilon_o m}} \quad (2.18c)$$

are respectively the resonant frequency with correction term to taken into consideration for the long range collective effects of the electrons associated with neighboring dipoles and the electron plasma frequency. For notation purposes,  $\omega_1$  will be denoted as the resonant frequency.

Based on this simple model both the dielectric and loss properties of the medium may be obtained. The model assumes that the source frequency is high enough that only the electrons in the medium can respond to an electric field. Since the loss is frequency dependent, knowing the properties of medium at one frequency, the model will predict the properties at a different frequency. This is valid since other resonant mechanisms appear not to exist. The absorption coefficient measured with a He-Ne laser at a frequency  $\omega = 2.97 \times 10^{15}$  (rad/sec) is used as a reference to determine the resonant frequency,  $\omega_1$ , at which the sample is tested. This resonant frequency gives a theoretical value for the absorption at the experimental frequency. Also the loss term  $\nu$  is obtained.

#### 2.4.2 Determination of resonant frequency ( $\omega_1$ ) & the damping term ( $\nu$ )

Because only partial information on the loss effects and the dielectric effects are known at any one frequency, one cannot apply Eq. 2.18a to find the

resonant frequency and the damping term. Consequently, a theory is developed to handle partial information at two different frequencies to obtain the damping and resonant frequency terms. Typically, resonance for electronic polarization occurs in the UV range. All other possible polarization resonance mechanisms typically occur at frequencies below the optical spectrum. With the aid of Eqs. (2.8) and (2.18a), the propagation constant is

$$\alpha + j\beta = j\omega \sqrt{\mu\epsilon_o \left( 1 + \frac{\omega_{pe}^2}{(\omega_1^2 - \omega^2 + j\omega\nu)} \right)} \quad (2.19)$$

Squaring both sides of Eq. (2.19) and separating the real and imaginary parts yields respectively

$$\alpha^2 - \beta^2 = -\omega^2 \mu\epsilon_o \left( 1 + \frac{\omega_{pe}^2 (\omega_1^2 - \omega^2)}{((\omega_1^2 - \omega^2)^2 + (\omega\nu)^2)} \right) \quad (2.20)$$

$$2\alpha\beta = \omega^2 \mu\epsilon_o \left( \frac{\omega_{pe}^2 \omega\nu}{((\omega_1^2 - \omega^2)^2 + (\omega\nu)^2)} \right) \quad (2.21)$$

Solving for Eqs (2.20) and (2.21) in terms of  $\alpha$ ,  $\omega_1$  and  $\nu$  the following general equation is obtained.

$$\alpha^4 - \frac{\omega^4}{4c^4} \left[ \frac{\omega_{pe}^2 \omega\nu}{((\omega_1^2 - \omega^2)^2 + (\omega\nu)^2)} \right] + \frac{\omega^2 \alpha^2}{c^2} \left[ 1 + \frac{\omega_{pe}^2 (\omega_1^2 - \omega^2)}{((\omega_1^2 - \omega^2)^2 + (\omega\nu)^2)} \right] = f(\omega_1, \nu) \quad (2.22)$$

The number of bound electrons per unit volume in Rexolite is  $N=3.41 \times 10^{29}$  electrons/m<sup>3</sup>. The mass of the electron bound to the atom or molecule in Rexolite is assumed to be the mass of the free electron. Therefore  $m_e=9.31 \times 10^{-31}$  kg. The charge of an electron is  $e=1.6 \times 10^{-19}$  C. Since Rexolite is non-

magnetic,  $\mu_r = 1$  and  $\mu = \mu_o \mu_r = 4\pi \times 10^{-7} H/m$ . Using these values the electron plasma frequency ( $\omega_{pe}$ ) is calculated as  $2.89 \times 10^{15} rad/sec$ . Let us define the first frequency of operation  $\omega = \omega_{01} = 2.97 \times 10^{15} rad/sec$  to be that based on the attenuation studies using the HeNe laser as described in Section 2.2. Here the measured attenuation  $\alpha = \alpha_{01}$  is 2.26 (Np/m). Let the second frequency of operation  $\omega = \omega_{02} = 3.2 \times 10^{15} rad/sec$  correspond to the 589 nm wavelength, where the relative permittivity of Rexolite is tabulated,  $\epsilon'_{r2} = 2.53$ . The relative permittivity of the medium can be directly related to the damping term by substituting Eq. (2.9) into Eq. (2.20). Allowing  $\omega = \omega_{02}$  and  $\epsilon' = \epsilon_o \epsilon'_{r2}$ , damping term may be re-expressed as

$$\nu = \left[ \frac{\omega_{pe}^2 (\omega_1^2 - \omega_{02}^2)}{\omega_{02}^2 (\epsilon_r' - 1)} - \frac{(\omega_1^2 - \omega_{02}^2)^2}{\omega_{02}^2} \right]^{1/2} \quad (2.23)$$

Using Eq. 2.23, the damping term in Eq. 2.22 may be expressed in terms of the relative permittivity at the second operating frequency. Now using  $\omega = \omega_{01}$  and  $\alpha = \alpha_{01}$  in Eq. 2.22, a Matlab program is developed to determine the value of  $\omega_1$  using a zero finding routine, fzero. The program exists in Appendix A. From computation,  $\omega_1$  is  $3.96 \times 10^{15} rad/sec$ . Subsequently from Eq. (2.23),  $\nu$  is  $1.29 \times 10^9 rad/sec$ . Knowing the value of the resonant frequency  $\omega_1$  and the damping term  $\nu$ , the value for  $\alpha$  and  $\beta$  at any wavelength of light within the limits of the model can be determined using Eqs (2.20) and (2.21). Therefore, for 1064 nm



infrared light ( $\omega = 1.77 \times 10^{15}$  rad/sec), the calculated values for  $\alpha$  and  $\beta$  are 0.2781 Np/m and  $7.58 \times 10^6$  rad/m respectively. These values represent the propagation characteristics of the plastic and are used in the calculation of energy dissipation.

## 2.5 Determination of energy dissipated

An energy transport analysis is a useful tool to determine the amount of power dissipated in the Rexolite plastic as the laser beam propagates through the medium. The energy dissipated can be obtained from the complex power conservation theorem

$$\begin{aligned}
 -\oint_{\mathcal{S}} \vec{\rho} \cdot \vec{ds} &= -\oint_{\mathcal{S}} \frac{1}{2} (\vec{E} \times \vec{H}^*) \cdot \vec{ds} = -2j\omega \iiint_V \left\{ \frac{\vec{E} \cdot \vec{D}^* - \vec{H}^* \cdot \vec{B}}{4} \right\} dV + \\
 &+ \frac{1}{2} \iiint_V \vec{E} \cdot \vec{J}^* dV + \frac{1}{2} \iiint_V \vec{E} \cdot \vec{J}_g^* dV
 \end{aligned} \tag{2.24a}$$

Separating Eq. (2.24a) in terms of its real and imaginary parts and using Eq. (2.7) and the point form of Ohms law [ $\vec{J} = \sigma \vec{E}$ ] yields the following equivalent expressions

$$\begin{aligned}
 -\oint_{\mathcal{S}} \frac{1}{2} \text{Re}(\vec{E} \times \vec{H}^*) \cdot \vec{ds} &= 2\omega \iiint_V \left\{ \frac{\epsilon'' |\vec{E}|^2}{4} \right\} dV \\
 &+ \frac{1}{2} \iiint_V \text{Re}(\vec{E} \cdot \vec{J}^*) dV + \frac{1}{2} \iiint_V \text{Re}(\vec{E} \cdot \vec{J}_g^*) dV
 \end{aligned} \tag{2.24b}$$

$$-\oint_S \frac{1}{2} \text{Im}(\vec{E} \times \vec{H}^*) \cdot \vec{ds} = -2\omega \iiint_V \left\{ \frac{\epsilon' |\vec{E}|^2 - \mu_o |\vec{H}|^2}{4} \right\} dV - \frac{1}{2} \iiint_V \text{Im}(\vec{E} \cdot \vec{J}_g^*) dV \quad (2.24c)$$

where  $\sigma$  is real representing the conductivity of the medium and  $\vec{J}_g$  represents generator sources in the volume  $V$  enclosed by the surface  $S$ . The symbol  $\vec{\phi}$  is the complex power flux density vector. The term on the left-hand side of Eq. (2.24b) represents the total time averaged power entering the volume  $V$  passing normal through the surface  $S$ . The first term on the right-hand side of Eq. (2.24b) is the energy dissipated in the volume due to dielectric losses while the second and third terms respectively represent ohmic losses and sources in the medium.

The term on the left-hand side of Eq. (2.24c) represent power oscillation between the electric and magnetic fields crossing the surface  $S$  entering the volume  $V$ . The first term on the right-hand side of Eq. (2.24c) represents the oscillation of energy or power between the electric and magnetic fields. The second term represents the reactance effects due to sources in the medium. Referring to Eq. (2.24b), it is assumed that the conductivity of the plastic is negligibly small and no sources exist in the medium. Consequently, the net time averaged power entering the medium is dissipated in the volume due to dielectric losses. This implies that the time averaged energy dissipated in the medium is given by

$$\xi_{diss} = \frac{1}{4} \iiint_V \epsilon'' |\vec{E}|^2 dV \quad (2.25)$$

The following assumptions are now made:

- (1) Electrical to mechanical conversion losses are contained along the volume of the laser beam, and
- (2) No scattering takes place inside the plastic.

The energy dissipated in the plastic region is dependent on the fields incident on the plastic. The source propagates normal through a medium sequentially composed of air (Region 1), a glass viewport (Region 2), Rexolite plastic (Rexolite 3) and air (Region 4). (Refer to Fig. B.1 in Appendix B). Cascading the complex wave equation solution by means of boundary conditions and phase shifts, the total electric field at any point in Region 3 (Rexolite plastic) may be expressed in terms of the incident electric field of Region 1 as

$$E_3(z) = \left\{ 4 E_{1i} e^{(\gamma_3 - \gamma_2)L_2} e^{(\gamma_2 - \gamma_1)L_1} \times \right. \\ \left. \left\{ 1 + \frac{\eta_1}{\eta_2} + \rho_{23} e^{-2\gamma_2(L_2 - L_1)} \left( 1 - \frac{\eta_1}{\eta_2} \right) \right\}^{-1} \right. \\ \left. \left\{ 1 + \frac{\eta_2}{\eta_3} + \rho_{34} e^{-2\gamma_3(L_3 - L_2)} \left( 1 - \frac{\eta_2}{\eta_3} \right) \right\}^{-1} \right\} e^{-\gamma_3 z} \left[ 1 + \rho_{34} e^{-2\gamma_3(L_3 - z)} \right] \quad (2.26)$$

where  $E_{1i}$  represents the incident electric field,  $\gamma_k$  and  $\eta_k$  are respectively the propagation coefficient and the intrinsic impedance of the  $k$ th medium, and  $L_k$  the distance of the  $k^{\text{th}}$  interface between the  $k$ th and  $k+1$  medium relative to an origin. Details leading to Eq. (2.26) are found in Appendix B. The air and the glass viewport regions are assumed to be perfect dielectrics. This implies from Eq. (2.8) for  $\varepsilon'' = 0$  that the propagation coefficient yields the phase coefficient  $\gamma_k = j\beta_k = j\omega\sqrt{\mu_0\varepsilon'_k}$  for  $k=1,2$  and 4. Consequently, for  $\varepsilon$  equaling  $\varepsilon_0$

and  $\varepsilon_r \varepsilon_o$  where  $\varepsilon_r = 3.75$  for the air and glass viewport mediums respectively, the associated wave numbers are  $\beta_1 = \beta_4 = 1.178 \times 10^7 \text{ rad/m}$  and  $\beta_2 = 2.289 \times 10^7 \text{ rad/m}$ . The intrinsic impedances are determined from

$$\eta_k = \sqrt{\frac{\mu_k}{\varepsilon_k}} = \sqrt{\frac{\mu_o \mu_{rk}}{\varepsilon_o \varepsilon_{rk}}} \text{ where } \eta_1 = \eta_4 \text{ and } \eta_2 \text{ yield } 377 \text{ } \Omega \text{ and } 194.59 \text{ } \Omega \text{ respectively.}$$

The three interfaces are marked as  $L_1=0$ ,  $L_2= 0.125''$  ( $3.175 \times 10^{-3} \text{ m}$ ) and  $L_3= 0.50''$  ( $12.7 \times 10^{-3} \text{ m}$ ) {Refer to the figure B.1 in Appendix B}.

The reflection coefficient at the  $k$ -  $k+1$  boundary is given by

$$\rho_{k,k+1} = \frac{Z_k(z = L_k) - \eta_k}{Z_k(z = L_k) + \eta_k} \quad (2.27a)$$

and

$$\tilde{\rho}_k(z) = \rho_{k,k+1} e^{-2\gamma_k(L_k-z)} \quad (2.27b)$$

where  $Z(L_k)$  is the wave impedance representing the load effects beyond the  $k$ th medium and  $z$  is any point in the  $k^{\text{th}}$  medium. Employing the appropriate parameters,  $\rho_{23}(L_2^+)$  and  $\rho_{34}(L_3^-)$  are respectively  $0.218e^{-j2.07 \times 10^7}$  and  $0.233e^{-j2.036 \times 10^{-5}}$ .

The incident electric field is given by

$$E_{1i} = \left[ \frac{2 \xi_{laser} \eta_1}{A \tau} \right]^{\frac{1}{2}} \quad (2.28)$$

Where  $\xi_{laser}$  represents the energy of the laser and is 70 mJ (the experimental value for both 532 nm and 1064 nm wavelength),  $A=3.31 \times 10^{-5} \text{ m}^2$  represents the area of a 6.5 mm in diameter laser beam, and  $\tau=6 \times 10^{-9} \text{ s}$  represents the time duration of the laser pulse. With the aid of these values, the incident electric field is  $1.628 \times 10^7 \text{ V/m}$ . With the knowledge of  $E_{1i}$  and other parameters, the value of  $E_{3i}$  is found to be  $1.276 \times 10^7 \text{ V/m}$ .

The power dissipated can now be evaluated using Eqs. (2.24b), (2.25) and (2.26)

$$P_{diss} = \omega A \varepsilon'' |E_{3i}|^2 e^{-2\alpha_3 L_3} \left\{ \frac{1}{4\alpha_3} \left[ (e^{2\alpha_3 \delta} - 1) + |\rho_{34}|^2 (1 - e^{-2\alpha_3 \delta}) \right] + |\rho_{34}| \left[ \frac{\cos(\beta_3 \delta + \varphi_{34}) \sin(\beta_3 \delta)}{\beta_3} \right] \right\} \quad (2.29)$$

where  $\rho_{34} = |\rho_{34}| e^{j\varphi_{34}}$  and  $E_{3i}$  is given by Eq. (B.14). The term  $\delta$  in Eq. (2.29) represents the monolayer length (in this case, the diameter of a Carbon atom=2.2 Å). For  $\delta \alpha_3 \ll 1$  and  $\beta_3 \delta \ll \frac{\pi}{2}$ , a Taylor expansion yields the following simplifications

$$e^{\pm 2\alpha_3 \delta} \approx 1 \pm 2\alpha_3 \delta, \quad \cos(\beta_3 \delta) \approx 1 - \frac{1}{2}(\beta_3 \delta)^2, \quad \sin(\beta_3 \delta) \approx (\beta_3 \delta), \quad \text{and}$$

$\cos(\beta_3 \delta + \varphi_{34}) \approx \cos \varphi_{34}$ . Therefore, Eq. (2.29) simplifies as

$$P_{diss} = \frac{\omega A \varepsilon'' \delta}{2} |E_{3i}|^2 e^{-2\alpha_3 L_3} \left\{ 1 + |\rho_{34}|^2 + 2|\rho_{34}| \cos \varphi_{34} \right\} \quad (2.30)$$

where  $\alpha_3$  is the calculated absorption coefficient in region 3;  $\rho_{34}$  is the reflection coefficient at the boundary between mediums 3 and 4;  $\beta_3$  is the calculated phase constant or the wave number in region 3;  $A= 3.31 \times 10^{-5} \text{ m}^2$  is the area of the beam.

The imaginary part of the permittivity in either Eq. (2.29) or (2.30) is calculated using the Eq. (2.10) at  $\omega=1.77 \times 10^{15} \text{ rad/sec}$  and the calculated values for  $\alpha= \alpha_3=0.2781 \text{ Np/m}$  and  $\beta= \beta_3= 7.58 \times 10^6 \text{ rad/m}$ . The permittivity value is obtained as  $\epsilon''=1.07 \times 10^{-18} \text{ F/m}$ . With the aid of these values and Eq. (2.30), the maximum power dissipated in a monolayer within the beam cross section is calculated to be  $1.697 \times 10^{-3} \text{ Watts}$ .

## 2.6 Determination of Temperature

The temperature and the energy dissipated are related by the specific heat capacity. The specific heat capacity of a solid or a liquid is defined as the heat required raising a unit mass of substance by one degree of temperature. The specific heat capacity at constant pressure may be written as

$$C_p = \frac{\Delta Q}{m \Delta T} \quad (2.31)$$

where  $\Delta Q$  is the heat supplied to the substance,  $m$  is the mass of the substance and  $\Delta T$  is the change in temperature. The heat supplied to the substance is equivalent to electromagnetic energy dissipated in the substance. Therefore,  $\Delta Q = \xi_{diss}$ . Neglecting the heat transfer from one solid layer to the next, the

localized change in temperature due to the localized dissipation of energy may be expressed as

$$\Delta T = \frac{\Delta \tau |E_3|^2 \left( \sigma + \frac{\omega \varepsilon''}{2} \right)}{4 C_p \rho_m} = \frac{\Delta \tau P_{diss,ave}}{C_p \rho_m} \quad (2.32)$$

where  $\Delta \tau$  is the time duration of the pulse. The electrical conductivity of Rexolite is  $9.09 \times 10^{-15} \text{ S m}^{-1}$ . From Eq. (2.10), the imaginary part of the dielectric constant at an angular frequency of  $\omega = 1.77 \times 10^{15} \text{ rad/sec}$  is  $\varepsilon'' = 1.07 \times 10^{-18} \text{ F/m}$ . Dielectric and conduction loss effects are related by  $\sigma + \omega \varepsilon''$  as observed from Ampere's law. Since  $\omega \varepsilon'' \gg \sigma$ , conduction losses are not significant and are omitted in the change in temperature calculation.  $C_p = 1.11 \text{ J g}^{-1} \text{ }^\circ\text{K}^{-1}$  is the tabulated specific heat capacity for polystyrene and  $\rho_m = 1.051 \times 10^6 \text{ g/m}^3$  is the mass density of the sample (1" diameter and 3/8" length) placed inside the vacuum system. The change in temperature is determined to be  $1.19 \times 10^{-3} \text{ }^\circ\text{K}$ .

## 2.7 Determination of Initial velocity

As a gross approximation in the limits of classical theory, the initial speed of atoms and/or molecules released from the surface of the plastic as a consequence of thermal losses is deduced. For generality, the transport of energy is assumed to flow from the laser beam to the plastic molecules in a sub monolayer to surface contaminants in a surface monolayer. One may allow the sub monolayer to be the surface monolayer if desired. Let  $n_p$  be the number of atoms/ molecules present in a closely packed, single-specie monolayer on the

plastic under test over the cross-section of the laser beam. Let  $A_p$  and  $A_b$  respectively yield the cross-sectional area of the molecule of plastic assumed in the shape of a sphere and the circular cross-section of the cylindrical shaped beam. Consequently, the number of plastic molecules in a single monolayer is

$$n_p = \frac{A_b}{A_p} \quad (2.33)$$

The energy dissipated in a single plastic molecule in the surface monolayer of the bulk medium is

$$\tilde{\xi}_{diss} = \frac{\xi_{diss}}{n_p} \quad (2.34)$$

where  $\xi_{diss}$  is the uniformly dissipated energy of the laser beam over the beam cross-section in the surface monolayer of the plastic medium. Let  $A_s$  be the cross-sectional area of the surface contaminant molecules being liberated due to a prorated transfer of thermal energy of plastic molecules within this area. The prorated energy transferred to the surface molecule is

$$\xi_s = \tilde{\xi}_{diss} \frac{A_p}{A_s} = \xi_{diss} \frac{A_p^2}{(A_s A_b)} \quad (2.35)$$

The Van der Waals energy of interaction to be expended by the liberated molecule is  $U$ . The speed of the liberated molecule as dictated from Newtonian mechanics is



$$v = \sqrt{\frac{2(\xi_s - U)}{m}} \quad (m/s) \quad (2.36)$$

where  $m$  is the mass of the emitted molecule. If  $\xi_s < U$ , the molecule is trapped on the surface of the plastic.

## CHAPTER 3

### LOCALIZED THERMAL AND PHOTON STIMULATED DESORPTION TEST

#### STAND AND LOGISTICS

##### 3.1 Introduction

Pulsed power experiments such as those conducted with the Nevada Shocker typically occur in vacuum pressures between  $10^{-5}$  to  $10^{-7}$  Torr ( $1.33 \times 10^{-3}$  –  $1.33 \times 10^{-5}$  Pa). The true outgassing and desorption properties of particular materials such as plastic barriers are difficult to study in such a poor vacuum. Therefore, a desorption test stand was designed to achieve vacuum pressures as low as  $10^{-10}$  Torr ( $1.33 \times 10^{-8}$  Pa) without the plastic sample under test. The purpose is to study the desorption process of the plastic under test when stimulated by an energetic source to determine if it is plausible that a low pressure gas layer separates the vacuum environment from the solid plastic. Because impurities may be a part of the surface morphology of the plastic, a practical polishing technique suitable for all sized plastic samples has been established. All experiments have been performed with a Rexolite plastic developed by C-Lec Plastics Inc. This plastic finds use as a barrier, as an insulator, and as a support for equipment in pulsed power experiments at the national laboratories. A diaphragm pump (Neuberger Inc., Model: PM 14542-

national laboratories. A diaphragm pump (Neuberger Inc., Model: PM 14542-813.4), a cryosorption pump (MDC Vacuum Inc., Model: SP-150, Part no: 500000), and an ion pump (Varian Inc., Model: Vaclon plus 20, Part no: 9191145) are used to bring the ultra-high vacuum (UHV) chamber of the desorption test stand to the desired vacuum level. Figure 3.1 illustrates a simple block diagram of the test stand. Figures 3.2 and 3.3 are mechanical drawings displaying relative placement of the components in the system. Figures 3.4a and 3.4b provide top views of the actual system with labels identifying components. In Figure 3.4a, the test stand contains a cryosorption pump and a dry diaphragm pump used to rough down the system. In Fig. 3.4b, the cryosorption pump is replaced by a Varian combination dry diaphragm pump, turbo molecular pump system. The latter was employed to significantly decrease the pump down time. A Surelite III Nd:YAG laser (Continuum Lasers Inc.) is used to illuminate a localized region in the plastic under test housed in a standard six way cross used as a vacuum chamber with zero profile quartz UHV series (manufactured by MDC vacuum corporation) viewport windows for the transmission of laser light. The quartz viewport has a manufacturer specified 92 % (92 %) transmission at 1064 nm (532 nm). The laser illumination stimulates, by thermal or photon energy transfer, the desorption of atoms and/or molecules from the plastic surface. Outside of pressure gauges, a Dycor LC series residual gas analyzer (RGA) with controlling software (System 200), manufactured by Ametek Inc., is the main sensing tool used to measure relative partial pressures and identify the dominant gas species present in the vacuum chamber. The RGA is slow in

analyzing and recording information therefore, the vacuum time constant is adjusted in such a manner that the molecules present in the system can be observed over the detection time of the scan. Further, one must be selective in choosing the elements to be monitored. More discussion on the elements chosen will be provided later. Both the Faraday cup mode and the electron multiplier mode of the RGA are used. The latter enhances and separates the partial pressures of the different gasses.

### 3.2 Vacuum Priming of the Desorption Test Stand

Priming the vacuum system is necessary in order to optimize the amount of pumping time and to minimize the amount of residual gas molecules in the system that are not easily pumped. Pumping sources were chosen based both on cost as well as its potential to pump without risking contamination to the vacuum chamber proper. Since oil backstreaming is a potential risk when using oil pumps thereby potentially contaminating the ultra high vacuum chamber, such pump sources (e.g., diffusion pumps and oil rotary pumps) were not employed. Diaphragm, cryosorption, ion and turbomolecular pumps are used. Refer to Figs. 3.2, 3.3, 3.4a and 3.4b for pump placement relative to the vacuum chamber. To minimize the use of liquid nitrogen and to decrease the pump down time, the cryosorption pump was replaced with a Varian Minitask turbomolecular/diaphragm pump system. To aid in the pumping process, a number of valves have been incorporated in the test stand. Figures 3.2, 3.3, 3.4a and 3.4b display the various types of high vacuum (HV) [namely the

diaphragm pump valve (sometimes called the inline valve) and either the turbomolecular pump valve or the cryosorption pump valve found in Figures 3.4a and 3.4b] and ultra high vacuum (UHV) [identified as 5 and 7 in Fig.3.2 where in Fig. 3.4a the UHV valve 2 is also labeled at the ion pump valve] valves in the system. For reference, component 5 in Fig. 3.2 or equivalently UHV Valve 1 in Fig. 3.4a separates the high vacuum (HV) side of the test stand from the ultra high vacuum (UHV) side of the test stand. Two different procedures are followed when priming the vacuum system. If the vacuum chamber is exposed to the atmosphere environment for a long period of time, then one must follow a more intensive procedure in bringing the vacuum system down in pressure. If the chamber is properly vented to a nitrogen atmosphere prior to momentary exposures to the environment as in the case when changing samples, a less extensive, less time consuming pump down procedure is followed.

### 3.2.1 System start-up procedure

For initializing the system when improperly vented or exposed to atmosphere for a long period of time, all valves are kept open. The diaphragm pump is then turned ON and the whole system including the ion pump is pumped down in pressure. Once the pressure reaches 300-400 Torr (half an atmosphere or  $4 \times 10^4 - 5.33 \times 10^4$  Pa) the diaphragm pump valve is closed. The system is then baked at about 150 °C over a period of 10-15 hours. As observed in Fig. 3.4b, amber-colored heat tapes (Watlow Inc) with controller (Solid State Relay-SSR330DC25 from OMEGA Engineering Inc.), monitored with an external self adhesive J type thermocouple (Manufactured by OMEGA Engineering Inc.),

is not the greatest thermal conductor hence the long baking period with a partial atmosphere environment allows for convection heating to take place. The 300-400 Torr ( $4 \times 10^4 - 5.33 \times 10^4$  Pa) pressure is maintained during bake-out in order to guarantee that the heat is evenly distributed over all surfaces internal to the entire system. After this segment of the baking process is completed, the diaphragm pump valve is opened and pumping is initiated again. External baking continues during the rough pump down process. This continued thermal stimulation aids in the desorption process of cleaning all surfaces within the chamber. As the pressure approaches about 300 mTorr the diaphragm pump valve is closed and the bake-out is stopped. Liquid nitrogen is poured into the cryosorption pump white Styrofoam dewar (refer to Fig. 3.4a) to start the pumping action. The cryosorption pump uses liquid nitrogen to refrigerate the zeolite crystals in the pump. Cryosorption pumps typically pump water and many other gases from the vacuum chamber in an efficient manner. However, these pumps do not pump hydrogen or neon gases efficiently on their own right. Even so, when convective flow is dominant, both hydrogen and neon atoms are directed towards the pump as a result of dominant collision processes. The cryosorption pump can attain vacuum pressures well below the mTorr range. Therefore, once the pressure reaches 1-10 mTorr, the UHV valve on the roughing side is first closed and then the cryosorption pump valve is closed. This is to isolate the system from ultra high vacuum and high vacuum regions. Although not performed at this stage, the dewar of liquid nitrogen could be removed allowing the crystals to warm and degas. The existing diaphragm pump

would then be used to regenerate or remove the gases being released in the HV section including the hydrogen and neon captured by convection flow but not necessarily captured by the crystals. After regeneration and cooling, the cryosorption pump would then be valved back into the main vacuum system for further pumping. Continuing the pump down process employed, the ion pump is switched ON and the high voltage is initiated. The ion pump starts its pumping action. The ion pump is allowed to pump till a pressure of  $10^{-9}$  Torr ( $1.33 \times 10^{-7}$  Pa) is reached. Usually without the plastic sample placed in the system, pressures of  $10^{-10}$  Torr ( $1.33 \times 10^{-8}$  Pa) are attained easily. With the plastic sample placed in the system, it takes approximately one week of pumping to reach the pressure levels of  $10^{-9}$  Torr ( $1.33 \times 10^{-7}$  Pa). Since the system was already pumped down with the cryosorption pump, a startup procedure was not required when the Varian Minitask turbo pump was attached to the system.

### 3.2.2 Venting and Vacuum Priming

Once the system is started initially, it is only required to follow a proper venting procedure when bringing the system up to atmospheric pressure thereafter, while changing sample plastics assuming that the chamber is momentarily exposed to the atmosphere. The venting procedure helps prevent the surfaces inside the vacuum chamber from adsorbing hard to pump atmospheric atoms and molecules like hydrogen and water.

Before the venting procedure is started, the nitrogen gas line attached to the nitrogen bottle needs to be conditioned. Typically this line has been exposed to the environment and contains a host of atoms and molecules that could

to the environment and contains a host of atoms and molecules that could compromise the clean surfaces inside the chamber. With the nitrogen bottle and cryosorption (Turbomolecular) pump valves closed and the nitrogen venting valve and diaphragm pump valve open, the nitrogen line is pumped down with the roughing diaphragm pump. Once pressures on the order of 350 to 400 mTorr (46.66 – 53.33Pa) have been reached, the main gas source valve is opened. Figure 3.4b identifies the nitrogen venting valve on the HV side of the test stand. This procedure ensures that there is pure nitrogen in the gas line. The pressure at the main gas source valve is maintained at about 4-5 psi. The nitrogen venting valve is closed 4 to 5 seconds after it is opened, so that the regeneration process of the cryosorption pump may be performed.

Before venting the system, the residual gas analyzer is switched off and the ion pump valve is closed. This is important because the residual gas analyzer stops functioning if the pressure is higher than  $10^{-5}$  Torr ( $1.33 \times 10^{-3}$  Pa) and if exposed to higher pressures may cause damage to the filament. Similarly, the ion pump has to be maintained at a pressure less than or equal to  $3.75 \times 10^{-2}$  Torr (5 Pa) to function properly. The system is kept warm at 40°C before and during the venting process.

With the UHV valve on the roughing side closed, the diaphragm pump is switched ON and the cryosorption pump valve is opened. This releases the molecules trapped in the cryosorption pump from a previous pump down and removes them from the HV side of the test stand. Once the pressure is around 300-400 mTorr (46.66 – 53.33Pa), the cryosorption pump valve is closed and the



diaphragm pump valve is kept half-opened. The dry nitrogen valve on the HV side of the test stand and the source valve are opened allowing dry nitrogen to flow in the HV side of the test stand. The UHV valve on the roughing side is still closed. After 10-15 seconds the UHV valve on the roughing side of the test stand is opened and the diaphragm pump valve is closed three-quarters of the way. At this stage, liquid nitrogen is poured into the cryosorption pump dewar to prepare the pump for pumping action. Note that the cryosorption pump valve is closed. Just before the viewport is opened for replacing the sample, the diaphragm pump valve is fully closed. This ensures that the system is filled with nitrogen to minimize the chance that air molecules will enter the system when the chamber ports are opened. A 4 to 5 psi nitrogen pressure at the source valve is maintained during the time that the viewport is open. Once the plastic sample is placed in the system and the viewport closed, the system is filled with dry nitrogen and heated up to 90°C for 25 minutes. The process of heating the system in the presence of dry nitrogen is to distribute the heat evenly throughout the system stimulating desorption and to an extent prevent the desorbed molecules from adsorbing to surfaces internal to the vacuum chamber. This process is repeated once at 60°C for 15 minutes and once at 40°C for another 15 minutes. After this process is completed, the diaphragm pump valve is opened with the diaphragm pump on. When a pressure of around 300 mTorr is reached, the diaphragm pump valve is closed and the cryosorption pump valve (Fig. 3.4a) or equivalently the turbo pump valve (Fig. 3.4b) is opened. If the liquid nitrogen cooled, zeolite crystal filled, cryosorption pump is being used, the pump pumps

the vacuum chamber down to pressures in the middle  $10^{-5}$  Torr ( $1.33 \times 10^{-3}$  Pa) scale. If the Varian Minitask pump is used, the combination pump is ON for about 20 to 25 minutes bringing the vacuum pressure of the chamber with test piece into the  $10^{-6}$  Torr ( $1.33 \times 10^{-4}$  Pa) range. After either HV pumping procedure is completed, the UHV valve near the roughing side of the test stand is closed. The turbo/cryosorption pump valve is closed as well. (Note: The cryosorption pump was used for all preliminary test studies and the turbomolecular pump was used for all test samples thereafter). Finally, the ion pump valve is opened for further pumping. The system is kept warm at  $40^{\circ}\text{C}$  for 8 hours after the ion pump valve is opened. Vacuum pressures on the order of  $5 \times 10^{-8}$  Torr ( $6.66 \times 10^{-6}$  Pa) to pressures in the  $10^{-10}$  Torr ( $1.33 \times 10^{-8}$  Pa) scales can be attained with ion pumping depending if the vacuum chamber contains a one or two plastic samples or is empty.

### 3.3 Polishing procedure

In order to stimulate desorption locally in the plastic piece under test, the Rexolite piece is polished on the top and bottom surface of the cylinder. In keeping with practical considerations in a national laboratory setting with potentially large structures, an optical quality grade polish is not necessarily desired. To qualitatively and quantitatively study the molecules desorbed from the plastic surface as compared to other surfaces in the chamber, one needs to manage the amount of scattering that occurs in and from the plastic under test. The quality of the polish plays a role in evaluating the desorption results. In order

to have some control in the surface properties of the cylindrical side of the cylinder, this side was polished as well. Hypothetically if there is no internal or surface scattering, then laser light directed through the ends of the cylinder should not be seen along the sides of the cylinder. If light is observed, there is a potential for the light to interact with the cylindrical surface causing some form of desorption. As a result, it is important to polish all three sides of the cylinder in nearly the same manner paying greater attention to the end surfaces.

A polishing technique is established based on a try and test technique using temperature and opacity/scattering studies as a guide in developing the process. Once developed, the process is no longer monitored with care. In a manufacturing or national laboratory setting, this would be a typical scenario. Consequently, the polishing process provided below has been monitored for average temperature but, as indicated, the monitoring process was not deemed necessary after a procedure was established.

The plastic piece is first cut to 1" in length using a bandsaw. It is cleaned with 200 proof ACS/USP grade alcohol before it is mounted onto the lathe for polishing. As displayed in Fig. 3.5, a small sample cooling system was built around the lathe to ensure a continuous flow of water mixed with coolant (Kool mist 77) drips on the sample to maintain a surface temperature that is below crazing while polishing. Initial polishing studies employed an infrared thermometer (Sperry STK-3020TL) and a K-type thermocouple, to monitor the temperature at the plastic surface. The sample is held onto the lathe by a chuck. Initially wet sandpaper is used to polish the surface. This is done once and is

compound is spread on a Wet Zwipes Micro fiber automotive cloth. Once the lathe is turned ON the piece rotates at a speed of around 320 rpm. The wet micro fiber cloth with the super duty rubbing compound is held against the plastic piece in a belt-like fashion. The wet cloth is dabbed with the rubbing compound at regular intervals (about twice for this procedure) to obtain a better finish. A wet cloth is used to prevent any friction between the surface of the Rexolite piece and the surface of the cloth. The friction causes heat which may affect the surface properties of the Rexolite. The above procedure is performed with continuous flow of water mixed with the coolant. After approximately 15-20 seconds, a fresh micro fiber cloth made wet either with water or 200 proof alcohol is held lightly against the piece to clean the piece while spinning on the lathe. Table 3.1 provides average temperatures measured during a polishing study.

The next round of polishing is performed with 3M Perfect-It II rubbing compound (a light duty rubbing compound). The procedure followed is exactly the same as for the heavy duty rubbing compound. Both the procedures together take about 5-6 minutes. A satisfactory degree of polish is determined by performing a quantitative study of light transmission through each plastic (opacity tests). The piece is then cleaned with an alcohol-wet cloth while the piece spinning on the lathe. The above procedure is followed exactly in the same manner for polishing the flat surfaces of the plastic piece. Again for the flat ends, opacity test is performed before final polishing is stopped. After polishing one flat end, the piece is turned around and covered with an absorbent cloth before placing it on the lathe chuck. This is to ensure that there are no imperfections

placing it on the lathe chuck. This is to ensure that there are no imperfections caused to the polished curved surface due to the chuck. The piece is then cut to 3/8<sup>th</sup> an inch in length and the flat end is polished the same way as before. The flat ends and the curved surfaces are cleaned with the 200 proof ethyl alcohol at the end of final polishing.

Table 3.1 Temperature studies on rexolite surface during polishing with cooling

Material	Initial temperature (F/C)	Final temperature (F/C)
Wet Sand paper	70 F / 21 C	110 F / 43.3 C
Wet Micro fiber cloth	66-68 F / 18.8-20 C	66-68 F / 18.8-20 C
Dry Micro fiber cloth	80 F / 26.6 C	140-150 F / 60-65 C

The 1" diameter samples, samples one through six, were polished using the technique above. Due to the nature of the polish of these samples, the ends of the three 1.25" samples, samples seven through nine, were polished using a lapping machine [UKAM Industrial Superhard tools, Inc.]. Figure 3.6 displays the lapping machine with grinding/polishing wheels and coolant container. The flat ends of the rexolite plastic were first grinded using a 45 micron resin bond diamond disc. This is done till the major scratches or imperfections on the flat surface are removed. The 30 micron and the 12 micron grinding discs are employed subsequently until a semi-transparent surface is obtained. The polishing wheel is then used to provide the final polishing touches to the surface. A mixed solution of cerium oxide powder and water is poured onto the spinning disc while polishing. The cerium oxide gives a finer polishing. Water was used

as a coolant. Since the lapping machine can be used to generate an optical grade polish, samples seven through nine are labeled as optically polished.

Figure 3.7 displays all nine samples. Table 3.2 provides the geometry of each sample shown in Fig. 3.7 along with a measure of the surface flatness and the polishing technique. Figures 3.8 and 3.9 respectively show the front surface, back surface, cylindrical surface and center top surface for the six 1" diameter and the three 1.25" diameter samples as viewed through a 20x long distance microscope (INFINITY Photo Optical Company) and then digitally enhanced. Near the center of the photos, an Edmund Scientific 0.5 mm reticle scale may be observed upon magnification. Samples one through six exhibits a definite undesired surface feature roughly one millimeter in diameter at the center of the samples that scatters the light. This is the result of the T-shaped cutoff tool used on the lathe not being exactly centered when separating the polished piece from the extended sacrificed piece in the lathe chuck. Away from the sample center and on the cylindrical side of the sample, fine circular scratches roughly between 5 and 50  $\mu\text{m}$  wide may be viewed when digitally magnified. The modified polishing technique employed on the 1.25" samples yield a higher quality polish as shown in Fig. 3.9. Of the three samples displayed, sample 9 tends to exhibit straight-line scratches across the flat end of the piece. Because a figure eight motion is employed when grinding and polishing, these scratches may have been inherent to the piece prior to the grinding and polishing procedure and were not removed during the procedure. On this magnified scale, samples seven and eight appear optically polished to the naked eye under magnification. To

examine their optical properties, two tests were performed. Figures 3.10a-f and 3.11a-c illustrate scattering studies of all plastic samples under test illuminated with a linearly polarized He-Ne laser with a Gaussian beam profile propagating nearly parallel to the cylindrical axis through the plastic sample. The yellow center of the beam is due to intensity saturation of the CCD elements (blooming) in the camera. The camera views the laser light projected onto a screen about 0.127 m behind the sample under test. When illuminating an arbitrary off-centered location on each of the six 1" diameter samples, a degree of scattering or diffraction is visibly apparent as observed in Figs. 3.10 (a-f) when comparing subfigures (i) with (ii). The intensity pattern is anisotropic in nature. When comparing the laser beam profile to the light profile centered on the cylinder ends [refer to Fig. 3.10 a and f subfigures (iii) and (iv)], extensive scattering is visually observed. Some degree of scattering can readily be viewed on the cylindrical side of the cylinder when laser light is directed along the cylindrical axis as shown in Fig. 3.10a subfigure (v). The 1 ¼" diameter piece exhibits nearly the same beam profiles with and without the plastic present [refer to Fig. 3.11 a-c subfigures (i) and (ii)]. Some scattering may be observed from the cylindrical sides of the sample as shown in Fig. 3.11a subfigure (iii). Because the surface polish is visually uniform, scattering at a single arbitrary location on the sample end was examined.

Qualitatively, these studies suggest that some degree of the light illuminating the piece under test is directed to other parts of the vacuum chamber out of the beam's path in the absence of the viewport and sample. In desorption

studies, light management is critical in understanding what surface is responsible for the desorption. Although providing interesting connotations, a quantitative comparison cannot be made on the same level due to the electronic magnifications employed. Consequently, MATLAB graphic utilities that places a measure on the light intensity profiles and color (subroutines: polyfit, polyval) on the raw data are used to provide a quantitative comparative study of the Figs. 3.10a-f and 3.11a-c subplots (i) and (ii) and when appropriate (iii) and (iv). Intensity profile studies of the HeNe scattering plots are examined for each sample along a horizontal line passing through the center of the laser beam. The main concern is to compare the laser beam geometry and the intensity outside of the central region of the laser beam without sample when the sample is present to the case when the sample is removed. The newly generated raw data sets are then fitted with a 9<sup>th</sup> order polynomial for comparison as show in Figs. 3.12 a-i. The ordinate axis is a normalized intensity axis where one implies a maximum intensity. Because the central part of the beam saturates the CCD camera, a relative normalized plot will be used for comparison. Maximum absolute values are meaningless for these observations. Four subfigures are contained in Fig. 3.12a labeled as (i) to (iv). Subfigures (i) and (ii) respectively show how the fitted curves compare to the raw data in the absence and in the presence of the plastic under test for sample one corresponding to Figs. 3.10a subfigures (i) and (ii). Good agreement is displayed. Subfigure (iii) provides a comparison between the two fitted curves without raw data present. Subfigure (iv) provides a comparison of the data fitted curves between the laser beam and the scattered beam when



the center of sample one is illuminated as corresponds to Figs. 3.10a subfigures (iii) and (iv). All remaining figures (Figs. 3.12b-i) show comparisons of the 9<sup>th</sup> order polynomials representing the intensity profiles of the off centered illuminations for samples two through nine. It is observed that scattering from center of the 1" samples decreases the beam intensity by more than 50 % of the incident beam. Noting the distance between the back side of the sample (relative to the laser beam) and the screen along with the radial extent of the light projected onto the screen and the distance between the sample top in the vacuum chamber to the exiting viewport (top viewport) and the area of the surface area of the viewport, about 3.8 % of the light is lost to the viewport walls assuming the intensity of the light over the screen is relatively uniform. Based on half power points for the cross section examined, the beam profiles of samples one through six expands on average to 112.5 % of the original laser beam while that for samples seven through nine expand on average to 105 %. The average diameter of the beam based on the half power points (relative to saturation) when the samples under test are not present, the 1" in samples are present, and the 1.25" present are respectively 2 mm, 2.25 mm and 2.1 mm. The average for the 1" sample assumes that the laser beam illuminates off center locations of this sample. When the beam illuminates the center location of the 1" plastic samples, scattering is so significant that a measure of the transmitted beam diameter between the half power points is not meaningful.

Opacity studies have also been conducted on all samples based on HeNe laser illuminations. Referring to Table 3.3(a) and 3.3(b) nearly 50% of the laser

light is lost due to un-captured scattering, attenuation, and reflections when the centers of the 1" samples are illuminated. The capture area of the detector is 95 mm<sup>2</sup> located a distance 35 mm behind the backside of the sample. Comparing the on and off axis opacities for samples seven through nine, less than a 2.2% change exists. This implies that the polishing procedure over the sample surface is fairly uniform. The average off-centered opacity of the polishing procedure employed for the 1" samples equals average opacity for the 1.25" samples.

Table 3.2 Sample geometry and polishing technique

Sample #	Dia. (in.)	Ave. Length (in.)	Min. Length (in.)	Max. Length (in.)	Polishing Technique.
1	1	0.375	0.374	0.376	Chemical
2	1	0.368	0.366	0.37	Chemical
3	1	0.3695	0.368	0.371	Chemical
4	1	0.3965	0.395	0.398	Chemical
5	1	0.404	0.403	0.405	Chemical
6	1	0.3965	0.395	0.398	Chemical
7	1.25	0.318	0.314	0.322	Optical
8	1.25	0.187	0.186	0.188	Optical
9	1.25	0.217	0.216	0.218	Optical

Table 3.3(a) Opacity studies on the Rexolite samples under test without viewport.

	Opacity (Center)	Opacity (off center)
Plastic 1 (1")	1.85	1.11
Plastic 2 (1")	2.5	1.12
Plastic 3 (1")	2.32	1.15
Plastic 4 (1")	1.78	1.16
Plastic 5 (1")	2.38	1.12
Plastic 6 (1")	3.125	1.13
Plastic 7 (1.25")	1.15	1.15
Plastic 8 (1.25")	1.14	1.14
Plastic 9 (1.25")	1.15	1.12

Table 3.3(b) Opacity studies on the Rexolite samples under test with viewport.

	Opacity (Center)	Opacity (off center)
Plastic 1 (1")	1.68	1.19
Plastic 7 (1.25")	1.17	1.16

### 3.4 Spectrometer experiment

In theory, Rexolite is composed of a cross-linked polystyrene and divinylbenzene. Based on conversations with a chemist [Dr.Pradip.K. Bhowmik, Associate Professor, Dept. of Chemistry, UNLV], Rexolite does not contain ionic bonds nor is it dipolar. Consequently, Rexolite should be free of dipolar and ionic resonances. Only electronic resonances should exist. Resonances are a means of coupling energy from the source wave to the material. Typically, dipolar, ionic and electronic resonances occur in the microwave, infrared, and ultraviolet spectrums respectively. By examining the transmission and reflection over the spectrum of a nearly white light source, one may determine the absorption properties of the material. The goal is to determine if the polished Rexolite sample has a preferred absorption frequency leading to a resonance property possibly due to impurities contained therein. Such a resonance would lead to a significant loss mechanism allowing for generation of heat due to molecular or atomic loss mechanisms. Consequently, the localized temperature of the medium in the presence of the beam would rise as a result of this mechanism.

A HR 2000 spectrometer, made by Ocean optics Inc., was used as a measuring device to detect the amount of light reflected and transmitted from a polished sample of Rexolite. Light from an incandescent lamp wrapped in tin foil is directed normal to the planar, nearly parallel ends of the cylinder. The experiment is performed with minimum external lighting in order to obtain a near accurate spectrometer reading. As shown in Figs. 3.13a and 3.13b, the light from the incandescent lamp is guided into a small black box, inside of which the

rexolite plastic is placed. The light propagates nearly normal to the surface of the planar surface of the plastic under test. The beam diameter on the plastic surface is approximately 10 mm. The detector head is placed at far end of the black box to measuring the light leaving normal from the plastic sample. Because the geometry of the detector head and source tube makes it difficult to measure the light reflected normal from the sample surface, the source and detector are slightly adjusted such that the angle of incidence equals the angle of reflection relative to the normal of the plastic surface and that the angles are as small as possible. Spectrometer readings are compared against the case without the plastic in the light's path. Figure 3.14 (a) and (b) shows the graphical representation of the light intensity transmitted through the plastic, reflected off the plastic and the light passing straight through without the plastic at normal incidence. Except for an overall gradual attenuation probably related more to scattering the transmitted and incident light spectra are very similar except at about 875 nm as shown in Fig. 3.14a. Roughly, a 12% change in the anticipated baseline power spectral strength appears to be present. This is more readily borne out in Fig. 3.14b when plotting the difference between the spectral signal strengths at each frequency. A 12% change does not constitute that a strong resonance exists in the bandwidth evaluated but does indicate that there might be some impurities in the material proper responsible for this characteristic.

### 3.5 Pretest on rexolite plastic and view port

In order to perform the laser tests on the sample placed inside the vacuum system, it is imperative to know the threshold limits of both the viewport and the Rexolite plastic. Therefore, before performing the tests, the Rexolite samples and the viewport were tested for their respective damage threshold limits using the Nd:YAG laser operating at the first (1064 nm) and second (532 nm) harmonics with an unfocused beam diameter of 6 to 7 mm. Rexolite plastic was exposed to unfocused 5 to 7 ns of 1064 nm and/or 3 to 5 ns of 532 nm, laser pulses at a 10 Hz pulsed repetition frequency for various energy values through the nearly parallel, polished, planar ends of the 1" diameter cylindrical cylinders roughly 1" in length.. The energy threshold value, at which the laser could be operated, without causing any visible damage to the Rexolite sample, was determined to be about 100 mJ. At about 100 mJ, visible damage in the form of small black spots as shown in Fig. 3.15a were observed. Two pretests were performed at the same energy with the duration of the continuous pulses being 30 minutes and 45 minutes. It was observed that in both the cases, the small black specs started appearing after 4 to 5 minutes of laser pulsing. The color of the specs is a sign of carbon being formed. The unusual seeming random location of the carbon internal to the plastic away from the plastic surface indicates that on a molecular or microscopic level a flaw in the molecular structure or possibly a material contaminant exists that absorbs enough energy over a long period of time to heat the material [Rexolite is a poor thermal conductor] at select locations breaking bonds to generate a noticeable carbon

signature. In five minutes, the plastic is exposed to about 3000 pulses. No visible damage was observed when the piece was tested at lower energies (30-90 mJ) for the same time durations. Figure 3.15b illustrates the type of laser damage that may result when 800 mJ of 1064 nm light impinges on the cylindrical side of the sample. To support the conclusions above, it is interesting that the damaged regions occur at random locations internal to the Rexolite piece. Further, the damaged region is thin having a silver or bronze like tint with a ring patterned mirror-like structure over the region damaged. The thin layer does not appear to be planar in most cases. Similar tests were performed on the viewport as well. The energy threshold was determined to be 250 mJ. All experiments were performed with laser energies below 100 mJ.

### 3.6 Experiment procedure

Because pump down times on the order of a week or longer were required to reach pressures in the middle to low  $10^{-9}$  Torr ( $1.33 \times 10^{-7}$  Pa) scale and because most national laboratory experiments are performed in the  $10^{-5}$  to  $10^{-7}$  Torr ( $1.33 \times 10^{-3}$  to  $1.33 \times 10^{-5}$  Pa) pressure range, simulated desorption experiments were performed at pressures around  $5 \times 10^{-8}$  Torr ( $6.66 \times 10^{-6}$  Pa). The residual gas analyzer (RGA) operates well at this pressure without the need for a differentially pumped system, possibly throttling the auxiliary pump, with controlled modulation of a leak valve required at the higher vacuum pressures. Once the pressure in the system reaches around  $5 \times 10^{-8}$  Torr ( $6.66 \times 10^{-6}$  Pa), the laser is aligned to perform the tests on the plastic sample. The first set of

samples tested were 1 inch in diameter and  $\frac{3}{8}$ <sup>th</sup> an inch in thickness. Since the diameter of the laser beam is 6.5 mm, it was possible to obtain only four virgin spots on the sample. The fifth spot, which is the center spot, was always susceptible to some overlapping due to the previous shots. The 1.25" diameter sample allows more room for more shots to be taken on the sample. Two right angle prisms are used to deflect the laser beam from its axis to the view port window. The second right angle prism placed below the view port is mounted on a linear stage controller. The linear stage controller is used to move the beam diametrically across the plastic in one dimension. This setup is shown in Figure 3.15. More will be said regarding the experimental procedures in Chapter 4.

At about  $7 \times 10^{-7}$  Torr ( $9.33 \times 10^{-5}$  Pa), preliminary outgassing studies with the Rexolite sample under vacuum in the Stimulated Desorption Test Stand based on residual gas analyzer (RGA) measurement were established. Diatomic Hydrogen, Nitrogen,  $\text{CH}_3$  (Mass 15 or referred to as methane), Oxygen, Water, Diatomic Nitrogen/ Carbon Monoxide, Diatomic Oxygen and Carbon Dioxide as the dominant gas molecules composing the vacuum environment as shown in Fig. 3.17. Therefore, it was concluded that for the desorption studies, only these dominant molecules need to be tracked and examined. The  $\text{CH}_3$  molecule was tracked in order to determine whether the 16 peak was Oxygen or Methane ( $\text{CH}_4$ ). Since the ion pump in the system produces methane on its own, there is distinct possibility that the peak 16 could be a methane molecule. The trend mode was used to track each of the mass numbers. Since the ion pump is positioned close to the residual gas analyzer and the gas analyzer requires a



long time to perform measurements relative to molecular transit times, the probability is high that desorbed molecules [due to laser stimulation] under molecular flow will be pumped by the system (e.g., the chamber walls, the ion pump, and the viewport) faster than the residual gas analyzer can detect their partial pressure presence. Therefore, to minimize pumping by the system, the chamber walls were kept at about 40° C and the UHV valve near the ion pump in Figs. 3.4a and b is carefully adjusted. Monitoring the partial pressures of the molecules listed above with time, the ion pump valve (UHV Valve 2) is course adjusted until the decay times [commonly known as the time constant] of the partial pressures of the monitored stimulated molecules is long enough to be detected over a desired duration in time. The time it takes for the RGA to measure all eight elements and begin repeating the process will be defined as the RGA's period of measurement. The time constant of the partial pressures is chosen to be large compared to the RGA's period of measurement. Once coarse adjusted, the valve is fine adjusted to provide enough time to make measurements but short enough for the system to relax to the equilibrium baseline pressure prior to the next stimulation. Typically, the time between single pulsed stimulations is roughly one to two minutes. The slower the pumping time, more time for the residual gas analyzer to detect and record the different peaks. Once set, the operator monitors the recording device and the laser controls to determine if the system has relaxed to baseline partial pressures prior to exciting the laser for the next shot. The results of the position of the ion pump valve are as follows:

- The ion pump valve was kept two turns open for all the plastic samples except for sample seven.
- The ion pump valve was kept 5-1/2 turns for sample seven.

The latter condition resulted because the partial pressure reading for sample seven in the electron multiplier mode for diatomic nitrogen remained at saturation at two turns open. Therefore the valve was opened up to 5-1/2 turns thereby increasing the time constant preventing the RGA from saturating for this molecule. Note that data recorded while the partial pressure readings in the RGA for any molecule remain in saturation is meaningless. Once adjusted, experiments were conducted. Further discussions on the RGA are provided in Chapter 4.

A total of 9 samples were tested for desorption studies with the laser. Of these, the first 6 samples were 1" in diameter and the rest were 1.25" in diameter. For each of the 1" samples, laser was fired at 5 different locations. While the first 3 locations were always single pulses, the 4<sup>th</sup> and 5<sup>th</sup> locations included both single pulse and multiple pulses. The multiple pulses were 10 seconds in duration. Whereas for the 1.25" samples, a total of 9 different locations on the sample were fired at, with each spot being subjected to single and multiple pulses. A laser burn paper was used as guide to position the beam at different locations on the plastic. Figures 3.18a and 3.18b show the different locations on the plastic where the laser was fired.

Burn paper studies indicate that the laser beam has a Gaussian like profile as observed in Fig. 3.19. This burn was generated by a single 70 mJ, 6 ns pulse of 1064 nm infrared light. The central region of each burn exhibits a dark brownish color that is an indication of a hot spot in the beam profile. The outer black fringe indicates that the paper became warm enough to be activated. The beige color implies that the paper was not hot enough to detect the presence of the signal. The beam diameter is chosen to be the average diameter of the outermost black perimeter of the burn. In this case, the average beam diameter is measured as 6.5 mm.

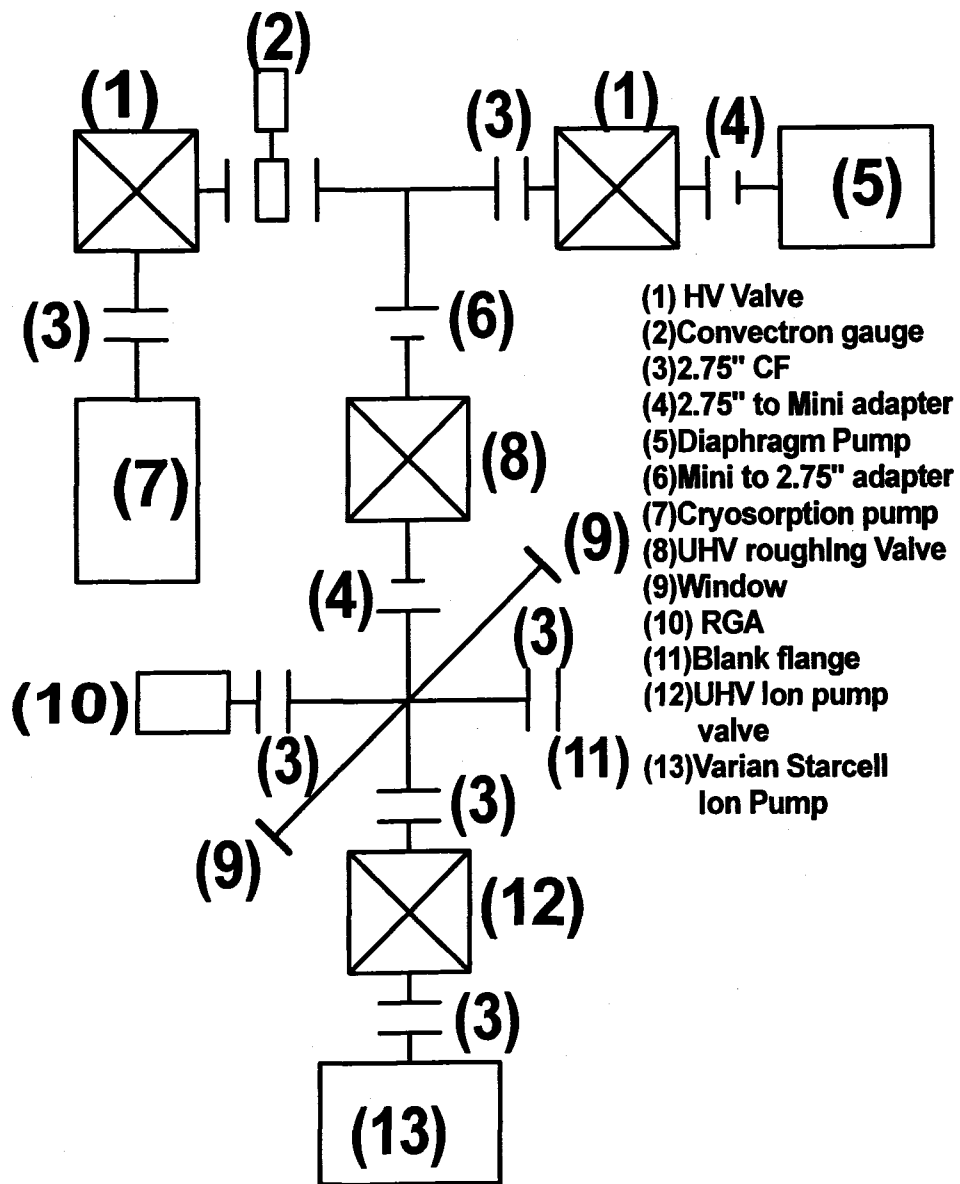


Figure 3.1 Experimental setup

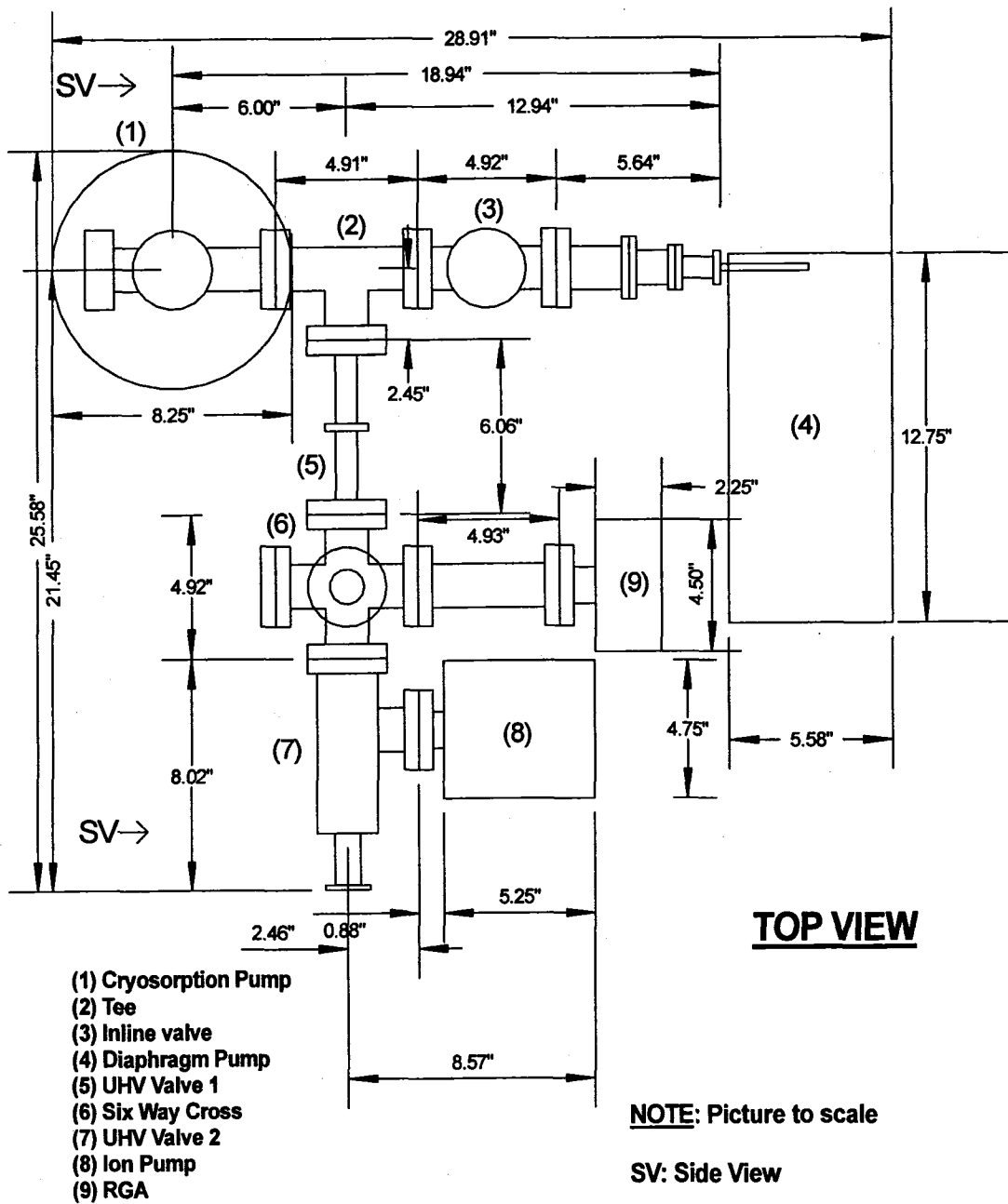


Figure 3.2 Vacuum system block diagram (TOP VIEW)

### SIDE VIEW

- (1) Cryosorption pump
- (2) Diaphragm pump
- (3) Ion pump
- (4) UHV Valve
- (5) Six Way Cross

NOTE :Picture to scale  
scale

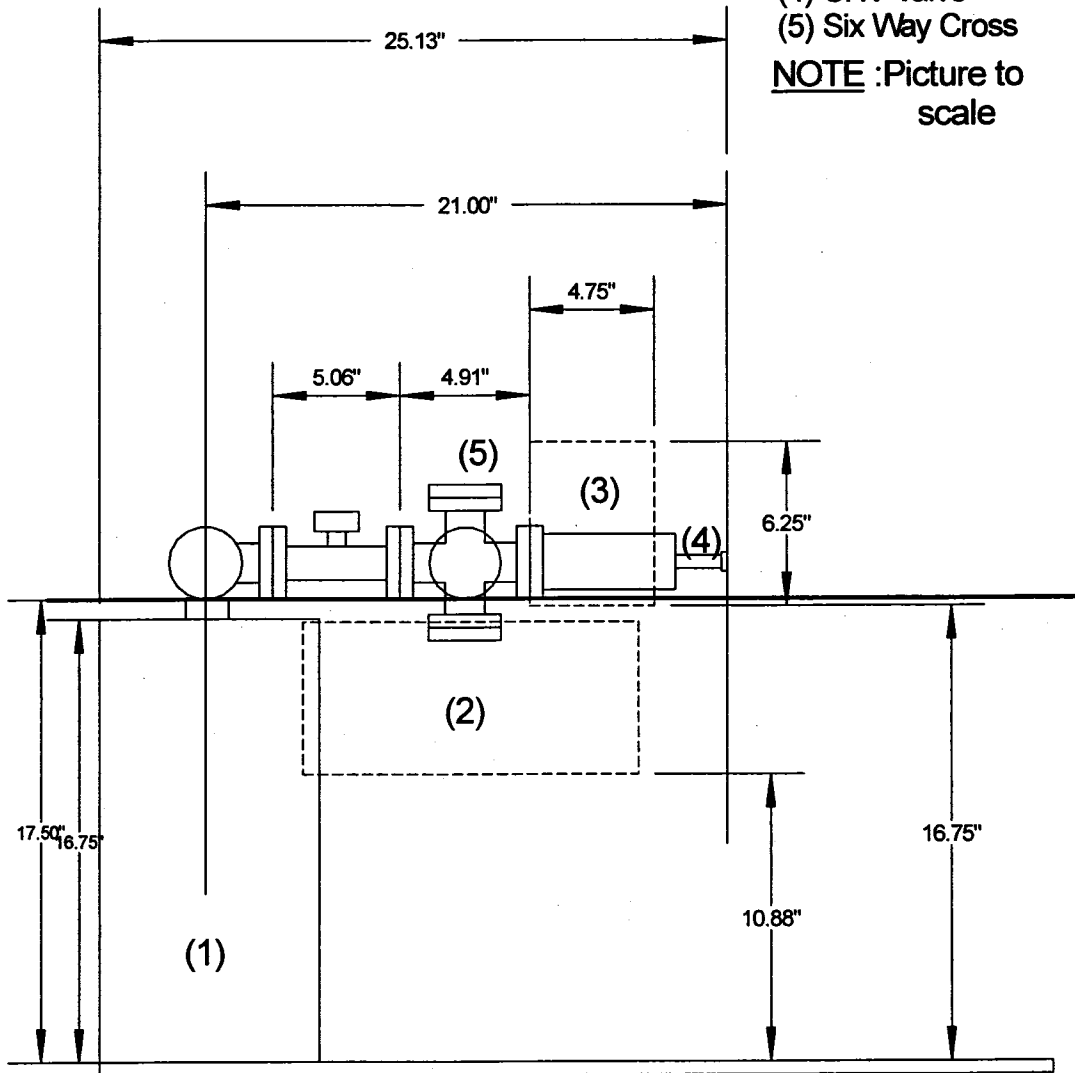


Figure 3.3 Vacuum system block diagram (SIDE VIEW)

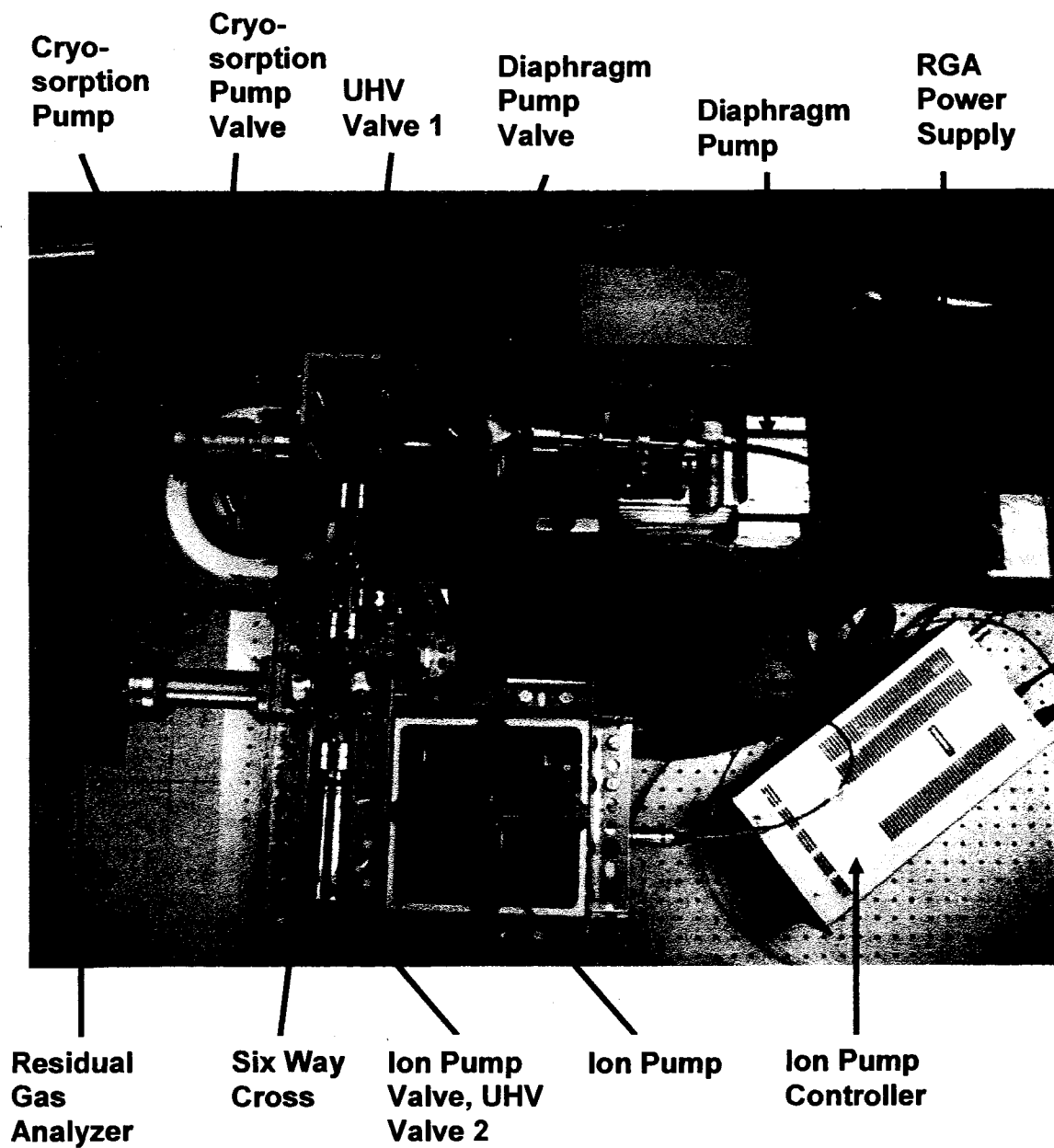


Figure 3.4 (a) Top view of the experimental set up

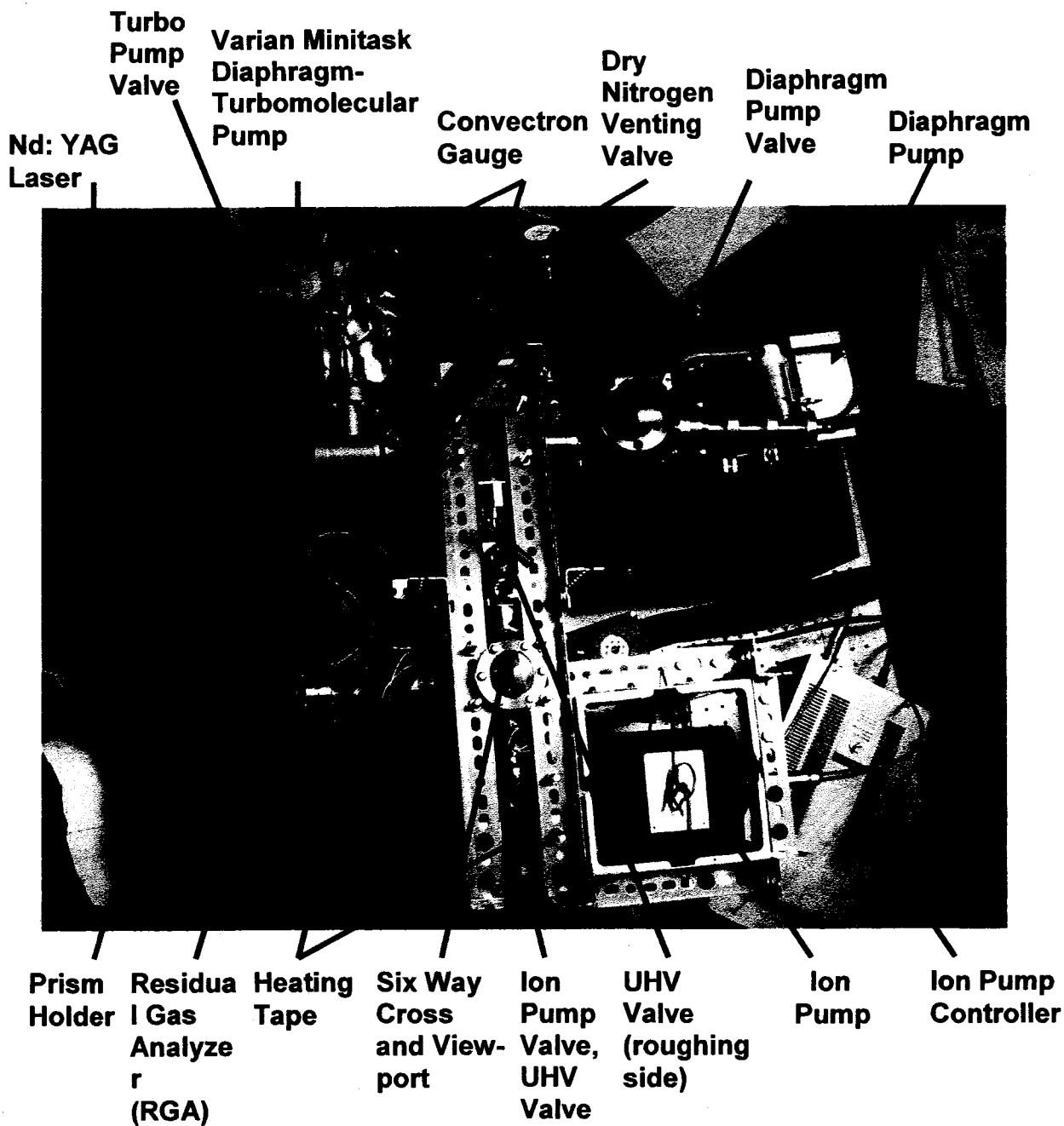


Figure 3.4 (b) Top view of the experimental set up



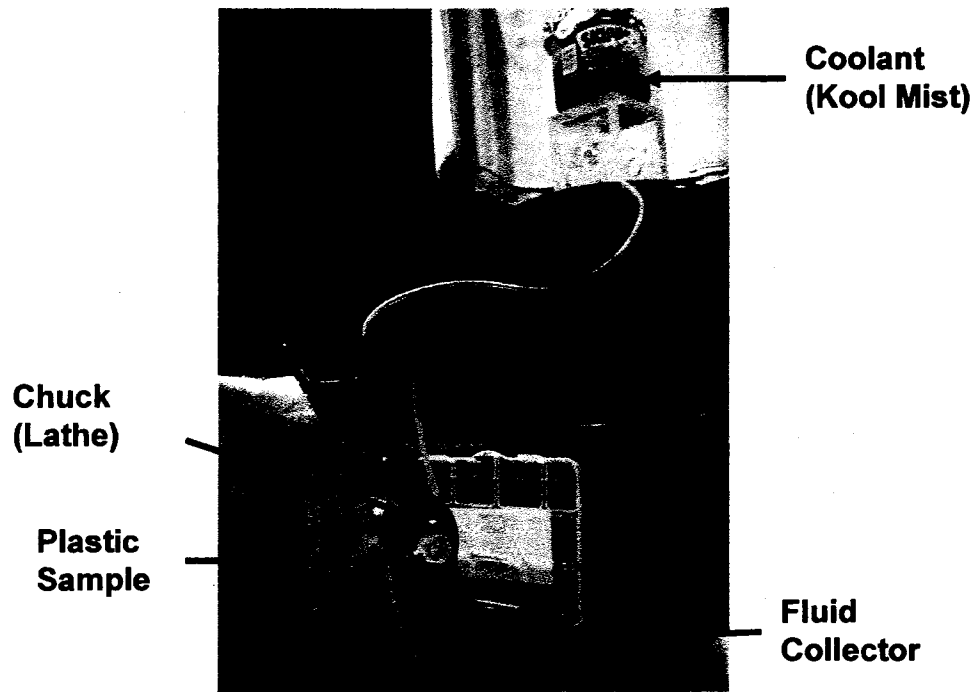


Fig 3.5 Cooling system for polishing on a lathe machine.



Fig. 3.6 Lapping machine used to grind and polish the ends of samples seven through nine.



Fig. 3.7 The nine samples examined are displayed. Samples one through six are 1" diameter while samples seven through nine are 1.25" in diameter.



**(i) Front surface**



**(ii) Back surface**

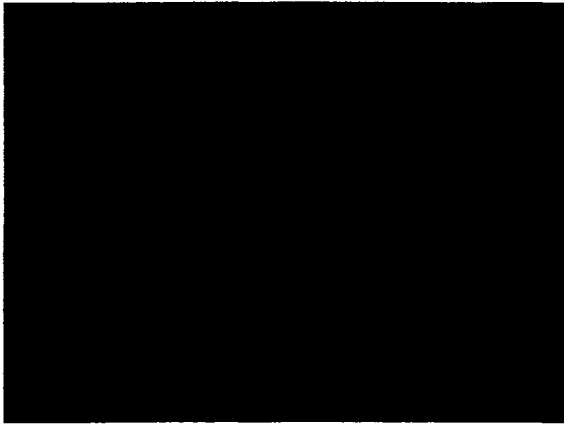


**(iii) Curved surface**

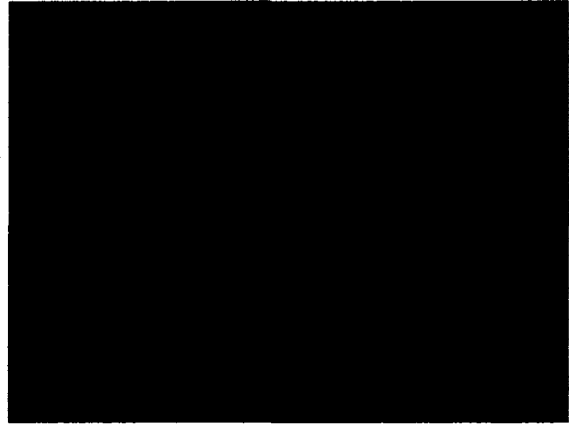


**(iv) Center**

**(a) Sample 1**



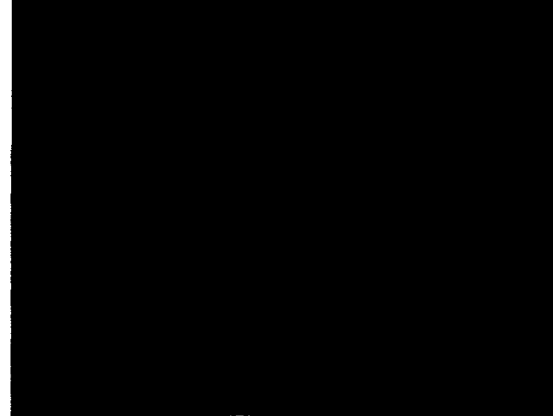
**(i) Front surface**



**(ii) Back surface**

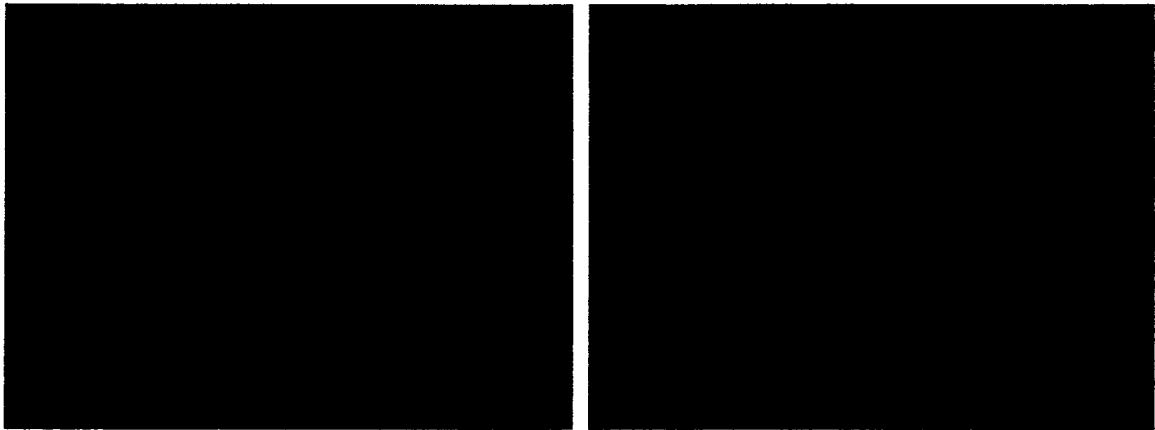


**(iii) Curved surface**



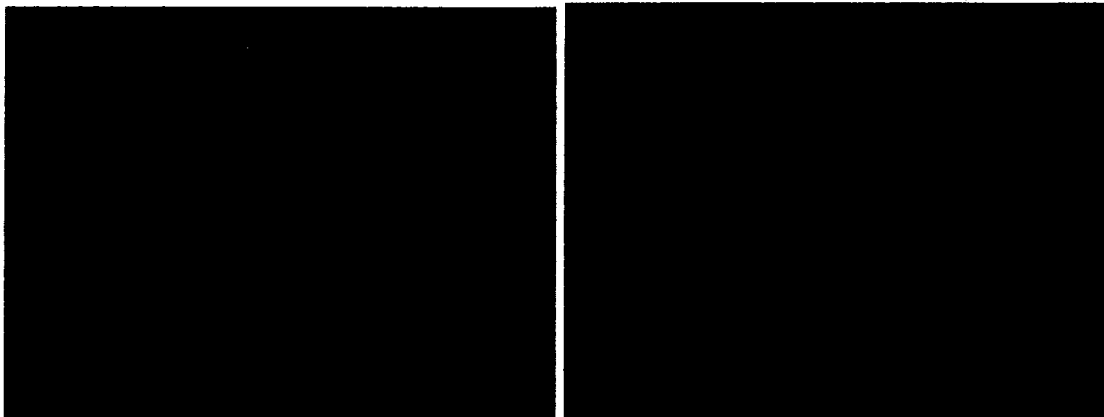
**(iv) Center**

**(b) Sample 2**



**(i) Front surface**

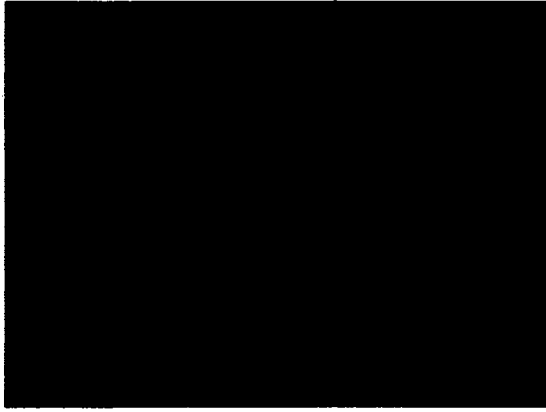
**(ii) Back surface**



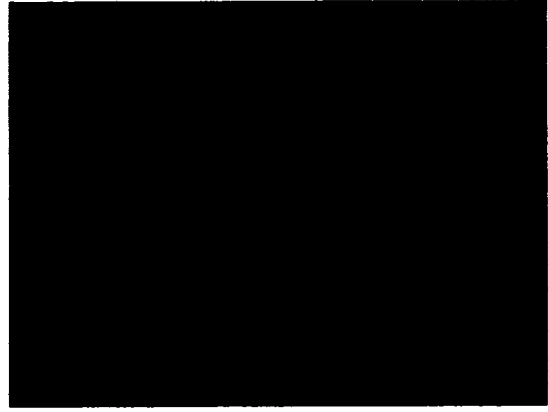
**(iii) Curved surface**

**(iv) Center**

**(c) Sample 3**



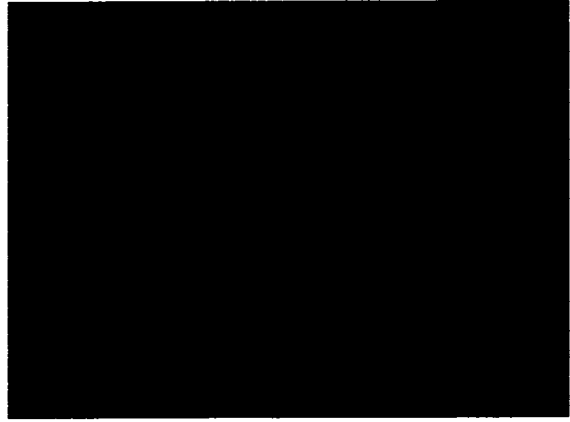
**(i) Front surface**



**(ii) Back surface**



**(iii) Curved surface**



**(iv) Center**

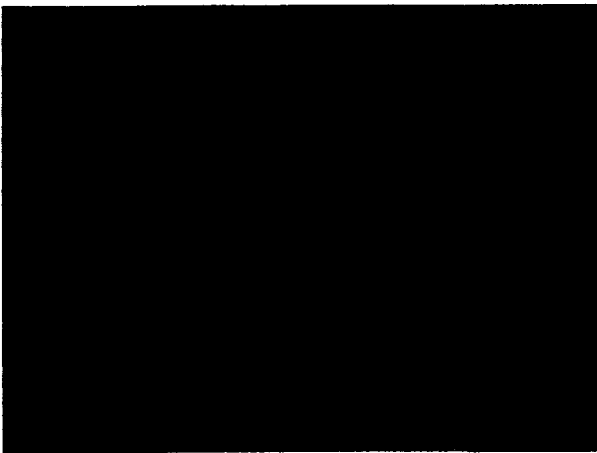
**(d) Sample 4**



(i) Front surface



(ii) Back surface

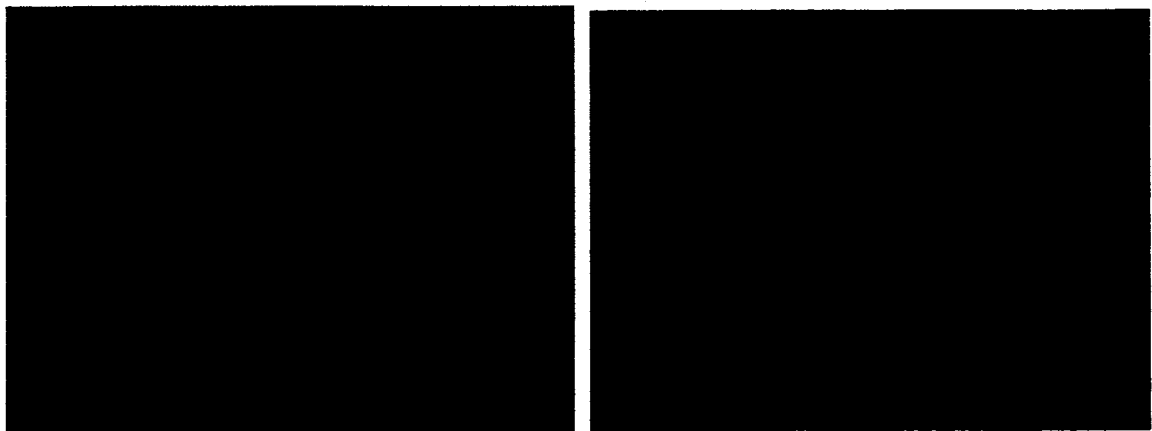


(iii) Curved surface



(iv) Center

(e) Sample 5



(i) Front surface

(ii) Back surface



(iii) Curved surface

(iv) Center

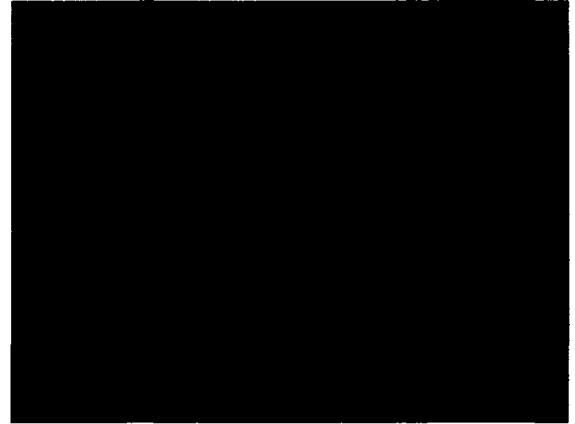
(f) Sample 6

Figure 3.8 (a-f) One inch diameter, polished, Rexolite samples (Samples 1 through 6) viewed through a 20x times optic microscope and digitally enhanced.

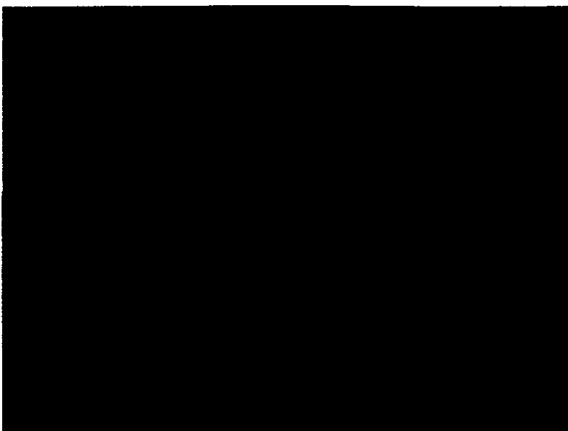




**(i) Front surface**



**(ii) Back surface**

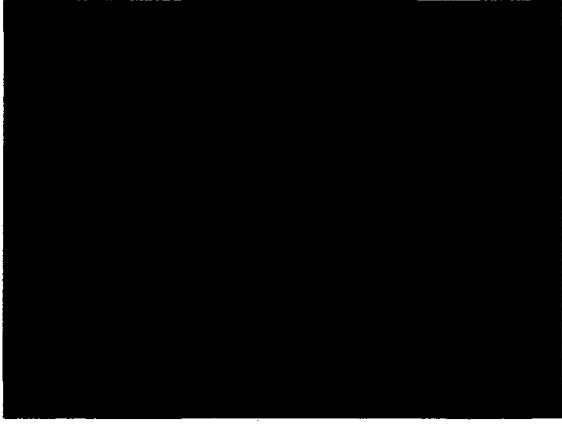


**(iii) Curved surface**



**(iv) Center**

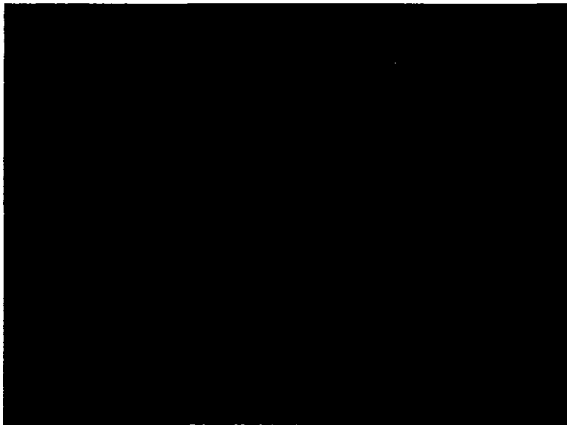
**(a) Plastic 7 (optically polished)**



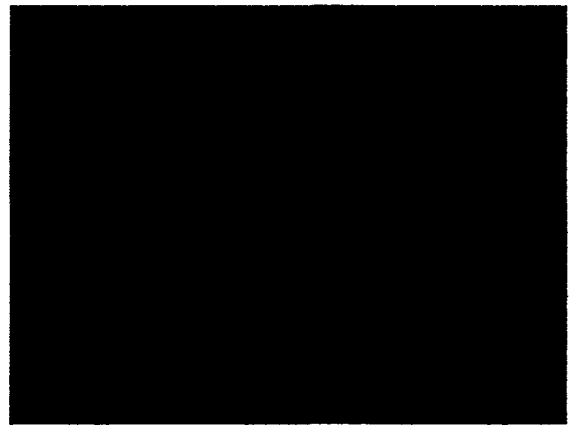
(i) Front surface



(ii) Back surface

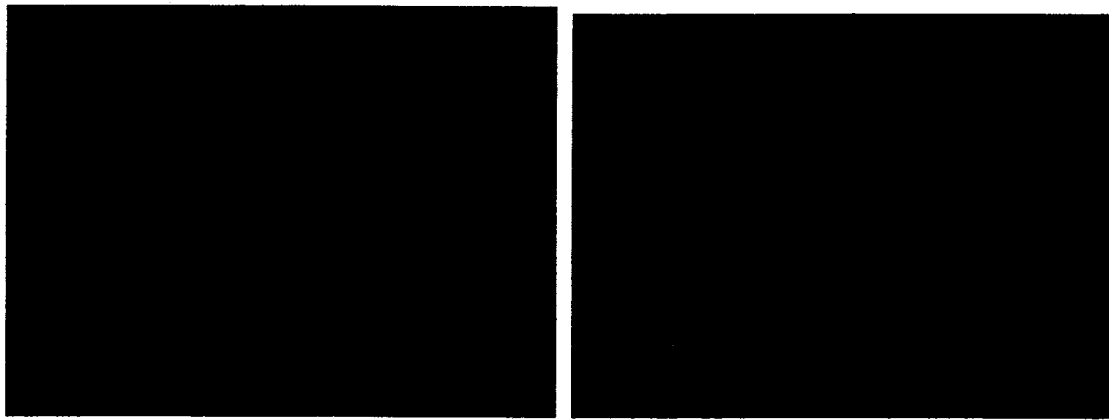


(iii) Curved surface



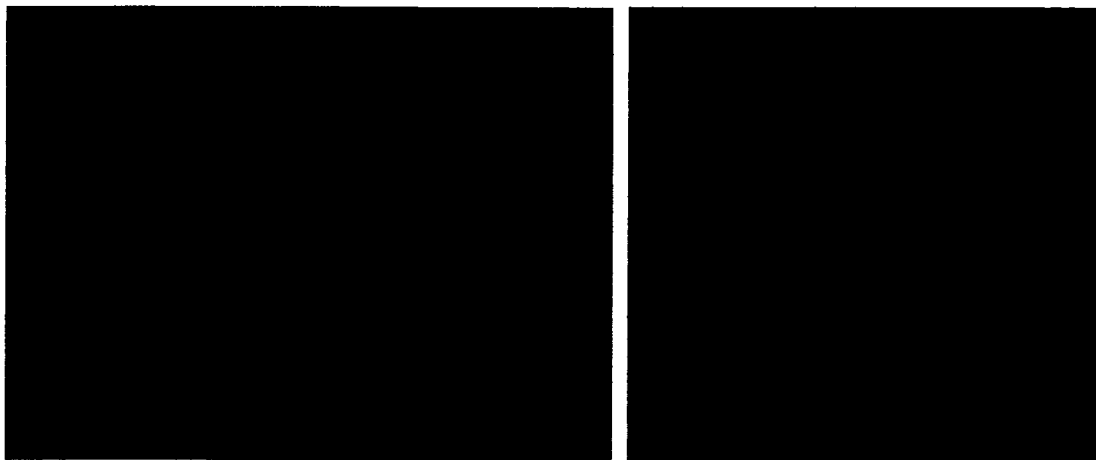
(iv) Center

(b) Plastic 8 (optically polished)



(i) Front surface

(ii) Back surface

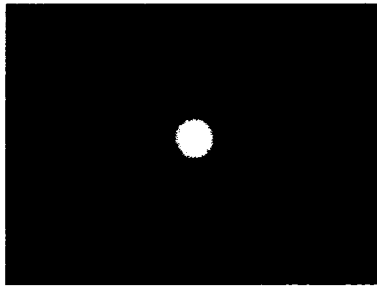


(iii) Curved surface

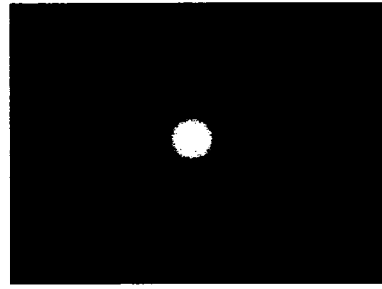
(iv) Center

(c) Plastic 9 (optically polished)

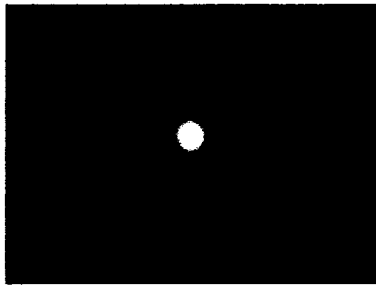
Figure 3.9(a-c) One and one quarter inch diameter, polished, Rexolite samples (Samples 7 through 9) viewed through a 20x times optic microscope and digitally enhanced.



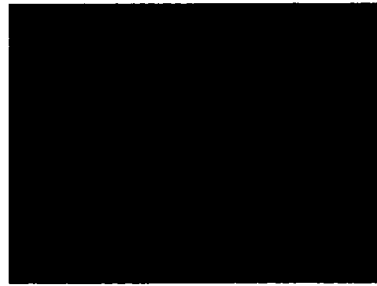
(i) Without sample



(ii) Through sample parallel to  
cylindrical axis but off center



(iii) Without sample

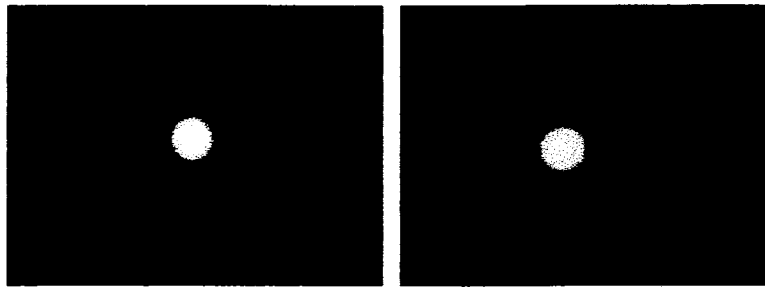


(iv) Through sample center along cylindrical axis



(v) Side View

(a) Sample 1



(i) Without sample

(ii) Through sample parallel to cylindrical axis but  
off center

(b) Sample 2



(i) Without sample

(ii) Through sample parallel to cylindrical axis but  
off center

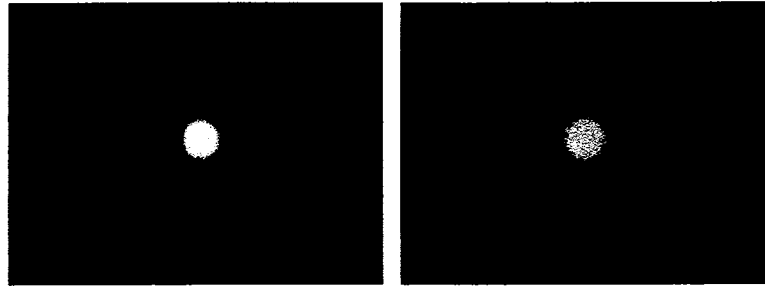
(c) Sample 3



(i) Without sample

(ii) Through sample parallel to cylindrical axis but  
off center

(d) Sample 4



(i) Without sample

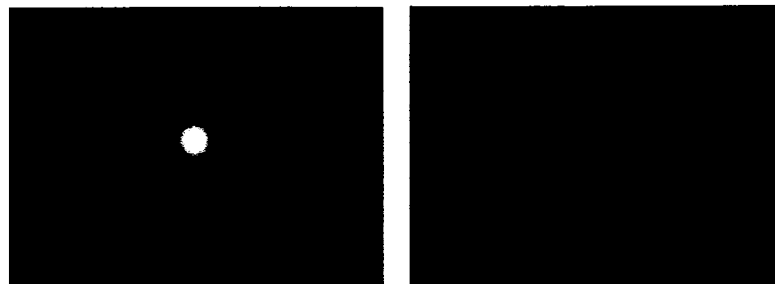
(ii) Through sample parallel to cylindrical axis but  
off center

(e) Sample 5



(i) Without sample

(ii) Through sample parallel to cylindrical axis but off  
center

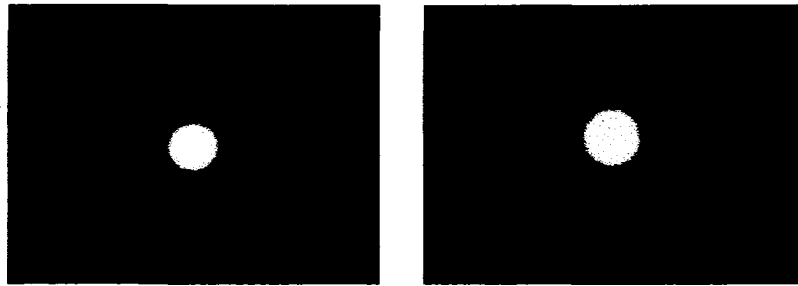


(iii) Without sample

(iv) Through sample center along cylindrical axis

(f) Sample 6

Figure 3.10a-f Scattering tests on 1" Rexolite plastic samples one through six  
using He-Ne Laser.



**(i) Without sample**

**(ii) Through sample parallel to cylindrical axis**



**(iii) Side view**

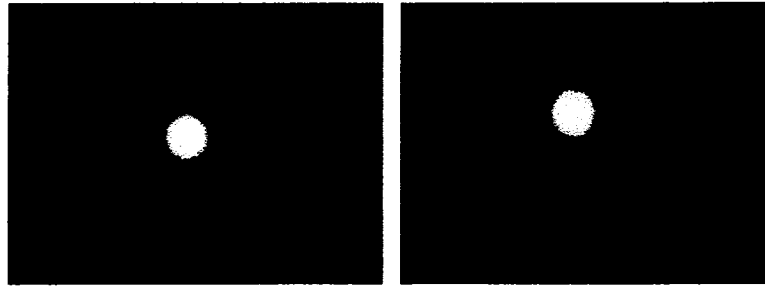
**(a) Sample 7 (optically polished)**



**(i) Without sample**

**(ii) Through sample parallel to cylindrical axis**

**(b) Sample 8 (optically polished)**

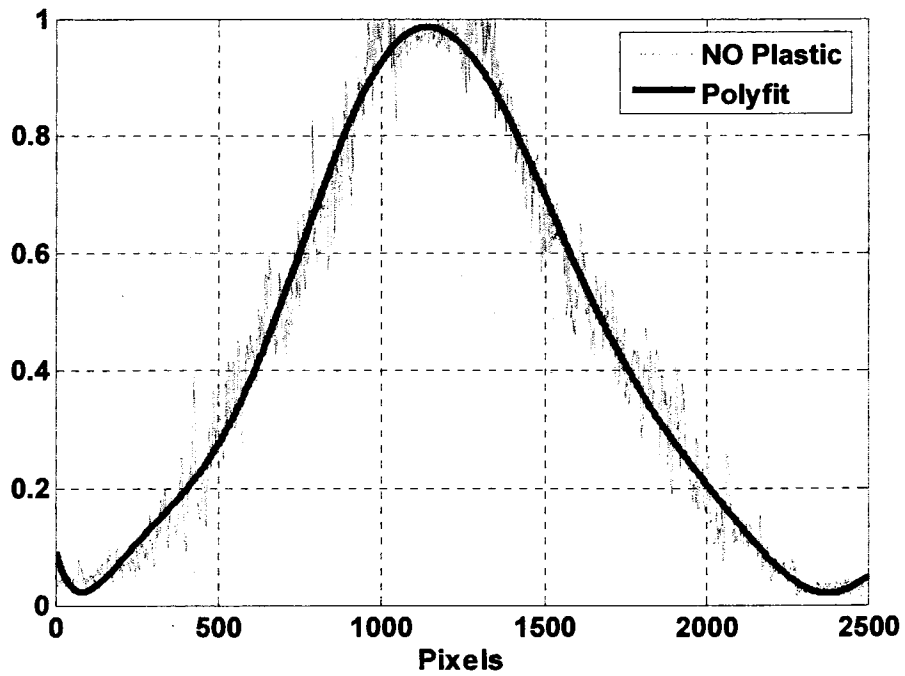


(i) Without sample

(ii) Through sample parallel to cylindrical axis

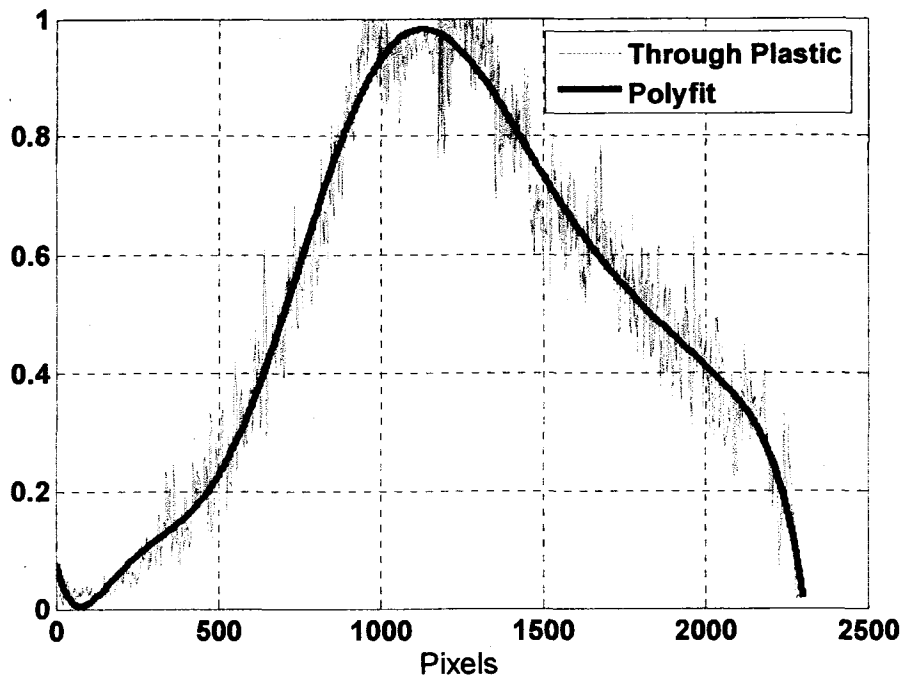
(c) Sample 9 (optically polished)

Figure 3.11a-c Scattering tests on 1.25" Rexolite plastic samples seven through nine using He-Ne Laser.

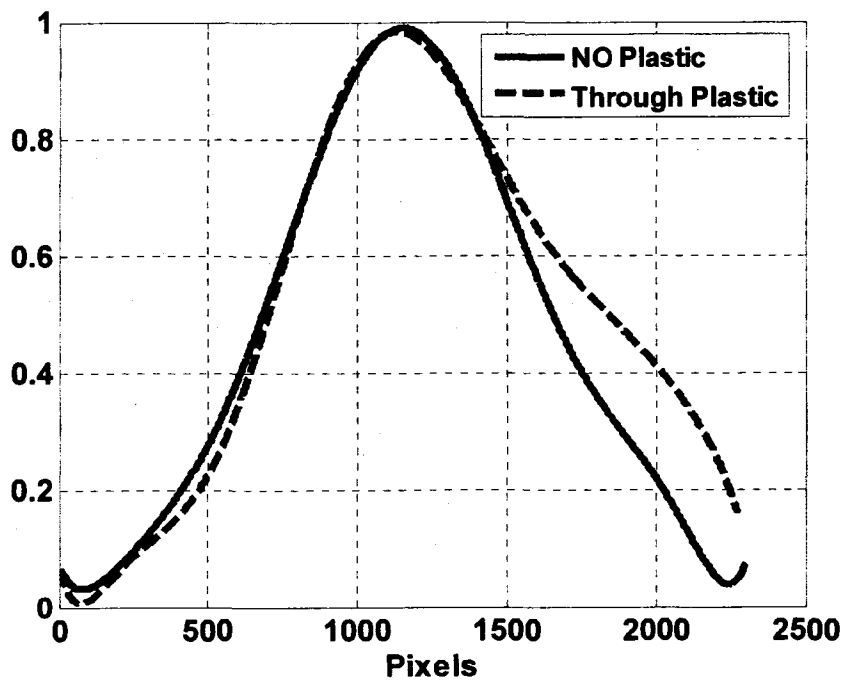


(i) Curve fitting to the data without plastic

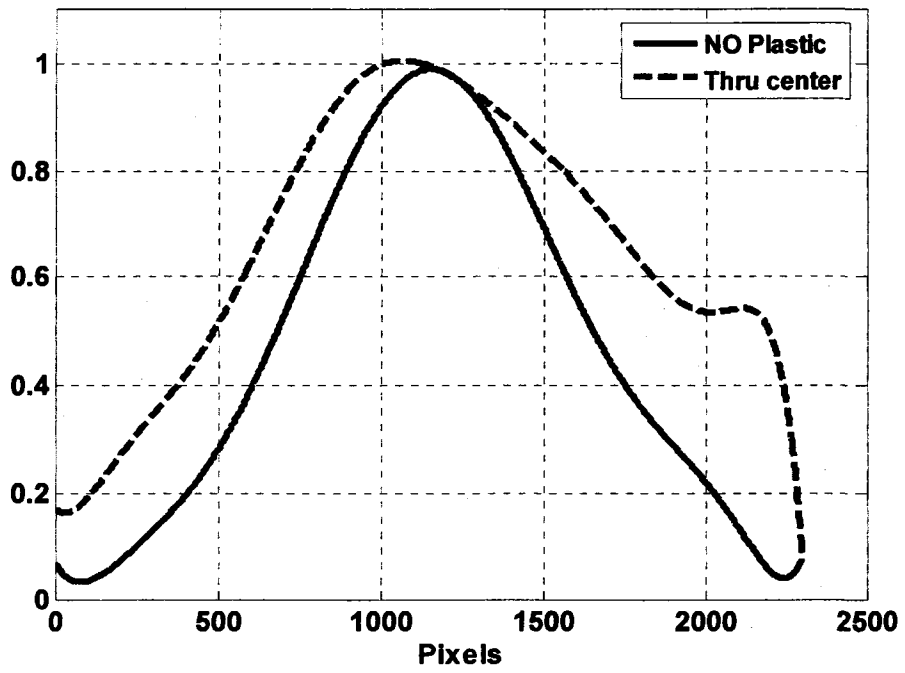




(ii) Curve fitting to the data through plastic

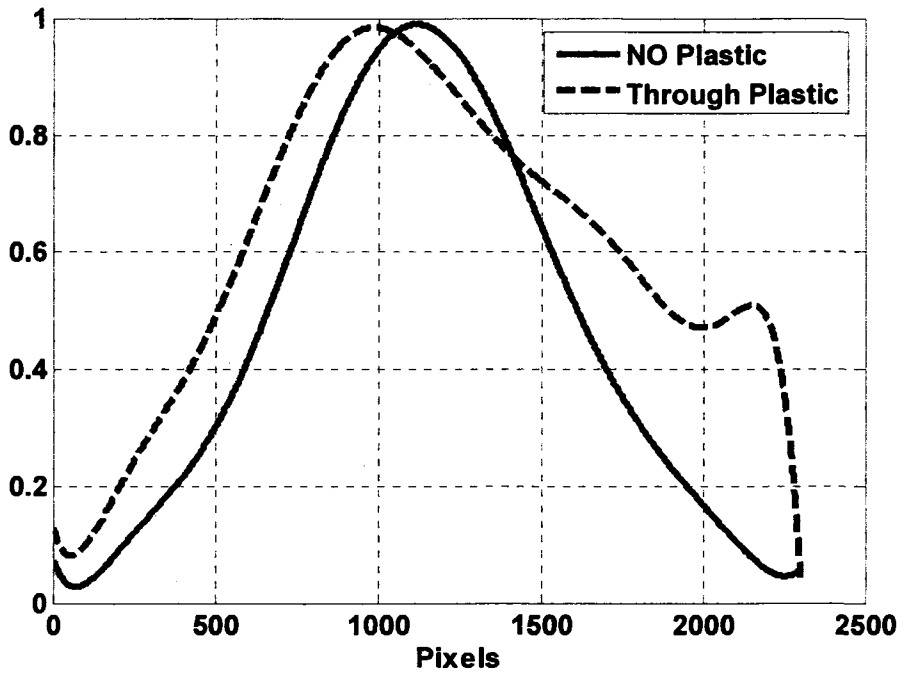


(iii) Curve fitting to the data with and without plastic

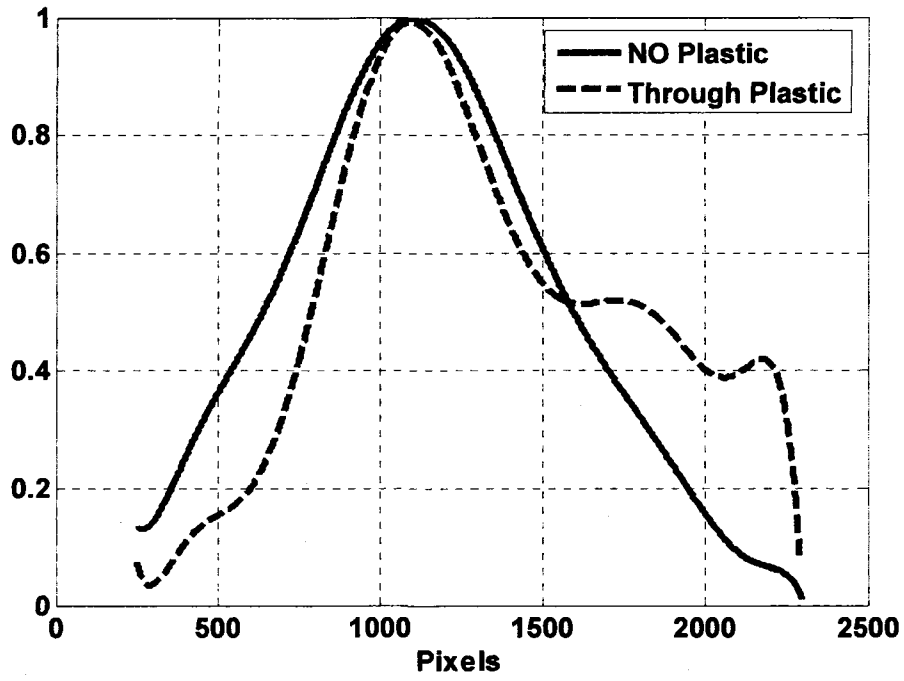


(iv) Curve fitting for beam through the center

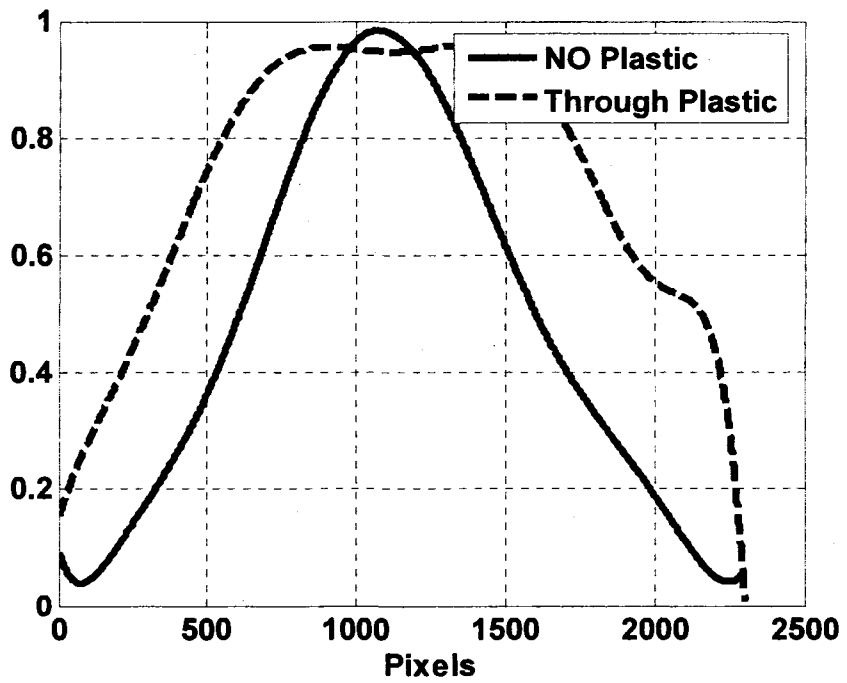
(a) Sample 1



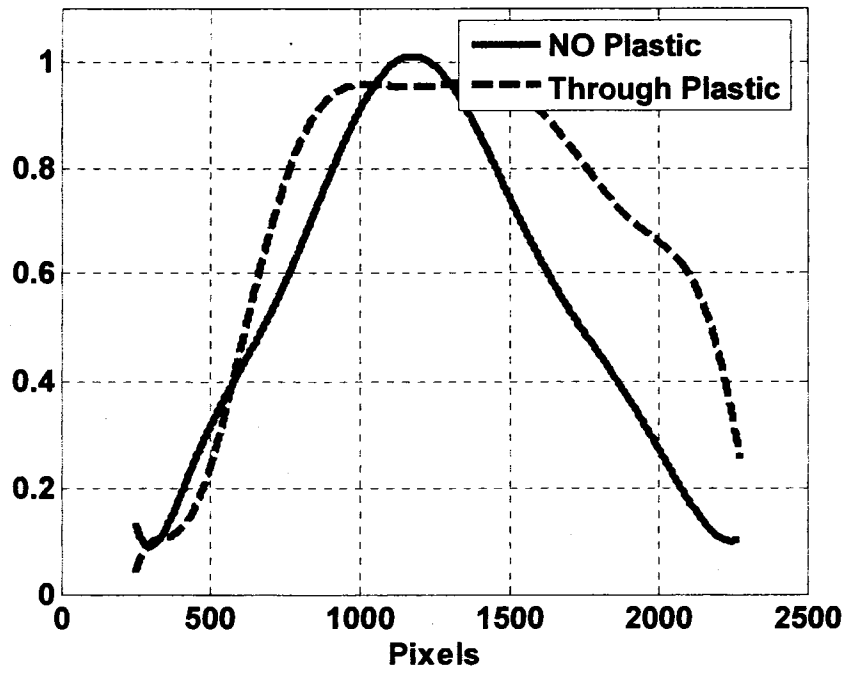
(b) Sample 2



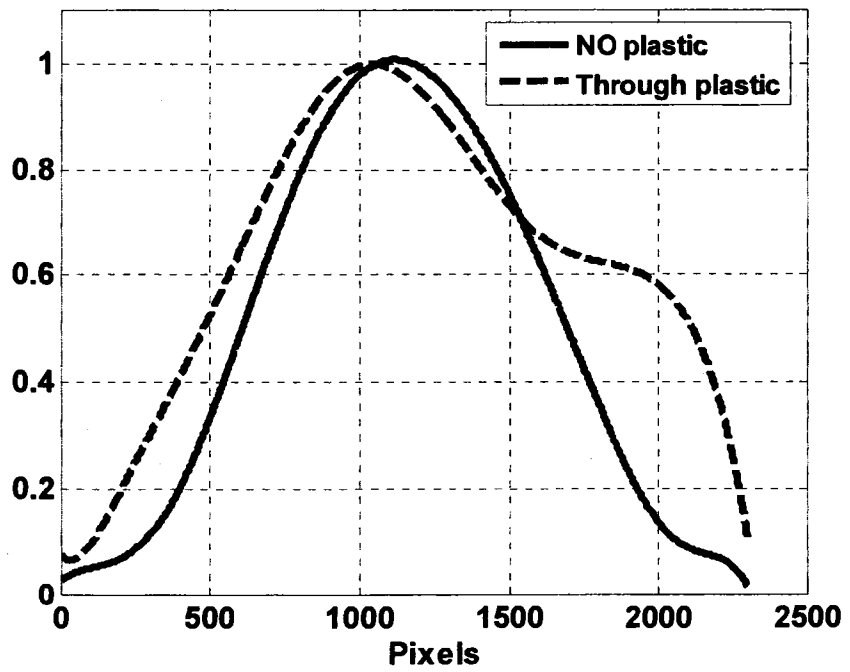
(c) Sample 3



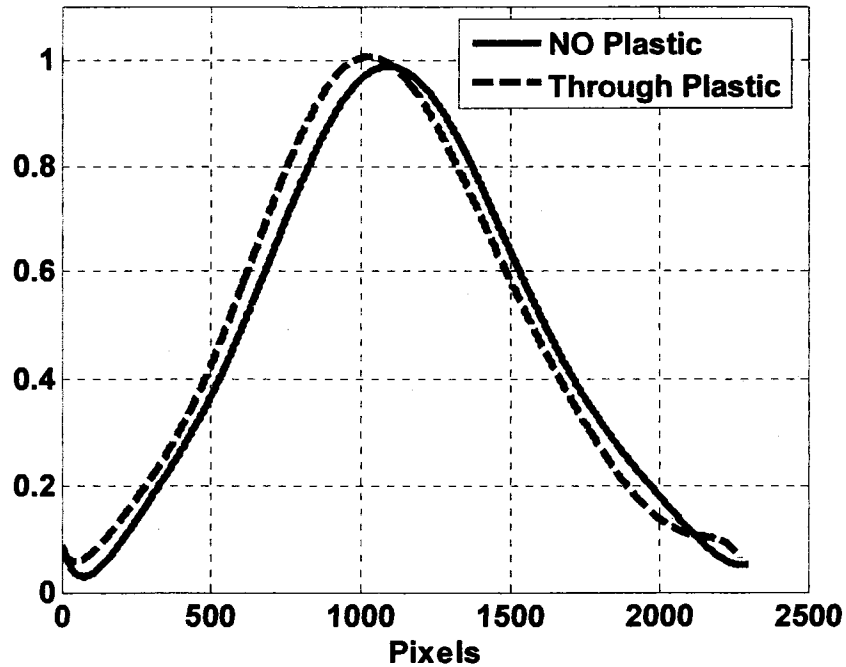
(d) Sample 4



(e) Sample 5



(f) Sample 6



(i) Sample 9

Figure 3.12 a-i Quantitative analysis of scattering through the plastic samples one through nine corresponding to Figs. 3.10a-f and 3.11 a-c subplots (i) and (ii) respectively. Light intensity profiles are for horizontal cross sections through the center of the laser beam in each subplot.

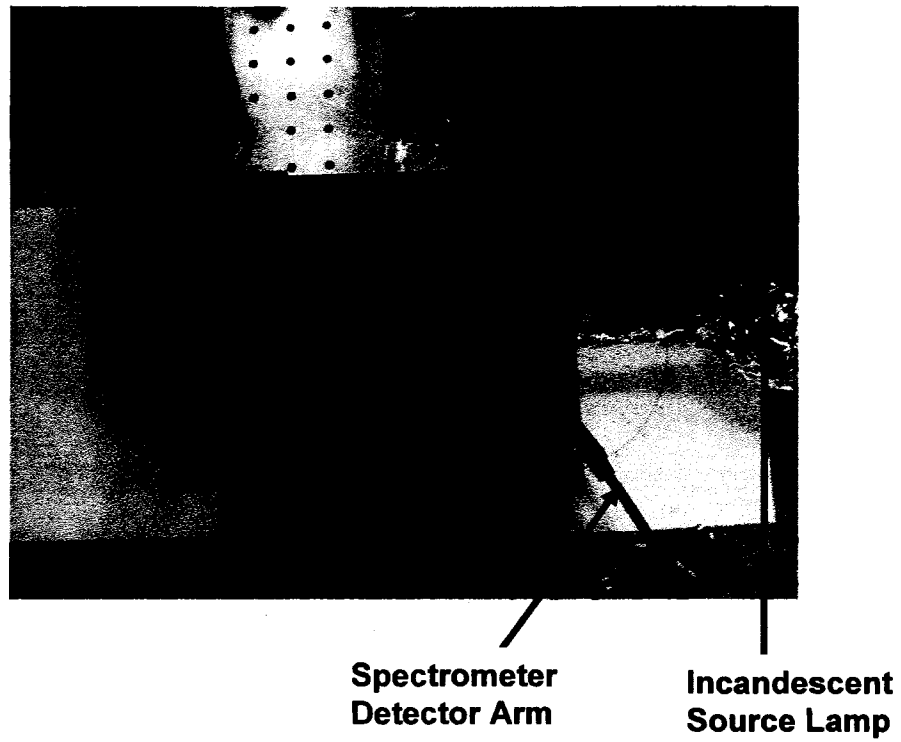


Figure 3.13a Top view of the Spectrometer Experiment Setup

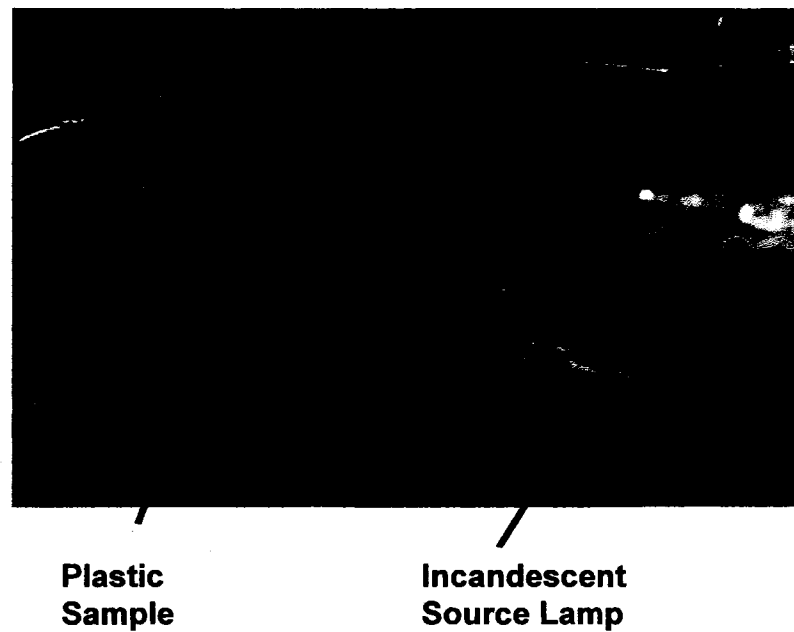


Figure 3.13b Side view of the Spectrometer Experiment Setup

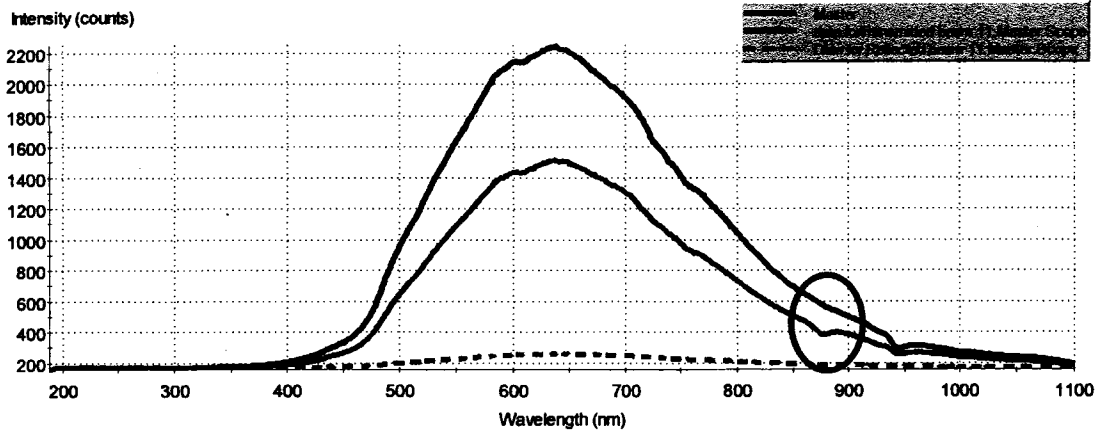


Figure 3.14a Spectrometer graph – transmitted light without plastic, transmitted and reflected light with plastic at normal incidence

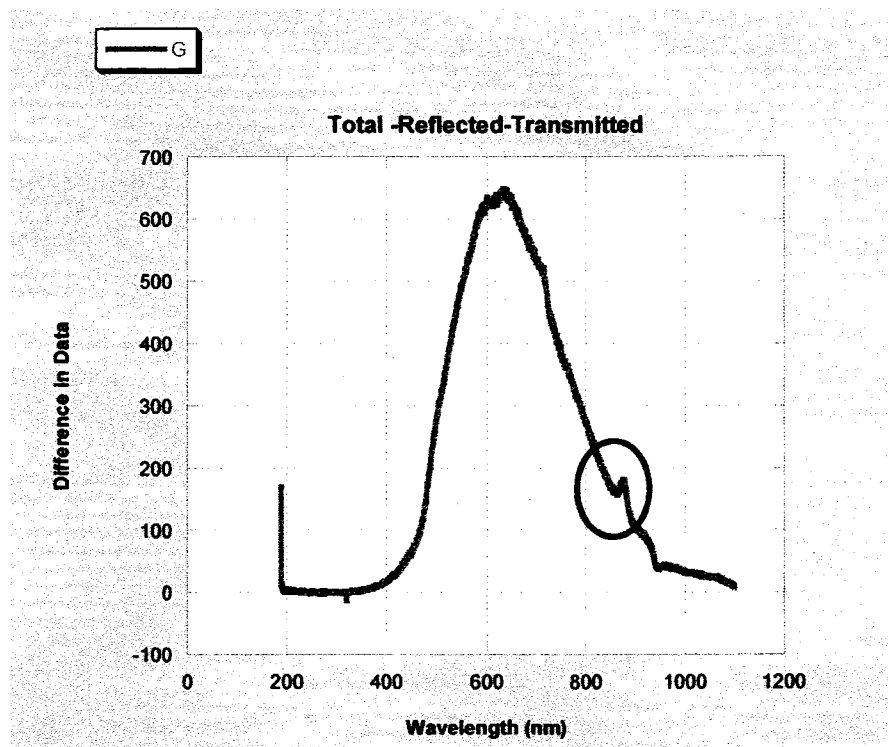
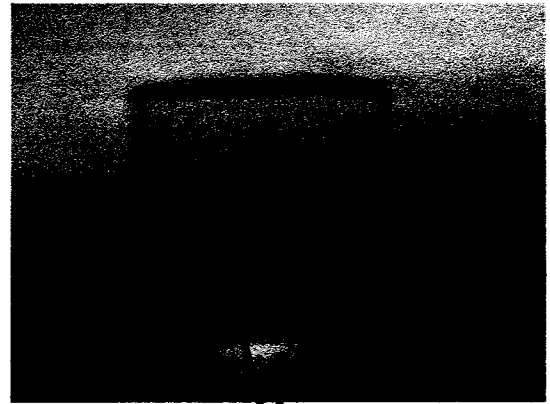


Figure 3.14b Difference between data points of transmitted light without plastic and, transmitted & reflected light with plastic at normal incidence



(a) Black dots formed due to continuous pulses from laser on the flat surface (Low power)



(b) Big dots inside the plastic due to laser incident on the curved surface (High power)

Figure 3.15 Pretests on rexolite sample



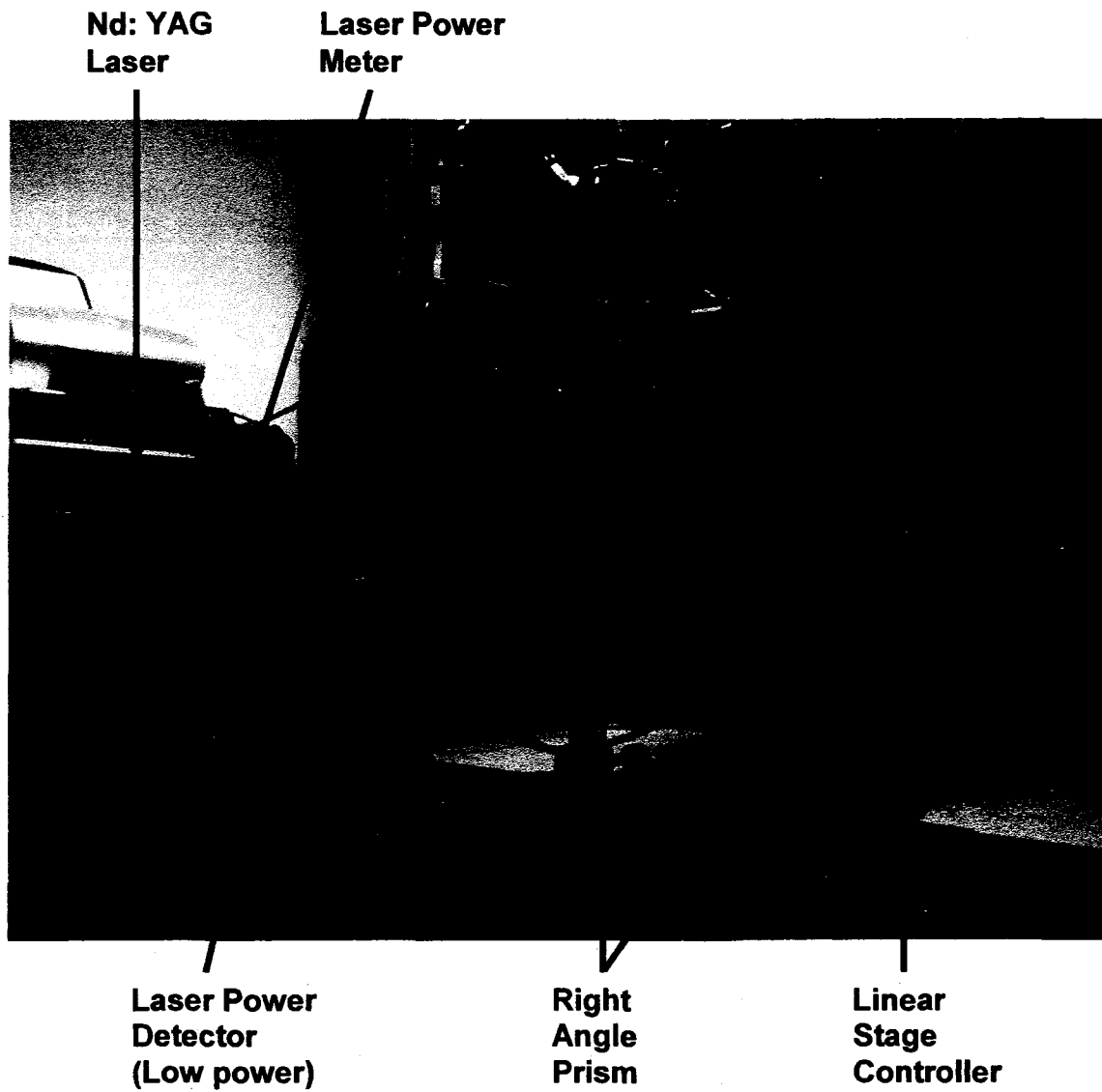


Figure 3.16 Optical Setup for deflecting the beam.

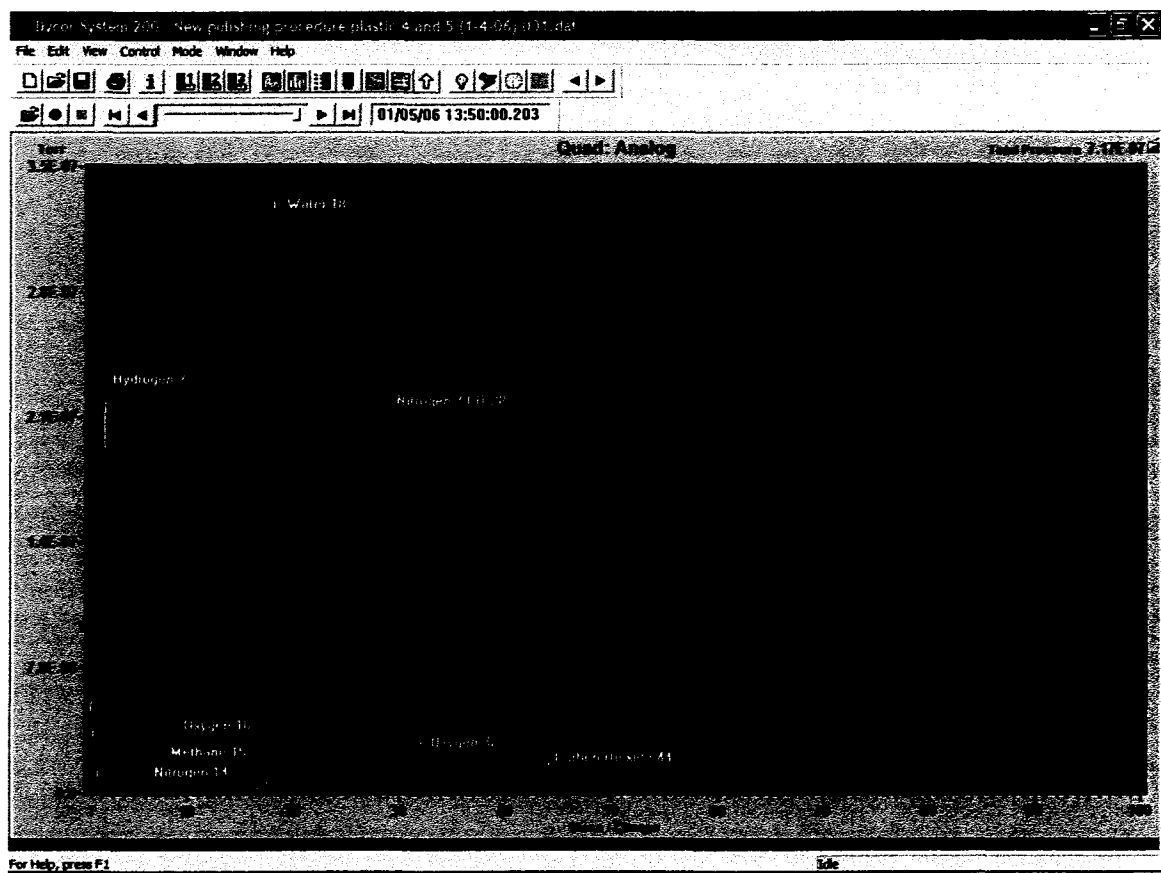
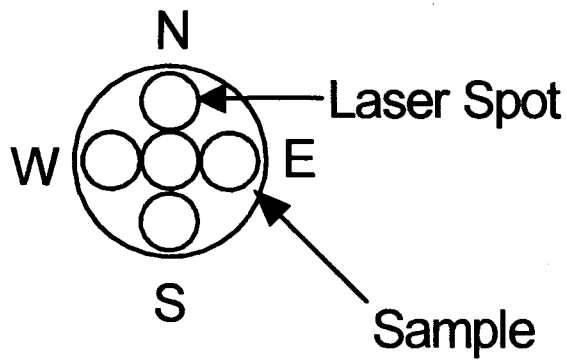
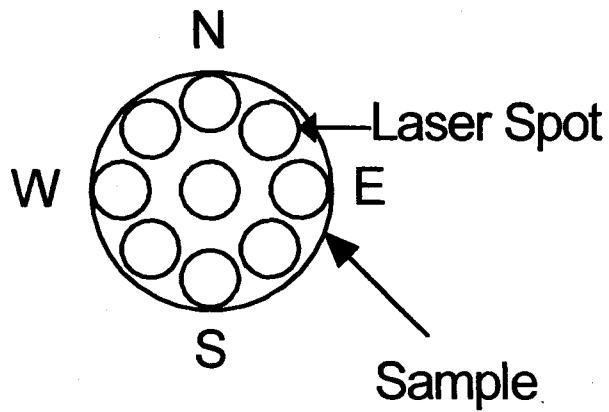


Figure 3.17 RGA scan for mass numbers between 1 and 100.



(a) 1" Rexolite samples



(b) 1.25" Rexolite samples

Figure 3.18 Ideal shot locations on the Rexolite samples



Figure 3.19 Laser beam profile

## CHAPTER 4

### EXPERIMENTAL STUDY AND DATA ANALYSIS

#### 4.1 Experimental Preparation

Pumping and venting procedures as discussed in the previous chapter have been followed throughout the experimental study. The first batch of polished cylindrical samples were 1" in diameter with lengths ranging between 9.29 mm and 10.28 mm. Ideally, the laser light was directed from below the vacuum chamber through the bottom viewport and the plastic under test resting on end on the viewport. As the beam passes through the plastic, the beam cross section is contained within the plastic over the length of the plastic cylinder, ideally. The beam exits the chamber through the top viewport. The laser energy prior to passing through the lower viewport and after passing through the upper viewport was monitored for a single shot. Other studies were conducted comparing HeNe laser light before and after the plastic under test in an air environment with and without a single viewport present. Table 3.3(a) & 3.3(b) (chapter 3) provides the information tabulated. As shown in Figs. 3.8(a-f), there is a significant difference between the quality of polish on plastic cylinder end when comparing off center and on center locations. The second batch of three samples was increased in diameter to 1.25" so that the entire viewport is nearly covered by the plastic under test. Their length's range from 4.72 mm to 8.18 mm. A fourth sample

about 9 mm long was machined to have a slightly larger diameter (33.02 mm) so that it could be wedged just below the upper viewport in the vacuum region. Two radial slits about a 4.75 mm long were cut in this plastic cylinder to allow free flow of chamber atmospheres above and below this cylinder. The larger area provides room to conduct more single laser pulse exposures on virgin plastic material. Further, the larger area enhances ones ability to locate the beam on the plastic such that the beam's cross section is totally contained in the plastic. The 1 ¼" diameter pieces were polished using a slightly different technique allowing for a more uniform polished surface over the entire surface. In all cases for all samples, the cylindrical portion of the plastic pieces under test were polished in the same manner to offer some control of the surface characteristics of the sample exposed to the vacuum environment.

To decrease the pump down time, polished samples are stored in a small vacuum chamber that is constantly being pumped with Varian's Mini Task turbomolecular/diaphragm combination pump. The pressures in this small chamber are not monitored but it is speculated that the pressure in this chamber reaches the  $10^{-6}$  to  $10^{-7}$  Torr scales ( $1.33 \times 10^{-4}$  to  $1.33 \times 10^{-5}$  Pa). This pressure range is achieved with the same pump on the desorption test stand during the roughing periods. Experiments were conducted when vacuum pressures reached about  $5 \times 10^{-8}$  Torr level. It is important to note that an ion pump is used in achieving this level. The ion pump speed is 20 liters/s for Ni. Ion pump was chosen because of its low pumping capacity in order that the residual desorbed gases generated by the 4-7 ns pulsed laser could be detected by the RGA on

gases generated by the 4-7 ns pulsed laser could be detected by the RGA on time scales of ms. For comparison purposes, the smallest Helix CTI-cryogenic Cryo-Torr cryopump (Cryo-Torr 4F) has pumping speeds of 1,100 liters/s for water, 370 liters/s for air, hydrogen and argon. Although the pumping speed for gases in common to the two pumps have not been provided for comparison, the pumping speed of the ion pump used is one to two orders smaller than other pumps in the market. This becomes an important point when considering future applications of Rexolite.

A Residual Gas Analyzer (RGA) is used to measure the partial pressures internal to the vacuum chamber. Eight mass-to-charge ratios were monitored. These eight were chosen based on a full scan study of the chamber. They were either dominant elements in the chamber or a trace element signifying the polishing agent used in the polishing procedure. The elements traced are: H<sub>2</sub> (2), N (14), methane (15), O (16), H<sub>2</sub>O (18), N<sub>2</sub>/CO (28), O<sub>2</sub> (32) and CO<sub>2</sub> (44). The numbers in parenthesis are the mass-to-charge ratios and H is hydrogen, N is nitrogen, O is oxygen, H<sub>2</sub>O is water, CO is carbon monoxide and CO<sub>2</sub> is carbon dioxide. The RGA may be set for Faraday cup mode or electron multiplier mode. The Faraday cup mode provides the true partial pressures of a particular mass-to-charge ratio normalized to nitrogen. A correction factor is required to determine the actual partial pressure for a specific species. The second mode, electron multiplier mode, enhances the signal due to partial pressures of the individual elements of different mass-to-charge ratios. Quantitatively, the recorded partial pressures are not meaningful without

knowledge of the gain factor associated with each mass-to-charge ratio being monitored. Even so, qualitative arguments may be made. With appropriate correction factors, the partial pressures may be determined normalized relative to nitrogen. Further corrections are not made relative to the particular mass-to-charge ratio. For all but one set of shots, the RGA is in electron multiplier mode. Sometimes the mass-to-charge ratio is presented in terms of atomic mass units (AMU) or the mass number. This interpretation is reasonable if the neutral atom or molecule ionized by the residual gas analyzer (RGA) removes only one electron from element. The RGA's quadrupole separates the elements based on the mass-to-charge ratio (or equivalently, the electron-to-mass ratio). The mass number is the closest integer value of the atomic mass. Prior to illuminating the eighth plastic piece the first time, the nude filament of the RGA broke and was promptly replaced. The response of the new filament was different than the old filament. This response is taken into consideration in the following discussions. For each AMU measurement recorded, the RGA takes about 25 ms to provide a measurement based on the maximum of five sample points around the AMU being measured. (NOTE: One atomic mass unit (AMU) equals  $1.66 \times 10^{-27}$  kg which is the mass of a single proton [1.0073 AMU] or a single neutron [1.0087 AMU]. Electrons are many orders of magnitude smaller [0.00055 AMU or  $9.1 \times 10^{-31}$  kg].) That is, when the RGA makes a measurement of the peak height of a particular m/e ion, it does in fact make a series of five measurements. The reason for this is that one can not be positive that there has been no drift in the electronics that might cause the top of the peak to have shifted slightly. If one

assumes, for example, that the  $m/e$  to be measured is the mass 28, singly charged ion, the first of five measurements will be made at a mass position 27.75; the second at 27.875; the third at 28.0, the fourth at 28.125; and the last at 28.25. The only data point stored will be the highest of the five, which corresponds very closely to the peak height even if the peak location has shifted somewhat over time. The dwell time parameter is set at 5 ms. This implies that each measurement (charge accumulation) would take approximately 5 ms. However, there is an unknown "settling time" between each measurement. Also, in the case of a large ion current (detected by monitoring the charge rate), the sampling time is automatically reduced by an unknown amount. Note that the RGA makes all measurements sequentially. The major source of measurement error is due to the fact that the system is not at steady state. The laser pulse desorbs material in an instant, but the partial pressure of the species attempting to be monitored decays rapidly. If the decay time is similar to the time taken to make a measurement, the specified number of AMUs being monitored (in these experiments the specified number of peaks being monitored is eight), one cannot be sure that their relative heights can be compared (having been measured at different points in time). Since eight AMUs are being monitored by the RGA, the RGA's period of measurement is about 200 ms. The RGA was set up to scan sequentially from the lowest AMU value to the highest AMU value. In many instances, the pulse width of the atoms detected is between one and two of the RGA's period of measurement. Initial studies show that the total background pressure measured by the RGA in the vacuum chamber is comparable to that



measured in the ion pump chamber when the plastic under test is not stimulated. Roughly a 1:1.3 ratio is observed between the two measurements where the ion pump is at a lower pressure than the vacuum chamber. The RGA is used to measure the total pressure of the vacuum chamber when the system is in a thermal equilibrium.

The following sections in this chapter address the interpretation of the data. The data is discussed and then applied to modeling some aspect of laser/thermal desorption dynamics.

## 4.2 Data Interpretation

The RGA data for the six 1" diameter, transparent grade, plastic test pieces are displayed in Figures 4.1 to 4.6 with corresponding tabulated data in Tables 4.1 to 4.6. The RGA data for the three 1.25" diameter, optically transparent grade, plastic test pieces are displayed in Figures 4.7 to 4.9 with corresponding tabulated data in Tables 4.7 to 4.9. The data in the tables provides the following select information in sequential order:

- Peak partial pressure of a particular AMU in electron multiplier mode equals the partial pressure in Faraday cup mode (Torr) times the gain of the electron multiplier of the particular AMU. The units of measure are defined as ARU (Arbitrary Relative Units) of pressure.
- Time duration of signal in units of second as measured from the front end of the peak to back end of the peak, a rise time and a decay time labeled as such may also be recorded and is measured from the background

partial pressure to the beginning or end of the maximum of the pulse. Usually, the maximum of the pulse stands out from the rise or decay nature of the pulse.

- Delay time of a particular partial pressure relative to initial partial pressures received if beyond a single system sampling time in units of seconds
- If an initial precursor pulse is observed in the 10 Hz continuous shot mode (Y for yes and N for no)
- Average partial pressure baseline of a particular AMU in electron multiplier mode (ARU) prior to illumination (prior to a shot)
- Standard deviation of the baseline pressure of a particular AMU in electron multiplier mode (ARU) prior to a shot.

If no signal was observed implying that the signal to noise ratio is equal to one or less, an entry of "n" is used. The time at which a laser pulse was initiated is provided in the table for each shot. Along with a particular shot number, the shot location is qualitatively represented using the directions on a compass where n, s, w, e, nw, ne, sw, se and c represent north, south, west, east, northwest, northeast, southwest, southeast, and center respectively. These qualitative measurements provide some input to the proximity of the 6.5 mm diameter beam relative to the edge of the sample. In all cases, the laser beam is unfocused prior to penetrating the viewport and plastic piece under test. Appropriately positioning the laser beam and test piece without illuminating the test piece based on burn paper markings for 1064 nm and opaque screens for

a major portion of the visible beam signature. The abbreviations SS and CS stand for single shot mode and continuous shot 10 Hz pulse repetition rate mode respectively. The time duration of the CS mode is 10 s for all experiments. The date on which the experiment was performed, the vacuum pressure as measured in the ion pump, and the laser wavelength may be found in the table caption. The ion pump pressure of the environment is within a factor of 1.3 from the total pressure as measured by the RGA. Except for special cases in which the vacuum wall of the chamber is purposely illuminated [corresponding to Figures 4.10 (a), (b), (c) and Tables 4.10 (a), (b), (c)], the laser beam was directed normal through the bottom viewport with plastic resting on one end on its surface. The degree of error between the laser beam and the normal to the viewport surface is roughly 3-5 %. The degree of error in the parallelism of the plastic cylinder ends is roughly 39  $\mu\text{m}$  (maximum change in plastic wall thickness).

After a number of test runs and procedural tuning, sample one is defined as the first test sample. The sample was illuminated with 70 mJ of unfocused 1064 nm of light at four locations near the circumference of the sample at a vacuum chamber pressure of  $4.8 \times 10^{-8}$  Torr. Shots 1 through 4 are single pulse shots and Shot 5 is conducted in continuous shot mode. Figures 4.1a-f and the appropriate tabulated data in Table 4.1 associated with these figures, display the relative partial pressures enhanced by the electron multiplier. These partial pressures are a result of the gain of the electron multiplier internal to the RGA. The twenty-six minute duration of the first experiment displayed in Fig. 4.1a is expanded in three minute intervals in Figs. 4.1b - 4.1f about the times that the

expanded in three minute intervals in Figs. 4.1b - 4.1f about the times that the RGA detected the emitted atoms/molecules. Shot number two shows no discernable signal outside of the background partial pressures. Figures 4.1b – 4.1f display the pulse durations. Shots one and three have a very discrete pulse duration roughly on the order of the RGA's period of measurement. Methane and carbon dioxide are common to both shots. Shot three also has a small oxygen and a large diatomic nitrogen/carbon monoxide peak. Shots number four and five, which occur at the same location, have a distinct decay time ranging from 0.5 s to 6.469 s for different peaks. In the continuous shot mode, excluding the two AMUs that have saturated, continuous pulsing tends to decrease the desorption properties with time but not necessarily in a monotonic manner. Further, in this mode, a precursor pulse was observed for each mass-to-charge ratio observed excluding diatomic oxygen. The presence of diatomic oxygen above the background pressure does not appear to exist for all shots conducted on this sample.

Five separate sets of 70 mJ, 1064 nm, pulsed laser illuminations (four single pulses and one continuous train of pulses) over four locations near the circumference of sample two were conducted. All experiments on sample 2 were conducted in a  $4.88 \times 10^{-8}$  Torr ( $6.5 \times 10^{-6}$  Pa) vacuum. Figure 4.2a and Table 4.2a indicate that there were no partial pressure changes detected relative to the background partial pressures. One might argue that the duration of the laser beam is about 6 ns and the RGA is too slow to be able to detect such a signal. The RGA employs a Faraday cup to collect charge over time. The integrating

nature of the device should be able to detect at least one mass number if present during the sampling process of the RGA over the time duration of the experiment. The studies with sample one illustrate that the RGA can detect atoms/molecules impinging upon the RGA sensor over the duration of the experiment. Prior to removing the sample from the chamber, a number of different tests were conducted. Figures 4.2b and 4.2c with corresponding Tables 4.2b and 4.2c illustrate the results when the pulse energy was increased to 77 mJ and to 85 mJ. Three sets of pulses (two single shots and one continuous shot) at each energy level were tested on the center of sample two. Only in the continuous shot mode was there a small methane change in partial pressure detected (approximately  $\Delta P_{15} = 1.3 \times 10^{-7}$  ARU based on an average partial pressure of  $3.55 \times 10^{-7}$  ARU in electron multiplier mode). Later it will be shown that the true partial pressures are about two to three orders of magnitude smaller than this value. As shown in Fig. 3.8 a (iv), the center of sample two is not polished with the same grade as that off center. [This tends to indicate that the desorption properties may not be strongly dependent on the grade of polish over the surface of the material. This point will be borne out later when compared to later samples polished using a slightly different technique]. Because the sample is not optically polished allowing for scattered photons to be directed to the surface of the vacuum chamber walls, the upper viewport could desorb material as a result of the transmitted beam impinging on its surface. The cross section of the laser beam near the circumference of the plastic may not completely overlap with the cross section of the plastic under test consequently leading to mixed desorption

viewport-sample interface diffuses along spaces around the plastic geometry to the RGA sensor. A number of 70 mJ, 1064 nm viewport and a combination of viewport-chamber wall illuminations were examined as shown in Figs. 4.2d and 4.2e. These figures are respectively associated with Tables 4.2d and 4.2e. In all cases, the sample 2 remained in the vacuum chamber. Because the diameter of the viewport is 33.02 mm and the diameter of the plastic under test is 25.4 mm diameter, there was significant amount of room to direct the 6.5 mm diameter beam through the viewport wall without intercepting the plastic under test. In each separate case, two single pulse shots and one continuous pulse shot were examined illuminating the same location. It is interesting to note that both nitrogen and water in the continuous mode case did not experience a precursor signal and diatomic oxygen was not observed in the viewport illuminations. Although the molecules/atoms released may be easily observed from the figure and table, what stands out is the time duration of the release of material. In all cases, the release of material appears to be discrete based on the speed limitations of the RGA. In the multiple pulse mode, on average desorption levels for the unsaturated cases appear to decrease with time but it is not a monotonic increase. This may imply that some of the gas molecules desorbed by the viewport may be adsorbed so to be desorbed at a later time. When the chamber walls and viewport are purposely illuminated, significant decay times are observed for all gases emitted. In nearly all shots, all AMUs monitored are released and a significantly long decay time is observed. Even after waiting for about 2 minutes between shots, the partial pressures of the gasses have not

about 2 minutes between shots, the partial pressures of the gasses have not relaxed to the initial partial pressures. When examining the overall decay lengths from one shot to the next in sequence, the decay rates markedly decreased. Even so, the signature even after multiple shots clearly stands out compared to the viewport data. When examining the magnitude of material released, it is very apparent that the chamber walls release more atoms and molecules as compared to the viewport. These tendencies will aid in discerning the partial pressure signatures obtained. Since all of the gases released in the chamber were a result of the viewport and vacuum walls being illuminated, it was questioned on what effect this had on the adsorption properties of sample two. Figure 4.2f and Table 4.2f display a sequence of three sets of shots (two single pulse and one continuous mode) taken at the center location of the sample. Note that the baseline partial pressures are very similar to that of Fig. 4.2a. The AMUs desorbed are carbon dioxide and methane. Considering the appropriate gain factors, these amounts would be typically a little over two orders of magnitude smaller than the partial pressures indicated normalized to nitrogen.

Similar to sample two, samples three [Figs. 4.3a and 4.3b and Tables 4.3a and 4.3b], four [Figs. 4.4a-4.4e and Tables 4.4a-4.4e], five [Fig. 4.5 and Table 4.5], and six [Fig. 4.6 and Table 4.6] are examined. The properties of the viewport and chamber wall are re-examined only for sample four. The number of shots has been increased to include the sample centers. Besides the five sets of shots at four locations near the circumference of the 1" Rexolite piece, two or three more sets of illuminations are made at the center of the piece (one or two in

single pulse mode and one in continuous pulse mode). Samples three and four were contained in a  $4.88 \times 10^{-8}$  Torr ( $6.35 \times 10^{-6}$  Pa) pressure. Experiments on samples five and six were conducted at thermodynamic equilibrium vacuum pressures of  $4.875 \times 10^{-8}$  Torr ( $6.499 \times 10^{-6}$  Pa) and  $1.5 \times 10^{-8}$  Torr ( $2 \times 10^{-6}$  Pa) respectively. Sample three displays little to no desorption effects for shots 1 in Fig. 4.3a and shots 1 and 2 in Fig. 4.3b beyond background partial pressures. The latter figure is a consequence of illuminations only at the center of sample three. The long decay time and the large changes in partial pressures of many of the AMUs is an indication that the laser beam interacted with the surface of the chamber wall. Since location of the beam was near the circumference of the piece, this is reasonable. Shots 2, 4 and 5 in Fig. 4.3a and shot 3 in Fig. 4.3b have the following common desorbed gas elements: methane ( $\text{CH}_3$ ), carbon dioxide, and oxygen. For shot 5 (continuous pulse mode) in Fig. 4.3a, diatomic hydrogen exhibited a delayed increase in partial pressure relative to its baseline partial pressure. This is a possible indication that the gas element was generated between the bottom viewport-test piece interface and took time to leak into the vacuum chamber proper. This is reasonable since earlier viewport studies have shown a significant amount of hydrogen being released in continuous pulse mode (refer to Fig. 4.2e). Sample four as observed in Fig. 4.4a shows very little desorption activity. Only one edge shot resulted in a measurable desorption of methane and carbon dioxide. Because the desorption properties of sample four appeared to be very minimal, its adsorption properties were examined at its center after the viewport and the viewport-vacuum chamber



times that are a little longer than anticipated but still small compared to that displayed with the chamber walls. The main elements released by the viewport are carbon dioxide, diatomic nitrogen/carbon monoxide and mass 15. It is noted that diatomic oxygen is also released. This is an indication that the chamber wall may have been part of the interaction. To be shown later, 532 nm green laser light at the same energies does not desorb diatomic oxygen from the viewports. Fig. 4.4c illustrates subsequent desorption results from the center location of the sample 4 when illuminated by two single pulses and one continuous train of pulses. The percentage of peak partial pressures detected measured relative to that of the viewport case are roughly 16% for mass 15 (84% decrease in peak amplitude) and less than 6% for diatomic nitrogen/carbon monoxide (greater than 94% decrease in peak amplitude). All remaining AMUs had signal-to-noise ratios less than or equal to one where noise in this case is the background partial pressures (with associated fluctuations) of the mass numbers monitored. The chamber wall and viewport was then purposely illuminated with results shown in Fig. 4.4d. The characteristic large changes in partial pressures are observed with relatively long decay rates. The strong characteristic diatomic oxygen is present in all shots performed related to this figure. Table 4.4d bears the hard to see partial peaks pressures quantitatively with characteristic decay times. Except for about a 93% decrease in methane no other AMUs were detected when the Rexolite plastic is illuminated in the center as shown in Fig. 4.4e after the chamber walls had been activated. Samples five and six tend to show similar characteristics as past samples but at a lower pressure. The continuous train of

characteristics as past samples but at a lower pressure. The continuous train of pulses (shot 7) directed at the center of sample five (refer to Fig. 4.5) appeared to have caused a significant amount of diatomic hydrogen to be desorbed. Because the decay rate is almost non-existent, the signature appears to be that of viewport desorption. Enough light may be reaching the top viewport causing undesired desorption. Referring to Fig. 3.8 e (iv), the center of sample five is not as highly polished as the remaining portions of the sample end. It is also possible that a fraction of the transmitted light is scattered towards the chamber wall resulting in a release of hydrogen and nitrogen/carbon monoxide. For most of the shots in samples five and six, traces of carbon dioxide, methane, and oxygen are present. On occasion diatomic hydrogen and nitrogen/carbon monoxide may be present as indicated above. As observed in sample six (Fig. 4.6 and Table 4.6) and many of the earlier samples, both diatomic hydrogen and nitrogen/carbon monoxide are not characteristic elements desorbed from the Rexolite material.

To minimize the effect of the top viewport, a Rexolite sample was wedged in the top nipple of the six-way cross acting as a partial barrier to the viewport. The vacuum chamber now contains two optically polished (Refer to Fig. 3.4 (b)) plastic samples each with roughly a 1.25" diameter. The background pressure for sample seven is  $6.37 \times 10^{-8}$  Torr ( $8.493 \times 10^{-6}$  Pa). Sample seven is illuminated with 1064 nm light on eight locations roughly evenly spaced in angle near the circumference of the sample end and in the center. Each location is first probed with a single pulse and then after the system relaxed or nearly relaxed to

its original base partial pressures, the sample is exposed to a train of pulses. Except for a few 28 AMU peaks, there is very little desorption for four near perimeter locations and the center location. This indicates that the beam cross section is totally contained in the sample. Traces of mass 15 and carbon dioxide may be observed. The reason for the presence of the 28 AMU is not clear. Figure 7b examines four more locations near the perimeter of the sample surface. Continuous shots two and four illustrate a unique characteristic rarely seen in the smaller diameter samples one through six. The water, diatomic hydrogen, and oxygen peaks exhibit a rise time relative to other desorbed elements such as carbon dioxide and mass 15. Further, a definite decay time is also present. These signatures do not appear to be characteristic of chamber wall desorption. Instead, it appears that the elements may have been desorbed from the lower viewport and not re-adsorbed on the viewport or adsorbed on other surfaces like the Rexolite surface. A pressure build-up occurs and the gas tends to leak to the vacuum chamber around the sides of the plastic. Although the argument sounds plausible, this phenomenon does not occur for all shots. Shots 5-8 show traces of carbon dioxide, mass 15 and oxygen molecules/atoms.

Sample eight was illuminated first with 70 mJ, 1064 nm laser light [Figs. 4.8a and 4.8b with Tables 4.8a and 4.8b] and then with 70mJ, 532 nm of laser light [Figs. 4.8c and 4.8d corresponding to Tables 4.8c and 4.8d] in a  $6 \times 10^{-8}$  Torr ( $7.99 \times 10^{-6}$  Pa) vacuum. The shot locations and pattern are like that of sample seven. Shots 3,4,7,8 13 and 14 on Figs. 4.8a and 4.8b appear to have desorption signatures similar to that of the chamber wall but with exceptionally

same vicinity. It takes nearly five minutes for mass 15 to reach pre-partial pressure equilibrium after shot 4 and after shot 8 a gradual increase in the baseline partial pressure is observed over a 25 minute time duration. A similar effect is observed in diatomic hydrogen from shot 8. It seems as if the metal flange beneath the piece under test was partially illuminated by the incident laser beam. Except for some "single spiky" effects noticed for the continuous train of pulses shot 16, all remaining shots show trace effects or no changes in partial pressures in agreement with past cases above. As shown in Figs. 4.8c and 4.8d, similar patterns are observed for 532 nm light. Shots 3, 4, 7, 8, 11, 12, 13, 14, 15 and 16 show signs that the chamber wall or flange underneath the plastic surface was grazed in varying degrees. In each case, diatomic oxygen and water were detected and nearly all, if not all, of the AMUs monitored yielded change in the partial pressure from the baseline pressure just prior to the shot taken. A base pressure change for mass 15 after shot 4 for over a 30 minute time duration as seen in the signature, indicate that a virtual leak was formed. Shots 1, 2, 5, 6, 9, 10, 17 and 18 display only traces of mass 15, oxygen, and carbon dioxide.

The optically polished sample nine was first illuminated with 532 nm green laser light [Figs. 4.9a and 4.9b corresponding to Tables 4.9a and 4.9b respectively] and then with 1064 nm infrared laser light [Figs. 4.9c and 4.9d with the associated Tables 4.9c and 4.9d respectively]. The vacuum chamber housing the sample maintained a  $6 \times 10^{-8}$  Torr ( $7.99 \times 10^{-6}$  Pa) vacuum pressure. Shots 3 and 4 in Fig. 4.9a and possibly 11 and 12 in Fig. 4.9b, appear to be due to some form of grazing with the chamber wall below or next to the sample under

to some form of grazing with the chamber wall below or next to the sample under test. Both data sets do not exhibit exceptionally long rise times or delay times. Outside of these cases, all remaining shots exhibit traces of mainly mass 15, carbon dioxide, oxygen. When the same piece was illuminated with infrared light in nearly the same locations, excluding shots 3 and 4, very little desorption activity was noticed outside of a single relatively large water (18 AMU) and nitrogen/carbon monoxide (28 AMU) peaks. Shots 3 and 4 exhibit vacuum chamber wall desorption effects.

To provide a baseline for green light, the viewport alone [ $6.75 \times 10^{-8}$  Torr,  $8.99 \times 10^{-6}$  Pa], viewport and wall combination [ $6.75 \times 10^{-8}$  Torr,  $8.99 \times 10^{-6}$  Pa], and the viewport, plastic sample nine, and wall combination [ $4.88 \times 10^{-8}$  Torr,  $6.5 \times 10^{-6}$  Pa] were illuminated with 70 mJ of 532nm green light in vacuum pressures designated in brackets. In each case, two single pulsed shots and then a single continuous train of pulses were delivered to the sample in the same location. The plastic sample has been pulsed numerous times. The original vacuum seal has not been compromised since the inception of the piece to the chamber. Figures 4.10a and 4.10b respectively display RGA results with the chamber wall purposely illuminated inside the vacuum chamber when sample nine is present and when it is not. For clarity, the chamber wall exposed was the region in the vacuum system above the sample, not in the region between the sample and the bottom viewport. There is virtually no difference between the two sets of data except that baseline pressure may be met a little sooner when the plastic piece is not present. These plots are also similar to Figs. 4.2e and 4.4d. Significant

diatomic oxygen and water are detected. The baseline of diatomic oxygen has a large standard deviation as seen in Tables 4.10a and 4.10b. Figure 4.10c is equivalent to Fig. 4.10b but in Faraday cup mode (sample nine is not present). The partial pressures measured in this mode are meaningful and normalized to nitrogen. Omitting the normalization factor, the partial pressures may span as much as three orders of magnitude partial pressure change when the chamber wall is illuminated. Figure 4.11 and Table 4.11 display the desorption tendencies of the viewport alone when pulsed with 70mJ, 532 nm light. Note that diatomic oxygen and water are not measurable quantities since the signal-to-noise ratios is one or less. All patterns observed here are similar to that with 1064 nm infrared light.

The electron multiplier enhances the partial pressure measurements allowing one to distinguish the differences among AMUs observed in trend mode. As indicated earlier, the partial pressure readings are meaningless in electron multiplier mode. In Faraday cup mode, the partial pressures have been normalized to nitrogen. By comparing the baseline pressures for a particular AMU in electron multiplier mode and in Faraday cup mode, a gain factor may be determined for the particular AMU allowing one to determine the equivalent true partial pressure normalized in terms of nitrogen. Over a long period of testing, the nude filament's characteristic changes causing differences in the gain factor. Consequently, the gain for each element is determined for samples 1, 6, 7, and 9 in Table 4.12. The electrometer cable was damaged and possibly the nude filament expired just after tests conducted on sample 7. Consequently, the gain

was examined both on samples 1 & 6 and samples 7 & 9. The gain for mass 15 varies as much as 53% between samples 1 and 6 and between samples 7 and 9. In all cases, the gain is between two to three orders of magnitude where methane has the lowest gain and diatomic hydrogen has the highest gain. Most of the baseline partial pressures for electron multiplier mode in Tables 4.1 to 4.11 when adjusted by the gain yield normalized baseline partial pressures (relative to nitrogen) between  $10^{-8}$  and  $10^{-9}$  Torr. Using the gain factors of sample 9, the desorption study from the vacuum chamber in electron multiplier mode given by Fig. 4.10b is nearly equivalent to that observed in Faraday cup mode (Fig. 4.10c). Over two orders of magnitude change in partial pressures are observed.

Based on three different polished surfaces, it appears that the desorption properties of Rexolite is only weakly linked to the polished surface. The desorption properties of Rexolite are weakly enhanced through laser stimulation at 1064 nm and 532 nm. Rexolite does not appear to readily adsorb and then desorb gases upon laser stimulation. Desorbed gases such as oxygen, methane and carbon dioxide may be detected in trace amounts. If the surface contained a significant amount of a particular mass number, multiple pulses tend to "clean" the Rexolite surface. Laser stimulated desorption of common ultrahigh vacuum viewports and stainless steel chambers can result in the release of significant amounts of gas elements well over the time duration when stimulated, especially for the vacuum chamber. Both water and diatomic oxygen is a key signature that the chamber walls in these experiments have been stimulated. Usually long

decay rates are observed probably due to the increase in surface chamber temperature and photon activation mechanisms. The relatively long decay times observed for the chamber walls are not present when the viewport is illuminated. This could be a result of negligible thermal losses at the surface of the viewport.

### 4.3 Analysis

Based on experimental data, the number of molecules released from the Rexolite sample are determined. This number is compared to theoretical estimates based on thermal and photon stimulated desorption assuming that the number of molecules desorbed from the surface is based on the existence of a closely packed single monolayer of molecules distributed over the sample surface in the path of the laser beam. The amount of energy available to liberate monolayer molecules is established in part from theoretical and experimental power dissipation studies described in Chapter 2. Because surface and bulk medium physics can vary significantly being both geometry and material dependent, two approximations are employed to narrow down estimates on desorption release mechanisms. The energy absorbed by the Rexolite plastic under test in one approximation is assumed to be uniformly distributed throughout that portion of the plastic volume intersecting the volume of the laser beam. Because Rexolite is not a good thermal conductor and/or assuming that scattering losses are small, it is assumed that the energy dissipated in the plastic due to laser stimulation at the time of stimulation through detection is contained within the volume of the beam. This implies that only a small fraction of the total



energy is available in the monolayer for desorption. In the other approximation, all of the energy dissipated by the medium is available at the monolayer surfaces over the cross sectional area of the laser beam. Since there are two surfaces, the total energy dissipated at the top surface is one half of the total energy dissipated by the sample.

Van der Waal's forces are weak forces binding a molecule to the surface of a material or binding molecules to molecules. Predominantly, this is an electrostatic force among dipoles arising from the rapid fluctuations in electron density in atoms or molecules. At any instant, the atom or molecule has a net dipole moment which through electrostatic forces induces the electron cloud surrounding a nearby atom to become distorted resulting in a weak dipole-dipole attraction. Typically, the dipole force is dependent on the gradient of the electric field as given by

$$\vec{F} = \vec{p} \cdot \vec{\nabla} \vec{E}(\vec{r}) \quad (4.1)$$

The force density acting on a large number of dipoles per unit volume expressed as the polarization  $\vec{P} = \epsilon_0(\epsilon_r - 1)\vec{E}$  is proportional to the gradient of the dipole field squared. When the dipoles are in close proximity, the dipole force is inversely proportional to the seventh power of the distance of separation (typical for distances less than a few tens of nanometers). For simplicity, complementing the polished planar surface of the plastic under test that an atom or molecule "sees" when adsorbed, the atom or molecule attracted to the surface is modeled as a hard solid sphere of radius "R<sub>0</sub>" with smooth surface a distance z<sub>0</sub> from a

smooth planar surface. The van der Waal's force and energy of Interaction respectively may be expressed as [32]

$$F = \frac{A_{12}R_o}{6z_o^2} \quad (4.2)$$

$$U = -\frac{A_{12}R_o}{6z_o} \quad (4.3)$$

Where  $A_{12}$  is the Hamaker constant for substances 1 and 2 which in this case is the contaminant adsorbed and the Rexolite plastic. For two dissimilar materials, this constant may be estimated in terms of the Hamaker's constant [33] for each material given as

$$A_{12} = \frac{2A_{11}A_{22}}{A_{11} + A_{22}} \quad (4.4)$$

where  $A_{kk}$  is the  $k^{\text{th}}$  substance in a  $k^{\text{th}}$  medium. The Hamaker's constant for water and a molecular component of Rexolite, polystyrene are respectively,  $3.7 \times 10^{-20}$  J and  $6.6 \times 10^{-20}$  J. Many of the hydrocarbons are within a factor of two relative to water ( $\sim 3.6 \times 10^{-20}$  J to  $5.5 \times 10^{-20}$  J) [34-38]. Using the values for water and polystyrene as being representative materials, the Hamaker's constant is  $A_{12} = 4.35 \times 10^{-20}$  J. If the substance lies on the surface, the distance of separation between the sphere and the planar surface is commonly taken as 0.4 nm. The radius of the water molecule is  $R_o = 1.7 \text{ \AA}$ . The energy of interaction is  $|U_{\text{water}}| = 3.08 \times 10^{-21}$  J (0.019 eV). In the same manner, for methane molecule radius, the energy of interaction is  $|U_{\text{methane}}| = 6.34 \times 10^{-21}$  J (0.039 eV). Here, the Hamaker constant used for methane is  $5 \times 10^{-20}$  J.

RGA studies suggest that methane and carbon dioxide molecules are representative of the molecules over the monolayer because of the repeated dominance of the molecules in each of the tests conducted. But only methane molecules are compared since the Van der Waals force for carbon dioxide could not be found. Assume that the energy dissipated in the Rexolite medium based on Eq. (2.30) for a 70 mJ, 1064 nm laser pulse, 6.5 mm beam diameter is transformed into heat. Then, the total amount of energy dissipated in this form is  $\xi_{dissT} = 5.53 \times 10^{-11}$  J ( $3.45 \times 10^8$  eV). Dividing the volume of the beam along the beam axis into layers one monolayer thick (diameter of a carbon atom:  $2.2 \text{ \AA}$ ) and assuming that the energy is uniformly distributed throughout the volume, the available thermal energy in a surface monolayer of Rexolite is  $\xi_{diss} = 9.59 \times 10^{-19}$  J (5.99 eV). The area of the 6.5 mm diameter beam is about  $3.31 \times 10^{-5} \text{ m}^2$ . The approximate area of a plastic molecule is  $A_p = 8.388 \times 10^{-19} \text{ m}^2$  (sum of the areas of 18 carbon and hydrogen atoms in a single rexolite molecule). Taking the ratio, the number of plastic molecules within the beam cross section is  $n_p = 3.94 \times 10^{13}$ . The number of closely packed methane molecules ( $\text{CH}_3$ ) within the beam cross section is  $n_{s, \text{methane}} = 5.18 \times 10^{14}$  (ratio of the area of the beam to the area of a  $\text{CH}_3$  molecule). Dividing the thermal energy available in a single monolayer by the van der Waal energy of interaction for methane, the total number of methane molecules released with zero initial kinetic energy is 153. This value is an insignificantly small number of molecules compared to the closely packed that might exist over the beam cross section in a single monolayer. For an extreme scenario if the total energy dissipated in the beam was due strictly to surface

effects, then half of the energy dissipated by the beam will liberate about  $4.362 \times 10^9$  methane molecules which is less than  $8.42 \times 10^{-6}\%$  of methane molecules closely packed on the surface.

If photon stimulated desorption is the dominant mechanism, then it is assumed that the energy dissipated, now called the energy lost, is photon energy released to the adsorbed molecules as the laser beam passes across the solid interface. Because two surfaces exist, only half of the energy is assumed to be available for desorption on a particular surface. In this case, we will assume that there are no losses internal to the Rexolite medium. A 1064 nm photon carries  $\xi_{\text{photon}} = h\nu = 6.626 \times 10^{-34} \times 2.81 \times 10^{14} = 1.86 \times 10^{-19}$  J (1.16 eV). For an energy loss of  $\xi_{\text{diss}} = 2.766 \times 10^{-11}$  J ( $1.728 \times 10^8$  eV), about  $1.48 \times 10^8$  number of 1064 nm photons are available for photon stimulated desorption across the beam cross section at the monolayer surface of the plastic. Assuming a single photon releases all of its energy to a single methane molecule, about  $1.48 \times 10^8$  number of methane molecules are released. This is approximately 0.0000285 % of the total possible number of methane molecules closely packed over the beam cross section over the surface.

Time stamped data from the RGA does not provide an accurate interpretation of the time taken for charge to be collected by the detector. Explanations on how the RGA makes a measurement have been provided at length in Section 4.1. The residual gas analyzer provides a partial pressure measurement that is representative of what would be measured if the sample period is equal to the dwell time regardless if the actual measurement is a result

of sampling over this entire time duration and if the sampling is uniform or nonuniform over this duration. Therefore, the total charge accumulated leading to a partial pressure-current equivalent measurement over the approximated 200 ms duration will be equal to current times the 5 ms dwell time. It is assumed that the RGA's ionizer imparts a single charge to each molecule captured. In reality, there is no reason that an ion is singly charged. For instance, the peak at  $m/e=14$  could be due to  $N^+$  or  $N_2^{++}$  (as well as  $CO^{++}$ ). The change in the partial pressure due to laser stimulation is of importance. Therefore, the change in the measured current in amperes of the  $j^{\text{th}}$  AMU,  $\Delta I_j$ , based on a time integration of charge, is linearly proportional to the change in the recorded  $j^{\text{th}}$  partial pressure relative to the baseline pressure,  $\Delta P_j$ , where the sensitivity constant of the ionizer,  $S$ , is the proportionality constant as given by

$$\Delta I_j(t) = S \Delta P_j(t). \quad (4.5)$$

The net increment in molecules of the  $j^{\text{th}}$  AMU captured by the RGA and ionized in a time interval approximated by the dwell time for a single specie,  $\Delta T$ , under the assumption that each AMU has a single electronic charge is

$$n_{ej}(t) = \frac{(S \Delta T P_j(t))}{e} \quad (4.6)$$

where  $e=1.6 \times 10^{-19}$  C is the electron charge. The total number of charges detected at the RGA sensor is the sum of the number of molecules captured and is given as

$$n_{CT}(t) = \sum_j n_{ej}(t) \quad (4.7)$$

The molecules of the  $j^{\text{th}}$  specie are assumed to be released over the upper hemispherical region with a uniform distribution (Figure 4.12). Under these assumptions, the total number of molecules released by the sample may be related to the total number of molecules detected by the RGA sensor. Let  $n_T$  be the total number of molecules emitted from the plastic surface. Assume that the cross sectional area of the laser beam is  $A_b$  and can be treated as a point. Let  $A_{dc}$  be the detector capture area with radius of capture  $R_{dc}$  equal to the radius of the inner ionizing filament of the RGA. The distance from the center of the cross sectional area of the ionizing filament to the center of the laser beam cross section at the top surface of the plastic sample under test is  $L_{dc}$ . For clarity, the top surface of the sample is the planar surface closest to the detector releasing the molecules to be detected. Let  $\mathcal{R}$  represent the ratio of the total number of molecules captured,  $n_{CT}$ , to the total number of molecules emitted,  $n_T$ . This is approximately equivalent to the ratio of that portion of a sphere of radius  $L_{dc}$  bounded by the perimeter of the capture area of the ionizer to the that portion of the area of the same sphere (hemisphere) in which emitted molecules are directed towards. Consequently,

$$\mathcal{R} = \frac{n_{CT}}{n_T} = \frac{A_C}{A_E} \quad (4.8)$$

where  $A_C$  and  $A_E$  are respectively the capture area and emission area over a spherical surface of radius  $L_{dc}$ . Choosing the  $z$  axis to be directed along the centers of the ionizing filament and sample surface and defining  $\theta_c$  to be the

conical angle demarcating the spherical region of capture from that not captured, the ratio  $\mathcal{R}$  can be expressed as

$$\mathcal{R} = \frac{n_{CT}}{n_T} = 1 - \cos \theta_C \quad (4.9)$$

where

$$\cos \theta_C = \frac{\sqrt{L_{dc}^2 - R_{dc}^2}}{L_{dc}} \quad (4.10)$$

Consequently, the total number of molecules released at the detector surface based on the number of molecules detected by the RGA can be expressed as

$$n_T(t) = \frac{\sum_j \frac{[S\Delta TP_j(t)]}{e}}{1 - \frac{\sqrt{L_{dc}^2 - R_{dc}^2}}{L_{dc}}} \quad (4.11)$$

where  $t$  is the macroscopic time with a resolution no finer than 200 ms. From the experimental setup,  $L_{dc}$  is measured as 2.5625". The RGA parameters  $S, \Delta T, R_{dc}$  are respectively  $2 \times 10^{-4}$  Amps/ Torr, 25 ms, and 0.5". With the aid of Fig. 4.12 and Eq. (4.11), the total number of molecules released as a result of the change in partial pressure due to laser stimulation is provided in Tables 4.13 (a)-(i) from samples 6 and 8.

In Chapter 2, an approximate theory was developed to determine the velocity of the molecules released. Approximate velocities will be based on the methane molecule ( $\text{CH}_3$ ) of mass  $2.49 \times 10^{-26}$  Kg. To determine the amount of energy provided to a methane molecule due to a plastic molecule, the available thermal energy that a single Rexolite molecule may gain, assuming that the

dissipated energy is uniformly distributed, is determined. Then, since a Rexolite molecule has a larger area cross section than methane, only a fraction of energy available in the Rexolite molecule is deposited in the methane molecule. Assuming that the total energy dissipated in the beam cross section is deposited at the two end surfaces, the energy transferred to the methane molecule under these crude approximations is

$$\xi_{\text{methane Thermal}} = \frac{A_{\text{methane}} \xi_{\text{dissT}}}{A_{\text{Rexolite}} 2n_p} \quad (4.12)$$

where  $A_{\text{methane}}=6.39 \times 10^{-20} \text{ m}^2$ ,  $A_{\text{Rexolite}}=8.388 \times 10^{-19} \text{ m}^2$ ,  $n_p=3.94 \times 10^{13}$ , and  $\xi_{\text{dissT}}=5.53 \times 10^{-11} \text{ J}$  ( $3.45 \times 10^8 \text{ eV}$ ) yielding roughly  $5.28 \times 10^{-26} \text{ J}$  ( $3.3 \times 10^{-7} \text{ eV}$ ).

The van der Waal's energy of interaction for methane is found to be  $U_{\text{methane}}=6.34 \times 10^{-21} \text{ J}$  (0.039 eV). Since the energy transferred to the methane molecule based on this model is less than the van der Waal's energy, the molecule is not released from the surface of the material. If we assume that the desorption mechanism is due to a photon releasing all of its energy to the molecule being released, then the amount of energy in a single 1064 nm photon transferred to the methane molecule is  $\xi_{\text{photon}} = 1.16 \text{ eV}$ . Based on Eq. (2.36), the initial velocity of a methane molecule equals about 3.8 km/s. Since a relative timing study could not be performed in experiment, there is no experimental data to compare these values to.



#### 4.4 Discussion of all calculations

The outgassing nature of the polished Rexolite plastic piece under test is observed by comparing the theoretical and experimental results. The number of molecules released by thermal and photon desorption are calculated to be  $4.362 \times 10^9$  and  $1.48 \times 10^8$  molecules respectively. While the experimental studies (Tables 4.13 (a)-(i)) suggests that at most the number of molecules released is roughly one order of magnitude less than models posed above. The numbers of molecules released could be as low as zero relative to base line partial pressures with partial pressure fluctuations yielding a standard deviation about the baseline. This implies that the polished Rexolite plastic has a very low *stimulated* desorption property. The stimulated desorption methods studied here do not seem to affect the outgassing properties. Even the baseline partial pressures with appropriate gains considered implies that Rexolite plastic has a very low outgassing property desired for high vacuum and ultrahigh vacuum environments. Experimental studies demonstrate that the vacuum chamber and the viewports, typically employed in high vacuum systems even with a semi-rigid baking procedure to clean the vacuum system, tend to desorb relatively large amounts of contaminants when stimulated. Further, the pumping action of Rexolite appears to be very small compared to other materials inside the test chamber. This is apparent when examining stimulated studies of Rexolite after wall studies have been conducted prior to opening the test chamber. Based on outgassing observations comparing background pressures to potential pressures attained without the sample, experiments suggest that a gaseous layer can exist.

Even so, experiments indicated that stimulated desorption above the baseline partial pressures are momentary on RGA time scales and, with longer pumping times, can be minimized. It is to be noted that the pumping capability of the ion pump is very low compared to other commercially available which tends to further support some of the properties suggesting that Rexolite may be a useful material for UHV environments.

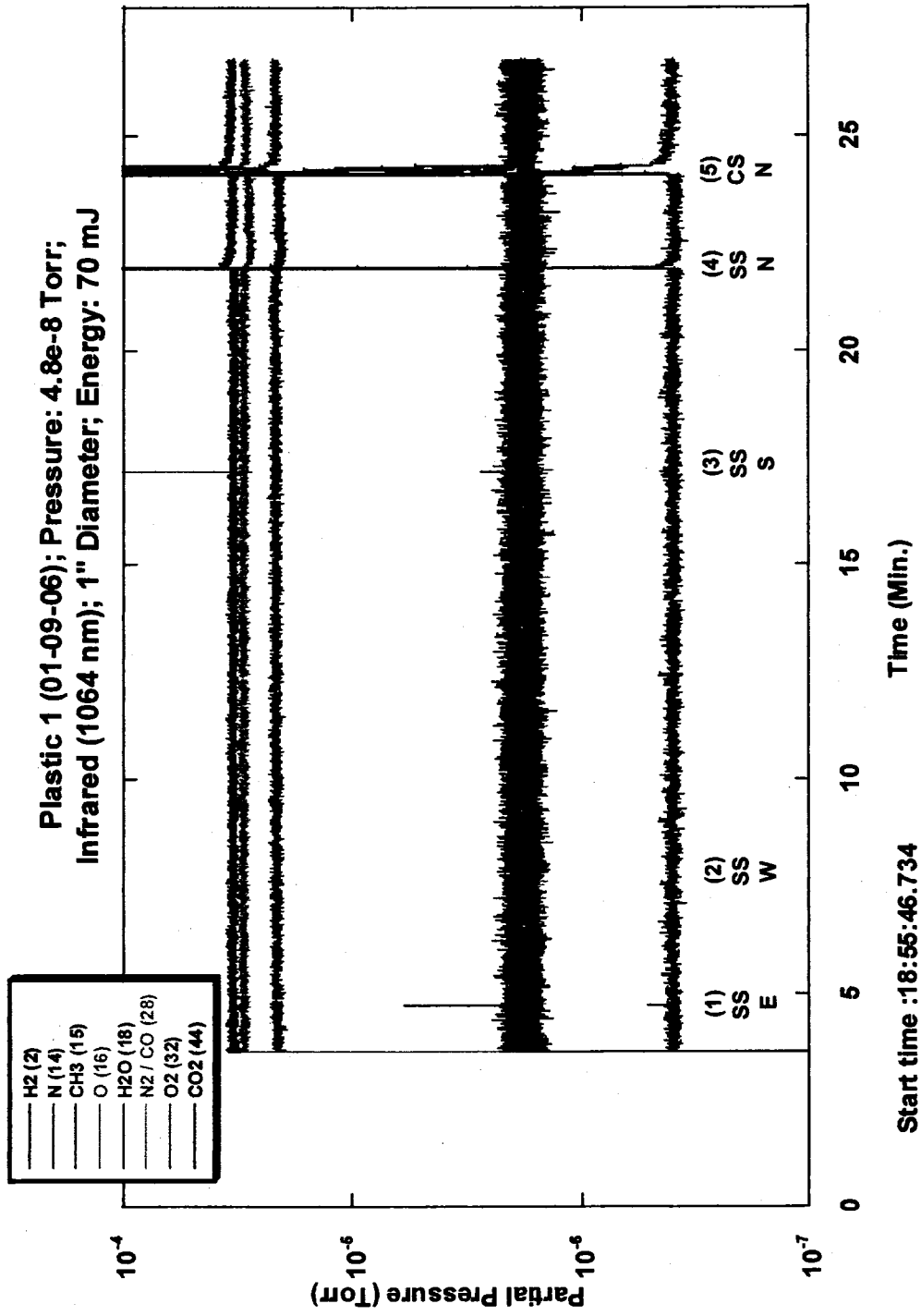


**Figure 4.1(a)**

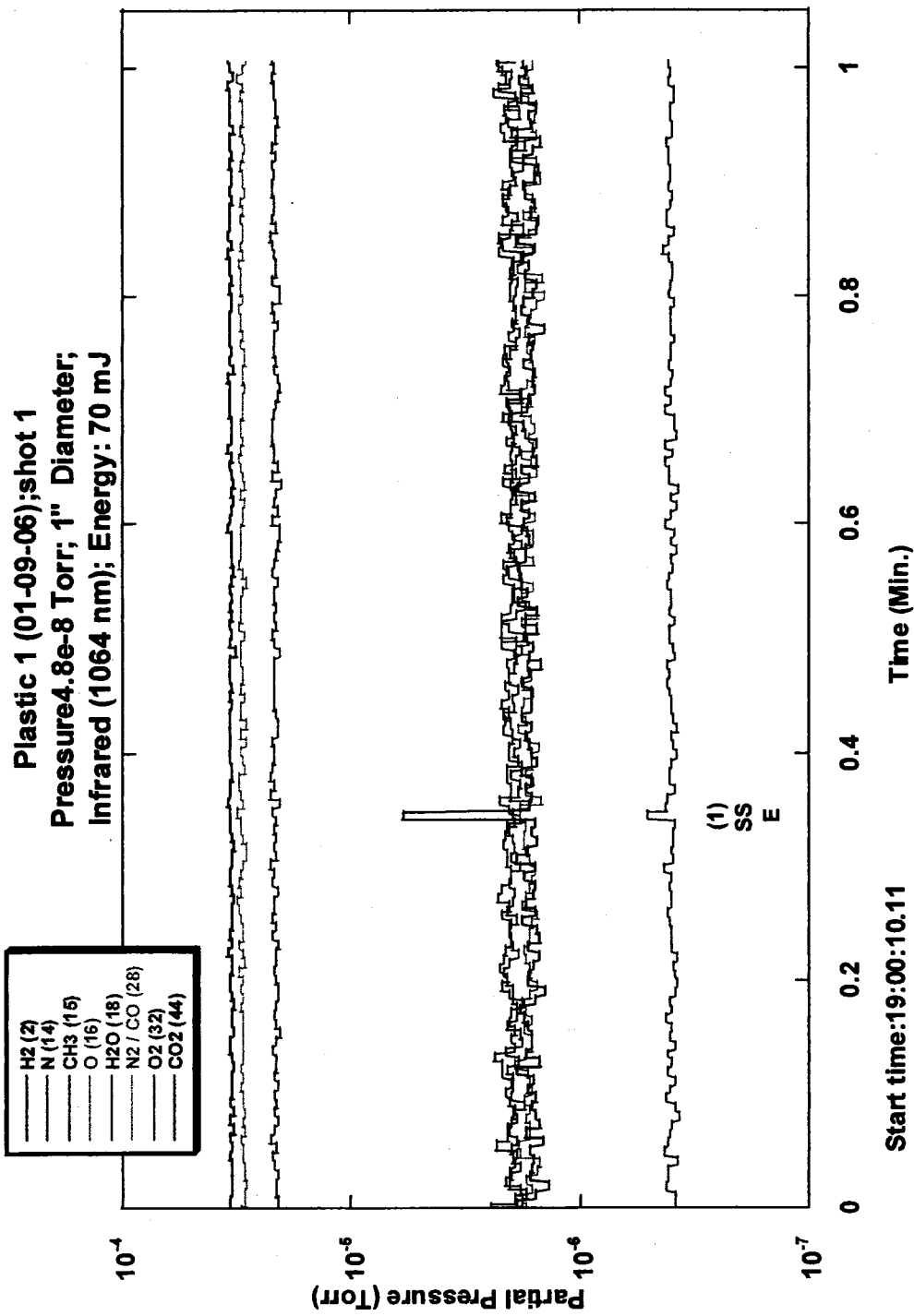


Figure 4.1(b)

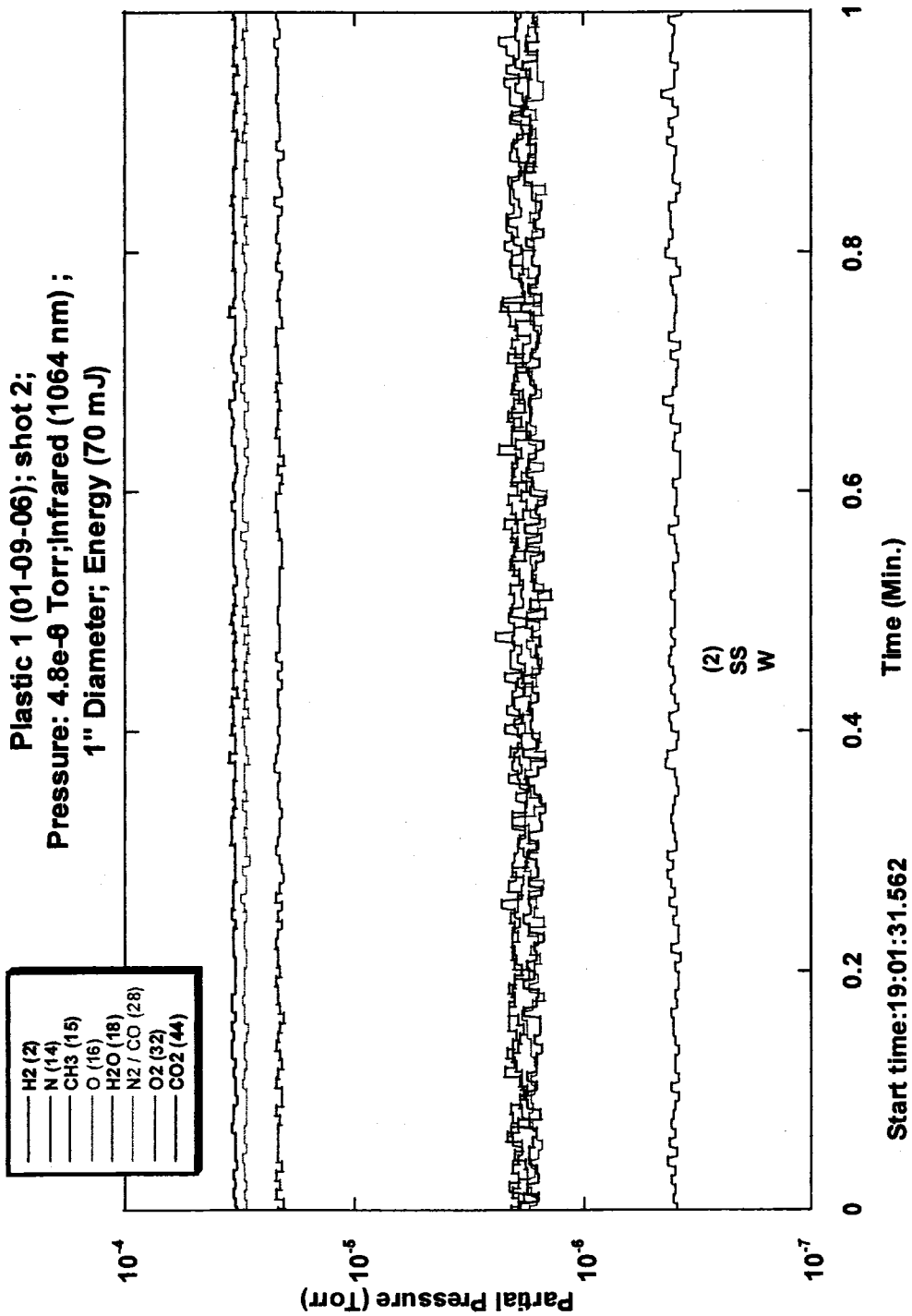


Figure 4.1(c)

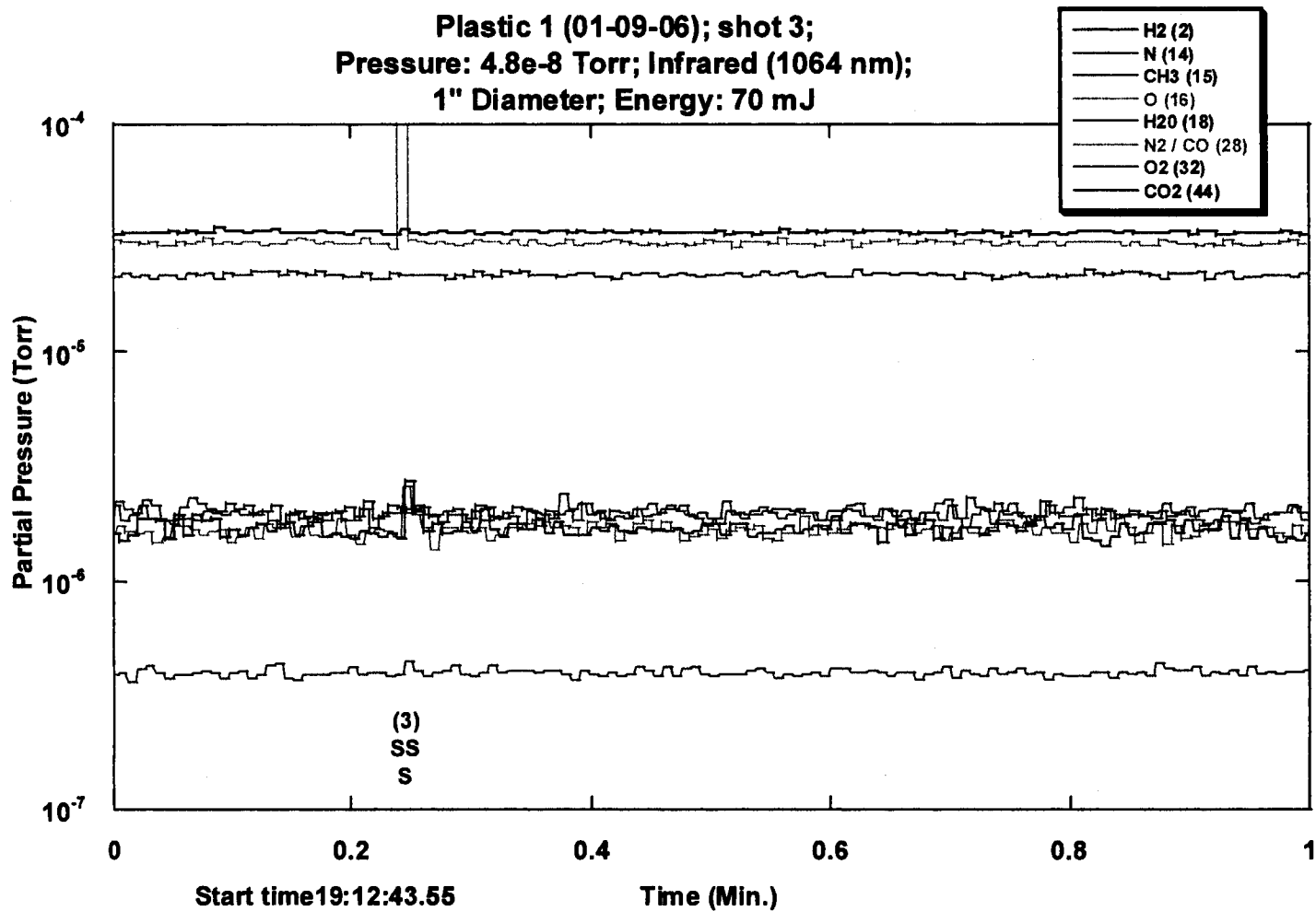
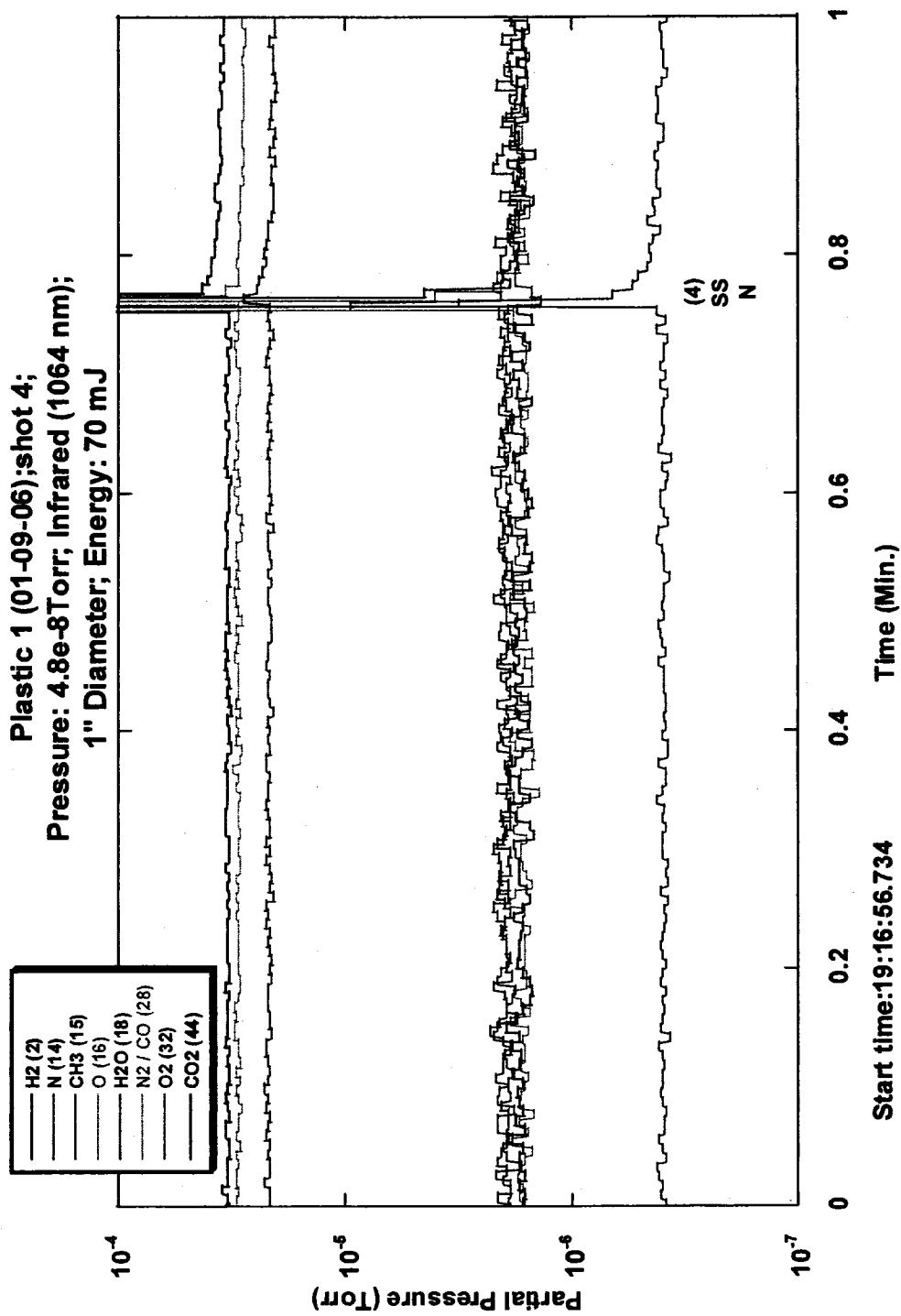


Figure 4.1(d)



**Figure 4.1(e)**

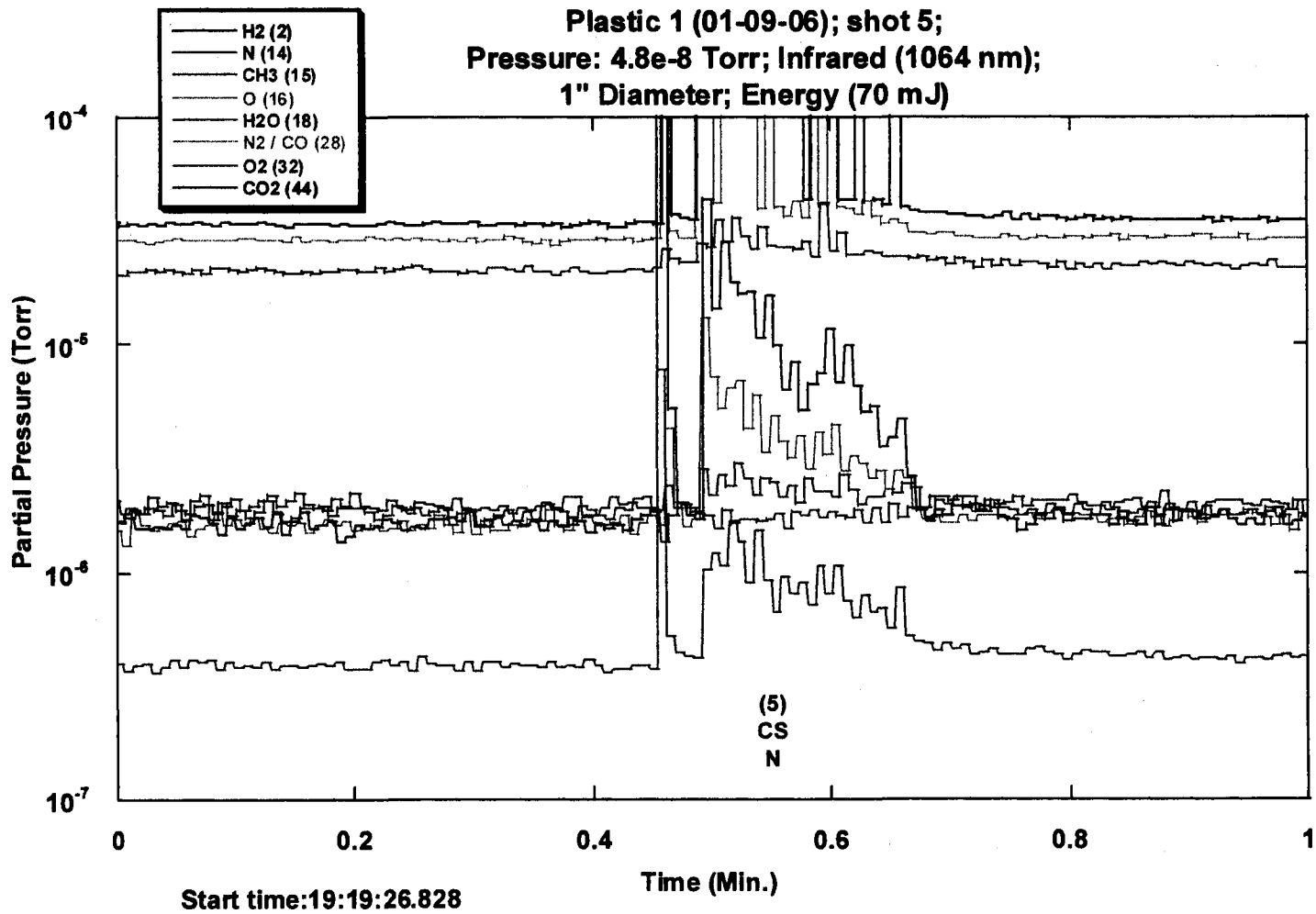
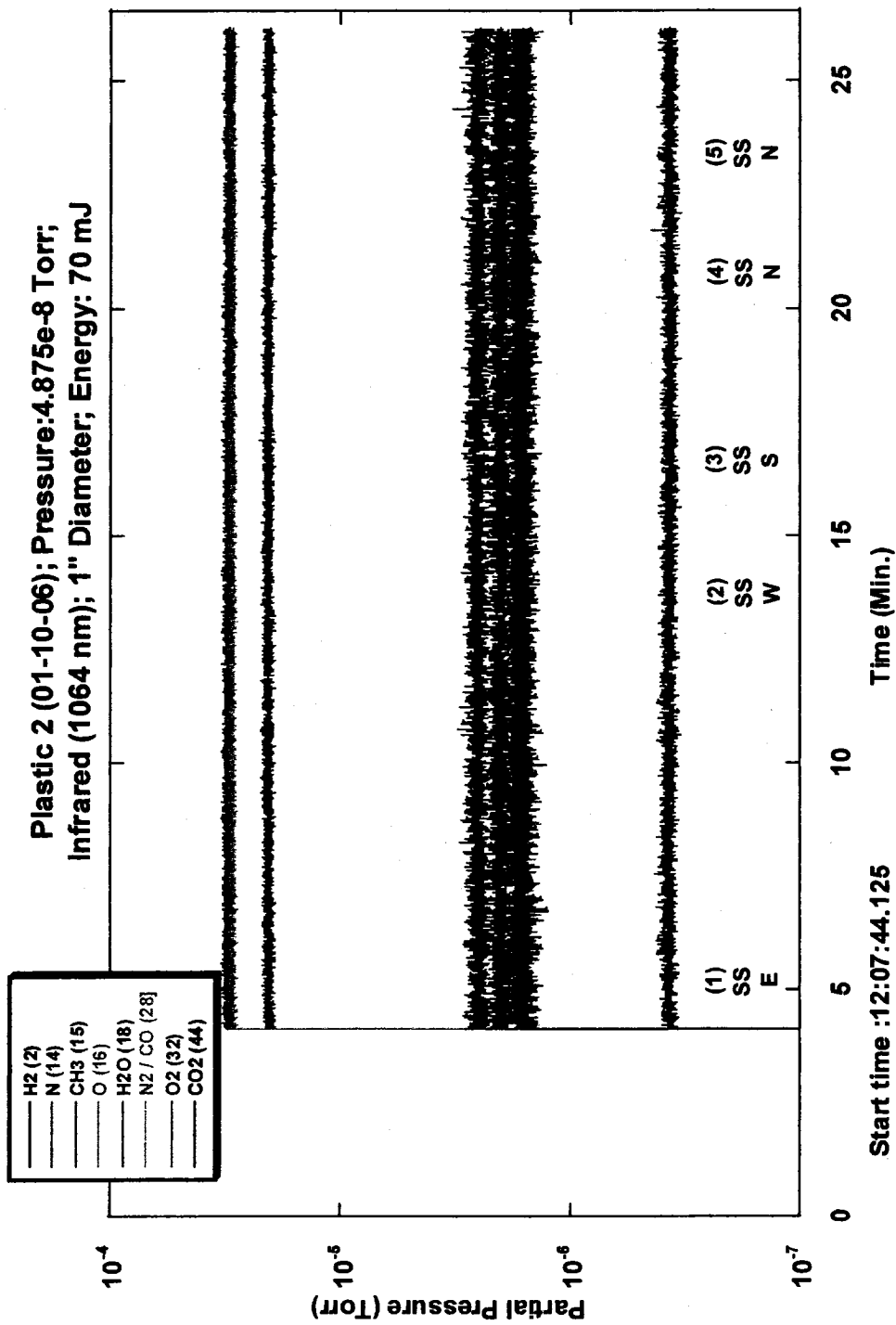
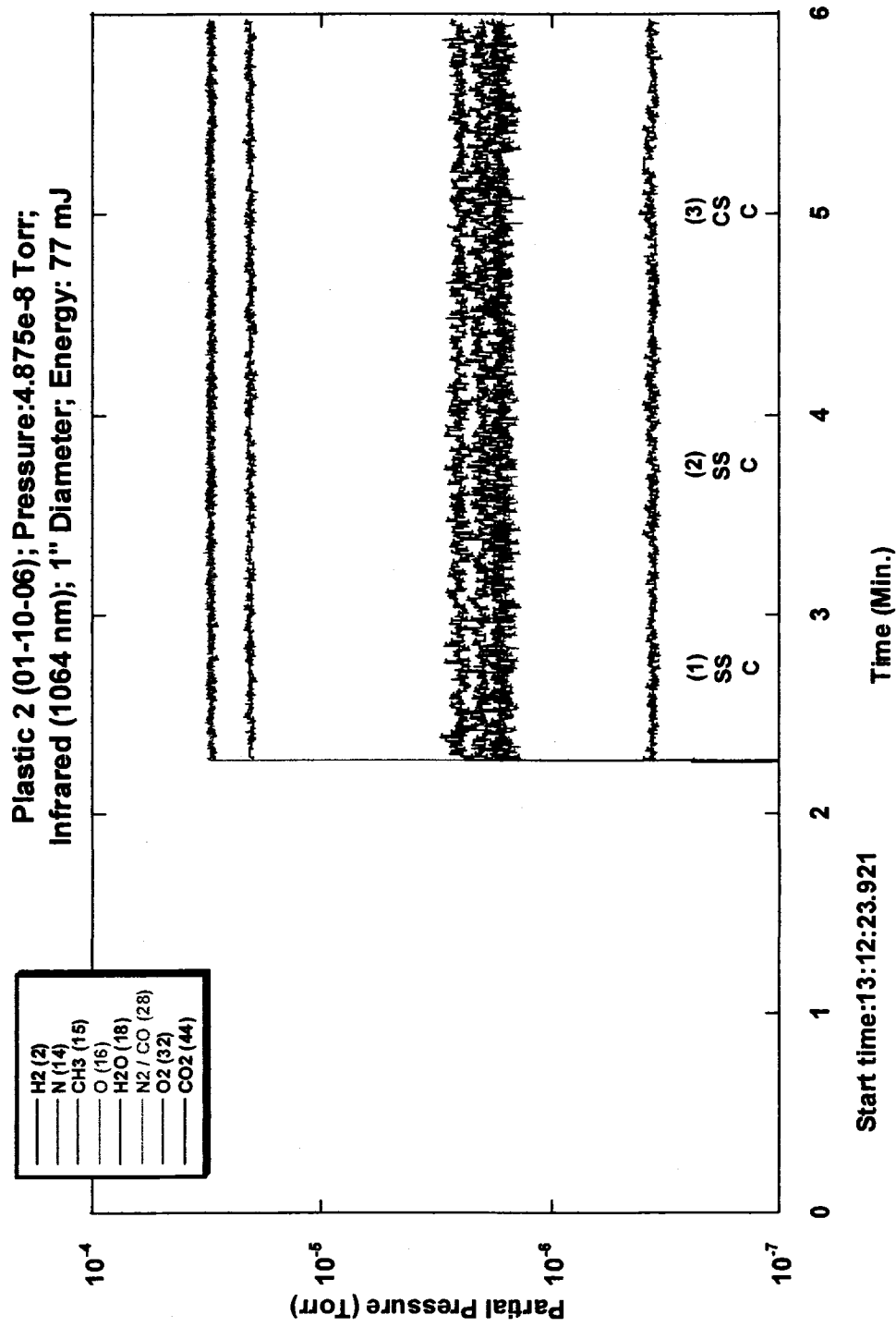


Figure 4.1(f)





**Figure 4.2(a)**



- |   |              |
|---|--------------|
| — | H2 (2)       |
| — | N (14)       |
| — | CH3 (15)     |
| — | O (16)       |
| — | H2O (18)     |
| — | N2 / CO (28) |
| — | O2 (32)      |
| — | CO2 (44)     |

Figure 4.2(b)

Plastic 2 (01-10-06); Pressure: 4.875e-8 Torr;  
 Infrared (1064 nm); 1" Diameter; Energy: 85 mJ

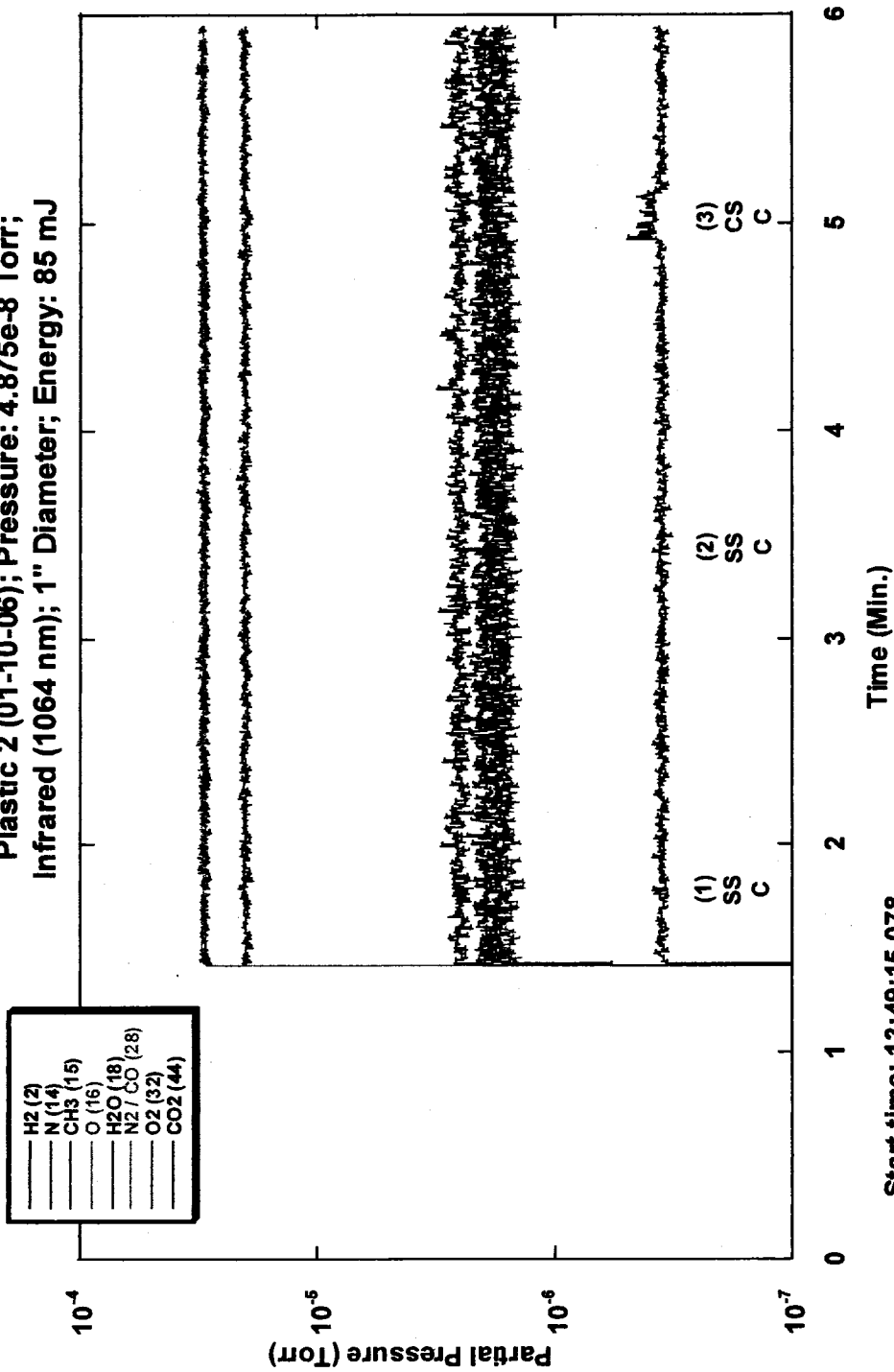


Figure 4.2(c)

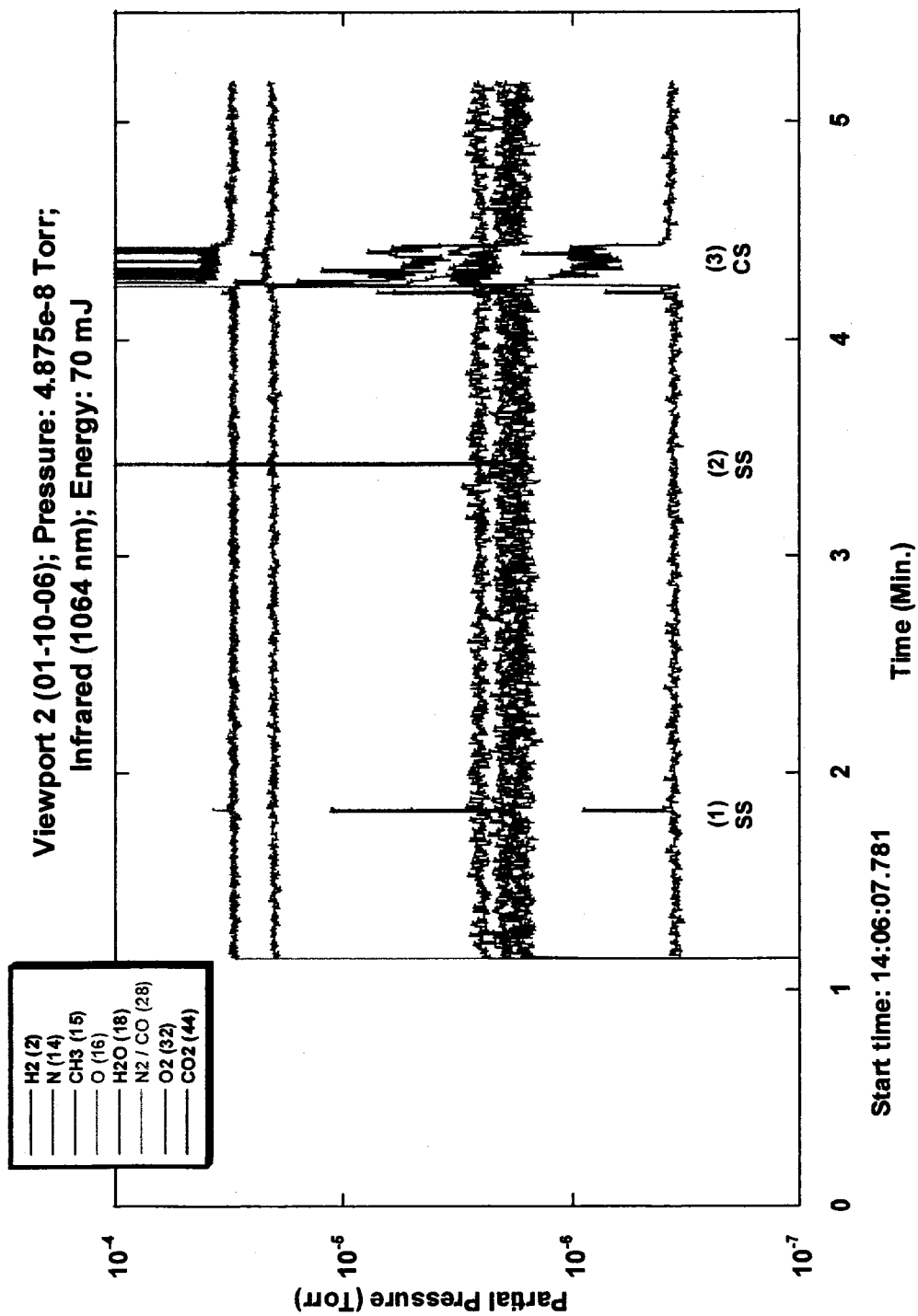
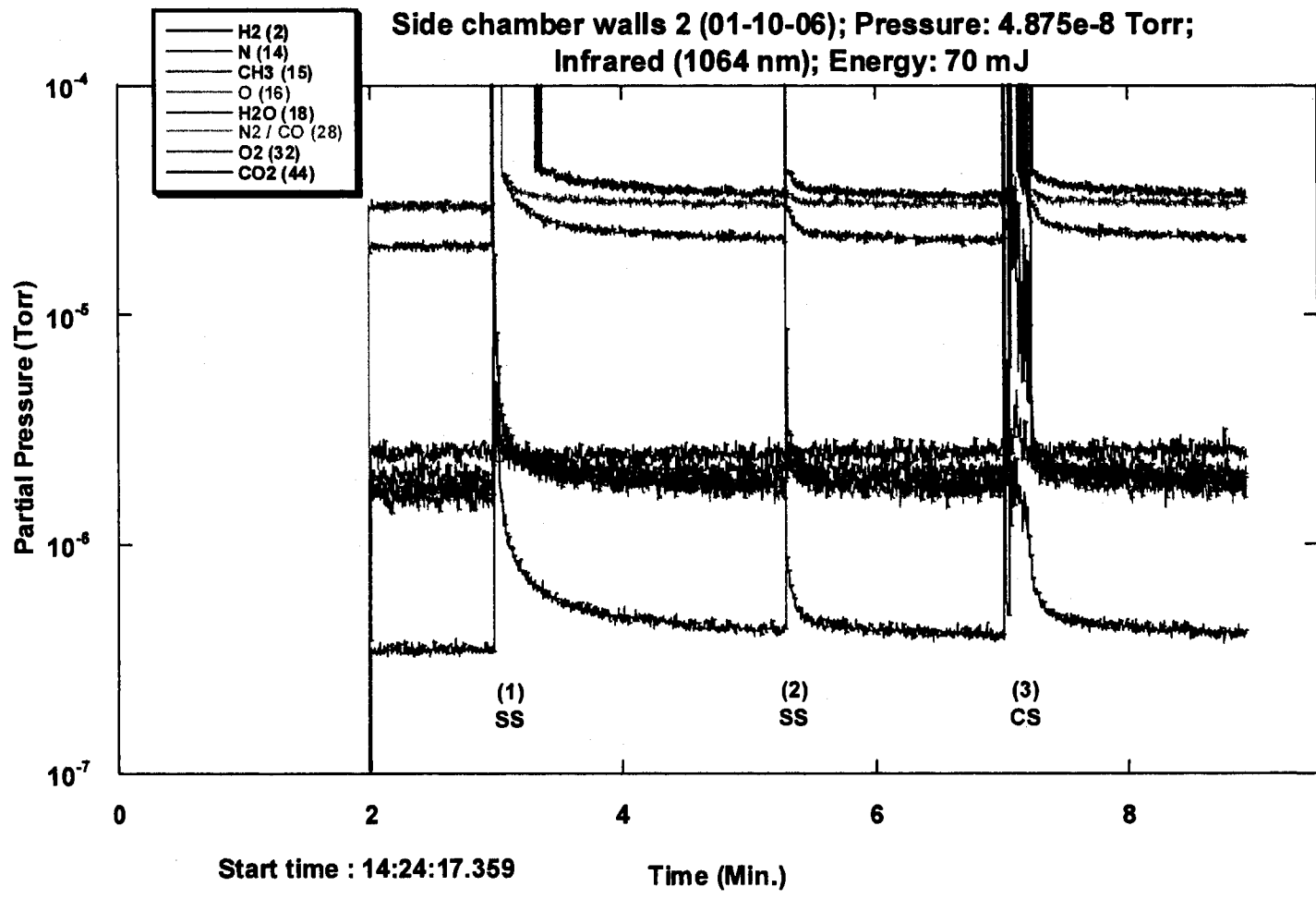


Figure 4.2(d)



**Figure 4.2(e)**

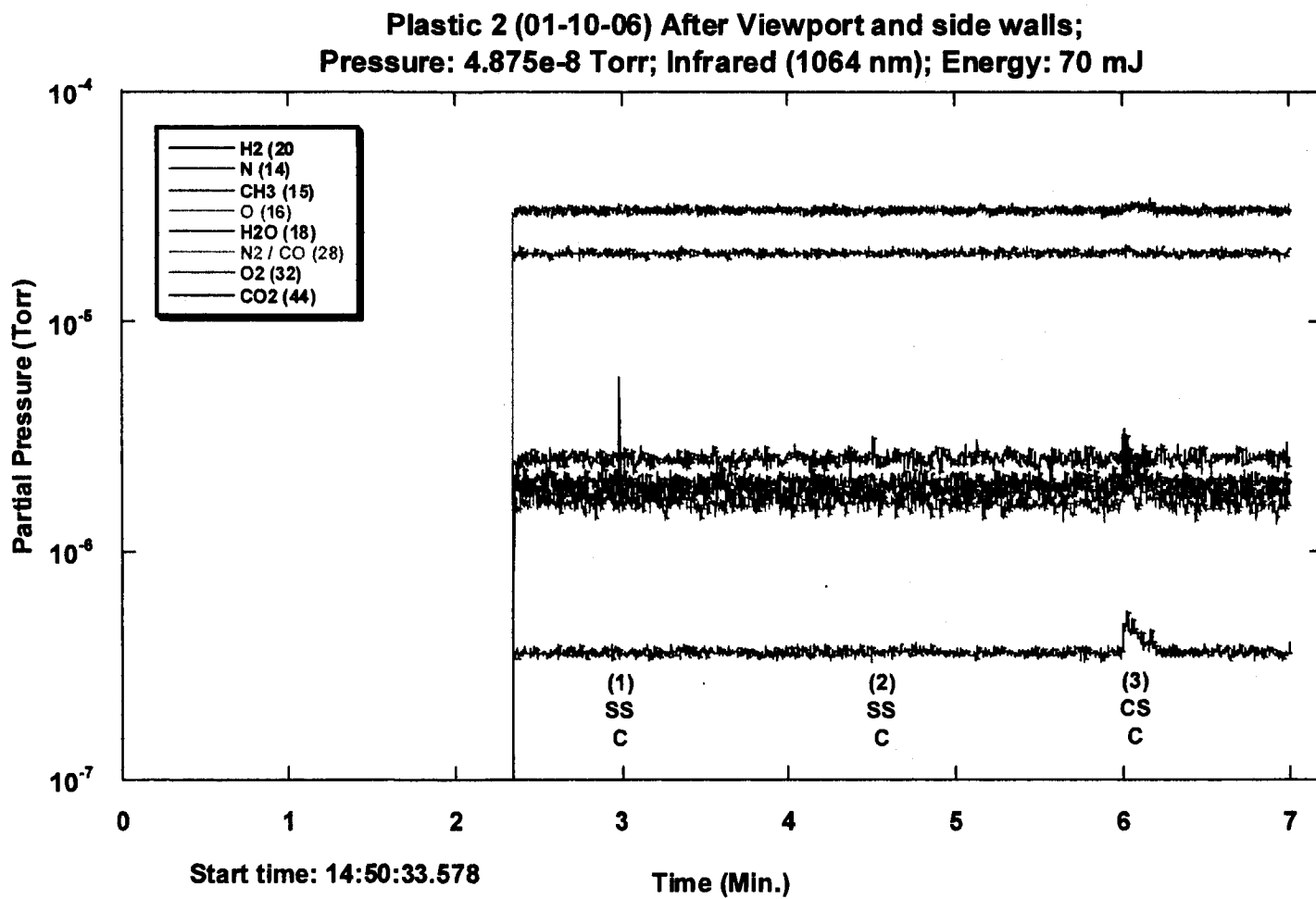


Figure 4.2(f)

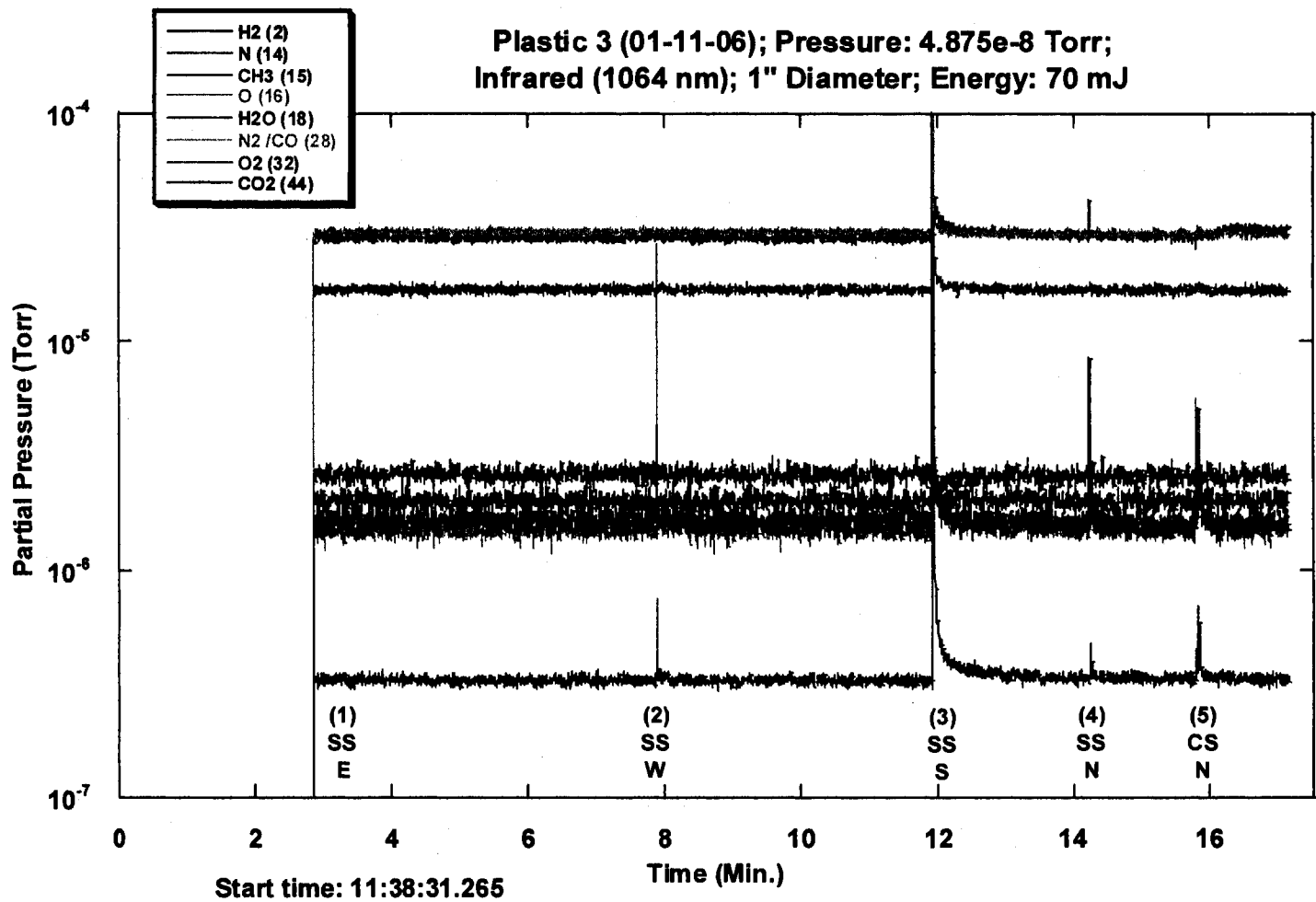


Figure 4.3(a)

Plastic 3 (01-11-06) Possible Overlapping;  
 Pressure: 4.875e-8 Torr; Infrared (1064 nm);  
 1" Diameter; Energy: 70 mJ

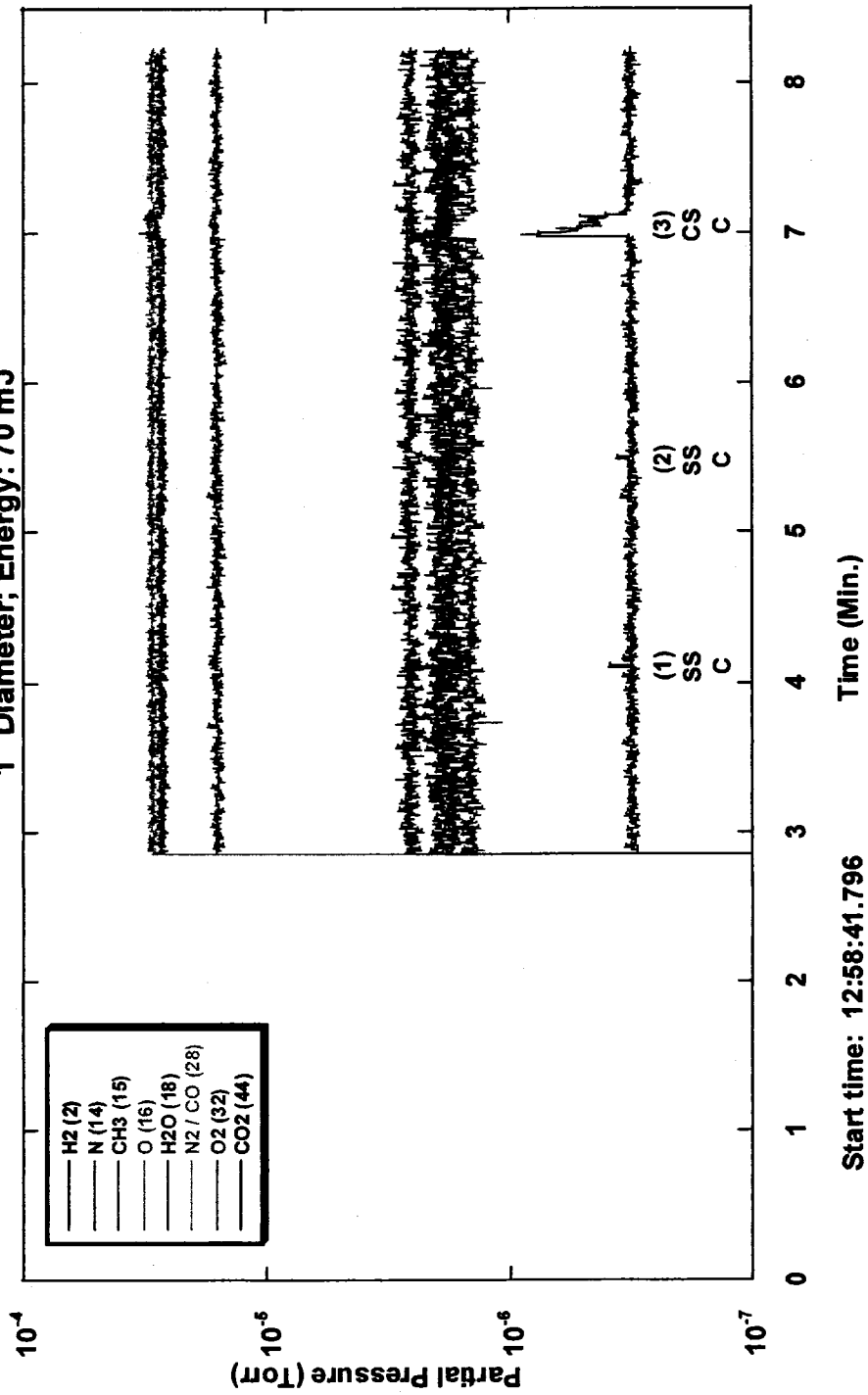


Figure 4.3(b)



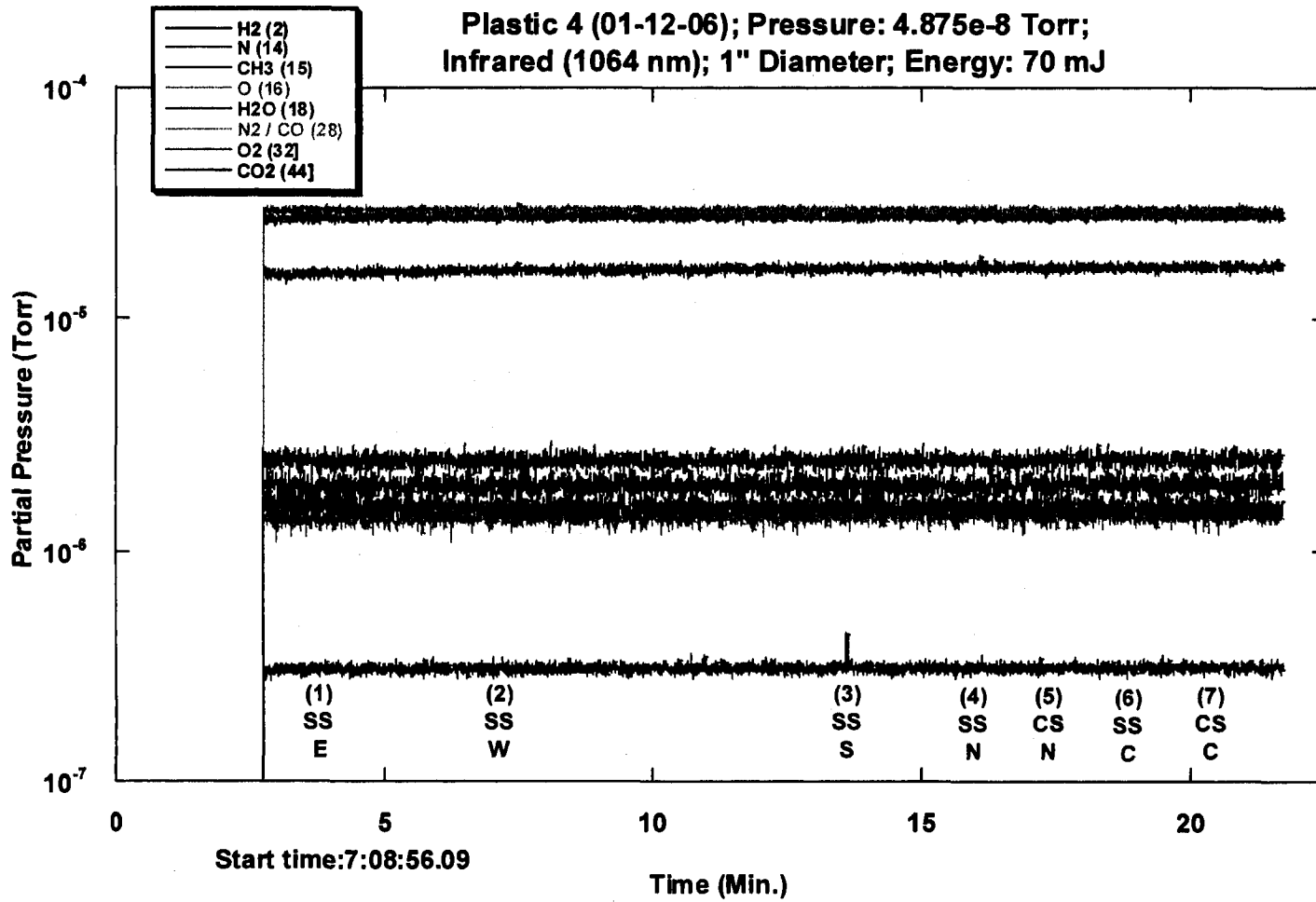
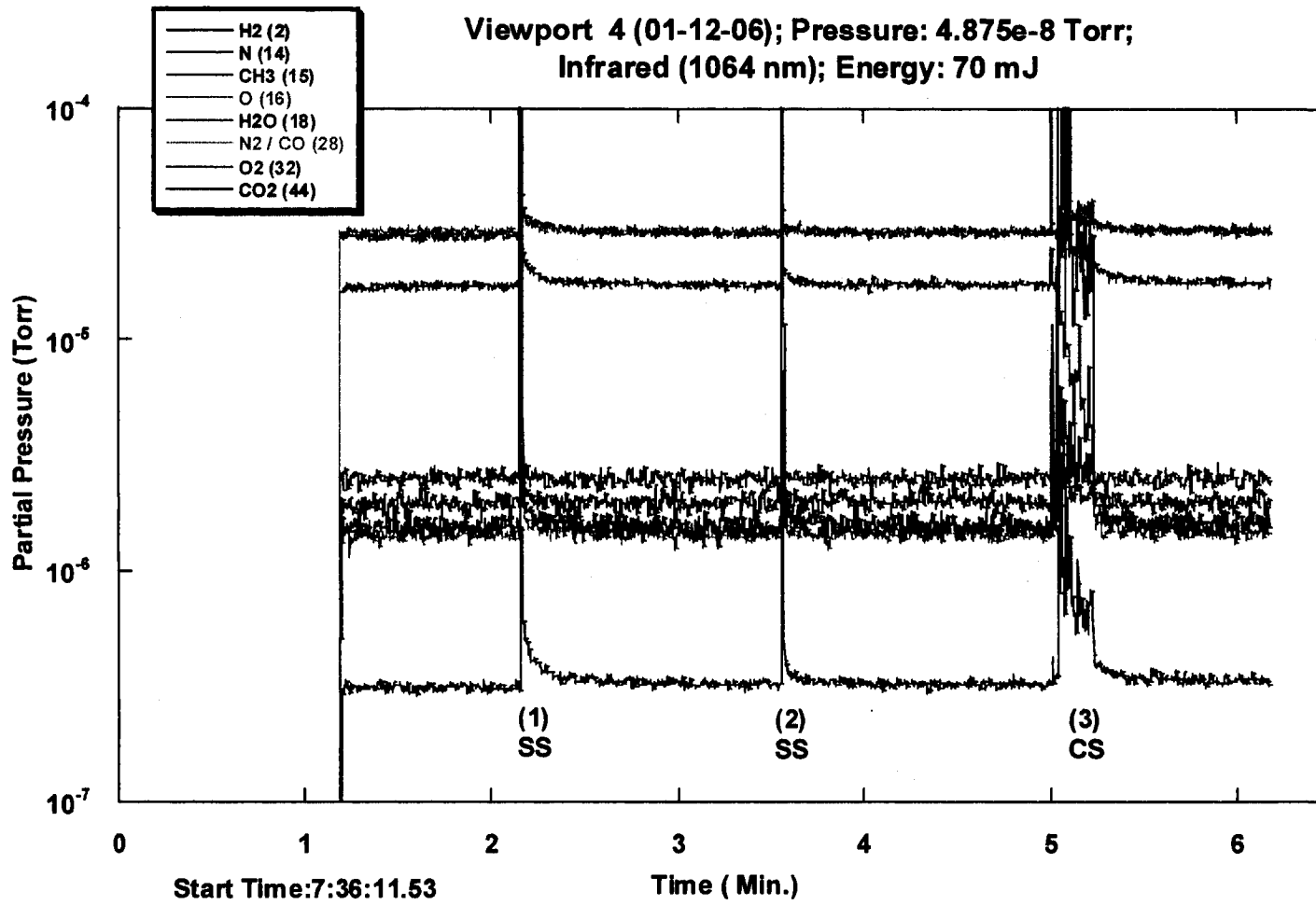


Figure 4.4(a)



**Figure 4.4(b)**

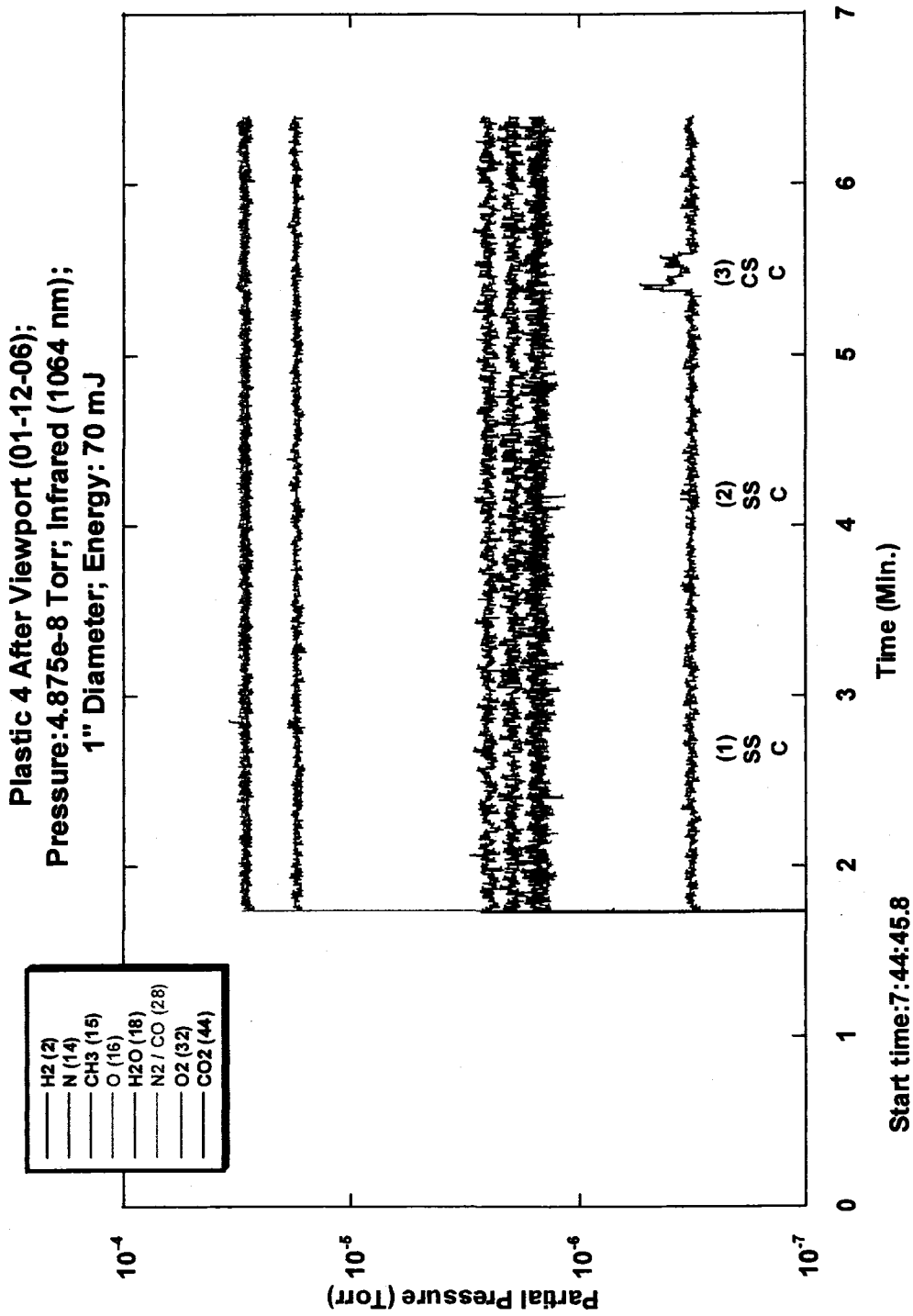


Figure 4.4(c)

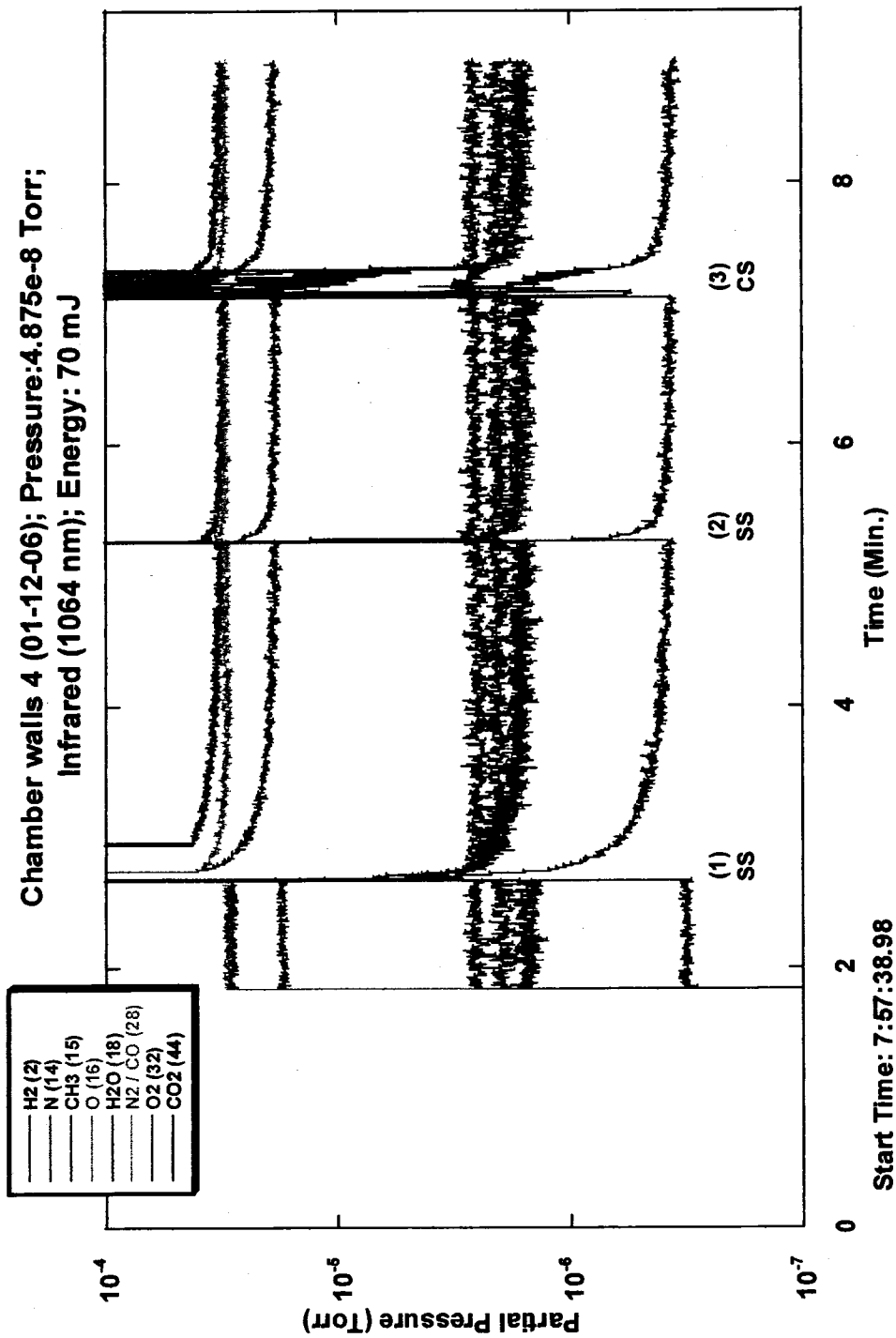


Figure 4.4(d)

Plastic 4 After Chamber walls (01-12-06);  
 Pressure: 4.875e-8 Torr; Infrared (1064 nm);  
 1" Diameter; Energy: 70 mJ

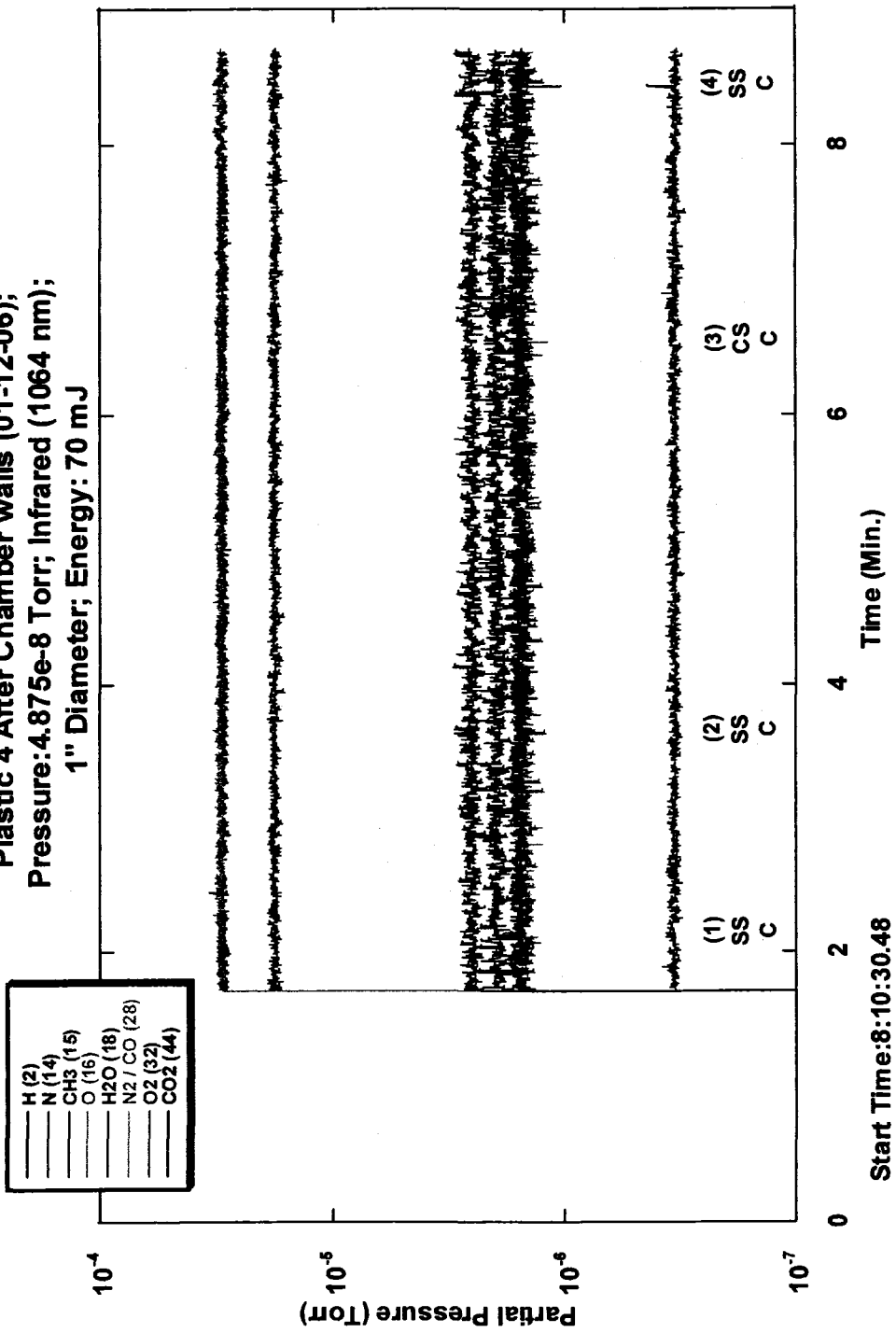
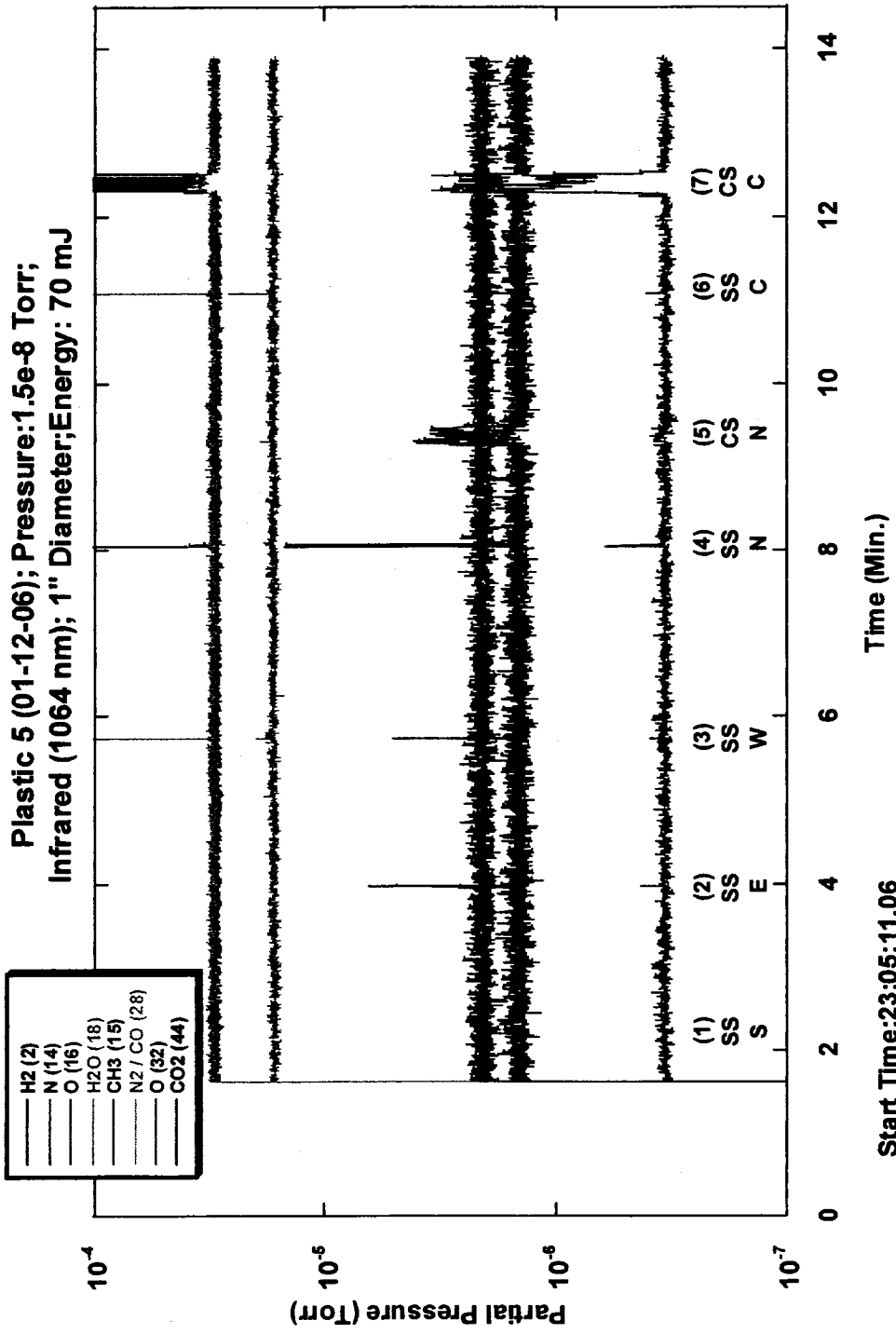
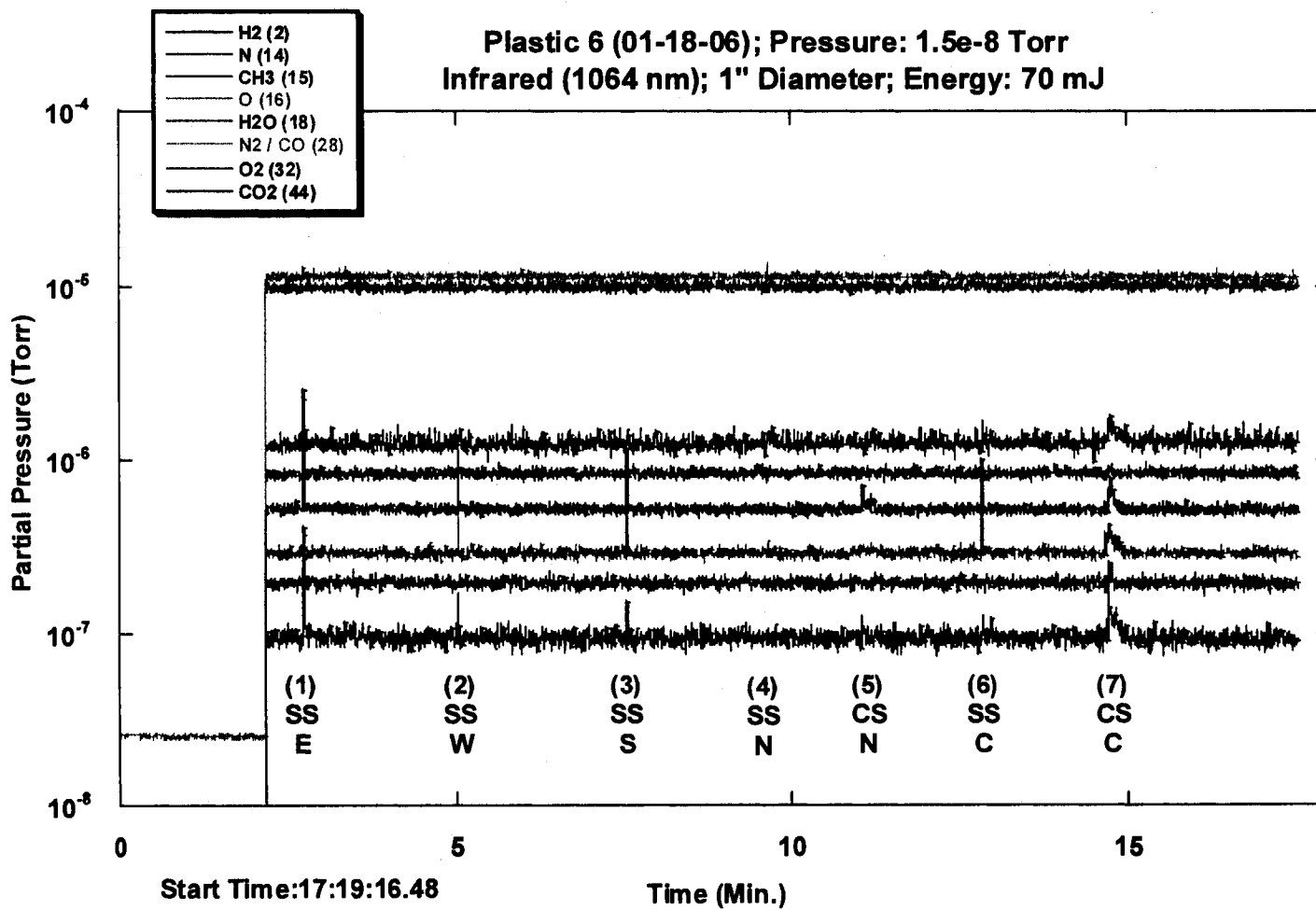


Figure 4.4(e)



**Figure 4.5**



**Figure 4.6**

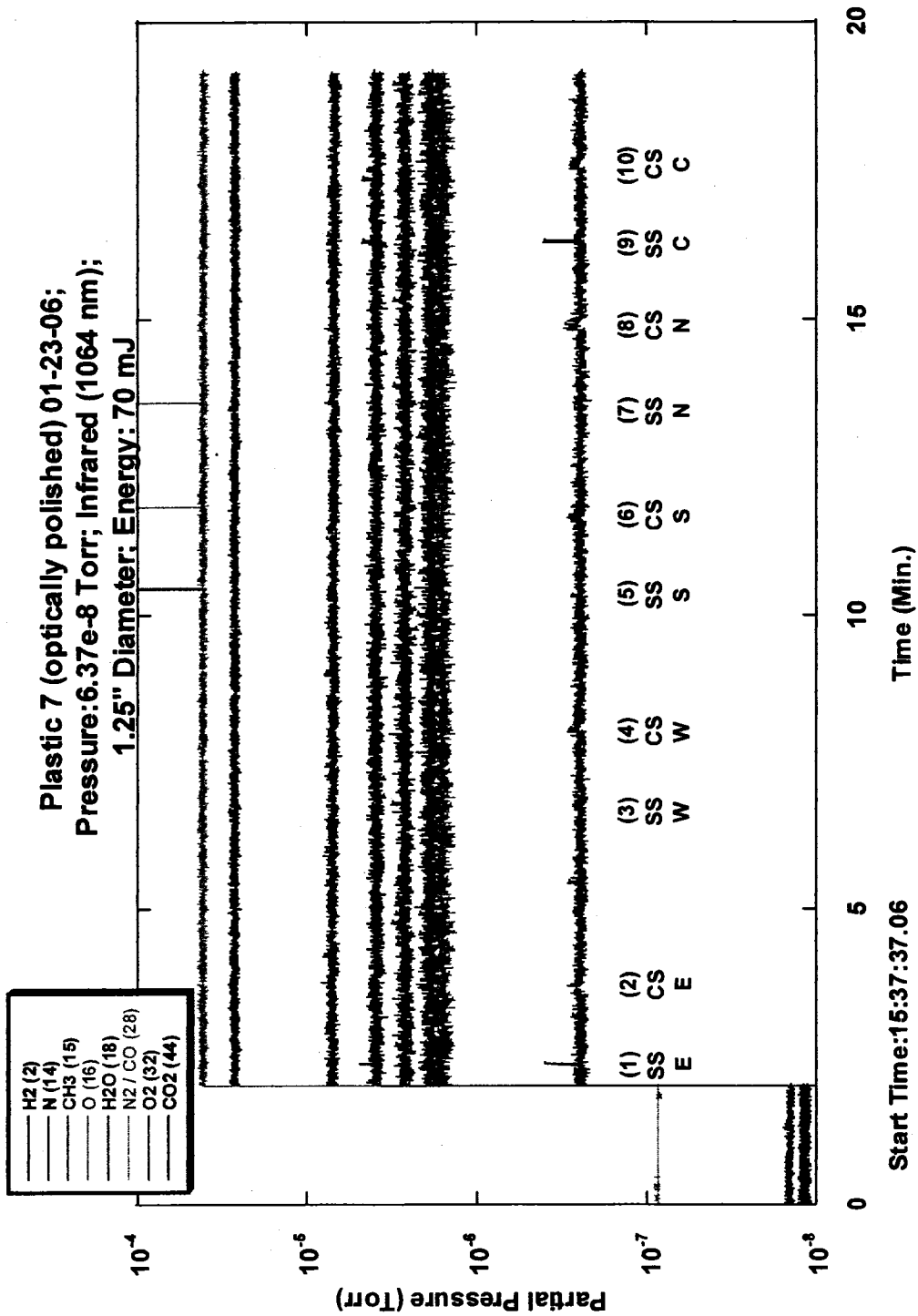


Figure 4.7(a)



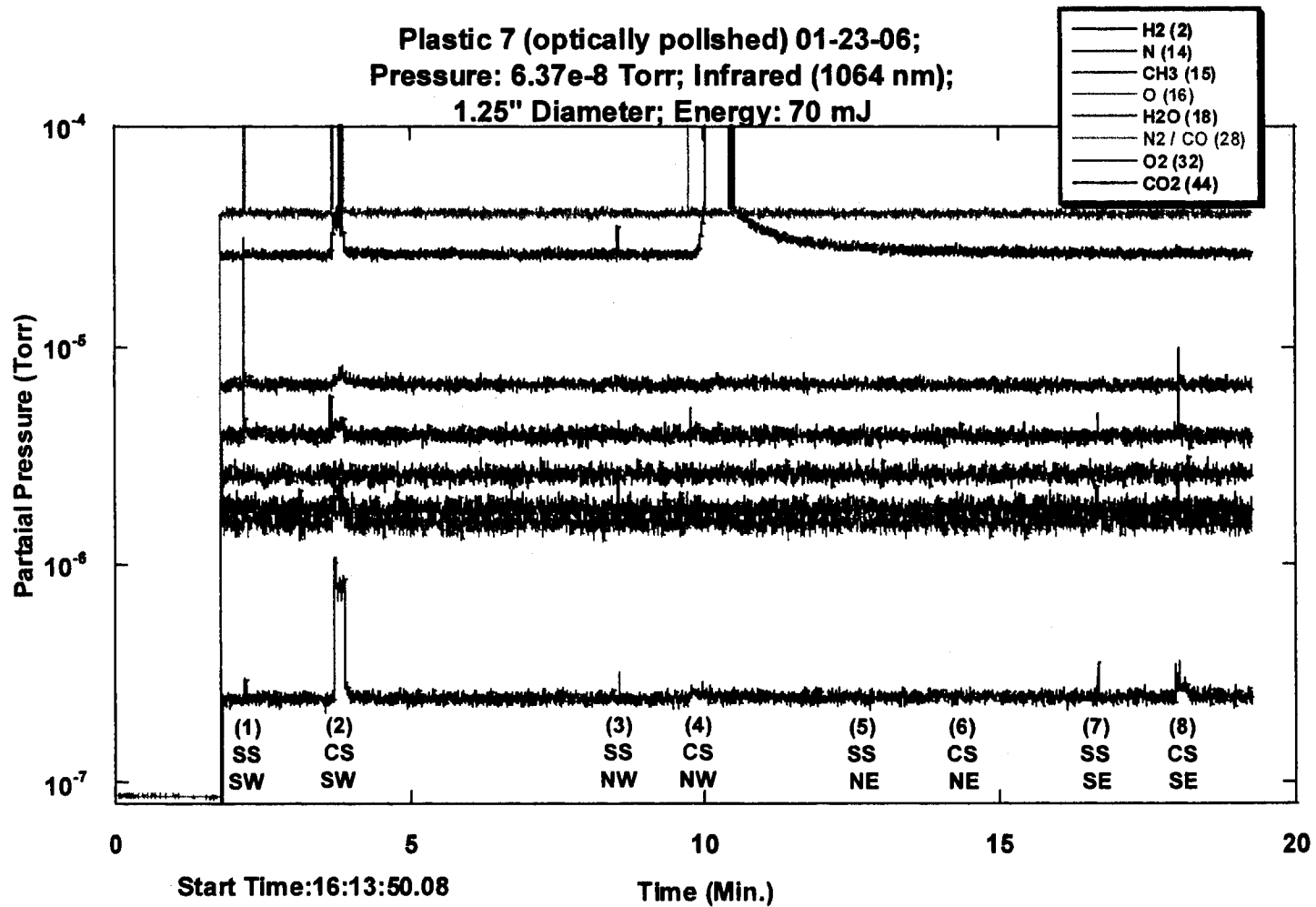


Figure 4.7(b)

Plastic 8 (optically polished);01-25-06;  
 Pressure:6e-8 Torr; Infrared (1064 nm);  
 1.25" Diameter; Energy: 70 mJ

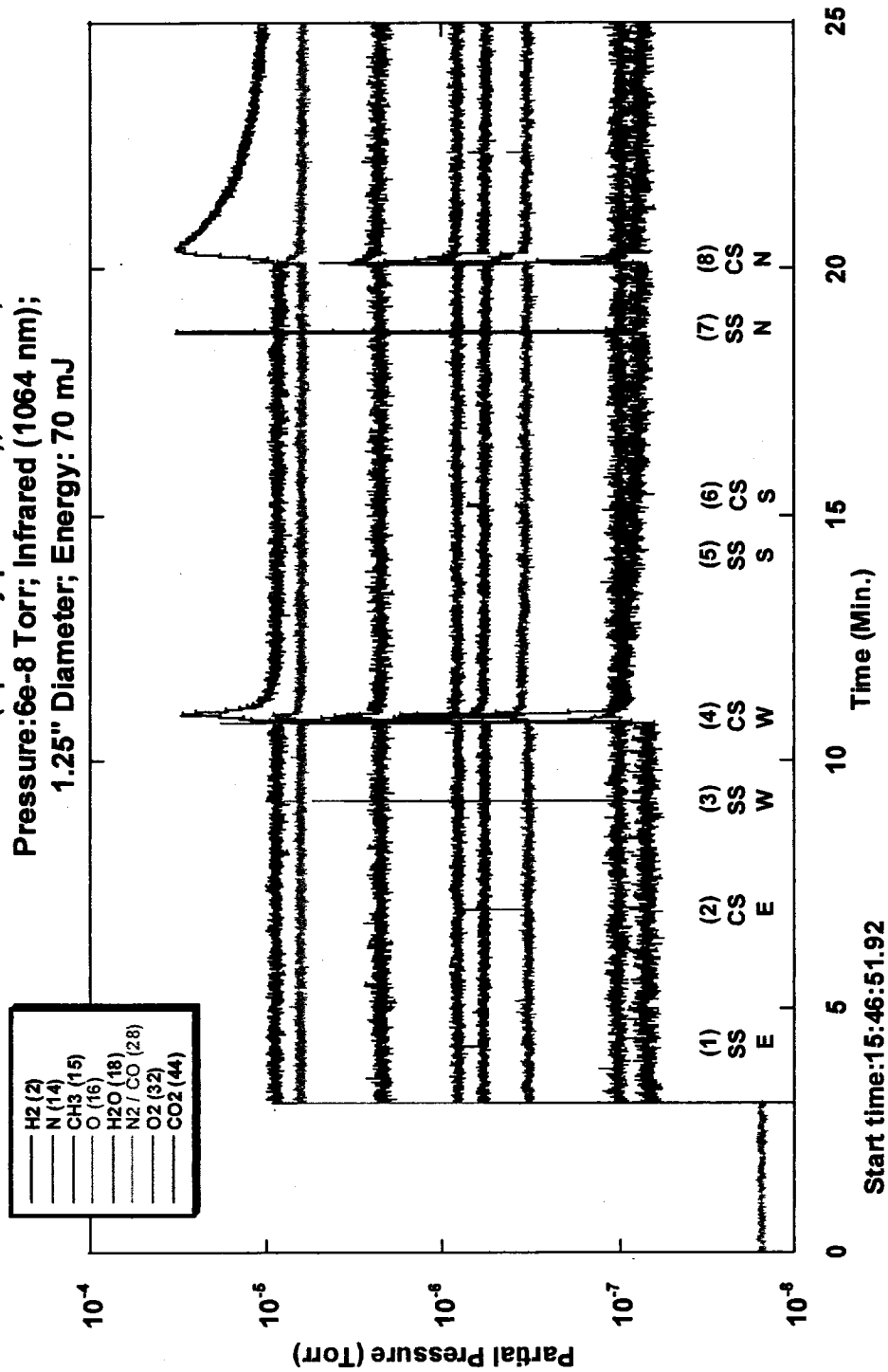


Fig.4.8(a)

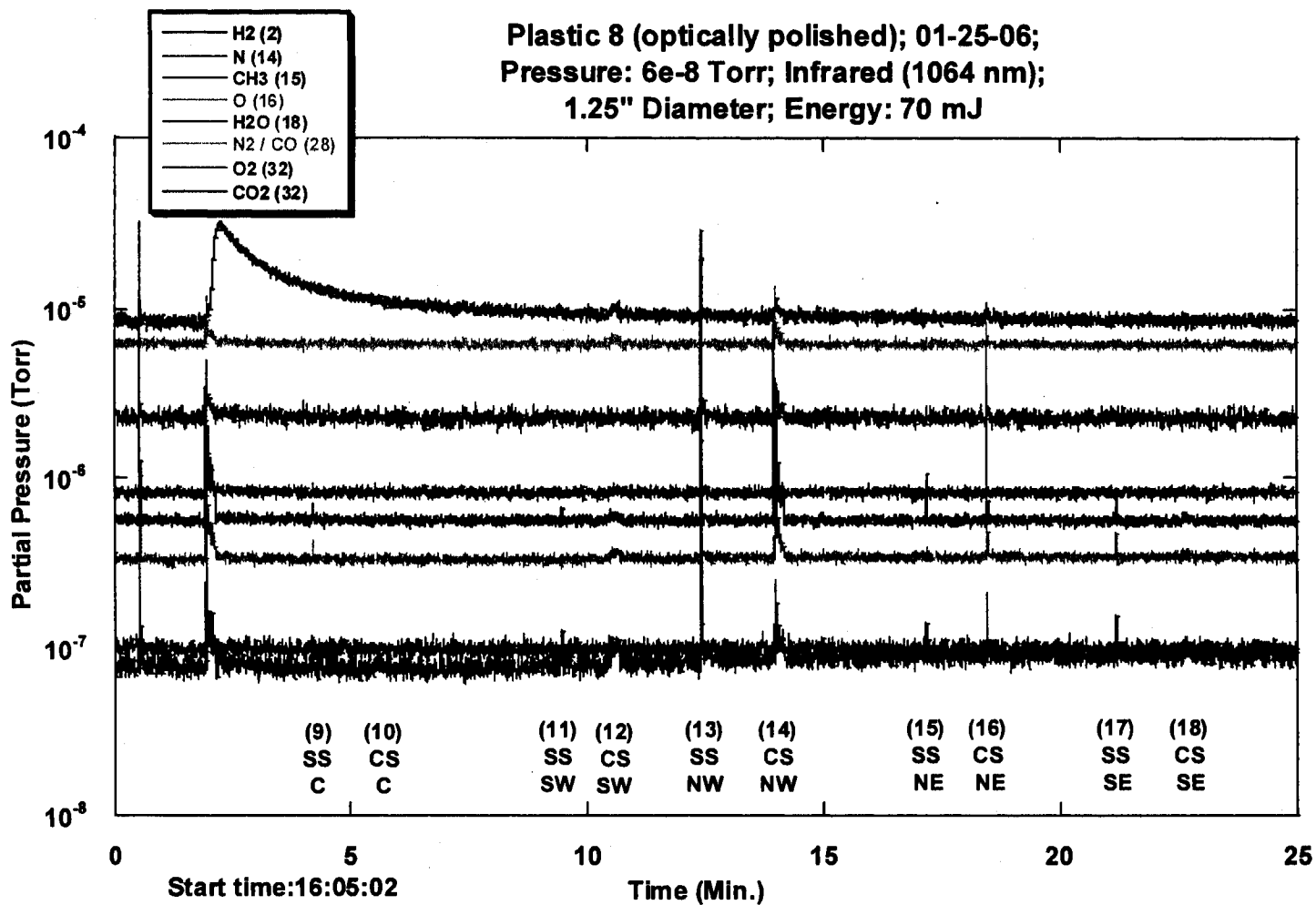


Figure 4.8(b)

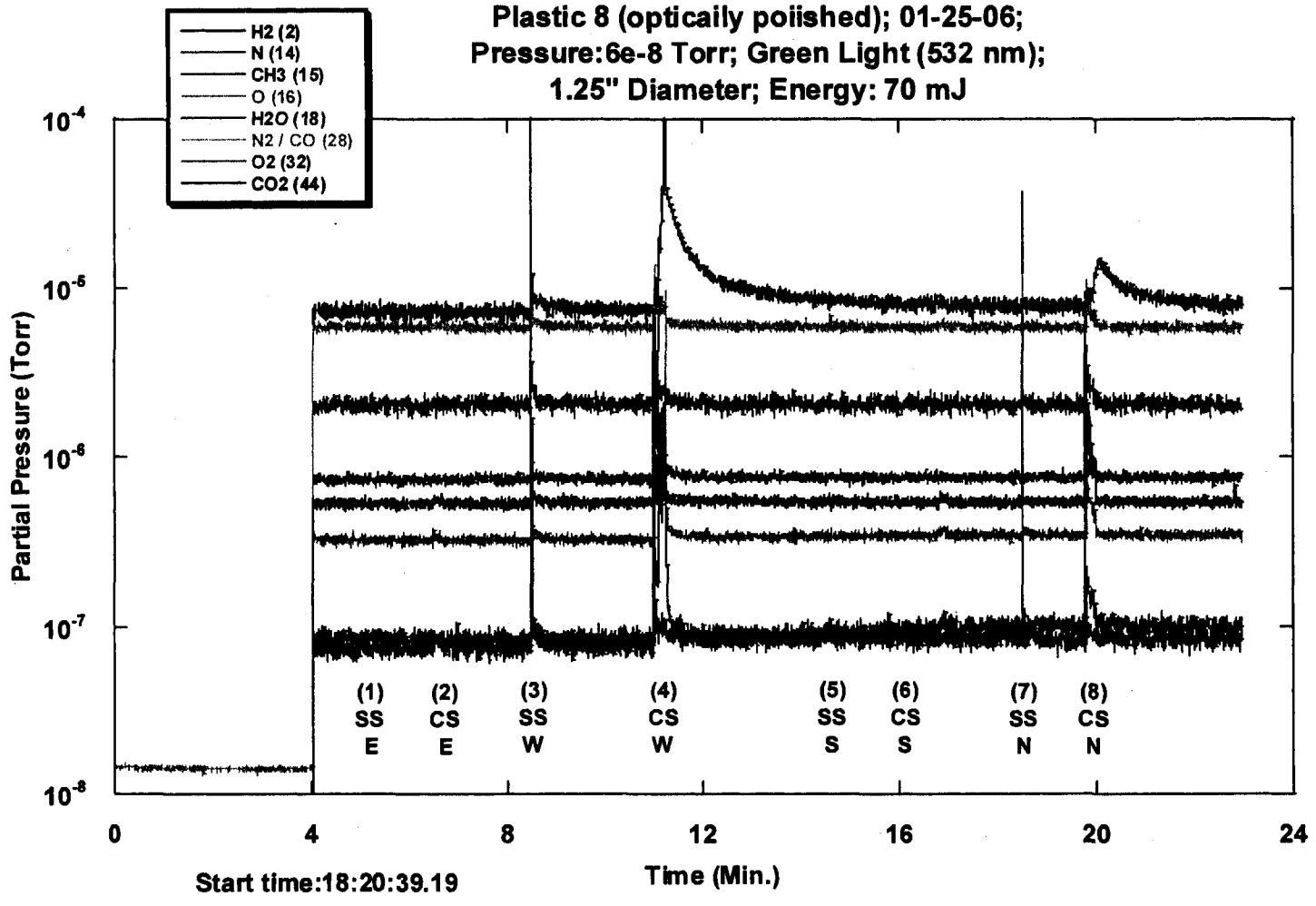


Figure 4.8(c)

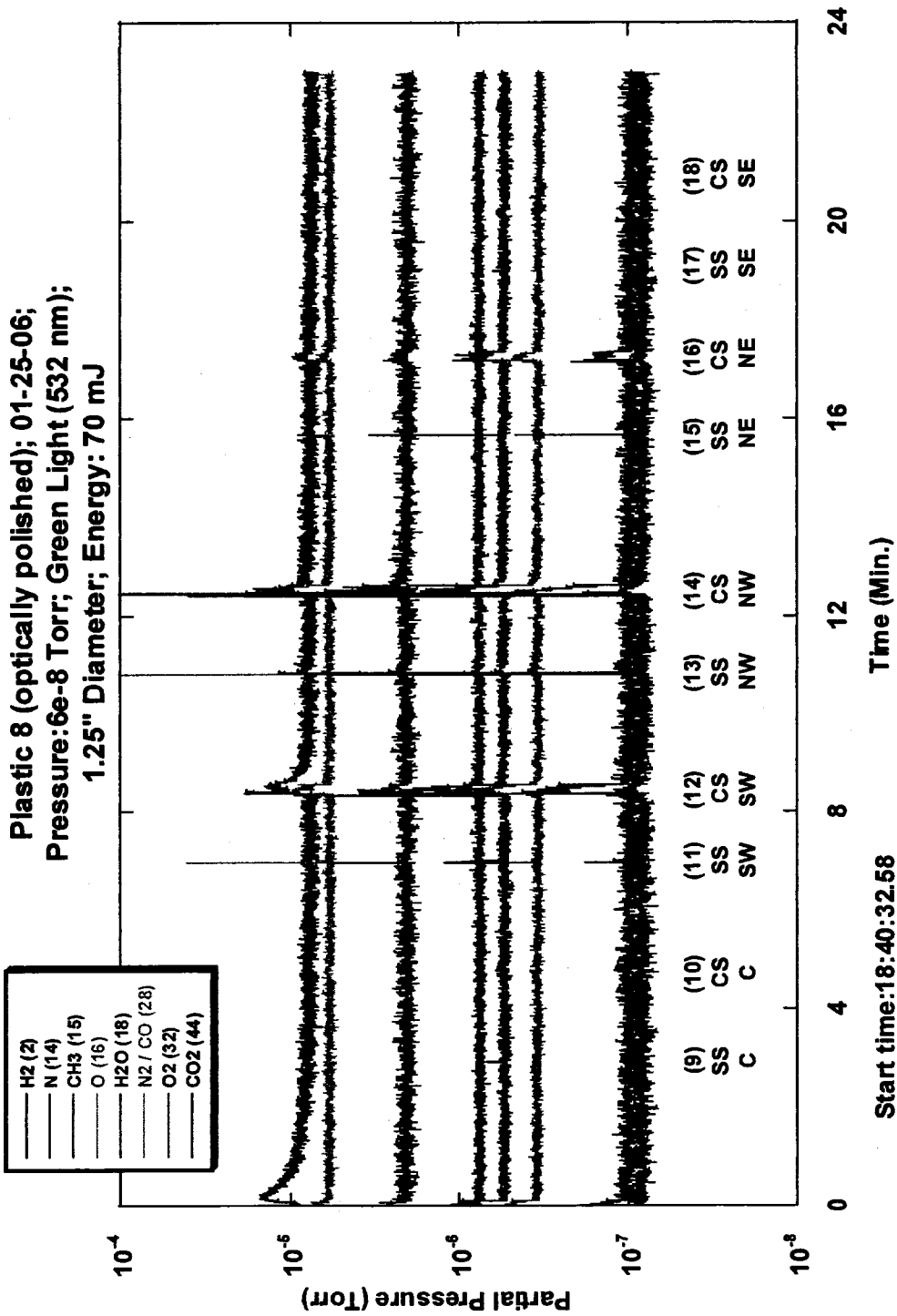


Figure 4.8(d)

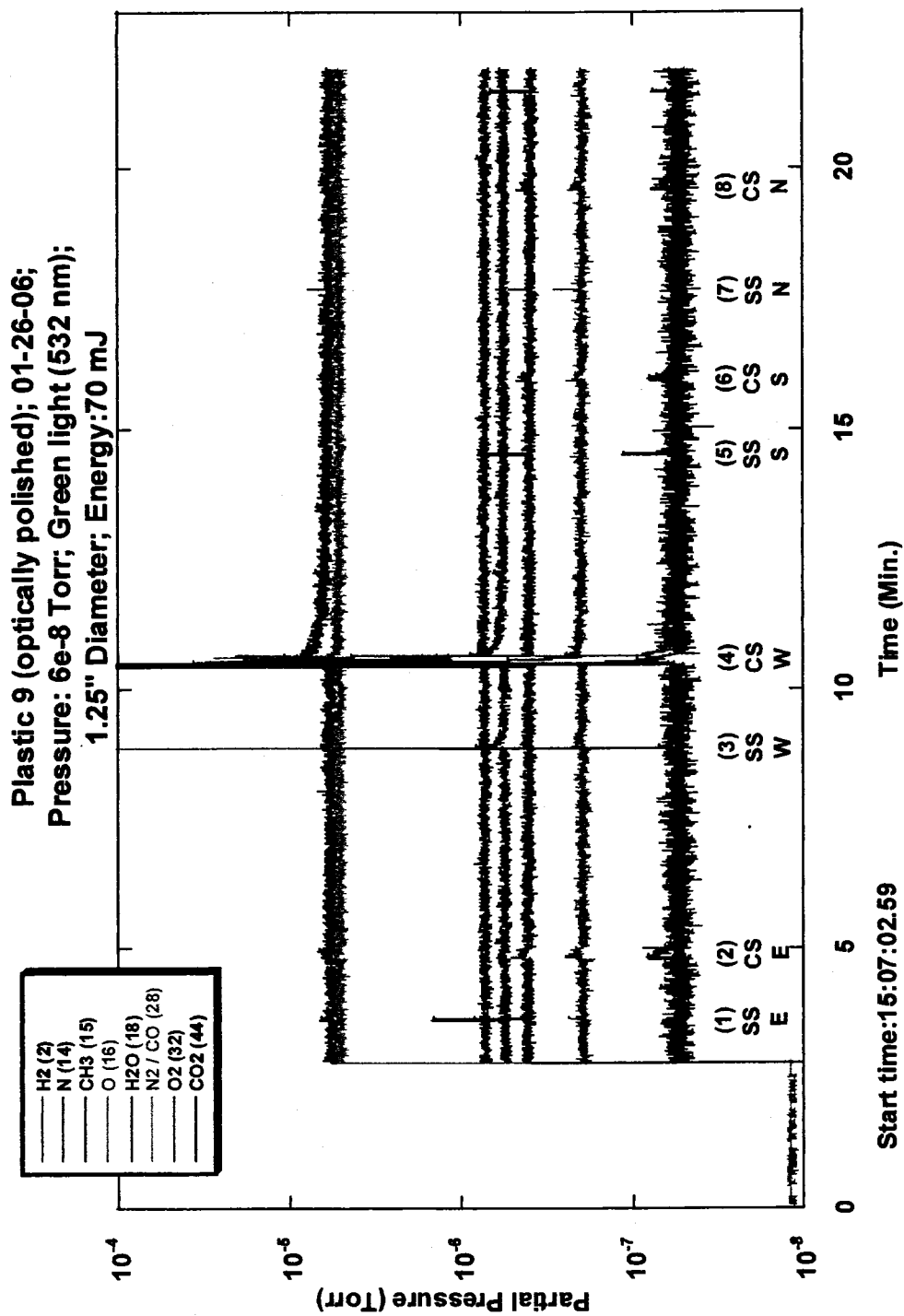
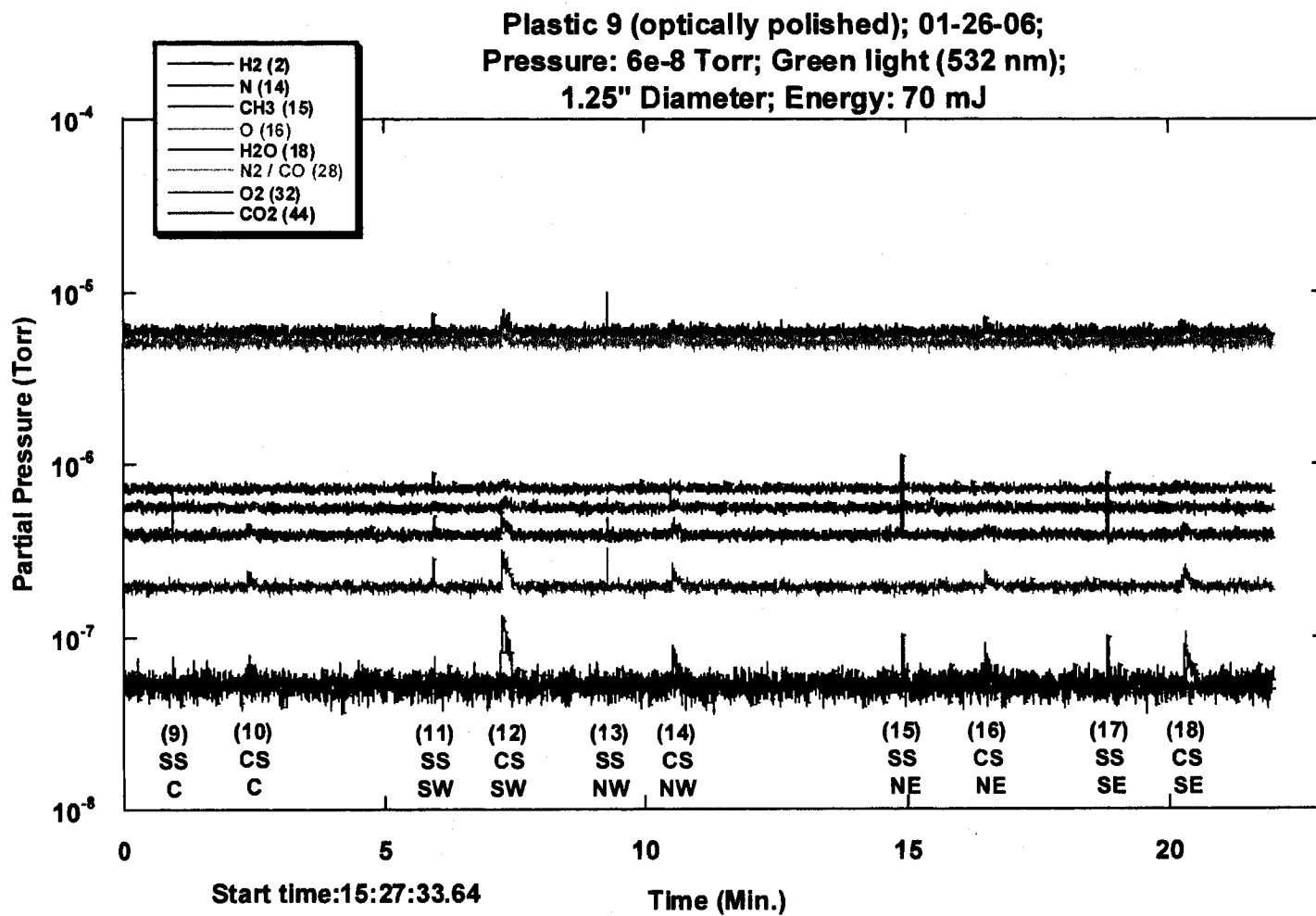


Figure 4.9(a)



**Figure 4.9(b)**

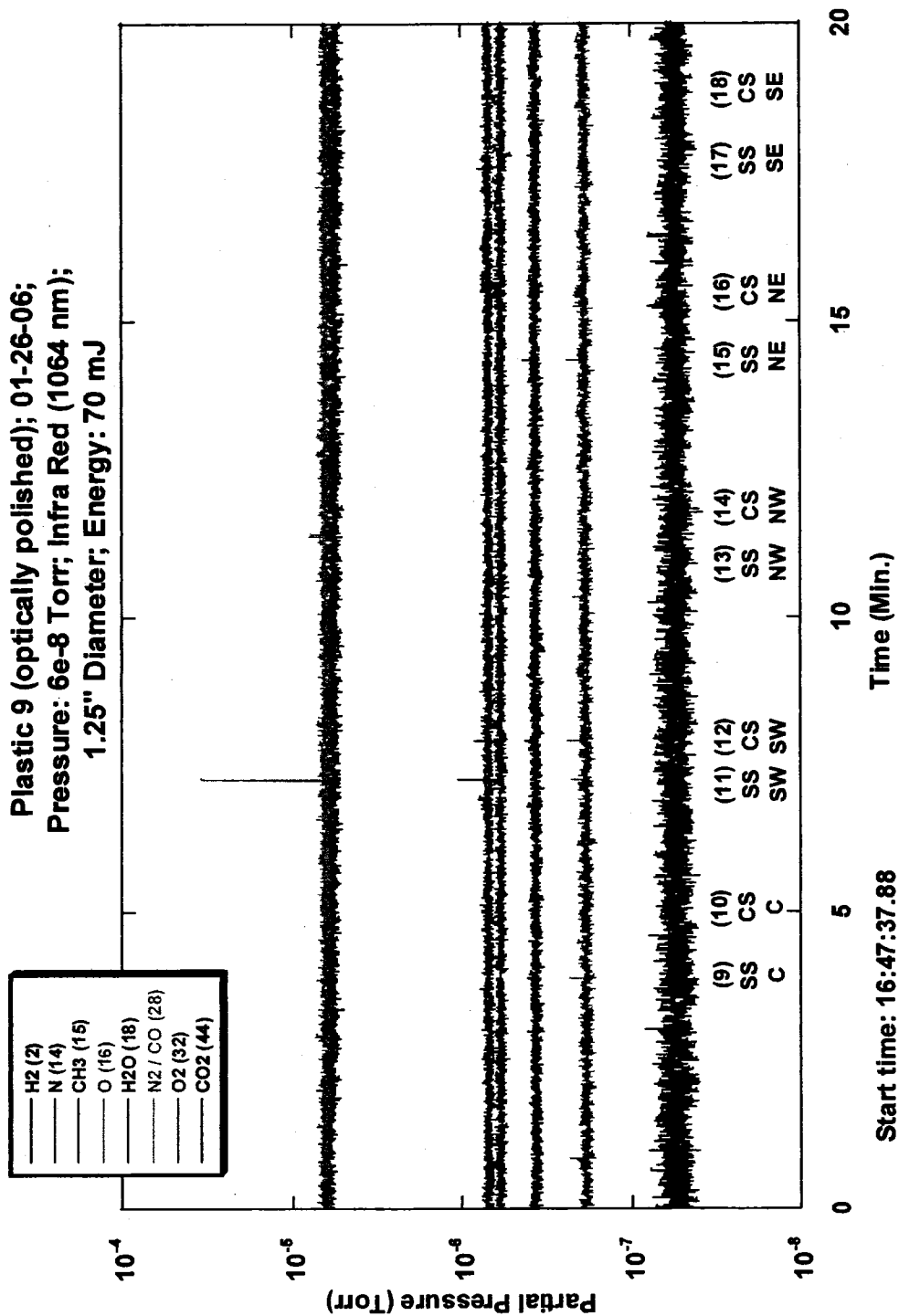
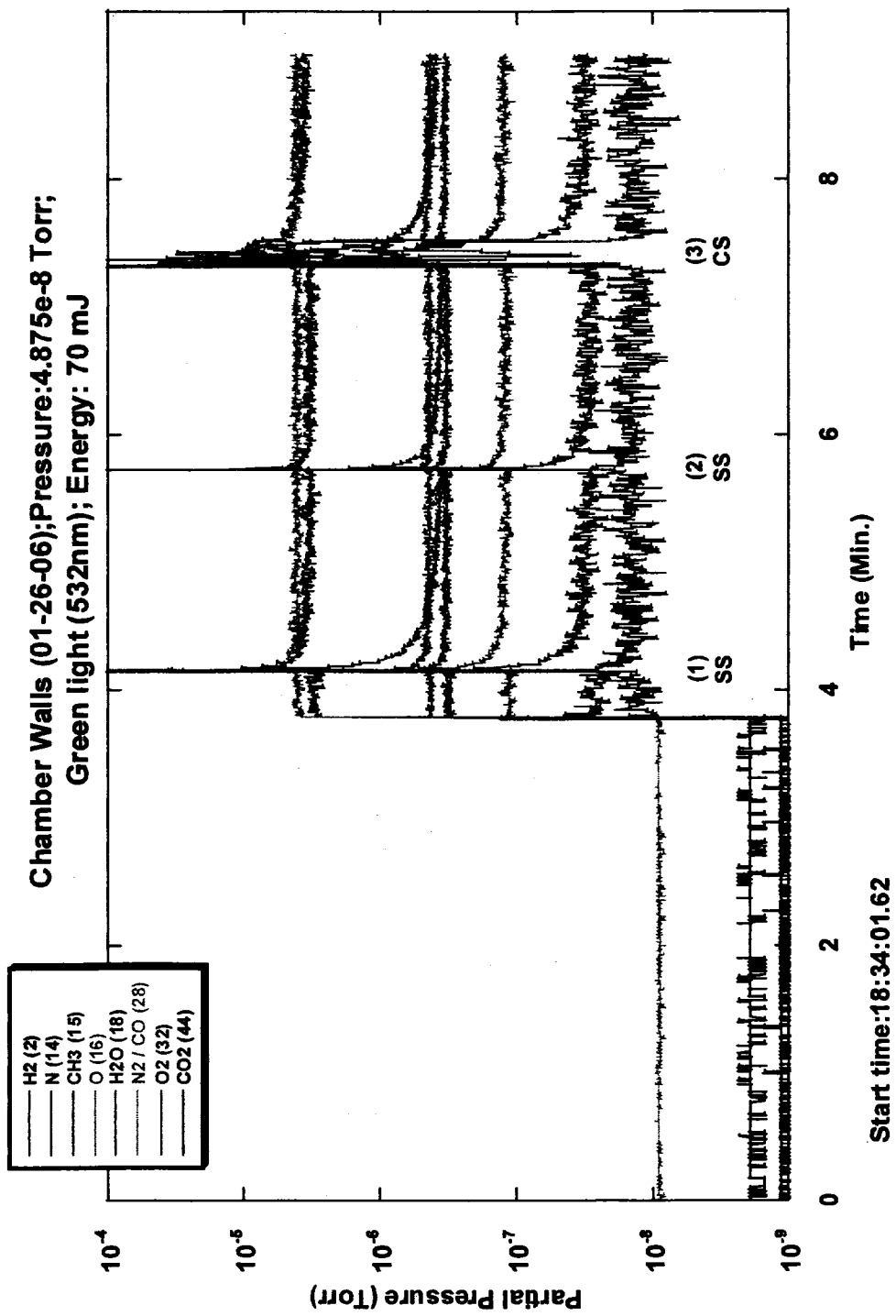


Figure 4.9(d)





**Figure 4.10(a)**

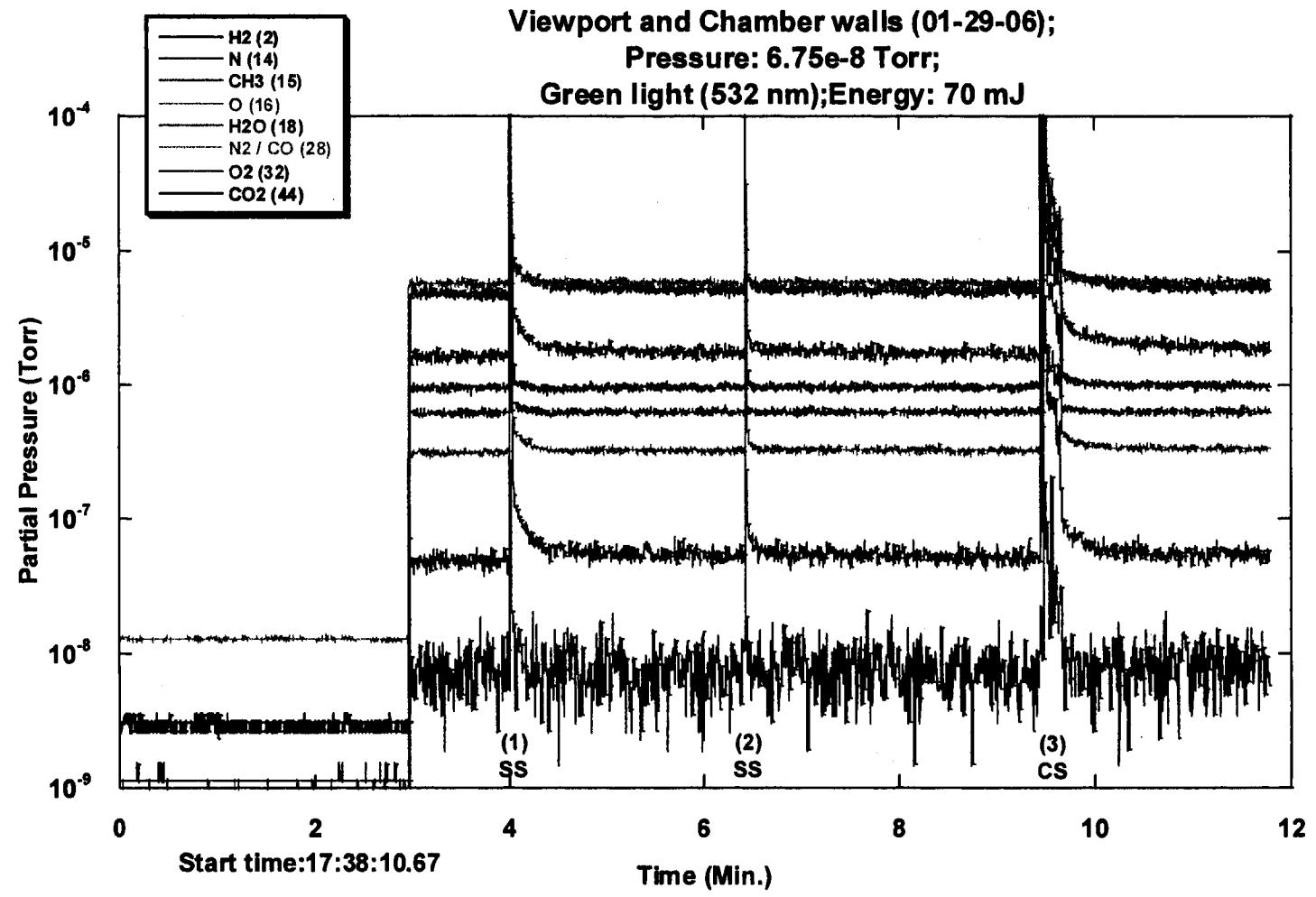


Figure 4.10(b)

Viewport and side walls (01-29-06) Faraday cup mode;  
Pressure:  $6.75 \times 10^{-8}$  Torr; Green light (532 nm);  
Energy: 70 mJ

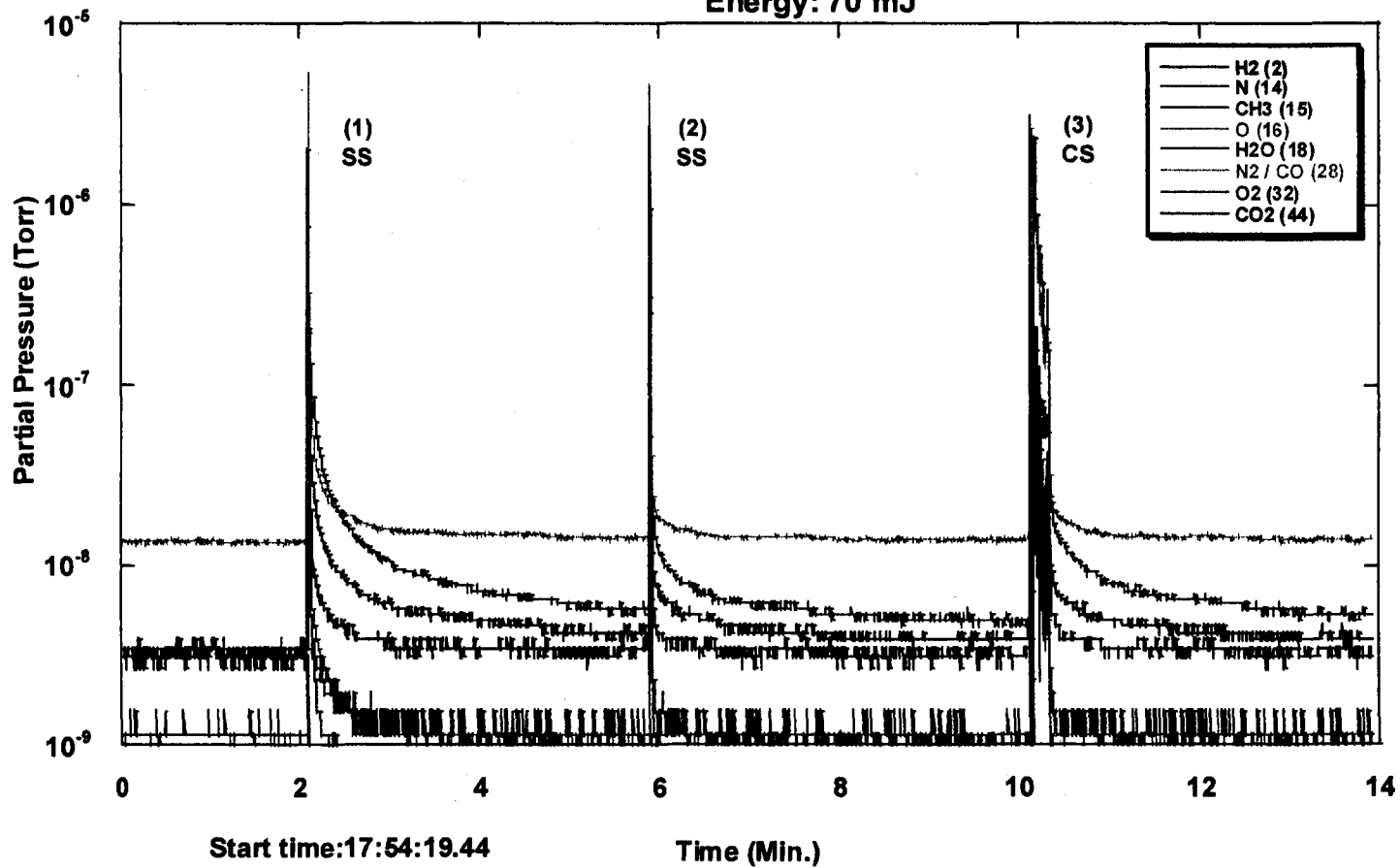
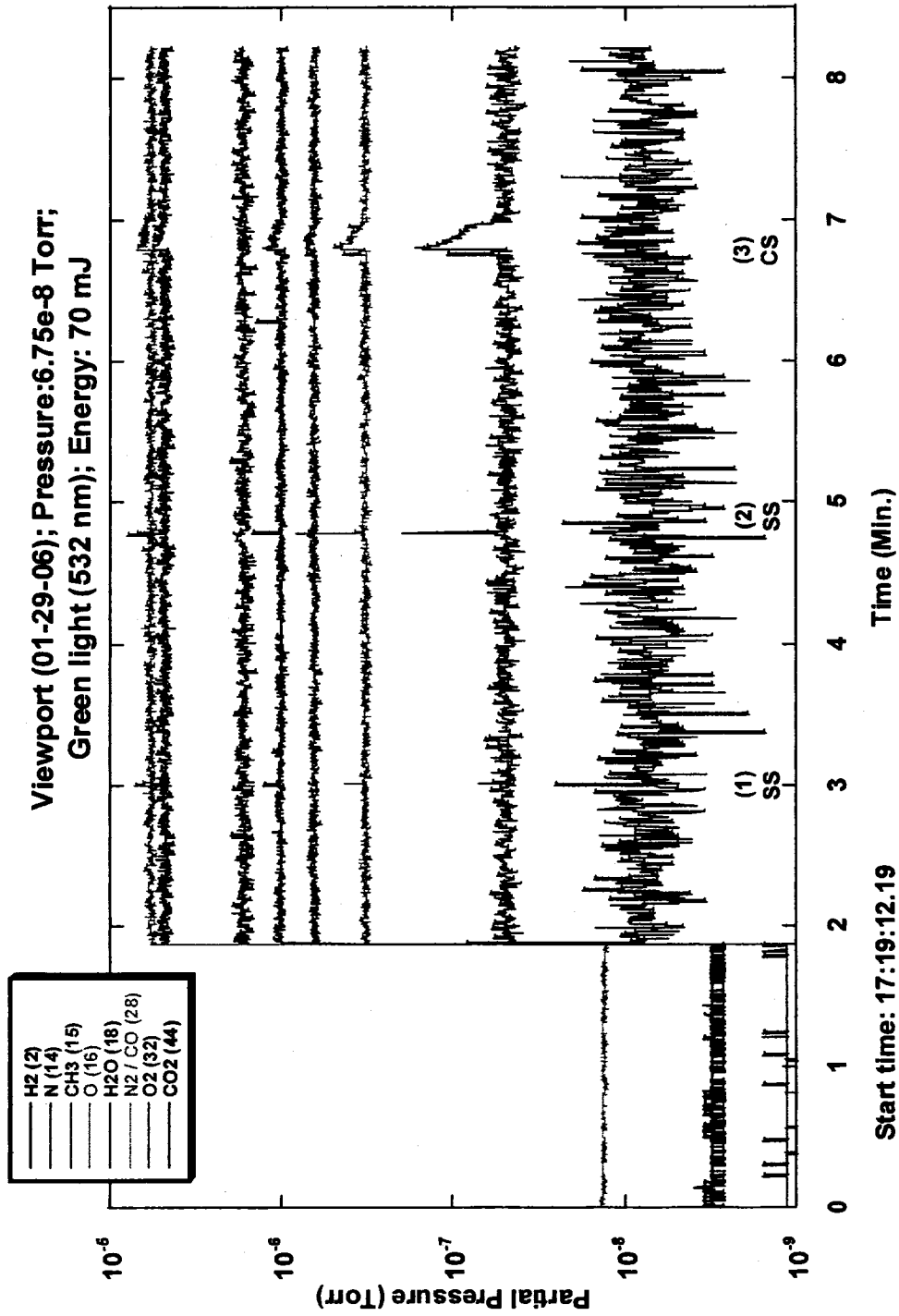


Figure 4.10(c)



**Figure 4.11**

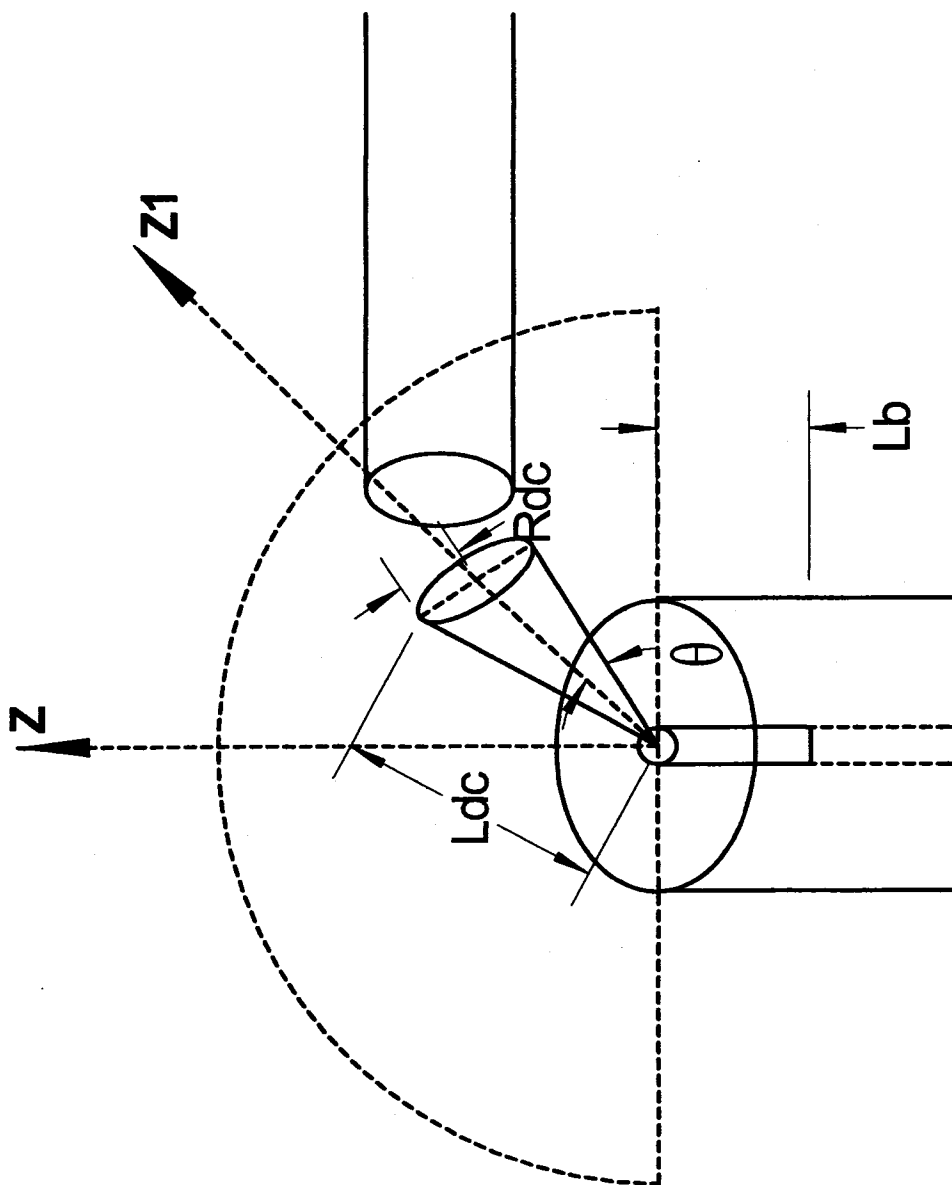


Figure 4.12 Detector Capture Area

Table 4.1. Select shot data\* corresponding to Figure 4.1. Shot Date 01/09/2006; Sample No. 1; 1064 nm light; Vacuum pressure  $4.8 \times 10^{-8}$  Torr

Time / Mode (SS/CS)	Shot No. / Pos.	H2 (2)	N (14)	Mass 15 (15)	O (16)	H2O (18)	N2/CO (28)	O2 (32)	CO2 (44)
19:00:30 / SS	1 / e	n	n	5.07e-7 ARU 0.36s None DNA 3.89e-7 ARU 1.6 e-8 ARU	n	n	n	n	5.89e-6 ARU 0.359 s WF Type: None DNA 1.65e-5 ARU 1.15e-7 ARU
19:03:33 / SS	2 / w	n	n	n	n	n	n	n	n
19:12:58 / SS	3 / s	n	n	4.49e-7 ARU 0.297 s None DNA 4.01 e-7 ARU 1.4 e-8 ARU	2.56 e-6 ARU 0.407 s None DNA 1.67 e-6 ARU 9.9e-8 ARU	n	Sat. 0.344 s None DNA 3.05e-5 ARU 5.06e-7 ARU	n	2.71e-6 ARU 0.25 s None DNA 1.67e-6 ARU 1.09e-7 ARU
19:17:34 / SS	4 / n	Sat. ARU 0.766 s; DT:6.469 s None DNA 6.51e-5 ARU 5.74e-7 ARU	9.52e-6 ARU 0.266 s None DNA 1.99e-6 ARU 1.18e-7 ARU	3.16e-6 ARU 0.344 s; DT:5.172 s None DNA 3.96e-7 ARU 1.36e-8 ARU	Sat. ARU 0.375 s; DT: 1.844 s None DNA 1.67e-6 ARU 1.07e-7 ARU	2.83e-5 ARU 0.358 s; DT:3.547 s 0.207 s DNA 2.18e-5 ARU 4.35e-7 ARU	Sat ARU 0.312s; DT: 0.563 s 0.207 s DNA 3e-5 ARU 5.51e-7 ARU	n	Sat ARU 0.391 s; DT: 2.297 s None DNA 1.68e-6 ARU 1.11e-7 ARU
19:19:54 / CS	5 / n	Sat ARU 10.11 s None Y 3.38e-5 ARU 5.78e-7 ARU	3.01e-6 ARU 7.469 s None Y 1.96e-6 ARU 1.13e-7 ARU	1.69e-6 ARU 9.672 s None Y 3.91e-7 ARU 1.28e-8 ARU	1.31e-5 ARU 10.609 s None Y 1.62e-6 ARU 1.0e-7 ARU	4.19e-5 ARU 7.469 s None Y 2.1e-5 ARU 4.21e-7 ARU	Sat ARU 7.015 s None Y 2.85e-5 ARU 4.94e-7 ARU	n	4.36e-5 ARU 10.172 s 0.128 s Y 1.64e-6 ARU 1.13e-7 ARU

\* Data displayed in the following sequential order: Peak Partial Pressure Value in Electron Multiplier Mode (ARU), time duration of signal (s), decay time in secs (if present), delay time relative to initial signals received if beyond a single system sampling time (s), if an initial precursor pulse is observed in the 10 Hz continuous shot mode, the average partial pressure baseline prior to illumination, and the standard deviation of the baseline pressure. Note: "DNA" means does not apply and "n" means a signal was not detected.



Table 4.2 c: Shot Date 01/10/2006; Sample No. 2; 1064 nm light; Vacuum pressure  $4.875 \times 10^{-8}$  Torr; Energy: 85 mJ

Time / Mode (SS/CS)	Shot No. / Pos.	H2 (2)	N (14)	Mass 15 (15)	O (16)	H2O (18)	N2/CO (28)	O2 (32)	CO2 (44)
13:51:59 / SS	1 / c	n	n	n	n	n	n	n	n
13:53:06 / SS	2 / c	n	n	n	n	n	n	n	n
13:54:10 / CS	3 / c	n	n	4.85e-7 ARU 11.36 s None N 3.55e-7 ARU 1.02e-8 ARU	n	n	n	n	n

Table 4.2 d: Shot Date 01/10/2006; Sample No. 2; 1064 nm light; Vacuum pressure  $4.875 \times 10^{-8}$  Torr; Energy: 70 mJ

Time / Mode (SS/CS)	Shot No. / Pos.	H2 (2)	N (14)	Mass 15 (15)	O (16)	H2O (18)	N2/CO (28)	O2 (32)	CO2 (44)
14:07:56 / SS	1 / Viewport	n	5.03e-6 ARU 0.297 s None DNA 2.e-6 ARU 1.2e-7 ARU	8.87e-7 ARU 0.359 s None DNA 3.53e-7 ARU 1.18e-8 ARU	1.11e-5 ARU 0.391 s None DNA 1.61e-6 ARU 9.59e-8 ARU	n	3.69e-5 ARU 0.406 s 0.097 s DNA 3.08e-5 ARU 4.71e-7 ARU	n	1.13e-5 ARU 0.606 s None DNA 1.75e-6 ARU 1.17e-7 ARU
14:09:33 / SS	2 / Viewport	n	n	n	n	n	Sat ARU 0.406 s None DNA 3.03e-5 ARU 4.97e-7 ARU	n	3.92e-5 ARU 0.391 s None DNA 1.77e-6 ARU 1.19e-7 ARU



		Sat ARU 8.875 s None Y	3.11e-6 ARU 0.328 s None N	3.08e-6 ARU 10.532 s None Y	1.27e-5 ARU 10.42 s 0.035 s Y	2.95 e-5 ARU 0.344 s None N	Sat ARU 10.578 s None Y		2.83e-5 ARU 11.079 s None Y
14:10:20 / CS	3 / Viewport	3.03e-5 ARU 5.26e-7 ARU	2.e-6 ARU 1.06e-7 ARU	3.56e-7 ARU 1.15e-8 ARU	1.62e-6 ARU 9.54e-8 ARU	2.02e-5 ARU 4.11e-7 ARU	3.04e-5 ARU 4.98e-7 ARU	n	1.76e-6 ARU 1.2e-7 ARU

Table 4.2 e: Shot Date 01/10/2006; Sample No. 2; 1064 nm light; Vacuum pressure  $4.875 \times 10^{-8}$  Torr; Energy: 70 mJ

Time / Mode (SS/CS)	Shot No. / Pos.	H2 (2)	N (14)	Mass 15 (15)	O (16)	H2O (18)	N2/CO (28)	O2 (32)	CO2 (44)
14:27:15 / SS	1 / Viewport & Walls	Sat ARU 23.391 s None DNA 3e-5 ARU 5.9e-7 ARU	1.39e-5 ARU 0.375 s; DT: 9.687 s None DNA 2e-6 ARU 1.16e-7 ARU	1.24e-5 ARU 0.297 s; DT:106.422 s None DNA 3.5e-7 ARU 1.06e-8 ARU	Sat ARU 0.375 s; DT:45.906 s None DNA 1.6e-6 ARU 9.3e-8 ARU	Sat. ARU 4.594 s; DT:71.313 s None DNA 1.99e-5 ARU 3.73e-7 ARU	Sat. ARU 4.625 s; DT48.393 s 0.109 s DNA 3e-5 ARU 5e-7 ARU	3.99e-6 ARU 2.516 s None DNA 2.53e-6 ARU 1.37e-7 ARU	Sat ARU 0.422 s; DT:7.844 s 0.109 s DNA 1.74e-6 ARU 1.17e-7 ARU
14:29:33 / SS	2 / Viewport & Walls	Sat. ARU 0.781 s None DNA 3.63e-5 ARU 2.3e-6 ARU	1.18 e-5 ARU 0.375 s None DNA 2.09e-6 ARU 1.17e-7 ARU	2.63e-6 ARU 0.344 s; DT:6.906 s None DNA 4.75e-7 ARU 4.88e-8 ARU	Sat ARU 0.375 s; DT:6.859 s None DNA 1.85e-6 ARU 1.37e-7 ARU	3.3e-5 ARU 0.407 s; DT:9.485 s None DNA 2.28e-5 ARU 1.15e-6 ARU	Sat ARU 0.344 s 0.035 s DNA 3.13e-5 ARU 7.45e-7 ARU	n	Sat ARU 0.406 s; DT:6.906 s 0.035 s DNA 1.89e-6 ARU 1.24e-7 ARU
14:31:18 / CS	3 / Viewport & Walls	Sat ARU 9.656 s 1.941 s y 3.42e-5 ARU 1.21e-6 ARU	6.2e-6 ARU 7.875 s None Y 2.07e-6 ARU 1.11e-7 ARU	2.5e-6 ARU 9.141 s None Y 4.29e-7 ARU 3.09e-8 ARU	Sat ARU 9.094 s None Y 1.77e-6 ARU 1.2e-7 ARU	Sat.ARU 9.641 s None Y 2.19e-5 ARU 8.55e-7 ARU	Sat. ARU 10.407 s None Y 3.08e-5 ARU 5.77e-7 ARU	Sat ARU 7.859 s 1.394 s Y 2.52e-6 ARU 1.41e-7 ARU	Sat ARU 10.031 s 0.113 s Y 1.88e-6 ARU 1.53e-7 ARU

Table 4.2 f: Shot Date 01/10/2006; Sample No. 2; 1064 nm light; Vacuum pressure  $4.875 \times 10^{-8}$  Torr; Energy: 70 mJ

Time / Mode (SS/CS)	Shot No. / Pos.	H2 (2)	N (14)	Mass 15 (15)	O (16)	H2O (18)	N2/CO (28)	O2 (32)	CO2 (44)
14:53:33 / SS	1 / c	n	n	n	n	n	n	n	5.62e-6 ARU 0.406 s None DNA 1.83e-6 ARU 1.53e-7 ARU
14:54:55 / SS	2 / c	n	n	n	n	n	n	n	n
14:56:33 / CS	3 / c	n	n	5.33e-7 ARU 9.031 None N 3.6e-7 ARU 1.01e-8 ARU	n	n	n	n	3.36e-6 ARU 5.422 s None N 1.83e-6 ARU 1.06e-7 ARU

172

Table 4.3(a): Shot Date 01/11/2006; Sample No. 3; 1064 nm light; Vacuum pressure  $4.875 \times 10^{-8}$  Torr; Energy: 70 mJ

Time / Mode (SS/CS)	Shot No. / Pos.	H2 (2)	N (14)	Mass 15 (15)	O (16)	H2O (18)	N2/CO (28)	O2 (32)	CO2 (44)
11:41:52 / SS	1 / e	n	n	n	n	n	n	n	n
				7.34e-7 ARU 0.359 s None DNA	2.65e-5 ARU 0.297 s None DNA				4.18e-6 ARU 0.406 s None DNA
11:46:25 / SS	2 / w	n	n	3.3e-7 ARU 1.01e-8 ARU	1.49e-6 ARU 8.49e-8 ARU	n	n	n	1.67e-6 ARU 1.02e-7 ARU

11:50:27 / SS	3 / s	Sat ARU 1.594 s None DNA 2.86e-5 ARU 5.42e-7 ARU	7.28e-6 ARU 0.328 s None DNA 2.01e-6 ARU 1.28e-7 ARU	4.17e-6 ARU 0.343 s; DT: 7.625s None DNA 3.29e-7 ARU 9.73e-9 ARU 4.69e-7 ARU 0.313 s None DNA 3.53e-7 ARU 2.2e-8 ARU	2.62e-5 ARU 0.328 s; DT: 7.25 s None DNA 1.5e-6 ARU 8.92e-8 ARU 3.76e-6 ARU 0.406 s None DNA 1.55e-6 ARU 1.1e-7 ARU	4.18e-5 ARU 0.359 s; DT: 4.04 s None DNA 1.69e-5 ARU 3.55e-7 ARU	Sat ARU 1.204 s None DNA 3.04e-5 ARU 4.79e-7 ARU 4.2e-5 ARU 0.36 s None DNA 3.01e-5 ARU 5.65e-7 ARU	1.48E-6 ARU 0.641 s None DNA 2.62e-6 ARU 1.37e-7 ARU	Sat ARU 0.375 s; DT: 3.937 s None DNA 1.66e-6 ARU 1.13e-7 ARU 8.3e-6 ARU 0.406 s None DNA 1.63e-6 ARU 1.12e-7 ARU
11:52:45 / SS	4 / n	n	n	6.8e-7 ARU 2.672 s None N 3.37e-7 ARU 1e-8 ARU	5.5e-6 ARU 2.719 s None Y 1.51e-6 ARU 9e-8 ARU	N	n	n	3.63e-6 ARU 4.516 s None Y 1.61e-6 ARU 1.04e-7 ARU
11:54:19 / CS	5 / n	Minor change at some time after the pulse duration began	n	n	n	n	n	n	n

Table 4.3 (b): Shot Date 01/11/2006; Sample No. 3; 1064 nm light; Vacuum pressure  $4.875 \times 10^{-8}$  Torr; Energy: 70 mJ

Time / Mode (SS/CS)	Shot No. / Pos.	H2 (2)	N (14)	Mass 15 (15)	O (16)	H2O (18)	N2/CO (28)	O2 (32)	CO2 (44)
13:02:47 / SS	1 / c	n	n	3.87e-7 ARU 0.375 s None DNA 3.1e-7 ARU 1.6e-8 ARU	2.66e-6 ARU 0.407 s None DNA 1.43e-6 ARU 9.74e-8 ARU	n	n	n	2.2e-6 ARU 0.406 s None DNA 1.73e-6 ARU 1.31e-7 ARU

13:04:10 / SS	2 / c	n	3.58e-7 ARU 0.359 s None DNA 3.13e-7 ARU 9.15e-9 ARU	n	n	n	n	n	n	2.48e-6 ARU 0.253 s None N 1.72e-6 ARU 1.13e-7 ARU
13:05:40 / CS	3 / c	n	3.24e-5 ARU 7.765 s None N 2.72e-5 ARU 5.09e-7 ARU	n	n	n	n	n	n	2.47e-6 ARU 7.312 s None N 1.46e-6 ARU 7.9e-8 ARU

Table 4.4 (a): Shot Date 01/12/2006; Sample No. 4; 1064 nm light; Vacuum pressure  $4.875 \times 10^{-8}$  Torr; Energy: 70 mJ

Time / Mode (SS/CS)	Shot No. / Pos.	H2 (2)	N (14)	Mass 15 (15)	O (16)	H2O (18)	N2/CO (28)	O2 (32)	CO2 (44)
7:12:40 / SS	1 / e	n	n	n	n	n	n	n	n
7:16:26 / SS	2 / w	n	n	n	n	n	n	n	n
7:22:32 / SS	3 / s	n	n	4.36e-7 ARU 0.36 s None N 3.1e-7 ARU 9.89e-9 ARU	n	n	n	n	2.72e-6 ARU 0.422 s None N 1.54e-6 ARU 9.35e-8 ARU
7:25:01 / SS	4 / n	n	n	n	n	n	n	n	n
7:28:21 / SS	6 / c	n	n	n	n	n	n	n	n
7:26:32 / CS	5 / n	n	n	n	n	n	n	n	n
7:29:18 / CS	7 / c	n	n	n	n	n	n	n	n

Table 4.4 (b): Shot Date 01/12/2006; Sample No. 4; 1064 nm light; Vacuum pressure  $4.875 \times 10^{-8}$  Torr; Energy: 70 mJ

Time / Mode (SS/CS)	Shot No. / Pos.	H2 (2)	N (14)	Mass 15 (15)	O (16)	H2O (18)	N2/CO (28)	O2 (32)	CO2 (44)
7:38:21 / SS	1 / VP	Sat ARU		1.51e-6 ARU	2.99e-5 ARU	3.97e-5 ARU	Sat ARU	Sat ARU	Sat ARU
		0.312 s;	4.29e-6 ARU	0.297 s;	0.359 s;	0.328 s;	0.812 s	0.234 s;	DT:7.797 s
		DT:7.204 s	0.312 s	DT:12.516 s	DT:2.844 s	DT:9.796 s	None	0.266 s	DT:7.797 s
7:39:44 / SS	2 / VP	None	None	None	None	None	None	None	0.082 s
		DNA	DNA	DNA	DNA	DNA	DNA	DNA	DNA
		2.81e-5 ARU	1.94e-6 ARU	3.11e-7 ARU	1.44e-6 ARU	1.7e-5 ARU	2.95e-5 ARU	2.51e-6 ARU	1.55e-6 ARU
7:41:12 / CS	3 / VP	6.04e-7 ARU	1.35e-7 ARU	1.78e-6 ARU	1.1e-7 ARU	5.05e-7 ARU	5.05e-7 ARU	1.19e-7 ARU	1.17e-7 ARU
		3.67e-5 ARU		7.32e-6 ARU	7.31e-6 ARU	2.06e-5 ARU	Sat ARU	6.58e-6 ARU	Sat ARU
		0.391 s		0.344 s;	0.453 s	0.297 s	0.25 s	0.344 s	0.391 s;
7:39:44 / SS	2 / VP	None		DT:7.093 s	None	None	None	None	DT:3.875 s
		N		0.19 s	DNA	N	DNA	DNA	None
		2.95e-5 ARU		DNA	1.48e-6 ARU	1.76e-5 ARU	2.98e-5 ARU	2.49e-6 ARU	DNA
7:39:44 / SS	2 / VP	1.2e-6 ARU		3.17e-8 ARU	9.08e-8 ARU	8.34e-7 ARU	7.45e-7 ARU	1.29e-7 ARU	1.23e-7 ARU
		3.74e-5 ARU	4.01e-6 ARU	3.18e-6 ARU	3.64e-5 ARU	Sat ARU	Sat ARU	6.22e-6 ARU	Sat ARU
		6.437 s	3.329 s	10.829 s	10.329 s	10.375 s	2.859 s	9.563 s	11.375 s
7:41:12 / CS	3 / VP	None	None	None	None	0.082 s	0.082 s	None	None
		N	Y	Y	Y	Y	Y	Y	Y
		2.91e-5 ARU	2e-6 ARU	3.24e-7 ARU	1.46e-6 ARU	1.74e-5 ARU	2.97e-5 ARU	2.5e-6 ARU	1.58e-6 ARU
7:41:12 / CS	3 / VP	6.28e-7 ARU	1.2e-7 ARU	1.09e-8 ARU	7.46e-8 ARU	4.26e-7 ARU	4.71e-7 ARU	1.23e-7 ARU	1.13e-7 ARU

Table 4.4 (c): Shot Date 01/12/2006; Sample No. 4; 1064 nm light; Vacuum pressure  $4.875 \times 10^{-8}$  Torr; Energy: 70 mJ

Time / Mode (SS/CS)	Shot No. / Pos.	H2 (2)	N (14)	Mass 15 (15)	O (16)	H2O (18)	N2/CO (28)	O2 (32)	CO2 (44)
7:47:37 / SS	1 / c	n	n	n	n	n	3.43e-5 ARU 0.452 s None DNA 2.98e-5 ARU 4.99e-7 ARU	n	n
7:48:55 / SS	2 / c	n	n	n	n	n	n	n	n
7:50:08 / CS	3 / c	n	n	5.35e-7 ARU 11.094 s None N 3.19e-7 ARU 9.73e-9 ARU	n	n	n	n	n

Table 4.4 (d): Shot Date 01/12/2006; Sample No. 4; 1064 nm light; Vacuum pressure  $4.875 \times 10^{-8}$  Torr; Energy: 70 mJ

Time / Mode (SS/CS)	Shot No. / Pos.	H2 (2)	N (14)	Mass 15 (15)	O (16)	H2O (18)	N2/CO (28)	O2 (32)	CO2 (44)
8:00:18 / SS	1 / VP & Walls	Sat ARU 17.718 s; DT:83.704 s None DNA 2.866e-5 ARU 5.48e-7 ARU	1.59e-5 ARU 0.313 s; DT:16.047 s None DNA 1.95e-6 ARU 1.54e-7 ARU	1.86e-5 ARU 0.282 s; DT:72.563 s None DNA 3.15e-7 ARU 1.95e-8 ARU	Sat ARU 0.36 s; DT:67.891 s None DNA 1.47e-6 ARU 1.04e-7 ARU	Sat ARU 3.656 s; DT:94.369 s 0.159 s DNA 1.73e-5 ARU 3.76e-7 ARU	Sat ARU 3.75 s; DT:31.641 s None DNA 2.98e-5 ARU 5.25e-7 ARU	1.15e-5 ARU 0.375 s; DT:4.297 s None DNA 2.55e-6 ARU 1.23e-7 ARU	Sat ARU 0.313 s; DT:33.578 s None DNA 1.54e-6 ARU 1.25e-7 ARU

8:02:53 / SS	2 / VP & Walls	n			5.04e-6 ARU 0.328 s; DT:9.75 s None DNA 4.23e-7 ARU 5e-8 ARU	Sat ARU 0.234 s; DT:5.594 s None DNA 1.66e-6 ARU 1.48e-7 ARU	3.07e-5 ARU 0.344s; DT:5.656 s None DNA 1.99e-5 ARU 1.42e-6 ARU	Sat ARU 0.25 s None DNA 3.04e-5 ARU 7.82e-7 ARU	1.08e-5 ARU 0.391 s None DNA 2.49e-6 ARU 1.36e-7 ARU	Sat ARU 0.329 s DT:9.875 s None DNA 1.66e-6 ARU 1.33e-7 ARU
8:04:45 / CS	3 / VP & Walls	1.04e-6 ARU	Sat ARU 2 s None Y	4.84e-6 ARU 3.265 s None Y	2.56e-6 ARU 9.593 s 0.066 s Y	4.2e-5 ARU 9.671 s 0.066 s Y	Sat ARU 10.015 s None Y	Sat ARU 9.578 s None Y	2.54e-6 ARU None Y	1.67e-6 ARU None Y
					3.85e-7 ARU 2.75e-8 ARU	1.59e-6 ARU 1.11e-7 ARU	1.89e-5 ARU 8.31e-7 ARU	3.06e-5 ARU 5.84e-7 ARU	1.33e-7 ARU	1.18e-7 ARU

Table 4.4 (e): Shot Date 01/12/2006; Sample No. 4; 1064 nm light; Vacuum pressure  $4.875 \times 10^{-8}$  Torr; Energy: 70 mJ

Time / Mode (SS/CS)	Shot No. / Pos.	H2 (2)	N (14)	Mass 15 (15)	O (16)	H2O (18)	N2/CO (28)	O2 (32)	CO2 (44)
8:12:57 / SS	1 / c	n	n	n	n	n	n	n	n
8:14:58 / SS	2 / c	n	n	n	n	n	n	n	n
				4.47e-7 0.375 s WF Type: None DNA 3.36e-7 ARU 1.08e-8 ARU					1.06e-6 ARU 0.406 s WF Type: None DNA 1.61e-6 ARU 1.16e-7 ARU
8:18:10 / CS	4 / c	n	n	n	n	n	n	n	n
8:17:17 / SS	3 / c	n	n	n	n	n	n	n	n

Table 4.5: Shot Date 01/12/2006; Sample No. 5; 1064 nm light; Vacuum pressure  $4.875 \times 10^{-8}$  Torr; Energy: 70 mJ

Time / Mode (SS/CS)	Shot No. / Pos.	H2 (2)	N (14)	Mass 15 (15)	O (16)	H2O (18)	N2ICO (28)	O2 (32)	CO2 (44)
23:07:33 / SS	1 / s	n	n	n	n	n	n	n	n
23:09:09 / SS	2 / e	n	n	n	n	n	n	n	n
23:10:55 / SS	3 / w	n	n	n	n	n	n	n	n
23:13:13 / SS	4 / n	n	n	n	n	n	n	n	n
23:16:15 / SS	6 / c	n	n	n	n	n	n	n	n



23:14:26 / CS	5 / n				3.87e-7 ARU 9.64 s None N 3.35e-7 ARU 1.1e-8 ARU	1.96 e-6 ARU 8.719 s None N 1.42e-6 ARU 8.27e-8 ARU	n			4.e-6 ARU 10.11 s None N 1.47e-6 ARU 8.75e-8 ARU
					2.08e-6 ARU 12.156 s None N 3.33e-7 ARU 1.08e-8 ARU	2.29e-6 ARU 13.094 s None N 1.41e-6 ARU 8.43e-8 ARU	n	4.1e-5 ARU 10.906 s None N 3.07e-5 ARU 4.96e-7 ARU		2.42e-6 ARU 13 s None N 1.48e-6 ARU 7.97e-8 ARU
23:17:26 / CS	7 / c	Sat ARU 13.109 s None N 2.96e-5 ARU 5.27e-7 ARU	n	n						

Table 4.6: Shot Date 01/18/2006; Sample No. 6; 1064 nm light; Vacuum pressure  $1.5 \times 10^{-8}$  Torr; Energy: 70 mJ

Time / Mode (SS/CS)	Shot No. / Pos.	H2 (2)	N (14)	Mass 15 (15)	O (16)	H2O (18)	N2/CO (28)	O2 (32)	CO2 (44)
17:22:00 / SS	1 / e	n	n	4.1e-7 ARU 0.407 s None DNA 9.47e-8 ARU 7.81e-9 ARU	n	2.26e-6 ARU 0.422 s None DNA 1.21e-6 ARU 5.8e-8 ARU	n	n	2.5e-6 ARU 0.813 s None DNA 5.24e-7 ARU 2.25e-8 ARU
17:24:18 / SS	2 / w	n	n	1.65e-7 ARU 0.437 s None DNA 9.44e-8 ARU 6.67e-9 ARU	1.35e-6 ARU 0.453 s None DNA 2.91e-7 ARU 1.14e-8 ARU	n	n	n	1.1e-6 ARU 0.469 s None DNA 5.27e-7 ARU 1.55e-8 ARU

17:26:49 / SS	3 / s	n				1.08e-6 ARU 0.437 s None DNA 2.92e-7 ARU 1.15e-8 ARU	1.52e-7 ARU 0.422 s None DNA 9.42e-8 ARU 6.74e-9 ARU	3.43e-7 ARU 0.453 s None DNA 2.91e-7 ARU 9.85e-9 ARU	1.08e-6 ARU 0.437 s None DNA 2.92e-7 ARU 1.15e-8 ARU				1.17e-6 ARU 0.453 s None DNA 5.23e-7 ARU 1.16e-8 ARU
17:28:54 / SS	4 / n	n				9.95e-7 ARU 0.453 s None DNA 2.91e-7 ARU 9.85e-9 ARU	1.23e-7 ARU 0.421 s None DNA 9.38e-8 ARU 7.08e-9 ARU	9.95e-7 ARU 0.453 s None DNA 2.91e-7 ARU 9.85e-9 ARU	1.33e-5 ARU 0.406 s None DNA 1.12e-5 ARU 2.57e-7 ARU				9.66e-7 ARU 0.359 s None DNA 5.18e-7 ARU 1.63e-8 ARU
17:32:06 / SS	6 / c	n				1.24e-7 ARU 0.421 s None N 9.34e-8 ARU 6.19e-9 ARU	1.24e-7 ARU 0.421 s None N 9.34e-8 ARU 6.19e-9 ARU	1.24e-7 ARU 0.421 s None N 9.34e-8 ARU 6.19e-9 ARU					6.99e-7 ARU 0.469 s None N 5.2e-7 ARU 1.73e-8 ARU
17:30:19 / CS	5 / n	n				4.14e-7 ARU 8.844 s None N 2.93e-7 ARU 1.01e-8 ARU	1.34e-7 ARU 7.235 s None N 9.4e-8 ARU 6.3e-9 ARU	4.14e-7 ARU 8.844 s None N 2.93e-7 ARU 1.01e-8 ARU	1.77e-6 ARU 7.281 s None N 1.25e-6 ARU 8.31e-8 ARU				7.72e-7 ARU 8.328 s None N 5.2e-7 ARU 1.48e-8 ARU
17:33:56 / CS	7 / c	n											2.57e-7 ARU 6.735 s None N 1.95e-7 ARU 8.06e-9 ARU

Table 4.7(a): Shot Date 01/23/2006; Sample No. 7; 1064 nm light; Vacuum pressure  $6.37 \times 10^{-8}$  Torr; Energy: 70 mJ

Time / Mode (SS/CS)	Shot No. / Pos.	H2 (2)	N (14)	Mass 15 (15)	O (16)	H2O (18)	N2/CO (28)	O2 (32)	CO2 (44)
15:39:58 / SS	1 / e	n	n	3.92e-7 ARU 0.375 s None DNA 2.46e-7 ARU 1.9e-8 ARU	n	n	n	n	4.71e-6 ARU 0.359 s None DNA 3.86e-6 ARU 2.75e-7 ARU
15:44:53 / SS	3 / w	n	n	n	n	n	Sat ARU 0.343 s None DNA 4.08e-5 ARU 7.52e-7 ARU	n	n
15:48:02 / SS	5 / s	n	n	n	n	n	Sat ARU 0.359 s None DNA 4.08e-5 ARU 7.51e-7 ARU	n	n
15:51:11 / SS	7 / n	n	n	3.96e-7 ARU 0.313 s None DNA 2.46e-7 ARU 8.92e-9 ARU	n	n	n	n	4.58e-6 ARU 0.343 s None DNA 3.85e-6 ARU 1.58e-7 ARU
15:53:54 / SS	9 / c	n	n	n	n	n	n	n	n

15:41:10 / CS	2 / e	n	n	n	n	n	n	n	n	n	n	n	n
					2.89e-7 ARU 7.782 s None N								
15:45:37 / CS	4 / w	n	n	n	2.47e-7 ARU 7.32e-9 ARU								
								Sat ARU 0.359 s None N					
15:49:10 / CS	6 / s	n	n	n									
					2.99e-7 ARU 4.516 s None N								
15:52:25 / CS	8 / n	n	n	n	2.44e-7 ARU 9.08e-9 ARU								
					2.82e-7 ARU 5.468 s None N								
15:55:07 / CS	10 / c	n	n	n	2.45e-7 ARU 7.82e-9 ARU								

Table 4.7(b): Shot Date 01/23/2006; Sample No. 7; 1064 nm light; Vacuum pressure  $6.37 \times 10^{-8}$  Torr; Energy: 70 mJ

Time / Mode (SS/CS)	Shot No. / Pos.	H2 (2)	N (14)	Mass 15 (15)	O (16)	H2O (18)	N2/CO (28)	O2 (32)	CO2 (44)
16:16:03 / SS	1 / sw	n	n	2.96e-7 ARU 0.297 s None DNA 2.4e-7 ARU 1.71e-8 ARU	n	8.68e-6 ARU 0.312 s None DNA 6.63e-8 ARU 1.99e-7 ARU	Sat ARU 0.875 s None DNA 4.07e-5 ARU 7.84e-7 ARU	n	3.e-5 ARU 0.406 s None DNA 3.9e-6 ARU 1.55e-7 ARU
16:22:22 / SS	3 / nw	3.51e-5 ARU 0.312 s None DNA 2.65e-5 ARU 5.72e-9 ARU	n	3.13e-7 ARU 0.359 s None DNA 2.45e-7 ARU 9.18e-9 ARU	2.48e-6 ARU 0.265 s None DNA 1.55e-6 ARU 9.38e-8 ARU	n	n	n	n
16:26:26 / SS	5 / ne	n	n	n	n	n	n	n	n
16:30:29 / SS	7 / se	n	n	3.53e-7 ARU 0.375 s None DNA 2.46e-7 ARU 8.65e-9 ARU	2.3e-6 ARU 0.407 s None DNA 1.56e-6 ARU 9.89e-8 ARU	7.99e-6 ARU 9.985 s None N	Sat ARU 11.22 s None Y	n	4.7e-6 ARU 10.297 s None Y 3.97e-6 ARU 1.84e-7 ARU
16:17:31 / CS	2 / sw	Sat ARU 9.594 s None N 2.62e-5 ARU 4.89e-7 ARU	n	1.06e-6 ARU 9.953 s None N 2.43e-7 ARU 7.89e-9 ARU	2.94e-6 ARU 10.5 s None N 1.56e-6 ARU 1.02e-7 ARU	6.69e-6 ARU 4.89e-7 ARU	4.09e-5 ARU 7.07e-7 ARU	n	5.17e-6 ARU 0.406 s 2.203 s N 3.92e-6 ARU 1.68e-7 ARU
16:23:35 / CS	4 / nw	Sat ARU 28.735 s 18.0 s N 2.63e-5 ARU 4.98e-7 ARU	n	2.73e-7 ARU 0.297 s 2.141 s N 2.42e-7 ARU 7.99e-9 ARU	n	n	Sat ARU 0.312 s None N 4.07e-5 ARU 7.09e-7 ARU	n	n

Time / Mode (SS/CS)	Shot No. / Pos.	H2 (2)	N (14)	Mass 15 (15)	O (16)	H2O (18)	N2/CO (28)	O2 (32)	CO2 (44)
16:27:40 / CS	6 / ne	n	n	n	n	n	n	n	n
				3.53e-7 ARU 3.141 s None N	2.88e-6 ARU 0.312 s None N				9.76e-6 ARU) 0.406 s None N
16:31:47 / CS	8 / se	n	n	n	n	n	n	n	3.89e-6 ARU 1.49e-7 ARU

Table 4.8(a) & (b): Shot Date 01/25/2006; Sample No. 8; 1064 nm light; Vacuum pressure  $6.0 \times 10^{-8}$  Torr; Energy: 70 mJ

Time / Mode (SS/CS)	Shot No. / Pos.	H2 (2)	N (14)	Mass 15 (15)	O (16)	H2O (18)	N2/CO (28)	O2 (32)	CO2 (44)
15:51:05 / SS	1 / e	n	n	n	n	n	n	n	n
				3.72e-7 ARU 0.406 s None DNA	5.32e-6 ARU 0.438 s None DNA		8.16e-6 ARU 0.422 s None DNA	1.35e-7 ARU 0.406 s None DNA	8.2e-7 ARU 0.453 s None DNA
15:56:03 / SS	3 / w	n	n	n	n	n	n	n	5.84e-7 ARU 2.98e-8 ARU
				6.97e-8 ARU 5.21e-9 ARU	3.27e-7 ARU 1.58e-8 ARU		6.31e-6 ARU 1.67e-7 ARU	1.02e-7 ARU 6.04e-9 ARU	5.79e-7 ARU 1.82e-8 ARU
16:02:00 / SS	5 / s	n	n	n	n	n	n	n	n
									7.04e-7 ARU 0.468 s None DNA
									5.79e-7 ARU 1.65e-8 ARU

16:05:35 / SS	7 / n	1.13e-5 ARU 0.406 s None DNA 8.45e-6 ARU 3.65e-7 ARU	2.76e-6 ARU 0.5 s None DNA 7.77e-8 ARU 5.56e-9 ARU	8.25 e-7 ARU 0.344 s 0.159 s DNA 3.33e-7 ARU 9.95e-9 ARU	4.09e-6 ARU 0.453 s 0.034 s DNA 2.23e-6 ARU 1.25e-7 Toff	2.03e-5 ARU 0.344 s None DNA 6.21e-6 ARU 1.7e-7 ARU	2.21e-7 ARU 0.456 s None DNA 9.98e-8 ARU 6.17e-9 ARU	3/15e-5 ARU 0.468 s None DNA 5.72e-7 ARU 1.84e-8 ARU
16:09:14 / SS	9 / c	n	n	4.18e-7 ARU 0.453 s None DNA 3.34e-7 ARU 1.06e-8 ARU	n	n	n	6.84e-7 ARU 0.469 s None DNA 5.73e-7 ARU 1.77e-8 ARU
16:14:31 / SS	11 / sw	n	1.25e-7 ARU 0.422 s None DNA 7.62e-8 ARU 5.85e-9 ARU	n	n	n	n	6.56e-7 ARU 0.453 s None DNA 5.59e-7 ARU 1.61e-8 ARU
16:17:27 / SS	13 / nw	n	1.95e-5 ARU 0.36 s None DNA 8.12e-7 ARU 2.87e-8 ARU	2.91e-5 ARU 0.438 s None DNA 3.33e-7 ARU 1.05e-8 ARU	4.42e-6 ARU 0.469 s 0.206 s DNA 2.25e-6 ARU 1.29e-7 ARU	1.34e-5 ARU 0.469 s 0.112 s DNA 6.15e-6 ARU 1.69e-7 ARU	1.38e-7 ARU 0.453 s None DNA 9.7e-8 ARU 5.5e-9 ARU	1.97e-5 ARU 0.39 s None DNA 5.58e-7 ARU 1.78e-8 ARU
16:22:12 / SS	15 / ne	n	1.36e-7 ARU 0.344 s None DNA 8.66e-8 ARU 5.97e-9 ARU	n	n	n	n	1.04e-6 ARU 0.39 s None DNA 5.61e-7 ARU 1.61e-8 ARU
16:26:13 / SS	17 / se	n	1.52e-7 ARU 0.453 s None DNA 8.8e-8 ARU 6.2e-9 ARU	4.67e-7 ARU 0.438 s None DNA 3.38e-7 ARU 9.4e-9 ARU	n	n	n	7.89e-7 ARU 0.453 s None DNA 5.59e-7 ARU 1.63e-8 ARU

15:51:48 / CS	2 / e	n	n	n	n	n	n	n	n	n	n	n
		2.98e-5 ARU 10.75 s None Y	3.31e-7 ARU 10.64 s None Y	1.8e-6 ARU 10.734 s None Y	9.41e-6 ARU 10.125 s 0.173 s Y	9.41e-6 ARU 10.125 s 0.173 s Y	1.13e-5 ARU 8.578 s None Y	2.04e-7 ARU 10.187 s None Y	2.98e-5 ARU 10.75 s None Y			
15:57:38 / CS	4 / w	n	n	n	n	n	n	n	n	n	n	n
		8.59e-6 ARU 3.58e-7 ARU	6.95e-8 ARU 5.13e-9 ARU	3.26e-7 ARU 9.38e-9 ARU	2.24e-6 ARU 1.28e-7 ARU	2.24e-6 ARU 1.28e-7 ARU	6.3e-6 ARU 1.73e-7 ARU	1.02e-7 ARU 6.04e-9 ARU	8.59e-6 ARU 3.58e-7 ARU			
16:03:17 / CS	6 / s	n	n	n	n	n	n	n	n	n	n	n
		3.09e-5 ARU 3.516 s; DT:41.891 s RT:14.328 s 4.378 s Y	3.99e-7 ARU 9.766 s None Y	2.24e-6 ARU 10.859 s None Y	4.46e-6 ARU 10.875 s 0.175 s Y	4.46e-6 ARU 10.875 s 0.175 s Y	1.08e-5 ARU 9.328 s None Y	1.44e-7 ARU 10.344 s None Y	3.09e-5 ARU 3.516 s; DT:41.891 s RT:14.328 s 4.378 s Y			
16:06:57 / CS	8 / n	n	n	n	n	n	n	n	n	n	n	n
		8.38e-6 ARU 3.58e-7 ARU	7.66e-8 ARU 5.82e-9 ARU	3.29e-7 ARU 1.01e-8 ARU	2.24e-6 ARU 1.25e-7 ARU	2.24e-6 ARU 1.25e-7 ARU	6.17e-6 ARU 1.87e-7 ARU	9.77e-8 ARU 5.75e-9 ARU	8.38e-6 ARU 3.58e-7 ARU			
16:10:34 / CS	10 / c	n	n	n	n	n	n	n	n	n	n	n
		1.04e-5 ARU 6.188 s None N	1.15e-7 ARU 0.422 s None Y	3.8e-7 ARU 7.343 s None N	3.8e-7 ARU 7.343 s None N	3.8e-7 ARU 7.343 s None N	6.91e-6 ARU 8.344 s None N	1.04e-5 ARU 6.188 s None N	1.04e-5 ARU 6.188 s None N			
16:15:31 / CS	12 / sw	n	n	n	n	n	n	n	n	n	n	n
		9.29e-6 ARU 3.44e-7 ARU	7.78e-8 ARU 5.75e-9 ARU	3.29e-7 ARU 1e-8 ARU	3.54e-6 ARU 9.981 s None Y	3.54e-6 ARU 9.981 s None Y	1.32e-5 ARU 0.344 s None Y	1.16e-7 ARU 10.906 s None Y	9.29e-6 ARU 3.44e-7 ARU			
16:19:00 / CS	14 / nw	n	n	n	n	n	n	n	n	n	n	n
		1.06e-6 ARU 0.422 s None N	2.03e-7 ARU 0.5 s None N	1.83e-6 ARU 0.421 s None N	6.7e-6 ARU 0.343 s None N	6.7e-6 ARU 0.343 s None N	8.9e-6 ARU 0.359 s None N	9.79e-8 ARU 5.86e-9 ARU	1.06e-6 ARU 0.422 s None N			
16:23:30 / CS	16 / ne	n	n	n	n	n	n	n	n	n	n	n
		8.13e-7 ARU 2.71e-8 ARU	8.76e-8 ARU 5.91e-9 ARU	3.37e-7 ARU 1.09e-8 ARU	2.27e-6 ARU 1.25e-7 ARU	2.27e-6 ARU 1.25e-7 ARU	6.14e-6 ARU 1.78e-7 ARU	1.78e-7 ARU	8.13e-7 ARU 2.71e-8 ARU			



16:27:40 / CS	18 / se	n				1.13e-7 ARU 3.5 s None N					n	n
						8.8e-8 ARU 5.69e-9 ARU					n	n

Table 4.8(c) & (d). Shot Date 01/25/2006; Sample No. 8; 532 nm light; Vacuum pressure  $6.0 \times 10^{-8}$  Torr; Energy: 70 mJ

Time / Mode (SS/CS)	Shot No. / Pos.	H2 (2)	N (14)	Mass 15 (15)	O (16)	H2O (18)	N2/CO (28)	O2 (32)	CO2 (44)
18:25:46 / SS	1 / e	n	n	n	n	n	n	n	n
		2.35e-5 ARU 0.375 s 0.315 s DNA	Sat ARU 0.359 s None DNA	2.09e-5 ARU 0.343 s None DNA	Sat ARU 0.312 s None DNA	8.18e-6 ARU 0.422 s 0.159 s DNA	Sat ARU 0.375 s 0.159 s DNA	3.1e-7 ARU 0.422 s 0.05 s DNA	Sat ARU 0.422 s 0.05 s DNA
18:29:10 / SS	3 / w	n	n	n	n	n	n	n	n
		7.15e-6 ARU 3.65e-7 ARU	7.36e-7 ARU 2.37e-8 ARU	7.44e-8 ARU 5.2e-9 ARU	3.22e-7 ARU 9.71e-9 ARU	2.05e-6 ARU 1.26e-7 ARU	5.81e-6 ARU 1.71e-7 ARU	8.41e-8 ARU 5.06e-9 ARU	5.28e-7 ARU 1.67e-8 ARU
18:35:15 / SS	5 / s	n	n	n	n	n	n	n	n
		3.57e-5 ARU 0.359 s None DNA	5.65e-6 ARU 0.359 s None DNA	7e-7 ARU 0.375 s None DNA	7.62e-6 ARU 0.437 s None DNA	3.24e-6 ARU 0.531 s None DNA	1.17e-5 ARU 0.359 s None DNA	1.34e-7 ARU 0.453 s None DNA	7.17e-6 ARU 0.391 s None DNA
18:39:09 / SS	7 / n	n	n	n	n	n	n	n	n
		7.83e-6 ARU 4.07e-7 ARU	7.52e-7 ARU 2.19e-8 ARU	9.83e-8 ARU 6.82e-9 ARU	3.44e-7 ARU 1.1e-8 ARU	2.04e-6 ARU 1.18e-7 ARU	5.83e-6 ARU 1.61e-7 ARU	8.36e-8 ARU 5.02e-9 ARU	5.36e-7 ARU 1.6e-8 ARU
18:43:29 / SS	9 / c	n	n	n	n	n	n	n	n
		1.56e-5 ARU 0.453s None DNA	1.17e-6 ARU 0.391 s None DNA	1.75e-7 ARU 0.422 s 0.081 s DNA	1.1e-6 ARU 0.391 s None DNA	9.55e-6 ARU 0.406 s None DNA	4.03e-5 ARU 0.468 s None DNA		1.18e-6 ARU 0.39 s 0.143 s DNA
18:47:30 / SS	11 / sw	n	n	n	n	n	n	n	n
		7.66e-6 ARU 6.4e-7 ARU	7.55e-7 ARU 3.62e-8 ARU	9.79e-8 ARU 8.3e-9 ARU	3.43e-7 ARU 4.39e-8 ARU	2.07e-6 ARU 4.89e-7 ARU	5.93e-6 ARU 2.18e-7 ARU		5.39e-7 ARU 4.48e-8 ARU

		4.23e-5 ARU 0.328 s None DNA 7.97e-6 ARU 5.53e-7 ARU	3.03e-6 ARU 0.375 s None DNA 7.58e-7 ARU 2.52e-8 ARU	6.39e-7 ARU 0.406 s 0.05 s DNA 9.84e-8 ARU 6.8e-9 ARU	6.22e-6 ARU 0.219 s None DNA 3.39e-7 ARU 1.02e-8 ARU	3.18e-5 ARU 0.375 s None DNA 2.04e-6 ARU 1.23e-7 ARU	Sat ARU 0.296 s None DNA 5.82e-6 ARU 1.73e-7 ARU	5.92e-6 ARU 0.469 s 0.096 s DNA 5.42e-7 ARU 1.62e-8 ARU
18:51:21 / SS	13 / nw			4.54e-7 ARU 0.359 s None DNA 9.95e-8 ARU 9.47e-7 ARU	4.44e-7 ARU 0.453 s 0.206 s DNA 3.44e-7 ARU 2.81e-8 ARU	2.5e-6 ARU 0.421 s 0.066 s DNA 2.07e-6 ARU 1.75e-7 ARU	7.98e-6 ARU 0.375 s None DNA 5.86e-6 ARU 2.32e-7 ARU	1.21e-7 ARU 0.422 s None DNA 8.3e-8 ARU 5.43e-9 ARU
18:56:11 / SS	15 / ne							
18:59:32 / SS	17 / se			8.95e-8 ARU 0.953 s None N 7.42e-8 ARU 4.86e-9 ARU	3.67e-7 ARU 0.359 s None N 3.22e-7 ARU 9.5e-9 ARU			
18:27:10 / CS	2 / e			1.14e-5 ARU 12.672 s None Y 7.76e-8 ARU 6.73e-9 ARU	8.51e-6 ARU 12.703 s None Y 3.26e-7 ARU 1.15e-8 ARU	4.25e-6 ARU 10.672 s None Y 2.08e-6 ARU 1.31e-7 ARU	1.01e-5 ARU 12.094 s None Y 5.89e-6 ARU 1.88e-7 ARU	3.31e-6 ARU 11.672 s None Y 5.38e-7 ARU 1.81e-8 ARU
18:31:38 / CS	4 / w							
18:37:28 / CS	6 / s							

18:40:25 / CS	8 / n	1.04e-5 ARU 7.781 s 10.11 s Y	7.8e-6 ARU 3.94e-7 ARU	1.05e-6 ARU 10.328 s None N	7.55e-7 ARU 2.43e-6 ARU	2.17e-7 ARU 10.703 s None Y	1.01e-7 ARU 5.97e-9 ARU	3.45e-7 ARU 1.17e-8 ARU	9.42e-7 ARU 10.343 s 0.207 s Y	4.05e-6 ARU 9.125 s None Y	2.04e-6 ARU 1.26e-7 ARU	5.58e-6 ARU 1.73e-7 ARU	8.34e-8 ARU 5.49e-9 ARU	1.15e-7 ARU 10.328 s None Y	1.08e-5 ARU 10.36 s None Y	4.5e-6 ARU 10.797 s None Y	5.4e-7 ARU 1.52e-8 ARU
18:45:11 / CS	10 / c	n	n	n	n	n	n	n	n	n	n	n	n	n	n	n	n
18:48:53 / CS	12 / sw	1.79e-5 ARU 10.735 s None Y	7.6e-6 ARU 4e-7 ARU	6.31e-6 ARU 9.891 s None Y	9.91e-8 ARU 7.34e-9 ARU 2.55e-8 ARU	2.46e-6 ARU 9.891 s: None Y	9.67e-8 ARU 6.62e-9 ARU	3.33e-7 ARU 1.03e-8 ARU	9.64e-6 ARU 9.906 s None Y	1.27e-5 ARU 8.86 s 0.222 s Y	2.01e-6 ARU 1.23e-7 ARU	5.78e-6 ARU 1.7e-7 ARU	8.2e-8 ARU 5.37e-9 ARU	1.65e-5 ARU 10.671 s None Y	3.87e-6 ARU 8.172 s None Y	5.38e-7 ARU 1.79e-8 ARU	
18:52:56 / CS	14 / nw	7.8e-6 ARU 4.39e-7 ARU	7.63e-7 ARU 2.55e-8 ARU	9.91e-8 ARU 7.34e-9 ARU	7.63e-7 ARU 2.55e-8 ARU	9.91e-8 ARU 7.34e-9 ARU	9.67e-8 ARU 6.62e-9 ARU	3.33e-7 ARU 1.03e-8 ARU	9.64e-6 ARU 9.906 s None Y	1.27e-5 ARU 8.86 s 0.222 s Y	2.06e-6 ARU 1.49e-7 ARU	5.83e-6 ARU 1.69e-7 ARU	8.26e-8 ARU 5.3e-9 ARU	8.26e-8 ARU 5.3e-9 ARU	8.26e-8 ARU 5.3e-9 ARU	5.47e-7 ARU 1.95e-8 ARU	1.05e-6 ARU 6.735 s None N
18:57:40 / CS	16 / ne	7.56e-6 ARU 3.86e-7 ARU	7.56e-6 ARU 3.86e-7 ARU	9.7e-8 ARU 2.19e-8 ARU	9.7e-8 ARU 2.19e-8 ARU	9.7e-8 ARU 2.19e-8 ARU	3.37e-7 ARU 1.03e-8 ARU	3.37e-7 ARU 1.03e-8 ARU	3.37e-7 ARU 1.03e-8 ARU	2.02e-6 ARU 1.33e-7 ARU	8.04e-6 ARU 1.54e-7 ARU	8.04e-6 ARU 1.54e-7 ARU	8.04e-8 ARU 5.68e-9 ARU	8.04e-8 ARU 5.68e-9 ARU	8.04e-8 ARU 5.68e-9 ARU	5.38e-7 ARU 1.54e-8 ARU	
19:00:37 / CS	18 / se	n	n	n	n	n	n	n	n	n	n	n	n	n	n	n	n

Table 4.9(a) & (b): Shot Date 01/26/2006; Sample No. 9; 532 nm light; Vacuum pressure  $6.0 \times 10^{-8}$  Torr; Energy: 70 mJ

Time / Mode (SS/CS)	Shot No. / Pos.	H2 (2)	N (14)	Mass 15 (15)	O (16)	H2O (18)	N2/CO (28)	O2 (32)	CO2 (44)
15:10:41 / SS	1 / e	6.56e-6 ARU			2.34e-7 ARU	1.44e-6 ARU			5.11e-7 ARU
		0.484 s			0.485 s	0.468 s			0.453 s
		None			None	None			None
		DNA			DNA	DNA			DNA
		5.64e-6 ARU			1.94e-7 ARU	5.54e-7 ARU			4.09e-7 ARU
		2.25e-7 ARU			6.53e-9 ARU	1.6e-8 ARU			1.85e-8 ARU
15:15:53 / SS	3 / w	1.1e-5 ARU	1.73e-6 ARU	1.43e-7 ARU	8.76e-7 ARU	5.6e-6 ARU	Sat ARU	4.87 e-6 ARU	1.33e-6 ARU
		0.422s	0.468 s	0.406 s	0.407 s	0.469 s	0.453 s	0.291 s	0.438 s
		None	None	0.253 s	0.034 s	None	None	None	0.128 s
		DNA	DNA	NDA	DNA	DNA	DNA	DNA	DNA
		5.76e-6 ARU	7.28e-7 ARU	5.32e-8 ARU	1.95e-7 ARU	5.59e-7 ARU	5.08e-6 ARU	5.39e-8 ARU	4.03e-7 ARU
		2.35e-7 ARU	2e-8 ARU	4.36e-9 ARU	7.3e-9 ARU	1.66e-8 ARU	1.71e-7 ARU	5.45e-9 ARU	1.34e-8 ARU
15:21:34 / SS	5 / s			1.12e-7 ARU					7.73e-7 ARU
				0.468 s					0.453 s
				None					None
				DNA					DNA
				5.71e-8 ARU					4e-7 ARU
				5.25e-9 ARU					3.6e-8 ARU
15:24:43 / SS	7 / n	7.53e-6 ARU			2.78e-7 ARU				5.12e-7 ARU
		0.485 s			0.484 s				0.438 s
		None		None					None
		DNA		DNA					DNA
		5.92e-6 ARU			1.96e-7 ARU				3.93e-7 ARU
		2.55e-7 ARU			7.56e-9 ARU				1.11e-8 ARU

15:28:31 / SS	9 / c					7.5e-8 ARU 0.484 s None DNA 5.47e-8 ARU 4.78e-9 ARU											6.73e-7 ARU 0.438 s None DNA 3.91e-7 ARU 1.18e-8 ARU		
						8.88e-7 ARU 0.469 s None DNA 7.25e-7 ARU 1.89e-8 ARU												4.95e-7 ARU 0.453 s None DNA 3.88e-7 ARU 1.08e-8 ARU	
15:33:30 / SS	11 / sw					7.36e-6 ARU 0.5 s None DNA 5.83e-6 ARU 2.23e-7 ARU												4.73e-7 ARU 0.437 s None DNA 3.85e-7 ARU 1.09e-8 ARU	
						9.63e-6 ARU 0.406 s None DNA 5.77e-6 ARU 2.19e-7 ARU												1.12e-6 ARU 0.453 s None DNA 3.87e-7 ARU 1.08e-8 ARU	
15:36:50 / SS	13 / nw																		8.85e-7 ARU 0.438 s None DNA 3.87e-7 ARU 1.08e-8 ARU
15:42:28 / SS	15 / ne																		5e-7 ARU 10.234 s None N 4.09e-7 ARU 1.28e-8 ARU
15:46:25 / SS	17 / se																		
15:11:49 / CS	2 / e																		

15:17:28 / CS		3.9e-5 ARU 8.469 s: 0.284 s Y	5.46e-6 ARU 7.812 s 0.284 s Y	5.18e-6 ARU 8.404 s None Y	1.47e-5 ARU 8.875 s None Y	1.01e-5 ARU 7.984 s 0.128 s Y	Sat ARU 8.766 s None Y	1.93e-7 ARU 8.859 0.128 s Y	Sat ARU 9.906 s None Y
	4 / w	5.79e-6 ARU 2.18e-7 ARU	7.3e-7 ARU 1.9e-8 ARU	5.47e-8 ARU 4.89e-9 ARU 8e-8 ARU 9.172 s None N	1.97e-7 ARU 7.35e-9 ARU 2.38e-7 ARU 8.156 s None N	5.74e-7 ARU 2.89e-8 ARU	5.09e-6 ARU 1.7e-7 ARU	5.4e-8 ARU 5.74e-9 ARU	4.01e-7 ARU 1.38e-8 ARU 4.66e-7 ARU 9.14 s None N
15:22:56 / CS	6 / s			5.5e-8 ARU 4.42e-9 ARU 7.58e-8 ARU 8.078 s None N	1.97e-7 ARU 7.67e-9 ARU 2.31e-7 ARU 7.547 s None N				3.96e-7 ARU 1.27e-8 ARU 4.6e-7 ARU 9.688 s None N
15:26:36 / CS	8 / n			5.85e-6 ARU 2.34e-7 ARU 7.81e-8 ARU 8.094 s None N	1.95e-7 ARU 7.02e-9 ARU 2.34e-7 ARU 5.969 s None N				3.92e-7 ARU 1.07e-8 ARU 4.44e-7 ARU 3.64 s None N
15:29:56 / CS	10 / c			5.45e-8 ARU 4.4e-9 ARU 1.31e-7 ARU 8.094 s None N	1.95e-7 ARU 6.32e-9 ARU 3.09e-7 ARU 8.078 s None N				3.88e-7 ARU 1.06e-8 ARU 5.03e-7 ARU 9.687 s None N
15:34:47 / CS	12 / sw	7.62e-6 ARU 10.75 s None N		5.44e-8 ARU 4.33e-9 ARU 8.72e-8 ARU 10.328 s None N	1.94e-7 ARU 7.69e-9 ARU 2.62e-7 ARU 8.094 s None N	5.58e-7 ARU 1.34e-8 ARU	5.04e-7 ARU 1.73e-7 ARU		3.88e-7 ARU 1.1e-8 ARU 4.73e-7 ARU 9.688 s None N
15:38:02 / CS	14 / nw			5.37e-8 ARU 4.42e-9 ARU	1.94e-7 ARU 6.86e-9 ARU	5.54e-7 ARU 1.64e-8 ARU			3.86e-7 ARU 1.14e-8 ARU

						2.35e-7 ARU					4.33e-7 ARU
						6.953 s					5.875 s
						None					None
						N					N
						1.92e-7 ARU					3.9e-7 ARU
15:44:02 / CS	16 / ne	n				5.84e-9 ARU			n		5.66e-8 ARU
						2.56e-7 ARU					4.36e-7 ARU
						7.547 s					6.906 s
						None					None
						N					N
						1.92e-7 ARU					3.85e-7 ARU
15:47:52 / CS	18 / se	n				6.99e-9 ARU			n		1.12e-8 ARU

Table 4.9(c) & (d): Shot Date 01/26/2006; Sample No. 9; 1064 nm light; Vacuum pressure  $6.0 \times 10^{-8}$  Torr; Energy: 70 mJ

Time / Mode (SS/CS)	Shot No. / Pos.	H2 (2)	N (14)	Mass 15 (15)	O (16)	H2O (18)	N2/CO (28)	O2 (32)	CO2 (44)
16:36:45	1 / e	n	n	n	n	n	n	n	n
					2.38e-7 ARU	9.36e-7 ARU	9.36e-6 ARU	1.46e-7 ARU	4.29e-7 ARU
					0.468 s	0.469 s	0.484 s	0.359 s	0.469 s
					0.097 s	None	None	None	0.268 s
					DNA	DNA	DNA	DNA	DNA
	3 / w	n	n	n	1.82e-7 ARU	5.88e-7 ARU	6.41e-6 ARU	5.85e-8 ARU	3.65e-7 ARU
16:40:34 / SS					6.85e-9 ARU	1.35e-8 ARU	2.06e-7 ARU	5.43e-9 ARU	1.07e-8 ARU
16:45:11 / SS	5 / s	n	n	n	n	n	n	n	n
					2.25e-7 ARU				
					0.469 s				
					None				
					DNA				
16:48:29 / SS	7 / n	n	n	n	1.84e-7 ARU	6.74e-9 ARU			

16:51:31 / SS	9 / c	n	n	n	n	n	n	n	2.27e-7 ARU 0.469 s None DNA 1.84e-7 ARU 6.68e-9 ARU	1.03e-6 ARU 0.422 s None DNA 5.89e-7 ARU 2.98e-8 ARU	3.47e-5 ARU 0.422 s None DNA 6.44e-6 ARU 1.64e-7 ARU	n	n	n	n
16:55:31 / SS	11 / sw	n	n	n	n	n	n	n	2.2e-7 ARU 0.532 s None DNA 1.83e-7 ARU 7.34e-9 ARU	7.8e-6 ARU 0.422 s None DNA 6.34e-6 ARU 1.96e-7 ARU	n	n	n	n	n
16:58:59 / SS	13 / nw	n	n	n	n	n	n	n	2.33e-7 ARU 0.469 s None DNA 1.85e-7 ARU 7.19e-9 ARU	5.11e-7 ARU 0.422 s None DNA 5.83e-7 ARU 1.68e-8 ARU	n	n	n	n	4.23e-7 ARU 0.469 s None DNA 3.61e-7 ARU 1.04e-8 ARU
17:01:57 / SS	15 / ne	n	n	n	n	n	n	n	n	n	n	n	n	n	n
17:05:25 / SS	17 / se	n	n	n	n	n	n	n	n	n	n	n	n	n	n
16:37:59 / CS	2 / e	n	n	n	n	n	n	n	n	n	n	n	n	n	n



		7.4e-6 ARU 4.641 s; DT:82.297 s RT:56.788 s 9.813 s N		1.32e-7 ARU 6.954 s 0.737s N	4.99e-7 ARU 3.172 s 0.644s N	1.89e-6 ARU 4.219 s 0.503 s N	8.27e-6 ARU 1.031 s None N	1.1e-6 ARU 6.422 s None N
16:41:41 / CS	4 / w	5.6e-6 ARU 2.53e-7 ARU		4.97e-8 ARU 4.71e-9 ARU	1.83e-7 ARU 6.89e-9 ARU	5.91e-7 ARU 1.69e-8 ARU	6.38e-6 ARU 2.08e-7 ARU	3.65e-7 ARU 1.04e-8 ARU
16:46:34 / CS	6 / s							
16:49:58 / CS	8 / n							
16:52:34 / CS	10 / c							
16:56:36 / CS	12 / sw			2.28e-7 ARU 0.469 s None N	8.28e-7 ARU 0.469 s None N	5.88e-7 ARU 1.56e-8 ARU	4.13e-7 ARU 0.39 s None N	3.62e-7 ARU 1.05e-8 ARU
17:00:05 / CS	14 / nw							
17:03:02 / CS	16 / ne							
17:06:43 / CS	18 / se							

Table 4.10(a): Shot Date 01/28/2006; Chamber Walls; 532 nm light; Vacuum pressure  $4.875 \times 10^{-8}$  Torr; Energy: 70 mJ

Time / Mode (SS/CS)	Shot No. / Pos.	H2 (2)	N (14)	Mass 15 (15)	O (16)	H2O (18)	N2/CO (28)	O2 (32)	CO2 (44)
		3.37e-5 ARU 0.422 s; DT:27.11 s 0.487 s DNA	2.43e-6 ARU 0.375s; DT:7.64 s 0.175 s DNA	3.63e-5 ARU 0.375 s; DT:24.781 s None DNA	2.46e-6 ARU 0.175 s; DT:21.922 s 0.175 s DNA	2.84e-5 ARU 0.422 s; DT:73.985 s 0.018 s DNA	Sat ARU 0.422 s; DT:4.7 s 0.018 s DNA	1.89e-6 ARU 0.375 s; DT:5.391 s None DNA	Sat ARU 0.421 s; DT:9.844 s None DNA
18:38:09 / SS	1 / VP & P& Walls	3.04e-6 ARU 1.77e-7 ARU	4.25e-7 ARU 2.69e-8 ARU	2.75e-8 ARU 5.04e-9 ARU	1.13e-7 ARU 1.12e-6 ARU	3.09e-7 ARU 8.01e-9 ARU	4.01e-6 ARU 1.78e-7 ARU	1.45e-8 ARU 9.66e-9 ARU	3.19e-7 ARU 2.46e-8 ARU

		1.3e-5 ARU 0.453 s; DT: 7.125 s None DNA	1.21e-6 ARU 0.391 s; DT:2.297 s 0.087 s DNA	2.52e-7 ARU 0.375 s; DT:8.422 s 0.253 s DNA	1.22e-6 ARU 0.297 s; DT:10.938 s 0.253 s DNA	1.04e-5 ARU 0.406 s; DT:17.032 s None DNA	Sat ARU 0.468 s; DT:1.25 s None DNA	1.73e-5 ARU 0.39 s; DT:8.25 s None DNA	Sat ARU 0.391 s; DT:10.375 s None DNA
18:39:44 / SS	2 / VP & P & Walls	3.51e-6 ARU 4.35e-7 ARU	4.5e-7 ARU 2.35e-8 ARU	3.52e-8 ARU 9.63e-9 ARU	1.28e-7 ARU 1.75e-8 ARU	4.68e-7 ARU 1.78e-7 ARU	4.18e-6 ARU 2.32e-7 ARU	1.46e-8 ARU 3.32e-9 ARU	3.32e-7 ARU 1.34e-8 ARU
		Sat ARU 6.859 s; DT:17.422 s 1.317 s Y	2.65e-6 ARU 9.172 s; DT:5.469 s 0.473 s Y	4.31e-6 ARU 10.219 s; DT:14.735 s 0.113s Y	3.78e-5 ARU 10.157 s; DT:9.984 s 0.113 s Y	2.69e-5 ARU 9.374 s; DT:34.969 s 0.317 s Y	2.52e-5 ARU 10.171 s 0.317 s Y	6.02e-6 ARU 9.703 s 0.270 s Y	4.22e-5 ARU 10.126 s; DT:10.375 s None Y
18:41:19 / CSP	3 / VP & Walls	3.31e-6 ARU 1.84e-7 ARU	4.43e-7 ARU 1.43e-8 ARU	3.16e-8 ARU 5.03e-9 ARU	1.23e-7 ARU 7.9e-9 ARU	3.9e-7 ARU 4.18e-8 ARU	4.11e-6 ARU 1.03e-7 ARU	1.47e-8 ARU 3.6e-9 ARU	3.31e-7 ARU 1.11e-8 ARU

Table 4.10(b): Shot Date 01/29/2006; Chamber Walls; 532 nm light; Vacuum pressure  $6.75 \times 10^{-8}$  Torr; Energy: 70 mJ

Time / Mode (SS/CS)	Shot No. / Pos.	H2 (2)	N (14)	Mass 15 (15)	O (16)	H2O (18)	N2/CO (28)	O2 (32)	CO2 (44)
17:43:10 / SS1	VP&W	Sat ARU 0.407 s 0.222 s DNA	Sat ARU 0.422 s None DNA	2.75e-5 ARU 0.343 s; DT: 25 s 0.331 s DNA	Sat ARU 0.437 s; None DNA	2.46e-5 ARU 0.359 s 0.222 s DNA	Sat ARU 0.828 s 0.113 s DNA	2.75e-7 ARU 0.39 s 0.066 s DNA	Sat ARU 0.828 s 0.066 s DNA
17:43:10 / SS1	VP&W	4.79e-6 ARU 2.2e-7 ARU	6.2e-7 ARU 2.65e-8 ARU	4.81e-8 ARU 4.72e-9 ARU	3.12e-7 ARU 1.7e-8 ARU	1.64e-6 ARU 9.94e-8 ARU	5.71e-6 ARU 2.05e-7 ARU	8.05e-9 ARU 5.57e-9 ARU	9.47e-7 ARU 5.22e-8 ARU
17:44:34 / SS2	VP&W	3.46e-5 ARU 0.375 s 0.081 s DNA	3.52e-6 ARU 0.328 s 0.128 s DNA	1.2e-6 ARU 0.39 s, DT: 8 s 0.222 s DNA	1.53e-5 ARU 0.437 s 0.128 s DNA	1.3e-5 ARU 0.313 s 0.081 s DNA	Sat ARU 0.469 s None DNA	3.76e-7 ARU 0.391 s None DNA	Sat ARU 0.469 s None DNA
17:44:34 / SS2	VP&W	5.29e-6 ARU 3.5e-7 ARU	6.3e-7 ARU 1.61e-8 ARU	5.56e-8 ARU 5.87e-9 ARU	3.25e-7 ARU 9.58e-9 ARU	1.8e-6 ARU 1.2e-7 ARU	5.81e-6 ARU 2.05e-7 ARU	7.56e-9 ARU 3.17e-9 ARU	9.53e-7 ARU 2.95e-8 ARU

	Sat ARU 9.984 s 0.207 s Y	4.61e-6 ARU 10.047 s None Y	5.56e-6 ARU 10.5 s None Y	1.59e-5 ARU 9.594 s None Y	4.06e-5 8.641 s 0.113 s Y	Sat ARU 10.516 s 0.17s Y	2.13e-7 ARU 9.172 s None Y	Sat ARU 10.063 s None Y
17:47:37 / CS3 / VP&W	5.13e-6 ARU 2.36e-7 ARU	6.31e-7 ARU 1.69e-8 ARU	5.28e-8 ARU 5.06e-9 ARU	3.26e-7 ARU 9.79e-9 ARU	1.76e-6 ARU 1.1e-7 ARU	5.8e-6 ARU 1.91e-7 ARU	7.93e-9 ARU 3.1e-9 ARU	9.64e-7 ARU 2.74e-8 ARU

Table 4.10(c): Shot Date 01/29/2006; Chamber Walls (Faraday Cup mode); 532 nm light;  
Vacuum pressure  $6.75 \times 10^{-8}$  Torr; Energy: 70 mJ

Time / Mode (SS/CS)	Shot No. / Pos.	H2 (2)	N (14)	Mass 15 (15)	O (16)	H2O (18)	N2/CO (28)	O2 (32)	CO2 (44)
17:56:23 / SS1 / VP&W		7.48e-7 ARU 0.469 s DT:166.25 s None DNA	5.9e-8 ARU 0.485 s; D:29.156 s 0.409 s DNA	6.4e-8 ARU 0.438 s; DT:21.64 s 0.034 s DNA	2.0e-7 ARU 1.031 s; DT:64.719 s None DNA	3.78e-7 ARU 0.484 s; DT:199.641 s 0.269 s DNA	5.28e-6 ARU 0.984 s; DT:93.641 s 0.269 s DNA	3.05e-9 ARU 0.484 s; DT:2.969 s 0.144 s DNA	1.97e-6 ARU 0.422 s; DT:51.109 s 0.144 s DNA
17:56:23 / SS1 / VP&W		3.37e-9 ARU 1.88e-10 ARU	1.15e-9 ARU 1.05e-10 ARU	3.14e-10 ARU 1.53e-10 ARU	7.38e-10 ARU 1.59e-10 ARU	1.92e-10 ARU	1.35e-8 ARU 2.48e-10 ARU	2.35e-10 ARU 1.8e-10 ARU	3.06e-9 ARU 2.25e-10 ARU
		2.5e-7 ARU 0.437 s; DT:49.96 s None DNA	5.22e-8 ARU 0.562 s; DT:4.532 s 0.066 s DNA	2.7e-8 ARU 0.406 s; DT:9.172 s 0.285s DNA	3.01e-8 ARU 0.563 s; DT:9.078 s 0.128 s DNA	3.04e-7 ARU 0.5 s; DT:50.61 s None DNA	4.49e-6 ARU 0.516 s; DT:16.578 s None DNA	9.79e-8 ARU 0.485 s; None DNA	2.64e-6 ARU 0.485 s; DT:10.843 s None DNA
18:00:11 / SS2 / VP&W		5.44e-9 ARU 1.65e-9 ARU	1.29e-9 ARU 2.31e-10 ARU	1.81e-10 ARU	3.62e-10 ARU	9.04e-9 ARU 4.96e-9 ARU	1.56e-8 ARU 2.06e-9 ARU	2.44e-10 ARU 1.86e-10 ARU	3.59e-9 ARU 5.22e-10 ARU
		1.02e-7 ARU 9.031 s; DT:73.781 s 0.285 s Y	4.38e-8 ARU 9.954 s; DT:4.487 s None Y	2.4e-8 ARU 9.5 s; DT:7.784 s 0.019 s Y	1.73e-7 ARU 9.594 s; DT:23.312 s None Y	2.1e-7 ARU 9.594 s; DT:143.016 s 0.222s Y	1.13e-6 ARU 0.144s; DT:34.657 s 0.144 s Y	1.34e-7 ARU 8.969 s 0.144 s 2.26e-10 ARU	2.3e-6 ARU 9.546 s; DT:37.485 s 0.132 s Y
18:04:26 / CS3 / VP&W		4.24e-9 ARU	1.19e-9 ARU	3.85e-10 ARU	9.3e-10 ARU	5.76e-9 ARU	1.43e-8 ARU	1.88e-10 ARU	3.27e-9 ARU

	5.78e-10 ARU	1.41e-10 ARU	1.235e-10 ARU	1.949e-10 ARU	1.09e-9 ARU	6.91e-10 ARU	2.87e-10 ARU
--	--------------	--------------	---------------	---------------	-------------	--------------	--------------

Table 4.11: Shot Date 01/29/2006; Viewport; 532 nm light; Vacuum pressure  $6.75 \times 10^{-8}$  Torr; Energy: 70 mJ

Time / Mode (SS/CS)	Shot No. / Pos.	H2 (2)	N (14)	Mass 15 (15)	O (16)	H2O (18)	N2/CO (28)	O2 (32)	CO2 (44)
17:22:12 / SS	1 / VP	n	n	4.46e-8 ARU 0.468 s None DNA 4.9e-8 ARU 3.95e-9 ARU	4.19e-7 ARU 0.353 s 0.175 s DNA 3.18e-7 ARU 8.61e-9 ARU	n	7.07e-6 ARU 0.469 s None DNA 5.77e-6 ARU 1.73e-7 ARU	2.51e-8 ARU 0.453 s None DNA 8.19e-9 ARU 3.5e-9 ARU	1.23e-6 ARU 0.408 s None DNA 1.0e-6 ARU 2.73e-8 ARU
		6.68e-6 ARU 0.344 s None DNA 4.79e-6 ARU 2.16e-7 ARU		1.92e-7 ARU 0.422 s 0.144 s DNA 4.92e-8 ARU 4.87e-9 ARU	6.96e-7 ARU 0.375 s None DNA 3.18e-7 ARU 8.31e-9 ARU	n	7.72e-6 ARU 0.344 s None DNA 5.79e-6 ARU 1.8e-7 ARU		1.45e-6 ARU 0.359 s None DNA 9.9e-7 ARU 2.45e-8 ARU
17:23:59 / SS	2 / VP	n	n	1.59e-7 ARU 10.469 s None Y 4.86e-8 ARU 4.82e-9 ARU	4.86e-7 ARU 9.635 s None Y 3.19e-7 ARU 9.2e-9 ARU	n	6.91e-6 ARU 9.938 s None N 5.78e-6 ARU 1.97e-7 ARU		1.24e-6 ARU 9.922 s None N 9.88e-7 ARU 3.85e-8 ARU
17:25:59 / CS	3 / VP	n	n	4.81e-6 ARU 2.19e-7 ARU	6.32e-7 ARU 1.89e-8 ARU	n			

Table 4.12 The partial pressure gains due to the electron multiplier mode are determined based on background partial pressures prior to laser illuminations both in Faraday cup mode and in electron multiplier mode.

Sample	Measurement Mode or Gain	H2 (2)	N (14)	Mass 15 (15)	O (16)	H2O (18)	N2/CO (28)	O2 (32)	CO2 (44)
1	Faraday Cup Mode (Torr)	2.01E-08	3.41E-09	1.08E-09	2.93E-09	4.36E-08	8.91E-08	6.50E-09	6.82E-09
	Electron Multiplier Mode (ARU)	3.35E-05	2.01E-06	3.98E-07	1.65E-06	2.13E-05	2.99E-05	1.95E-06	1.65E-06
	Gain	1666.66	589.44	368.51	563.13	488.53	335.57	300	242.64
6	Faraday Cup Mode (Torr)	5.09E-09	1.56E-09	5.50E-10	7.30E-10	2.86E-09	3.68E-08	9.59E-10	2.55E-09
	Electron Multiplier Mode (ARU)	9.73E-06	8.31E-07	9.47E-08	2.89E-07	1.21E-06	1.13E-05	1.95E-07	5.24E-07
	Gain	1911.59	532.69	172.18	395.89	423.07	307	203.33	205.49
7	Faraday Cup Mode (Torr)	1.45E-08	4.38E-09	8.73E-10	2.63E-09	1.56E-08	1.39E-07	7.58E-09	1.68E-08
	Electron Multiplier Mode (ARU)	2.62E-05	2.59E-06	2.46E-07	1.53E-06	6.81E-06	4.09E-05	1.85E-06	3.86E-06
	Gain	1806.8	591.32	281.78	581.75	436.54	294.24	244.06	229.76
9	Faraday Cup Mode (Torr)	3.44E-09	1.29E-09	3.34E-10	4.90E-10	1.33E-09	1.83E-08	3.68E-10	1.21E-09
	Electron Multiplier Mode (ARU)	5.49E-06	6.93E-07	4.99E-07	1.81E-07	5.84E-07	6.34E-06	5.81E-08	3.64E-07
	Gain	1595.93	537.21	134.43	369.38	439.09	346.45	157.88	300.8

Table 4.13 Total number of emitted molecules from the RGA Data

(a) Plastic 6: Shot 1: Energy: 70 mJ, Infrared (1064 nm)

Peaks detected	Change in Partial pressure at $t_1$ (Torr)	Change in Partial pressure at $t_2$ (Torr)
Mass 15	5.37e-10	1.83e-9
Water 18	2.74e-9	2.48e-9
CO 2	2.6e-9	9.61e-9
Total number of emitted molecules ( $n_T$ )	9.562e6	2.244e7

(b) Plastic 6 Shot 2: Energy: 70 mJ, Infrared (1064 nm)

Peaks detected	Change in Partial pressure at $t_1$ (Torr)	Change in Partial pressure at $t_2$ (Torr)
Mass 15	0	3.69e-11
O 16	0	2.67e-9
CO 2	0	2.78e-9
Total number of emitted molecules ( $n_T$ )	0	8.929e6

(c) Plastic 6 Shot 3: Energy: 70 mJ, Infrared (1064 nm)

Peaks detected	Change in Partial pressure at $t_1$ (Torr)	Change in Partial pressure at $t_2$ (Torr)
Mass 15	9.17e-11	3.35e-10
O 16	3.03e-11	1.99e-9
CO 2	0	1.57e-14
Total number of emitted molecules ( $n_T$ )	1.98e5	7.891e6

(d) Plastic 8 Shot 3: Energy: 70 mJ, Infrared (1064 nm)

Peaks detected	Change in Partial pressure at $t_1$ (Torr)	Change in Partial pressure at $t_2$ (Torr)
Mass 15	0	2.78e6
O 16	5.9e-14	5.9e-14
N2 / CO 28	1.58e-15	2.25e-14
O2 32	0	6.5e-16
CO2 44	0	5.05e-14
Total number of emitted molecules ( $n_T$ )	1.97e7	4.591e7

(e) Plastic 8 Shot 7: Energy: 70 mJ, Infrared (1064 nm)

Peaks detected	Change in Partial pressure at $t_1$ (Torr)	Change in Partial pressure at $t_2$ (Torr)
Hydrogen 2	0	1.7e-9
Mass 15	0	1.52e-8
O 16	2.37e-11	1.16e-9
Water 18	3.49e-9	3.49e-9
N2 / CO 28	4.86e-11	3.43e-8
O2 32	3.65e-11	4.8e-10
CO2 44	1.07e-7	4.5e-11
Total number of emitted molecules ( $n_T$ )	5.93e6	2.65e8

(f) Plastic 8 Shot 13: Energy: 70 mJ, Infrared (1064 nm)

Peaks detected	Change in Partial pressure at $t_1$ (Torr)	Change in Partial pressure at $t_2$ (Torr)
N 14	5.14e-11	3.54e-8



Mass 15	0	8.8e-9
O 16	0	6.81e-8
Water 18	5.82e-10	4.07e-9
N2 / CO 28	2.43e-10	1.76e-8
O2 32	1.62e-10	1.62e-10
CO2 44	3.82e-11	6.65e-8
Total number of emitted molecules ( $n_T$ )	1.751e6	3.26e8

(g) Viewport 2(c) Shot 1: Energy: 70 mJ, Infrared (1064 nm)

Peaks detected	Change in Partial pressure at $t_1$ (Torr)	Change in Partial pressure at $t_2$ (Torr)
N 14	1.25e-10	5.41e-9
Mass 15	1.74e-11	1.16e-9
O 16	3.52e-10	1.85e-8
N2 / CO 28	0	1.45e-8
CO2 44	1.96e-10	3.13e-8
Total number of emitted molecules ( $n_T$ )	1.12e6	1.15e8

(h) Viewport 12 Shot 2: Energy: 70 mJ, Green light (532 nm)

Peaks detected	Change in Partial pressure at $t_1$ (Torr)	Change in Partial pressure at $t_2$ (Torr)
H 2	0	1.09e-9
Mass 15	4.49e-11	1.145e-9
O 16	2.39e-11	6.95e-10
N <sub>2</sub> / CO 28	1.58e-10	4.36e-9
CO <sub>2</sub> 44	2.26e-11	1.3e-9
Total number of emitted molecules ( $n_T$ )	4.065e5	1.396e7

(i) Chamber Walls 2 (d) Shot 2: Energy: 70 mJ, Infrared (1064 nm)

Peaks detected	Change in Partial pressure at $t_1$ (Torr)	Change in Partial pressure at $t_2$ (Torr)
H 2	0	3.84e-8
N 14	0	1.73e-8
Mass 15	0	4.7e-9
O 16	0	1.92e-7

Water 18	0	1.85e-8
N2 / CO 28	1.63e-7	1.63e-7
CO2 44	1.61e-12	1.61e-12
Total number of emitted molecules ( $n_T$ )	7.89e8	1.223e9

## CHAPTER 5

### FUTURE STUDIES

#### 5.1 Future studies

The thesis has dealt with studies on the outgassing properties of a polished Rexolite plastic. The existence of a thin layer of gas on the surface of the Rexolite plastic has been studied carefully within the constraints of our measuring instruments. The energies at which the tests were conducted indicate minimum stimulated desorption from the surface of the Rexolite plastic. However, the light generated from large pulsed power machines both up and down stream from the plastic barrier relative to the propagation of the pulse may be intense enough to release atoms and molecules from the surface of the plastic barrier and/or the vacuum chamber. It is anticipated then, that the atoms/molecules that are released may be charged. A pair of electrodes on the sides of the Rexolite plastic, with a voltage source and an ammeter could indicate the presence of charged atoms/ molecules. It would be interesting to study the effect of the charged molecules, if present, on the surface flashover.

Detailed observation of the experimental results showed that there is a delay time associated with most of the molecules detected. More prominently for hydrogen where, in some cases, the signature detected is significantly delayed compared to other AMU signatures. The exact reason for this delay is not

thoroughly understood at this point of time. One could assume it to be due to diffusion through the sides of the plastic or due to molecules trapped between the Rexolite plastic and the viewport. It would be interesting to look at the various possible reasons for this time delay. One possible way could be by sealing the Rexolite plastic to the viewport and observing the results.

Synchronization of the time of laser triggering and the detecting time of the residual gas analyzer could lead to time of flight studies. This time of flight study could also provide an insight to the time delays observed in the experimental results.

It is interesting to note the different time scales in the experiment. The laser stimulates the mediums on time scales on the order of 4 to 7 ns. The RGA performs measurements on time scales on the order of 25 ms. There is about seven orders of magnitude difference in time between stimulation and detection. When the walls of the chamber are stimulated, the detection of residual molecules may take up to ones and tens of minutes. One might argue that the metal wall is thermally heated and there is not enough atmosphere to transport the heat, plus stainless steel is a poor thermal conductor. Consequently, heat loss is mainly due to radiation and emission of adsorbed material. It is not clear if this accounts for such long delays for partial pressure baselines to be achieved. The Rexolite piece, on the other hand, tends to yield an impulse of material being released over the RGA's transit time of measurement (~200 ms). Detection times for viewports are somewhere in-between. It would be interesting to study if there is a correlation between thermal losses and desorption effects.

## Appendix A

Matlab program to determine the resonant frequency and the restoring force:

RF.m

```
function wr=RF(w1)
wo1=2.97e15;
wo2=3.2e15;
uo=1.256e-6;
eo=8.85e-12;
wpe=2.89e15;
alp1=2.26;
er=2.53;
a02=((w1.^2)-(wo2.^2));
b02=(er-1);
c02=((wpe.^2).*a02)/((wo2.^2).*b02);
d02=((a02.^2)/(wo2.^2));
u=sqrt(c02-d02);
a01=((w1.^2)-(wo1.^2));
b01=((a01.^2)+((wo1.*u).^2));
X001=(1+((wpe.^2.*(a01))/(b01)));
Y001=((wpe.^2.*wo1.*u)/(b01));
Z001=((wo1.^2).*(uo.*eo));
wr=((alp1.^4)-((0.5.*Z001.*Y001).^2)+((Z001.*(alp1.^2)).*(X001)));
end
```

testRF.m

```
wre=fzero(@RF,8.89e15)
```

## Appendix B

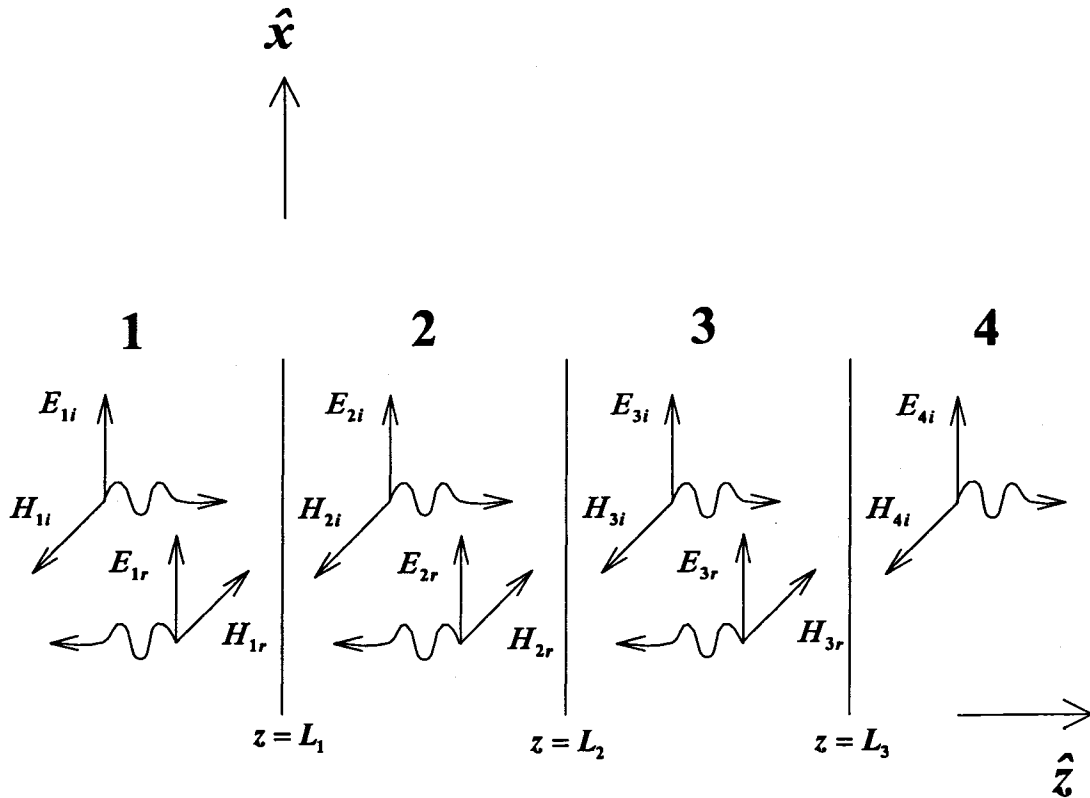


Fig: B.1 View showing the wave components in four region system in which a uniform plane wave normally incident.

This section of the thesis deals with the boundary value problems in multiple regions. A boundary value problem in electromagnetics is one involving two or more regions, separated by interfaces, for which solutions are desired such that Maxwell's equations are satisfied by the field solutions in the each region and the boundary conditions for each regions are also satisfied. Figure B.1 shows a four region system with a uniform plane wave normally incident on the surface  $z=L_1$ . The regions are sequentially divided as region 1 (air), region 2 (viewport), region 3 (Rexolite plastic) and region 4 (air). The goal of this section is

to solve for the electric field at any point in region 3, which is the plastic, in terms of the electric field in the region 1. This is to study the total energy dissipated in the plastic. A time harmonic field solution of the form  $e^{j\omega t}$  is assumed while solving for the wave components.

Consider, the total time harmonic electric and magnetic fields in  $k^{\text{th}}$  region

$$\vec{E}_k(\vec{r}, t) = \hat{x} \left\{ E_{ki} e^{-(\gamma_k z - j\omega t)} + E_{kr} e^{(\gamma_k z + j\omega t)} \right\} \quad (\text{B.1})$$

$$\vec{H}_k(\vec{r}, t) = \hat{y} \left\{ \frac{E_{ki}}{\eta_k} e^{-(\gamma_k z - j\omega t)} - \frac{E_{kr}}{\eta_k} e^{(\gamma_k z + j\omega t)} \right\} \quad (\text{B.2})$$

where

$$\gamma_k = \alpha_k + j\beta_k \approx j\omega \sqrt{\mu_k \epsilon_{\text{eff},k}}$$

and

$$\eta_k = \sqrt{\frac{\mu_k}{\epsilon_{\text{eff},k}}}$$

Here,  $\epsilon_{\text{eff},k} = \epsilon_r' - j\epsilon_r''$  or  $\epsilon_k \left[ 1 + \frac{\sigma_k}{j\omega\epsilon_k} \right]$  depending on the model describing the

medium. The terms  $E_{ki}$  and  $E_{kr}$  are the magnitudes of the incident and reflected electric fields in the  $k^{\text{th}}$  region;  $\eta_k, \gamma_k, \alpha_k$  and  $\beta_k$  are the intrinsic impedance, propagation coefficient, attenuation constant and the phase constant of the  $k^{\text{th}}$  region.

The tangential electric and magnetic field intensities are continuous across the boundary interfaces between the  $k$  and  $k+1$  mediums yielding



$$E_{ki} e^{-(\gamma_k L_k - j\omega t)} + E_{kr} e^{(\gamma_k L_k + j\omega t)} = E_{(k+1)i} e^{-(\gamma_{(k+1)} L_k - j\omega t)} + E_{(k+1)r} e^{(\gamma_{(k+1)} L_k + j\omega t)} \quad (B.3)$$

$$\frac{E_{ki}}{\eta_k} e^{-(\gamma_k L_k - j\omega t)} - \frac{E_{kr}}{\eta_k} e^{(\gamma_k L_k + j\omega t)} = \frac{E_{(k+1)i}}{\eta_{(k+1)}} e^{-(\gamma_{(k+1)} L_k - j\omega t)} - \frac{E_{(k+1)r}}{\eta_{(k+1)}} e^{(\gamma_{(k+1)} L_k + j\omega t)} \quad (B.4)$$

where  $k=1, 2, 3$  and  $E_{4r} = 0$  since the fourth region contains one planar boundary interface.

Dividing Eq. (B.3) by the incident field at the interface ( $z=L_k$ ), the reflection and transmission coefficients at the  $k, k+1$  boundary interfaces are defined as respectively,

$$\rho_{k,k+1} = \frac{E_{kr}}{E_{ki}} e^{2\gamma_k L_k} \quad (B.5)$$

and

$$\tau_{k,k+1} = \frac{E_{(k+1)i}}{E_{ki}} e^{-(\gamma_{k+1} - \gamma_k) L_k} \quad (B.6)$$

The reflection coefficient at any point in the  $k^{\text{th}}$  region is given as

$$\tilde{\rho}_k(z) = \rho_{k,k+1} e^{-2\gamma_k(L_k - z)} \quad (B.7)$$

Dividing Eq. (B.3) by  $E_{ki} e^{-(\gamma_k L_k - j\omega t)}$  and Eq. (B.4) by  $\frac{E_{ki}}{\eta_k} e^{-(\gamma_k L_k - j\omega t)}$  yields

$$1 + \rho_{k-1,k} = \frac{E_{ki}}{E_{(k-1)i}} e^{-(\gamma_k - \gamma_{k-1}) L_{k-1}} \left\{ 1 + \rho_{k,k+1} e^{-2\gamma_k(L_k - L_{k-1})} \right\} \quad (B.8)$$

$$1 - \rho_{k-1,k} = \frac{E_{ki}}{E_{(k-1)i}} \frac{\eta_{k-1}}{\eta_k} e^{-(\gamma_k - \gamma_{k-1}) L_{k-1}} \left\{ 1 - \rho_{k,k+1} e^{-2\gamma_k(L_k - L_{k-1})} \right\} \quad (B.9)$$

Adding Eqs (B.8) and (B.9) the incident electric field in region  $k-1$  can be written in terms of the incident electric field in region  $k$  as

$$E_{(k-1)i} = \frac{E_{ki}}{2} e^{-(\gamma_k - \gamma_{k-1})L_{k-1}} \left\{ 1 + \frac{\eta_{k-1}}{\eta_k} + \rho_{k,k+1} e^{-2\gamma_k(L_k - L_{k-1})} \left( 1 - \frac{\eta_{k-1}}{\eta_k} \right) \right\} \quad (\text{B.10})$$

Now making use of Eq (B.10) the incident electric fields in regions 2 and 3 is written as

$$E_{ki} = E_{(k-1)i} e^{(\gamma_k - \gamma_{k-1})L_{k-1}} \left\{ 1 + \frac{\eta_{k-1}}{\eta_k} + \rho_{k,k+1} e^{-2\gamma_k(L_k - L_{k-1})} \left( 1 - \frac{\eta_{k-1}}{\eta_k} \right) \right\}^{-1} \quad (\text{B.11})$$

$$E_{3i} = E_{2i} e^{(\gamma_3 - \gamma_2)L_2} \left\{ 1 + \frac{\eta_2}{\eta_3} + \rho_{34} e^{-2\gamma_3(L_3 - L_2)} \left( 1 - \frac{\eta_2}{\eta_3} \right) \right\}^{-1} \quad (\text{B.12})$$

$$E_{2i} = E_{1i} e^{(\gamma_2 - \gamma_1)L_1} \left\{ 1 + \frac{\eta_1}{\eta_2} + \rho_{23} e^{-2\gamma_2(L_2 - L_1)} \left( 1 - \frac{\eta_1}{\eta_2} \right) \right\}^{-1} \quad (\text{B.13})$$

Using Eqs. (B.12) and (B.13), a relation for the incident electric field in region 3 in terms of the incident electric field in region 1 can be obtained as:

$$E_{3i} = 4E_{1i} e^{(\gamma_3 - \gamma_2)L_2} e^{(\gamma_2 - \gamma_1)L_1} \times \left\{ 1 + \frac{\eta_1}{\eta_2} + \rho_{23} e^{-2\gamma_2(L_2 - L_1)} \left( 1 - \frac{\eta_1}{\eta_2} \right) \right\}^{-1} \left\{ 1 + \frac{\eta_2}{\eta_3} + \rho_{34} e^{-2\gamma_3(L_3 - L_2)} \left( 1 - \frac{\eta_2}{\eta_3} \right) \right\}^{-1} \quad (\text{B.14})$$

Consequently from Eq. (B.1), the total field at any point in region 3 is

$$E_3(z) = \left\{ 4E_{1i} e^{(\gamma_3 - \gamma_2)L_2} e^{(\gamma_2 - \gamma_1)L_1} \times \left\{ 1 + \frac{\eta_1}{\eta_2} + \rho_{23} e^{-2\gamma_2(L_2 - L_1)} \left( 1 - \frac{\eta_1}{\eta_2} \right) \right\}^{-1} \right\}^{-1} \times \left\{ 1 + \frac{\eta_2}{\eta_3} + \rho_{34} e^{-2\gamma_3(L_3 - L_2)} \left( 1 - \frac{\eta_2}{\eta_3} \right) \right\}^{-1} e^{-\gamma_3 z} \left[ 1 + \rho_{34} e^{-2\gamma_3(L_3 - z)} \right] \quad (\text{B.15})$$

where

$$\rho_{k,k+1} = \frac{Z_k(z = L_k) - \eta_k}{Z_k(z = L_k) + \eta_k}$$

$$\text{and } Z_k(L_{k-1}) = \eta_k \left\{ \frac{1 + \tilde{\rho}_k(z = L_{k-1})}{1 - \tilde{\rho}_k(z = L_{k-1})} \right\} = Z_{k-1}(L_{k-1})$$

and Eq. (B.7) defines  $\tilde{\rho}_k(z)$

## REFERENCES

- [1] H. Craig Miller, "Surface Flashover of Insulators", IEEE Transactions on Electrical Insulation Vol. 24 No. 5, pp.765-786, October 1989
- [2] R.A.Anderson and J.P.Brainard, "Mechanism of pulsed surface flashover involving electron stimulated desorption", J.Appl.Phys.51 (3), pp.1414-1420, March1980
- [3] R.A.Anderson and W.K.Tucker, "Vacuum Surface Flashover from bipolar stress", J.Appl.Phys. Vol 58, No 9, 1 November 1985
- [4] J.D.Cross, "High speed photography of surface flashover in vacuum", IEEE Trans. Electr. Insul. Vol.13, pp.145-148, 1978.
- [5] S. P. Bugaev, A. M. Iskol'dskii and G. A. Mesyats, "Investigation of the Pulsed Breakdown Mechanism at the Surface of a Dielectric in a Vacuum I. Nonuniform Field", Sov. Phys. Tech. Phys. Vol. 12, pp. 1358-1362, 1967
- [6] S. P. Bugaev and G. A. Mesyats, "Investigation of the Pulsed Breakdown Mechanism at the Surface of a Dielectric in a Vacuum II. Nonuniform Field", Sov. Phys. Tech. Phys. Vol. 12, pp. 1363-1369, 1967
- [7] J. P. Vigouroux, O. Lee-Deacon, C. Le Gressus, C. Juret, and C. Boiziau, "Surface Processes Occurring During Breakdown of HV Devices", IEEE Trans. Electr. Insul. Vol. 18, pp. 287-291, 1983.

- [8] J. P. Vigouroux, C. Le Gressus, and J. P. Durand, "Electrical Surface Breakdown: Secondary Electron Emission and Electron Spectroscopy of Insulators", *Scan. Electron Micro.* 11, pp. 513-520, 1985.
- [9] N. C. Jaitly and T. S. Sudarshan, "DC Surface Flashover Mechanism along solids in vacuum based on a collision-ionization Model", *J. Appl. Phys.* Vol. 64, pp. 3411-3418, 1988.
- [10] R. A. Anderson, "Anode-Initiated Surface Flashover", *Conf. Electr. Insul. Dielectr. Phen.*, pp. 173-179, 1979.
- [11] V. Belyaev, "Model of surface flashover of insulator in vacuum", *IEEE 18<sup>th</sup> Int. Symp. On Discharges and Electr. Insul.*, pp.151-154, 1998.
- [12] I.D.Smith, "Pulse Breakdown of Insulator Surfaces in poor vacuum", *Proc. Int. Sym. Insul. High Volt. Vac.*, Cambridge, USA, pp. 261-280, 1964.
- [13] A.Sivathanu Pillai and Reuben Hackam, "Surface Flashover of Solid Dielectric in Vacuum", *J.Appl.Phys.*53 (4), April 1982.
- [14] Eoin W. Gray, "Vacuum Surface Flashover: A high- pressure phenomenon", *J.Appl.Phys.*58 (1) 1 July 1985.
- [15] E.W.Gray and J.R.Pharney, "Statistical Behavior of Break Arc Durations and the Minimum Arc Sustaining Current" *IEEE Transactions on components and Hybrid Manufacturing Technology*, CHMT-2, 12 [1979]
- [16] A.A.Avdienko and A.V.Kiselev, *Sov. Phys. Tech. Phys.* 12, 381 [1967]
- [17] A.A.Avdienko and M.D.Malev, *Vacuum* 27, 643 [1977]

- [18] W.A.Stygar *et al*, "Improved Design of a high-voltage vacuum-insulator interface", *Physical Review Special Topics – Accelerators and Beams* 8, 050401,2005.
- [19] C. R. Li and T. S. Sudarshan, "Dielectric surface preflashover processes in vacuum", *J. Appl. Phys.* 76 (6), 15 September 1994.
- [20] N Schindler, D SchleuRner and Chr Edelman, Otto-von-Guericke- "Measurements of partial outgassing rates" University, Institute of Experimental Physics, D-39 106 Magdeburg, Germany received 9 September 1995, *Vacuum*, volume 47, number 4, pp 351-355, 1996, Published by Elsevier Science Ltd.
- [21] E.D.Erikson, T.G.Beal, D.D.Berger and B.A.Frazier, "Vacuum outgassing of various materials", *J.Vac.Sci.Technol.A* 2 (2), Apr-June 1984.
- [22] P.A.Redhead, National Research Council, Ottawa ON K1A 0R6, Canada, "Recommended practices for measuring and reporting outgassing data", pp.1667-1675, 1965. 2002 American Vacuum Society.
- [23] M.L.Knotek, "Stimulated Desorption," *Rep. Prog. Phys.* 47,. 1499-1561, 1984.
- [24] Karl Jousten, " Thermal Outgassing", *Physikalisch- Technische Bundesanstalt, Berlin, Germany.*
- [25] A. Neuber, M. Butcher, H. Krompholz, L. L. Hatfield and M. Kritiansen, H. Krompholz, "Dielectric surface flashover in vacuum" *IEEE Transactions on Dielectrics and Electrical Insulation* Vol. 6 No. 4, pp.512-515, August 1999

- [26] R.A. Murray, D.E. Pierce, R. Laureau, S. Laffey and J.R. Vig, "Thermal desorption of quartz crystals", IEEE International Frequency Control Symposium pp.696-704, 1995
- [27] Andreas A. Neuber, M. Butcher, H. Kromphloz, Lynn L. Hatfield and Magne Kritiansen, "The Role of Outgassing in surface flashover under vacuum", IEEE TRANSACTIONS ON PLASMA SCIENCE, VOL. 28, NO. 5, OCTOBER 2000
- [28] P.A.Redhead, Research Emeritus, Institute of Microstructural Sciences, National Research Council, Ottawa ON K1A 0R6, Canada; "Effects of readsorption on outgassing rate measurements", J.Vac.Sci.Technol.A 14(4),Jul/Aug 1996.
- [29] Osborne Milton, "Pulsed Flashover of insulators in vacuum" IEEE Transactions on Electrical Insulation Vol. EI-7, No. 1, pp.9-15, March 1972.
- [30] Markus Zahn, "Electromagnetic Field Theory, a problem solving approach"
- [31] Akira Ishimaru, "Electromagnetic Wave Propagation, Radiation and Scattering"
- [32] J.A. Cross, "Electrostatics Principles, Problems and Applications", Adam Hilger, Bristol, pp. 387-396, 1987.
- [34] Egon Matijevic, "Surface and Colloid Science", Vol.8
- [34] R. Allen Bowling, "A Theoretical Review of Particle Adhesion," in K.L. Mittal, ed., Particles on Surfaces I: Detection, Adhesion, and Removal, Plenum Press, NY, pp.129-142, 1988.
- [35] Jacob N. Israelachvili, Intermolecular and Surface Forces, Second Edition, Academic Press, NY, 1992

[36] Kevin Kendall, "Adhesion: Molecules and Mechanics," *Science* 263(25 March 1994):1720-1725.

[37] Geoffrey V. F. Seaman, "Chapter 27. Electrokinetic Behavior of Red Cells," in Douglas MacN. Surgenor, ed., *The Red Blood Cell, Second Edition, Volume II*, Academic Press, NY, pp. 1135-1224, 1975.

[38] K. Eric Drexler, *Nanosystems: Molecular Machinery, Manufacturing, and Computation*, John Wiley & Sons, NY, 1992



## VITA

Graduate College  
University of Nevada, Las Vegas

Hari Krishnan

**Home Address:**

1455, E. Rochelle Ave., Apt 57  
Las Vegas, NV-89119

**Degrees:**

Bachelor of Engineering, Electrical and Electronics Engineering, 2002  
University of Madras, India

**Thesis Title:**

Study of Gas Density Profile About a Plastic Test Piece under Vacuum

**Thesis Examination Committee:**

Chairperson, Dr. Robert A. Schill, Jr., Ph. D.  
Committee Member, Dr. Rama Venkat, Ph. D.  
Committee Member, Dr. Yahia Baghzouz, Ph. D.  
Graduate College Representative, Dr. William Culbreth, Ph. D.